



TECHNISCHE
UNIVERSITÄT
DARMSTADT

Physik

Families of
Chiral Two- plus Three-Nucleon Interactions
for
Accurate Nuclear Structure Studies

Dem Fachbereich Physik
der Technischen Universität Darmstadt

zur Erlangung des Grades
eines Doktors der Naturwissenschaften (Dr. rer. nat.)

genehmigte Dissertation von
M. Sc. Thomas Hüther
aus Offenbach am Main

Referent: Prof. Dr. Robert Roth
Korreferent: Priv.-Doz. Dr. Kai Hebeler

Darmstadt 2021
D17

Families of Chiral Two- plus Three-Nucleon Interactions for Accurate Nuclear Structure Studies

Familien chiraler Zwei- plus Dreiteilchenwechselwirkungen für präzise Kernstrukturuntersuchungen

Referent: Prof. Dr. Robert Roth

Korreferent: Priv.-Doz. Dr. Kai Hebel

Tag der Einreichung: 13.4.2021

Tag der mündliche Prüfung: 17.5.2021

Hüther,Thomas: Families of Chiral Two- plus Three-Nucleon Interactions for Accurate Nuclear Structure Studies

Darmstadt, Technische Universität Darmstadt

Veröffentlichungsjahr der Dissertation auf TUPrints: 2021

URN: urn:nbn:de:tuda-tuprints-185888

URL: <https://tuprints.ulb.tu-darmstadt.de/id/eprint/18588>



Veröffentlicht unter [CC BY-NC-ND 4.0 International](https://creativecommons.org/licenses/)

<https://creativecommons.org/licenses/>

Abstract

Chiral effective field theory allows for a systematically improvable construction of nuclear interactions and currents rooted in quantum chromodynamics (QCD). In this thesis we propose families of chiral nucleon-nucleon (NN) plus three-nucleon (3N) interactions and develop a framework to incorporate nuclear exchange-current contributions to the $M1$ operator in importance-truncated no-core shell model (IT-NCSM) calculations.

The interaction families base on the Entem, Machleidt and Nosyk NN interactions, which are supplemented at next-to-next-to-leading order (N^2LO) and next-to-next-to-next-to-leading order (N^3LO) with 3N interactions consistent in chiral order, non-local regulator, and cutoff values. We study the dependence of observables of light- and medium-mass nuclei on the 3N low-energy constants (LECs). Based on the results, we propose two alternative optimization procedures for the LECs. One optimizes the ground-state energies of 3H and 4He and the other the ground-state energies of 3H and ^{16}O .

The performance of both interaction families is explored for ground-state energies and radii of light- and medium-mass nuclei as well as for spectra of p-shell nuclei. In these calculations, we give a fully estimation of the uncertainties for both the many-body method and the interaction. The uncertainties due to the chiral truncation are estimated with a state-of-the-art approach rooted in Bayesian statistics. Both interaction families lead to robust results for the considered observables. In particular, the inclusion of the ground-state energy of ^{16}O in the optimization procedure leads to energies and radii, which reproduce the experimental values up to the nickel isotopes well.

For precision studies of electromagnetic observables like multipole moments and transition strengths, we need in addition to an accurate interaction also consistent exchange currents. In this work, we develop the necessary framework to include exchange-current contributions to the $M1$ operator in IT-NCSM calculations. This comprises the correct treatment in the similarity renormalization group (SRG) as well as the transformation into a suitable single-particle basis representation. This leads to the first fully chiral determination of the magnetic dipole moment of the ground state of 6Li as well as the magnetic dipole transition strength from the first 0^+ to the 1^+ ground state of 6Li including the next-to leading order (NLO) current contribution to the $M1$ operator. This study shows that both the consistent treatment in the SRG and the exchange-current contribution to the $M1$ operator are important to match theory and experiment.

Zusammenfassung

Die chirale effektive Feldtheorie ermöglicht die Konstruktion von systematisch verbesserbaren Kernwechselwirkungen und -strömen, die in der Quantenchromodynamik verwurzelt sind. In dieser Arbeit schlagen wir Familien von chiralen Nukleon-Nukleon (NN) plus Dreinukleon (3N) Wechselwirkungen vor und entwickeln einen Rahmen, um Beiträge von Austauschströmen zum $M1$ -Operator in das Importance-Truncated No-Core Shell Model (IT-NCSM) mit einzubeziehen.

Diese Wechselwirkungsfamilien basieren auf den Entem, Machleidt und Nosyk NN Wechselwirkungen, welche mit nächst-zu-nächst-zu-führender Ordnung ($N^2\text{LO}$) und nächst-zu-nächst-zu-führender Ordnung ($N^3\text{LO}$) 3N Wechselwirkungen kombiniert werden. Diese sind konsistent in chiraler Ordnung, nichtlokalem Regulator und Cutoff-Werten. Wir untersuchen die Abhängigkeiten von leichten und mittelschweren Kernen von den Niederenergiekonstanten (LECs) der 3N Wechselwirkungen. Basierend auf diesen Ergebnissen schlagen wir zwei Optimierungsmöglichkeiten der LECs vor. Eine optimiert die Grundzustandsenergien von ^3H und ^4He und die andere die Grundzustandsenergien von ^3H und ^{16}O .

Die Leistungsfähigkeit beider Wechselwirkungsfamilien wird für Grundzustandsenergien und -radien von leichten und mittelschweren Kernen sowie für Spektren von p-Schalen Kernen untersucht. Bei diesen Berechnungen geben wir eine vollständige Abschätzung der Unsicherheiten sowohl für die Vielteilchenmethode als auch für die Wechselwirkung an. Die Unsicherheiten aufgrund der chiralen Trunkierung werden mit einem modernen, auf der Bayes'schen Statistik basierenden Ansatz abgeschätzt. Beide Wechselwirkungsfamilien führen für die betrachteten Observablen zu robusten Ergebnissen. Insbesondere die Einbeziehung der Grundzustandsenergie von ^{16}O in das Optimierungsverfahren führt zu Energien und Radien, die die experimentellen Werte bis zu den Nickelisotopen gut reproduzieren.

Für Präzisionsstudien elektromagnetischer Observablen wie Multipolmomenten und Übergangsstärken benötigen wir zusätzlich zu einer genauen Wechselwirkung auch konsistente Austauschströme. In dieser Arbeit entwickeln wir den notwendigen Rahmen, um Austauschstrombeiträge zum $M1$ -Operator in IT-NCSM Rechnungen miteinzubeziehen. Dies umfasst die korrekte Behandlung in der Similarity Renormalization Group (SRG) sowie die Transformation in eine geeignete Ein-Teilchen-Basisdarstellung. Dies führt zur ersten vollständig chiralen Bestimmung des magnetischen Dipolmoments des Grundzustands von ^6Li sowie der magnetischen Dipol-Übergangsstärke vom ersten 0^+ zum 1^+ -Grundzustand von ^6Li einschließlich des Strombeitrags nächst-zu-führender Ordnung (NLO) zum $M1$ -Operator. Diese Untersuchung zeigt, dass sowohl die konsistente Behandlung in der SRG als auch der Austauschstrombeitrag zum $M1$ -Operator wichtig für die Übereinstimmung von Theorie und Experiment sind.

Contents

Acronyms and Abbreviations	vii
1 Introduction	1
2 Chiral Effective Field Theory	5
2.1 Quantum Chromodynamics and Chiral Perturbation Theory	5
2.2 Effective Interactions	8
2.3 Two Nucleon Interactions	10
2.3.1 Entem and Machleidt Interaction	11
2.3.2 Entem, Machleidt and Nosyk Interactions	11
2.3.3 Semi-local Regularized Interactions	11
2.4 Three Nucleon Interactions	13
2.4.1 Basic Structures	13
2.4.2 Local 3N Interaction	15
2.4.3 Non-Local 3N Interaction	16
2.4.4 Semi-Local 3N Interaction	17
2.5 Uncertainty Quantification	17
3 Solving the Nuclear-Many-Body Problem	21
3.1 No-Core Shell Model	21
3.1.1 Single-Particle Formulation	22
3.1.2 Jacobi Formulation	23
3.1.3 Importance Truncated No-Core Shell Model	26
3.1.4 Basis Optimizations	27
3.1.5 Normal-Ordered Two-Body Approximation	27
3.2 Similarity Renormalization Group	28
3.3 In-Medium Similarity Renormalization Group	32
3.3.1 Second Quantization and Normal Ordering	32
3.3.2 IM-SRG Concept	33
3.3.3 Uncertainties	35
3.4 Calculation of Radii	35
4 Optimization of Non-Local 3N Interactions	37
4.1 EM Local vs Non-Local 3N	37
4.2 EMN Complemented with the Non-Local 3N	39
4.2.1 Fitting the LECs to the Triton Binding Energy	39
4.2.2 Exploring c_D in the ${}^4\text{He}$ Energy-Radius Plane	40
4.2.3 Performance in Medium-Mass Nuclei	42
4.3 Many-Body Optimized Interactions	45
4.4 Few-Body Optimized Interactions	49
4.5 Globally Optimized Interactions	52
4.6 Results for Many-Body Systems	54
4.6.1 Few-Body Results	54

4.6.2	Medium-Mass Properties	55
4.6.3	Results of p-Shell Isotopes	60
5	Interactions with Semi-Local Regulators	67
5.1	Results of the NN Interaction	67
5.2	Modifications of the NN Interaction	69
5.3	Effects of the 3N Interaction	74
6	Next-to-Leading Order Contributions to the Magnetic Moment	79
6.1	Electromagnetic Interaction	80
6.2	Static Multipole Moments	83
6.3	Multipole Transitions	85
6.4	Magnetic Dipole Moment Operator	86
6.5	Matrix Elements of the M1 Operator in a Relative HO Basis	88
6.6	Consistent SRG Transformation	89
6.7	Transformation into Single-Particle Coordinates	90
6.8	${}^6\text{Li}$ Results	94
7	Conclusion	101
A	Appendix	103
A.1	Isospin and Projection Operators	103
A.2	Jacobi Coordinates	103
A.3	Harmonic Oscillator Basis	104
A.4	Clebsch Gordan, 3J, 6J and 9J	104
A.5	Harmonic Oscillator Brackets	105
A.6	Wigner-Eckart Theorem	105
A.7	Embedding an Operator That Depends Only on One Angular Momentum	106
A.8	M1 Operator with Spherical Tensor Matrix Elements Expressions	106
	Bibliography	107
	Danksagung	123
	Lebenslauf	125

Acronyms and Abbreviations

3N	nucleon nucleon nucleon
4N	nucleon nucleon nucleon nucleon
CFP	coefficient of fractional parentage
CHPT	chiral perturbation theory
cont	contact
EFT	effective field theory
EKM	Epelbaum, Krebs, and Meißner
EM	Entem and Machleidt
EMN	Entem, Machleidt, and Machleidt
FBO	few-body optimized
GBO	globally optimized
HF	Hartree-Fock
HO	harmonic oscillator
HOBs	harmonic oscillator brackets
IM-SRG	in-medium similarity renormalization group
IT-NCSM	importance truncated no-core shell model
LEC	low energy constant
LENPIC	Low Energy Nuclear Physics International Collaboration
LO	leading order
MBO	many-body optimized
MEC	mesons exchange current
NAT	natural orbital
NCSM	no-core shell model
NLO	next-to-leading order
N ² LO	next-to-next-to-leading order
N ³ LO	next-to-next-to-next-to-leading order
N ⁴ LO	next-to-next-to-next-to-next-to-leading order
N ⁵ LO	next-to-next-to-next-to-next-to-next-to-leading order
NN	nucleon nucleon
NN+3N _{ind}	nucleon nucleon plus induced three nucleon
NN+3N _{full}	nucleon nucleon plus full three nucleon
NO2B	normal-ordered two-body
np	neutron proton
OLS	Okubo–Lee–Suzuki
OPE	one-pion exchange
pp	proton proton
πN	pion nucleon
QCD	quantum chromodynamics
SCS	semi-local coordinate space
SMS	semi-local momentum space
SRG	similarity renormalization group
TPE	two-pion exchange
UCOM	unitary correlation operator method

1 | Introduction

In recent years, many advances have been made in *ab initio* nuclear structure physics, where we try to understand properties of nuclei and their reactions. Under an *ab initio* description of nuclei we understand a microscopic description of nuclei, where all introduced approximations can be systematically improved. From a fundamental point of view one might start with the theoretical framework of quantum chromodynamics (QCD), since it is the theory of the strong interaction and explains the properties and dynamics of quarks and gluons. The direct description of many-quark systems beyond the lightest hadrons and nuclei is quite challenging, because the QCD is non-perturbative in the low-energy regime.

Using nucleons as degrees of freedom with inter-nucleon interactions is a more productive ansatz to describe many-nucleon systems. Phenomenological high-precision potentials like the Argonne V18 [1] or CD-Bonn [2] potentials provide an excellent description of experimental nucleon-nucleon (NN) data with χ^2 per degree of freedom of the order of 1.

Discrepancies between many-body calculations based on NN interactions and experiments indicated that the inclusion of three-nucleon (3N) interactions is necessary [3]. Phenomenological 3N interactions like the Illinois 3N interactions [4] in combination with the Argonne V18 NN interactions improved the theoretical description of the investigated systems.

In the spirit of *ab initio*, interactions based on chiral effective field theory (EFT) [5–8] have taken over in the recent years. This framework uses nucleons and pions as degrees of freedom and incorporates the symmetries of QCD. These interactions are not only rooted in the underlying QCD, but are also systematically improvable. Based on a separation of scales, a low-momentum expansion is employed. This separation limits the occurring contributions to a finite number at a given chiral order. With increasing chiral order the interactions can be improved and many-body interactions as well as nuclear currents emerge naturally. This so-called chiral expansion orders the importance of the different contributions automatically starting with only NN interactions at leading order (LO), 3N interactions emerge at next-to-next-to-leading order (N²LO), 4N interactions at next-to-next-to-next-to-leading order (N³LO) and so on. Different contributions of these interactions come with low-energy constants (LECs) that need to be determined. Currently, these LECs are fitted to experimental data, but with increasing computational power and ongoing improvements in lattice QCD [9–12] the matching to the underlying theory is in prospect.

The systematic improability of the chiral EFT interactions gives the opportunity to estimate theoretical uncertainties for resulting observables. How to estimate these uncertainties is currently a topical subject in nuclear theory. A first approach based on the chiral expansion proposed by Epelbaum, Krebs, and Meißner (EKM) [13] gives an initial assessment of these uncertainties and has been used frequently [13–16]. Extended approaches based on Bayesian statistics have been developed in the BUQEYE collaboration [17–19], which allow for a statistical interpretation and the quantification of a degree-of-belief interval.

Besides the conceptional improvements in the construction of the interactions, a lot of advances have been made in the development of many-body methods, which solve the stationary A -body Schrödinger equation. At the same time, a significant increase in computational resources extended the reach of established methods further. Different methods are used in different nuclear mass regions. For light nuclei within the p-shell we use the powerful no-core shell model (NCSM) [20, 21] in single-particle as well as in Jacobi formulation. The basic

idea of the NCSM is to formulate the stationary Schrödinger equation as a matrix eigenvalue problem and solve it in a suitable finite basis representation. By systematically increasing the model-space dimension one improves the solution until it converges. The NCSM allows to calculate besides the energies of the low-lying states, in principle, any observable, since we explicitly calculate the wave functions and can obtain, for example, radii and electromagnetic multipole moments via the evaluation of the expectation values of the corresponding operator with the wave functions. In the importance-truncated no-core shell model (IT-NCSM) [22] the range of computable nuclei can be extended by using an additional truncation that probes the importance of a state a priori and excludes states from the model space that do not fulfill an importance condition motivated by perturbation theory.

The convergence of the NCSM and similar methods with model-space dimension is relatively slow for bare interactions obtained, amongst others, within chiral EFT. This convergence behavior is particularly connected to short-range correlations that are difficult to represent in typical basis choices. The similarity renormalization group (SRG) [23, 24] approach is a successfully applied tool to enhance the convergence. The SRG is based on a unitary transformation of the Hamiltonian carried out with a flow-equation ansatz that decouples low- and high-momentum states and thereby effectively prediagonalizes the Hamiltonian. In contrast to other methods, which aim to accelerate the convergence, like the Okubo–Lee–Suzuki (OLS) approach [21, 25, 26] or the unitary correlation operator method (UCOM) [23], the unitary transformation operator does not need to be constructed explicitly, but can be tailored flexibly to a specific task via a so-called generator. Furthermore, many-body forces can be treated straight forward in the SRG, even though current applications are usually restricted up to 3N forces. The use of the SRG introduces induced many-body forces, which need to be taken into account. By neglecting these forces one introduces uncertainties. Therefore, the use of the SRG comes with a trade off between a non-converged many-body calculation and uncertainties due to induced many-body forces, where the uncertainties due the former one are usually larger.

In addition to the use as a prediagonalization approach, the SRG can be used to solve the stationary Schrödinger equation. This leads to the in-medium similarity renormalization group (IM-SRG) [27–32]. In this approach, the Hamiltonian is rewritten in a normal ordered form with respect to a reference state and the SRG flow equation is used to decouple the reference state from all excited states, such that the reference state becomes an eigenstate of the Hamiltonian. In the simplest formulation, the single-reference IM-SRG is restricted to closed shell nuclei, but this formulation is also computationally affordable and extends the range of calculable nuclei far into the medium-mass regime [33], which makes the IM-SRG an excellent method to benchmark interactions.

The many-body methods introduced before are the main methods that we use in this work. As indicated before, there are additional methods available. For example, the coupled cluster method [34, 35] is a decoupling method of the Hamiltonian similar to the IM-SRG, but does not use a unitary transformation. It is also possible to combine the IM-SRG and the NCSM, which leads to the in-medium no-core shell model [36, 37]. In this method the IM-SRG is used as an additional intermediate step to enhance the convergence of the NCSM. An additional class of many-body approaches are quantum Monte Carlo methods [38, 39]. Here, one focuses on optimizing the many-body wave function. By probing the different many-body approaches against each other [33], we can learn about sensitivities of these methods and gain a good understanding of the uncertainties of the different approaches.

With these advances in many-body approaches, we are now in the position to probe interactions based on chiral EFT. In the past, many applications have not exhausted the opportunities provided by chiral EFT. A widely used chiral EFT interaction is the NN in-

teraction at $N^3\text{LO}$ by Entem and Machleidt [40] complemented with a local 3N interaction at $N^2\text{LO}$ [41]. However, with a single interaction at a specific chiral order we cannot perform a systematic uncertainty quantification. Furthermore, between the NN and 3N force the chiral orders as well as the regularization schemes are inconsistent. This interaction also systematically underestimates nuclear radii, particularly in the medium-mass regime [42–44].

There are other interactions available, for example the NNLO_{sat} interaction [45], which is a pure $N^2\text{LO}$ interaction with a consistent regularization scheme. This interaction benefits from a simultaneous fitting procedure, which takes into account NN phase-shifts as well as few- and many-body observables. Hence, this interaction also leads to a better description of radii. However, here also only a single chiral order is available such that a systematic order-by-order analysis cannot be applied.

At the moment there are three NN interaction families available. A family of interactions consists of multiple chiral orders and, ideally, of multiple cutoffs. These families are the semi-local coordinate space (SCS) [13, 14], the semi-local momentum space (SMS), and the non-local Entem, Machleidt and Nosyk (EMN) [46] interactions. Following the chiral power counting, starting from $N^2\text{LO}$ the 3N interactions contribute to the same extent as the NN interactions. Hence, for a systematic order-by-order analysis of many-body observables, we need 3N interactions.

Within the low energy nuclear physics international collaboration (LENPIC) [47] we aim to construct consistent chiral EFT NN and 3N interactions as well as exchange currents for the semi-local interactions SCS and SMS. The EMN interactions can be complemented with non-local 3N interactions at $N^2\text{LO}$ and $N^3\text{LO}$ [48, 49].

In this thesis, we aim to construct families of NN plus 3N interactions that can accurately describe nuclear observables. In particular, we supplement the EMN NN with optimized 3N interactions, such that we can estimate uncertainties of many-body observables originating from the interactions and from the many-body approaches.

For the comparison of theory with experiment, electromagnetic observables are of special interest, since electromagnetic observables, like multipole moments and transition strengths, probe different aspects of the wave functions than the energy or radii. For precision studies of other observables than the energy, contributions from so-called exchange currents can play a role. These exchange currents can also be constructed consistently within chiral EFT. Recently, first explorative results on the impact of electromagnetic currents derived in chiral EFT have been obtained by Marcucci *et al.* [50] as well as by Pastore *et al.* [51]. They show that these current contributions are not negligible. An additional goal of this work is to probe the NLO current contributions to the $M1$ operator in ${}^6\text{Li}$ in a fully chiral framework.

This thesis is organized in 7 chapters. Following this introduction, we start with a discussion of the chiral EFT in chapter 2, where we introduce its basic concepts as well as the interactions used in this thesis. Thereafter, we introduce in chapter 3 details of the different many-body approaches and optimizations that we employ to solve the stationary Schrödinger equation, in particular the NCSM, SRG, and the IM-SRG. In chapter 4 we explore the EMN interactions in combination with non-local 3N interactions and introduce two optimization procedures. These optimizations lead to two interaction families that we probe in light- and medium-mass nuclei. In chapter 5 we study ground-state energies and radii of medium-mass nuclei based on the semi-local interactions developed within LENPIC and investigate the effect of different regularization choices for the 3N interaction. The inclusion of the exchange-current contributions to the $M1$ operator is described in chapter 6. Finally, in chapter 7 we conclude this work with a short summary and outlook.

2 | Chiral Effective Field Theory

In nuclear structure theory one uses nucleons as degrees of freedom to describe nuclei. Nucleons are not fundamental particles and thus have an intrinsic structure. The forces between nucleons can be regarded as a residual interaction of the subnuclear interaction between quarks and gluons. Thus, the interaction between the nucleons is only an effective description of the underlying theory of quantum chromodynamics (QCD). Phenomenological high-precision potential models such as Argonne V18 [1] or CD-Bonn [2] potentials provide an excellent description of experimental NN data. In recent years, much effort has been put into the development of interactions based on chiral effective field theory (EFT) to gain a link to the underlying theory of the strong interaction, the QCD. This framework allows the construction of consistent many-body forces and nuclear current operators. In addition, interactions derived in chiral EFT can be systematically improved in terms of dominant dynamical contributions, and therefore a systematic uncertainty quantification is possible. In this chapter we will discuss the basic foundation of chiral EFT and the interactions we are using in this work. This chapter covers only the basic concepts and for more details the reader is referred to the extensive literature [5–8].

We start this chapter with a short introduction to QCD and chiral perturbation theory. This is followed by the description of how the interaction is constructed as well as the chiral power counting. Thereafter, we give an overview about the NN and 3N interactions we are using in this thesis. We end this chapter with a discussion of how we obtain theoretical uncertainties from the chiral EFT.

2.1 | Quantum Chromodynamics and Chiral Perturbation Theory

The fundamental theory of the strong interaction is QCD. QCD uses quarks and gluons as degrees of freedom to construct composite particles called hadrons. In total, there are six quark flavors. They are fermions, carry an electric charge and in addition a color charge (red, green, blue). Their antiparticles are antiquarks, which carry anticolors. The concept of color has been introduced since isolated quarks are not observed. They exist only as constituents of color-neutral objects, for instance quark-antiquark pairs (mesons) or three-quark systems (baryons). This phenomenon is referred to as color confinement. For completeness, also candidates of four and five quark systems have recently been observed experimentally [52–54].

Besides the color confinement, asymptotic freedom is the second main property of QCD. With increasing energy the strong coupling constant decreases [55]

$$\alpha_s(Q^2) \approx \frac{1}{\beta_0 \ln(Q^2/\Lambda_{\text{QCD}}^2)}, \quad (2.1)$$

where Q is the momentum scale, $\Lambda_{\text{QCD}} \approx 200$ MeV is the so called QCD scale and β_0 is a constant, which depends on the number of active flavors. Hence, the coupling constant is often referred to as a running coupling constant. For high energies the coupling α_s goes to

zero and a perturbative treatment of QCD is possible. For the low-energy regime, which is of interest for nuclear structure calculations, the coupling constant increases and a perturbative treatment is not applicable. Without a perturbative treatment, in lattice QCD [12] one tries to solve the problem with a computationally demanding ansatz. Currently, lattice QCD is limited to unnaturally large quark masses and only the lightest nuclear systems.

Another approach is the construction of an effective theory, which is appropriate for the energy scale of the process of interest. Chiral perturbation theory (CHPT) is the effective theory of QCD. It was formulated by Weinberg [56] and further elaborated by Glasser and Leutwyler [57, 58]. In CHPT the symmetries of QCD play a crucial role, in particular the approximate chiral symmetry, which is valid for the two and, to some extent, also for the three lightest quarks.

Lets start with the QCD Lagrangian for the two lightest quark flavors up and down

$$\mathcal{L}_{\text{QCD}} = \bar{q}(i\gamma_\mu D^\mu - \mathcal{M})q - \frac{1}{4}G_{\mu\nu,a}G_a^{\mu\nu}, \quad (2.2)$$

with the gauge covariant derivative $D^\mu = \partial_{mu} - ig_s G_\mu^a \lambda_a / 2$, where G_μ^a is the gluon field for the eight different gluons $a = 1, \dots, 8$, λ_a are the SU(3) Gell-Mann matrices, and g_s is the coupling constant which connects to the strong coupling constant in equation (2.1) via $\alpha_s = g_s^2 / (4\pi)$. Further, q are the quark fields and $G_a^{\mu\nu}$ is the gluon field strength tensor, and $\mathcal{M} = \text{diag}(m_u, m_d)$ is the quark mass matrix.

By redefining the quark fields in terms of left- and right-handed fields with

$$q_L = \frac{1 - \gamma_5}{2}q, \quad (2.3)$$

$$q_R = \frac{1 + \gamma_5}{2}q, \quad (2.4)$$

one can rewrite the Lagrangian (2.2) into

$$\mathcal{L}_{\text{QCD}} = \bar{q}_L i\gamma_\mu D^\mu q_L + \bar{q}_R i\gamma_\mu D^\mu q_R - \bar{q}_L \mathcal{M} q_R - \bar{q}_R \mathcal{M} q_L - \frac{1}{4}G_{\mu\nu,a}G_a^{\mu\nu}. \quad (2.5)$$

This notation shows that the left- and right-handed quark fields only connect through the mass term. Compared to the hadron mass scale of approximately 1 GeV the masses of the up and down quarks $m_u \approx 2.2$ MeV and $m_d \approx 4.7$ MeV [59] are very small. Therefore, it is a good approximation to assume them to be zero. This limit of vanishing quark masses is called the chiral limit. In this limit the Lagrangian (2.5) is invariant under global flavor rotations of the left- and right-handed quark fields

$$q_L \rightarrow q'_L = \exp\left(\frac{-i\Theta_L \cdot \tau}{2}\right)q_L, \quad (2.6)$$

$$q_R \rightarrow q'_R = \exp\left(\frac{-i\Theta_R \cdot \tau}{2}\right)q_R. \quad (2.7)$$

Here, τ and $\Theta_{L/R}$ represent the Pauli matrices in flavor space and their corresponding rotation angles. These rotations corresponding to a global SU(2)_L × SU(2)_R symmetry are also referred to as the chiral symmetry. In total, the Lagrangian in the chiral limit fulfills the SU(2)_L × SU(2)_R × U(1)_V × U(1)_A symmetry group, where the vector symmetry U(1)_V corresponds to the quark number conservation and the axial symmetry U(1)_A is broken by quantum effects, the so-called U(1)_A anomaly.

From the hadronic spectrum we have evidence that the chiral symmetry is spontaneously broken. We speak about a spontaneously broken symmetry, if the ground state of a system

exhibits less symmetries than the underlying Lagrangian. If the symmetry was not broken, we would expect degenerate hadron multiplets of opposite parity [5]. This is not the case. For example the vector meson ρ has a negative parity ($J^P = 1^-$) and a mass of 776 MeV [59], while the corresponding a_1 meson with positive parity ($J^P = 1^+$) has a much larger mass of 1230 MeV. Instead, the ρ meson comes in three charged states (ρ^-, ρ^0, ρ^+) with a small mass differences (≈ 1 MeV). This indicates that the chiral symmetry is spontaneously broken down to its subgroup $SU(2)_V$, which is the isospin symmetry. In a spontaneously broken system, we expect the existence of massless Goldstone bosons. These Goldstone bosons can be identified with the very light isospin triplet of the pions. The pions are not massless $M_\pi \approx 140$ MeV [59], but are very light in comparison to other hadrons. That the pions are not massless can be traced back to the – in reality – non vanishing masses of the up and down quarks. Therefore, the chiral symmetry is also explicitly broken. Due to the non-vanishing pion masses we call these the pseudo-Goldstone bosons.

Now, we have identified the pions as degrees of freedom for the effective theory. The most general Lagrangian with the pions as degrees of freedom has an infinite number of terms

$$\mathcal{L}_\pi = \mathcal{L}_\pi^{(2)} + \mathcal{L}_\pi^{(4)} + \dots \quad (2.8)$$

In CHPT we can order these contributions in a systematic improvable way via dimensional analysis. We analyze the different terms in powers of $(Q/\Lambda_\chi)^\nu$, where Q is the soft scale associated with a typical momentum or the pion mass, and $\Lambda_\chi \approx 1$ GeV the chiral breakdown scale. This breakdown scale is expected to be of the order of the ρ -meson mass and has an upper bound at $4\pi F_\pi$ [60], where F_π is the pion-decay constant. This expansion is often referred to as the chiral expansion and allows us to evaluate only a finite number of Feynman diagrams at a given order.

Adding nucleons in this scheme leads to the problem that the nucleon mass M_N is of the same order as the breakdown scale Λ_χ . This problem can be overcome in the so called heavy baryon formalism [61, 62], where we separate the four-momentum of the baryons into a massive Mv_μ and an additional small momentum k_μ part

$$p_\mu \rightarrow Mv_\mu + k_\mu. \quad (2.9)$$

Here v_μ is the four-velocity of the baryon satisfying $v_\mu v^\mu = 1$ as well as $v_\mu k^\mu \ll M$ and the small momentum k_μ is of the order of the soft scale. In this formalism the baryon mass M is used as an additional hard scale in the theory. In the chiral limit, this allows to expand the pion-nucleon Lagrangian $\mathcal{L}_{\pi N}$ in powers of the inverse baryon mass $1/M$:

$$\mathcal{L}_{\pi N} = \mathcal{L}_{\pi N}^{(1)} + \mathcal{L}_{\pi N}^{(2)} + \mathcal{L}_{\pi N}^{(3)} + \dots \quad (2.10)$$

In addition to these terms, where pions interact with the nucleons, we need to incorporate purely nucleonic contact terms in the theory. These terms have multiple purposes: They renormalize loop integrals in the theory, make the results independent of regulator parametrizations and are needed to absorb unresolved short-range dynamics of the nuclear force

$$\mathcal{L}_{NN} = \mathcal{L}_{NN}^{(0)} + \mathcal{L}_{NN}^{(2)} + \mathcal{L}_{NN}^{(4)} + \dots \quad (2.11)$$

Finally, we obtain the most general Lagrangian, which uses pions and nucleons as degrees of freedom and fulfills the exact and broken symmetries of QCD

$$\mathcal{L}_{\text{eff}} = \mathcal{L}_\pi + \mathcal{L}_{\pi N} + \mathcal{L}_{NN} + \dots, \quad (2.12)$$

where the ellipsis stands for further terms with more than two nucleons with and without pions. All these terms come with so called low-energy constants (LECs), which need to be determined through fits on experimental data or through matching with lattice QCD calculations. However, the lattice QCD calculations are as of today not accurate enough to extract the LECs reliably.

2.2 | Effective Interactions

Once the effective Lagrangian is constructed, we can obtain the purely nucleonic effective interaction. This decoupling can be achieved for example through time-ordered perturbation theory [63] or the method of unitary transformation [64, 65]. Here, we sketch the method of unitary transformation.

Using the projection operators $\hat{\eta}$ and $\hat{\lambda}$ on the purely nucleonic and the remaining subspace, the stationary Schrödinger equation can be written as

$$\begin{pmatrix} \hat{\eta}\hat{H}\hat{\eta} & \hat{\eta}\hat{H}\hat{\lambda} \\ \hat{\lambda}\hat{H}\hat{\eta} & \hat{\lambda}\hat{H}\hat{\lambda} \end{pmatrix} \begin{pmatrix} |\phi\rangle \\ |\psi\rangle \end{pmatrix} = E \begin{pmatrix} |\phi\rangle \\ |\psi\rangle \end{pmatrix}. \quad (2.13)$$

With the ansatz of Ôkubo [66] for a unitary transformation for the Hamiltonian $\hat{U}^\dagger \hat{H} \hat{U}$ with the unitary operator

$$\hat{U} = \begin{pmatrix} \hat{\eta}(1 + \hat{A}^\dagger \hat{A})^{-\frac{1}{2}} & \hat{A}^\dagger(1 + \hat{A}^\dagger \hat{A})^{-\frac{1}{2}} \\ \hat{A}(1 + \hat{A}^\dagger \hat{A})^{-\frac{1}{2}} & \hat{\lambda}(1 + \hat{A}^\dagger \hat{A})^{-\frac{1}{2}} \end{pmatrix} \quad (2.14)$$

the different subspaces can be decoupled. Here, the operator \hat{A} fulfills

$$\hat{A} = \hat{\lambda} \hat{A} \hat{\eta}. \quad (2.15)$$

With this ansatz the unitary transformation decouples the subspaces, if the operator \hat{A} solves the following nonlinear equation:

$$\hat{\lambda}(\hat{H} - [\hat{A}, \hat{H}] - \hat{A}\hat{H}\hat{A})\hat{\eta} = 0. \quad (2.16)$$

Here, $[\dots, \dots]$ is a commutator. Equation (2.16) can be solved perturbatively, if we separate the Hamiltonian into a free \hat{H}_0 and an interacting \hat{H}_I part:

$$\hat{H} = \hat{H}_0 + \hat{H}_I. \quad (2.17)$$

The effective potential can then be obtained via

$$\hat{V}_{\text{eff}} = \hat{\eta} \hat{U}^\dagger \hat{H} \hat{U} \hat{\eta} - \hat{H}_0. \quad (2.18)$$

To solve equation (2.16), the interacting part \hat{H}_I is expanded in a power series. This allows to solve for the operator \hat{A} in an iterative manner. For chiral potentials the chiral power counting is used and the interacting part is expanded in powers of Q^ν . Different interaction parts are usually depicted in diagrammatic form as illustrated in figure 2.1.

We employ interactions based on the chiral power counting of Weinberg [67–69]. There are discussions to improve the power counting by, for example, promoting short-range couplings to lower orders [70, 71]. However, no suitable interactions for nuclear structure calculations

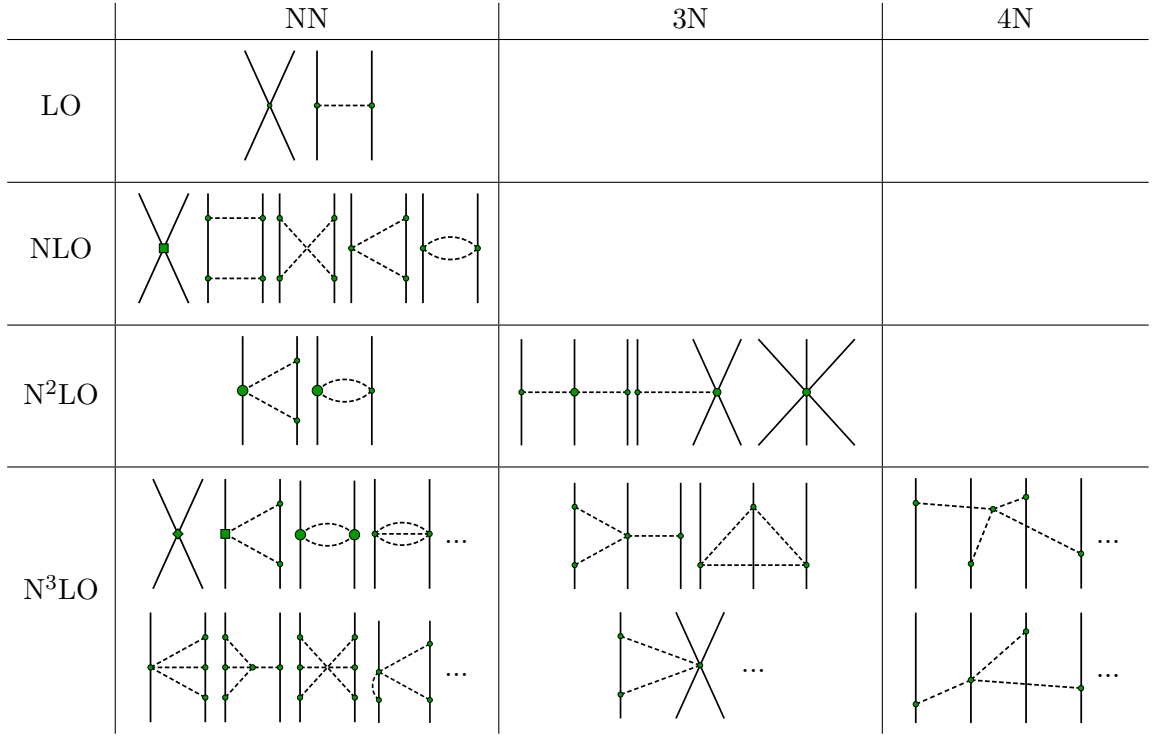


Figure 2.1: Diagrammatic representation of the hierarchy of nuclear forces in chiral EFT. The nucleons are depicted as solid lines, while the dashed lines represent pions. The different vertex dimensions are indicated through dots, circles, squares, and diamonds according to $\Delta_i = 0, 1, 2,$ and 4 .

have been developed yet. Weinberg obtained the following power counting via dimensional analysis

$$\nu = -2 + 2A - 2C + 2L + \sum_i \Delta_i, \quad (2.19)$$

where A is the number of nucleons, C is the number of separately connected pieces, L is the number of loops in the diagram, and

$$\Delta_i = d_i + \frac{n_i}{2} - 2, \quad (2.20)$$

where d_i is the number of derivatives or pion-mass insertions and n_i the number of nucleon legs of the vertex i . This power counting is illustrated in figure 2.1 with the diagrams depicting the different interaction processes between the nucleons via contacts or pionic interactions. Here, the leading order (LO) diagrams have $\nu = 0$ and all contributions to $\nu = 1$ are vanishing due to parity and time-reversal invariance. Therefore, the next-to-leading order (NLO) has $\nu = 2$, the next-to-next-to-leading order (N²LO) has $\nu = 3$, and so on. At LO and NLO only NN interactions are contributing, while higher particle-rank forces like the 3N interactions appear at N²LO.

For example, the LO contribution

$$\hat{V}_{\text{LO}}^{\text{NN}} = \hat{V}_{\text{cont}}^{\text{NN}} + \hat{V}_{\text{OPE}}^{\text{NN}} \quad (2.21)$$

consists of a contact interaction

$$\hat{V}_{\text{cont}}^{\text{NN}} = C_S + C_T(\hat{\sigma}_1 \cdot \hat{\sigma}_2) \quad (2.22)$$

with the LECs C_S and C_T , and the one-pion exchange (OPE)

$$\hat{V}_{\text{OPE}}^{\text{NN}}(\vec{q}) = -\frac{g_A^2}{4F_\pi^2} \frac{(\hat{\sigma}_1 \cdot \vec{q})(\hat{\sigma}_2 \cdot \vec{q})}{q^2 + M_\pi^2} (\hat{\tau}_1 \cdot \hat{\tau}_2) \quad (2.23)$$

with \vec{q} the momentum transfer

$$\vec{q} = \vec{p}_1 - \vec{p}'_1 = \vec{p}_2 - \vec{p}'_2 \quad (2.24)$$

with initial and final momenta of the nucleons \vec{p}_1, \vec{p}_2 and \vec{p}'_1, \vec{p}'_2 respectively.

2.3 | Two Nucleon Interactions

The chiral EFT interactions are only valid in the low-energy regime. Furthermore, the interactions applied in the Lippmann-Schwinger equation lead to infinities. To avoid these infinities and ensure that the interactions are physical, the usual procedure is to regularize the interactions by multiplying them with a regulator function that cuts off external momenta at a specific cutoff Λ , which is larger than a typical momentum but smaller than the breakdown scale

$$q \ll \Lambda < \Lambda_\chi. \quad (2.25)$$

There is no unique way to chose this regulator function. A typical regulator function is of Gaussian form

$$F(q, \Lambda) = \exp \left[-\left(\frac{q}{\Lambda}\right)^{2n} \right], \quad (2.26)$$

where q is related to the nucleon momentum and Λ is the cutoff scale, which is usually chosen in the range of 300-700 MeV. In this range, we do not cut off relevant physics but are smaller than the chiral breakdown scale Λ_χ , hence, we suppress all momenta for which the theory is not valid.

In principle, the theory should not depend on the chosen regulator function or scale. The dependence on the regulation should be incorporated in the contact interactions by rescaling the LECs. Hence, the LECs have multiple purposes: they are used to renormalize the theory and to absorb neglected physics from higher orders, for example heavier mesons. In chiral EFT, the LECs need to be determined order by order by fitting to experimental data. The usual procedure is to fit the NN interaction to NN data, the 3N interaction to 3N data, and so on. Later, in chapter 4, we will also discuss alternative fitting strategies. The interactions constructed in chiral EFT are not unique. They distinguish themselves through different regularization schemes, fit procedures as well as unambiguous parameters that need to be chosen in the construction of the relativistic correction or in the short-range contact interactions. In the following sections, we introduce the different interactions we use in this work. As already mentioned, the result should be independent of the regulator choice, but the regulators can generate regulator artifacts [72] or for technical reasons one regulator can be more favorable than another. For example, many-body methods based on coordinate-space wave functions like quantum Monte Carlo methods [38, 39] prefer local interactions as an input and the usage of non-local regularized interactions can be more involved. Nevertheless, it is a good idea to explore various regulator schemes and scales. This also gives an idea of the uncertainties of the theory. Now, we discuss the different NN interactions used in this thesis.

2.3.1 | Entem and Machleidt Interaction

A widely used NN interaction was the Entem and Machleidt (EM) NN interaction [73]. This interaction is the first chiral interaction with terms up to N³LO and is regularized with a non-local regularization scheme. Thus, the regularized interaction is given by

$$\hat{V}^{\text{reg}}(p', p) = F(p', \Lambda_{\text{NN}}) \hat{V}(p', p) F(p, \Lambda_{\text{NN}}). \quad (2.27)$$

Here p and p' are the initial and final momenta. The powers n in $F(q, \Lambda)$ are chosen differently for the different contributions of the interaction, but at least as large such that the regulator function

$$F(q, \Lambda) = \exp \left[- \left(\frac{q}{\Lambda} \right)^{2n} \right] \approx 1 - \left(\frac{q}{\Lambda} \right)^{2n} + \dots \quad (2.28)$$

does not introduce terms with powers lower than the order $\nu = 4$. In particular, LO contributions use $n \geq 3$ and NLO as well as higher orders use $n \geq 2$. The cutoff is chosen to be $\Lambda_{\text{NN}} = 500$ MeV. With this interaction we are restricted to one chiral order and one cutoff. Hence, this interaction does not allow for an uncertainty quantification via order-by-order analysis. Nevertheless, this interaction has been used in many applications [74–76], therefore it is still used as a benchmark interaction. Furthermore, the accuracy of an interaction is also strongly dependent on the data to which it is fitted. The EM interaction is fitted to phase shifts and other NN data based on published worldwide data up to 1999 defined in reference [2] and is in an energy range of 0 – 290 MeV. In this range, the data is reproduced with a $\chi^2/\text{datum} = 1.1$.

2.3.2 | Entem, Machleidt and Nosyk Interactions

The Entem, Machleidt and Nosyk NN interactions [46] are an advancement to the EM interaction. In fact, it is not only one interaction, but an interaction family. These interactions allow for a consistent chiral order-by-order analysis with chiral orders available from LO to N⁴LO. Similar to the EM interaction, a non-local regularization scheme is used with three different cutoffs $\Lambda_{\text{NN}} = 450, 500, \text{ and } 550$ MeV. Besides these additional chiral orders and cutoffs, the π N LECs are not fitted to the NN data base, but are rather obtained by matching the Roy-Steiner equations to the chiral expansion [77]. Furthermore, the NN data base is extended up to worldwide data up to 2016 [46]. The data set increased during this years from 2403 to 4853 data points. In the energy range 0 – 290 MeV the data is reproduced with a $\chi^2/\text{datum} = 1.63$ at N³LO and $\chi^2/\text{datum} = 1.15$ at N⁴LO.

2.3.3 | Semi-local Regularized Interactions

Complementary to the EM and EMN interaction, also interactions with a semi-local regularization scheme have been developed. These interactions come in two forms, the semi-local coordinate space (SCS) [13, 14] and the semi-local momentum space (SMS) [78] regularized interactions. They were developed to overcome deficiencies by using a non-local regulator. Chiral interactions consist of two distinct parts, the long-range part, which is governed by pion exchanges, and the short-range part, which is parameterized through contact interactions. Hence, the long-range part is unambiguously determined from the chiral symmetry and the corresponding LECs should be obtained from experimental data of the pion-nucleon system. The authors of [13] argue that the non-local regulator can cut into this long-range part, if the cutoff value is chosen too small. These artifacts reveal themselves as a cutoff dependence of observables or, in particular, oscillations of the deuteron wave function. Hence,

a SCS regularization scheme was introduced, which regularizes long-range contributions with a regulator function in coordinate space

$$f\left(\frac{r}{R}\right) = \left[1 - \left(-\frac{r^2}{R^2}\right)\right]^n \quad (2.29)$$

and $n = 6$. This regulator choice does not influence the long-range part and removes the short-range parts of the pion-exchange contributions, thus, an additional spectral function regulator is not necessary. For short-range contact contributions one still uses a non-local regulator in a Gaussian form

$$\hat{V}_{\text{cont}}^{\text{reg}}(p', p) = \hat{V}_{\text{cont}}(p', p) \exp\left[-\frac{p'^2 + p^2}{\Lambda^2}\right]. \quad (2.30)$$

with $\Lambda = 2R^{-1}$. This interaction is available for the cutoffs $R = 0.8, 0.9, 1.0, 1.1,$ and 1.2 fm and from LO to N⁴LO. This regularization scheme exploits that the long-range contribution is mainly of local nature and that only the relativistic corrections starting from N³LO are non-local.

Using a regulator in coordinate space comes with increasing numerical cost especially for the 3N interactions, since in order to regularize the interaction one needs to apply a Fourier transformation into coordinate space and after the regularization back into momentum space. Hence, based on the same idea as the SCS interaction, but using a regulation in momentum space, the SMS interactions were developed. This interaction family is available from LO to N⁴LO+, where the + indicates additional short-range terms from N⁵LO. The five available cutoffs Λ range from 350 MeV to 550 MeV. In practical calculations, the regularization in momentum space is easier to implement for interactions defined in momentum space. The regularization of the long-range part of the SMS interactions is carried out by replacing the Feynman propagators for the pions by a spectral integral

$$\frac{1}{l^2 + M_\pi^2} \rightarrow \int_0^\infty d\mu^2 \frac{\rho(\mu^2)}{l^2 + \mu^2 + i\epsilon}, \quad (2.31)$$

where l is the four-momentum of the pion and $\rho(\mu^2)$ a spectral function that ensures that the pion propagators get regularized

$$\int_0^\infty d\mu^2 \frac{\rho(\mu^2)}{l^2 + \mu^2} \rightarrow \frac{F(\vec{l}^2)}{l^2 + M_\pi^2}. \quad (2.32)$$

For the SMS interactions the form factor $F(\vec{l}^2)$ has been chosen to be

$$F(\vec{l}^2) = \exp\left[-\frac{l^2 + M_\pi^2}{\Lambda^2}\right]. \quad (2.33)$$

In addition to the different regularization of the long-range terms, redundant short-range off-shell terms have been removed in the SMS interaction, which simplified the fits and lead to softer interactions, in section 5.2 we will come back to these terms and probe modifications of those. Furthermore, the SCS and SMS interactions differ by the choice of the π N LECs. The SCS interactions use π N LECs that are obtained in the Karlsruhe-Helsinki partial-wave analysis [79, 80], while the SMS interactions use the π N LECs from the Roy-Steiner equation analysis [77] similar to the EMN interactions. Both SCS and SMS describe the NN data in excellent agreement.

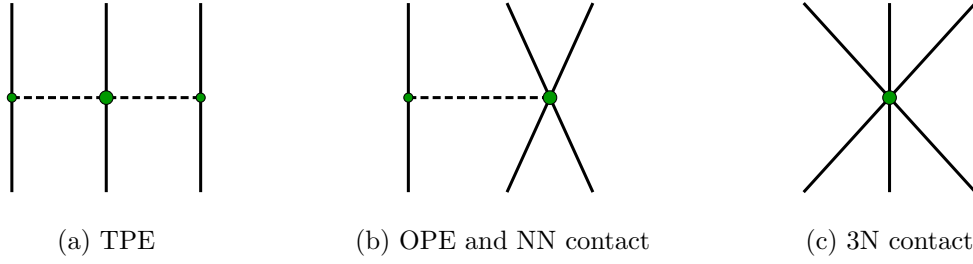


Figure 2.2: The 3N diagrams entering at N²LO. The nucleons are depicted as solid lines, while the dashed lines represent the pions. The different vertex dimensions are indicated through different thicknesses.

2.4 | Three Nucleon Interactions

In this section we give a short overview of the basic structures of the 3N interactions in chiral EFT. Afterwards, we discuss the various regularization schemes that we are using.

2.4.1 | Basic Structures

In the Weinberg counting scheme the first 3N interactions appear in N²LO and are derived in [81, 48]. These leading terms are illustrated in figure 2.2.

The long-range part is determined through the two-pion exchange (TPE) potential, which is given by [48]

$$\hat{V}_{\text{TPE}}^{3\text{N}}(\vec{q}_1, \vec{q}_2, \vec{q}_3) = \sum_{i \neq j \neq k} \frac{1}{2} \left(\frac{g_A}{2F_\pi} \right)^2 \frac{(\hat{\sigma}_i \cdot \vec{q}_i)(\hat{\sigma}_j \cdot \vec{q}_j)}{(\vec{q}_i^2 + M_\pi^2)(\vec{q}_j^2 + M_\pi^2)} \hat{F}_{ijk}^{\alpha\beta} \hat{\tau}_i^\alpha \hat{\tau}_j^\beta \quad (2.34)$$

with

$$\hat{F}_{ijk}^{\alpha\beta} = \delta^{\alpha\beta} \left[-\frac{4c_1 M_\pi^2}{F_\pi^2} + \frac{2c_3}{F_\pi^2} \vec{q}_i \cdot \vec{q}_j \right] + \sum_\gamma \frac{c_4}{F_\pi^2} \epsilon^{\alpha\beta\gamma} \hat{\tau}_k^\gamma \hat{\sigma}_k \cdot [\vec{q}_i \times \vec{q}_j]. \quad (2.35)$$

Here, $\vec{q}_i = \vec{p}'_i - \vec{p}_i$ is the momentum transfer of nucleon i with \vec{p}_i and \vec{p}'_i the initial and final momentum, respectively. The spin and isospin operators of the i -th nucleon are $\vec{\sigma}_i$ and $\vec{\tau}_i$. Further, g_A is the axial-vector coupling constant, F_π is the weak pion decay constant and M_π the pion mass. The LECs c_1 , c_3 , and c_4 are already part of the TPE in the NN interaction and should be chosen accordingly.

In addition, we have two contributions, which include contact interactions: the one-pion exchange absorbed or emitted by NN contact interactions

$$\hat{V}_{\text{OPE}}^{3\text{N}}(\vec{q}_1, \vec{q}_2, \vec{q}_3) = - \sum_{i \neq j \neq k} \frac{g_A c_D}{8F_\pi^4 \Lambda_\chi} \frac{\hat{\sigma}_j \cdot \vec{q}_j}{\vec{q}_j^2 + M_\pi^2} (\hat{\tau}_i \cdot \hat{\tau}_j) (\hat{\sigma}_i \cdot \vec{q}_j) \quad (2.36)$$

and the three-nucleon contact (cont) term

$$\hat{V}_{\text{cont}}^{3\text{N}}(\vec{q}_1, \vec{q}_2, \vec{q}_3) = \sum_{j \neq k} \frac{c_E}{2F_\pi^4 \Lambda_\chi} (\hat{\tau}_j \cdot \hat{\tau}_k). \quad (2.37)$$

These contributions come with two new LECs, c_D and c_E , which cannot be determined with NN observables only.

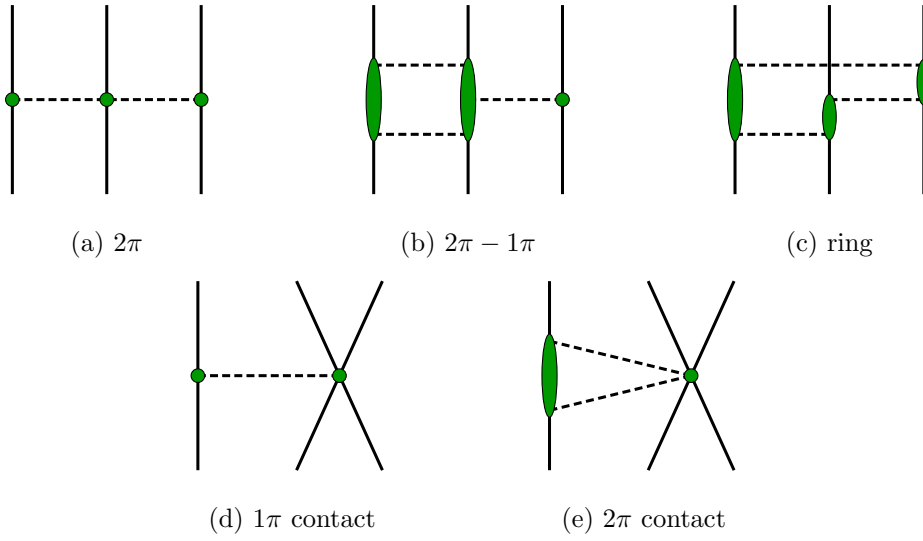


Figure 2.3: The 3N diagrams entering at $N^3\text{LO}$. The nucleons are depicted as solid lines, while the dashed lines represent the pions. The different vertex dimensions are indicated through different thicknesses. The two-pion exchange (a), the two- and one-pion exchange (b), and the ring (c) diagrams are considered as long-range while the one-pion exchange and NN contact (d) as well as the two-pion exchange and NN contact (e) are considered as short-range contributions.

The $N^3\text{LO}$ terms are derived in [82, 83] and their expressions in momentum space can be found in said papers. The expressions can be rather involved, hence, we do not show them and only give an overview. The diagrams can be categorized into long- and short-range terms as well as relativistic corrections to the $N^2\text{LO}$ one- and two-pion exchange contributions. These contributions are illustrated in figure 2.3 and come with no additional LECs. The long-range terms are simply defined as those terms that do not contain any contact terms, while the short-range terms do have contact contributions.

The TPE terms at $N^3\text{LO}$ have a similar structure as the one at $N^2\text{LO}$ in equations (2.34) and (2.35). Hence, we can partly absorb these contributions with a shift of the LECs c_i

$$\tilde{c}_1 = c_1 - \frac{g_A^2 M_\pi}{64\pi F_\pi^2} = c_1 - 0.13 \text{ GeV}^{-1}, \quad (2.38)$$

$$\tilde{c}_3 = c_3 + \frac{g_A^4 M_\pi}{16\pi F_\pi^2} = c_3 + 0.89 \text{ GeV}^{-1}, \quad (2.39)$$

$$\tilde{c}_4 = c_4 - \frac{g_A^4 M_\pi}{16\pi F_\pi^2} = c_4 - 0.89 \text{ GeV}^{-1}. \quad (2.40)$$

Please note that the numerical values for the shift of c_3 and c_4 given in [82] are wrong and therefore differ from those in equations (2.39) and (2.40). For the numerical values, we used $g_A = 1.29$, $M_\pi = 138.039 \text{ MeV}$ and $F_\pi = 92.4 \text{ MeV}$ such that they fit the values to the EMN NN interaction in [46].

The other long-range contributions at $N^3\text{LO}$ – the TPE with OPE (figure 2.3b), the ring diagrams contributions (figure 2.3c), which are the most involved ones, and the residual part of the TPE – cannot be included with simple LEC shifts.

From the short-range topologies only the TPE with contact (figure 2.3e) leads to additional contributions, since the new $N^3\text{LO}$ contributions to the OPE and contact topology (figure 2.3d) cancel out after asymmetrization.

	$\Lambda[\text{MeV}]$	$C_S[\text{fm}^2]$	$C_T[\text{fm}^2]$
N ³ LO	450	-4.60	-0.010
	500	-4.78	-0.163
	550	-4.56	-0.069
N ⁴ LO	450	-4.62	-0.028
	500	-4.62	-0.078
	550	-4.36	0.031

Table 2.1: The C_S and C_T values for the EMN interaction appearing in the 3N interaction at N³LO. The values are isospin averaged and taken from [85].

	$c_1[\text{GeV}^{-1}]$	$c_3[\text{GeV}^{-1}]$	$c_4[\text{GeV}^{-1}]$	$\tilde{c}_1[\text{GeV}^{-1}]$	$\tilde{c}_3[\text{GeV}^{-1}]$	$\tilde{c}_4[\text{GeV}^{-1}]$
N ² LO	-0.74	-3.61	2.44	-0.74	-3.61	2.44
N ³ LO	-1.07	-5.32	3.56	-1.20	-4.43	2.67
N ⁴ LO'	-1.10	-5.54	4.17	-1.23	-4.65	3.28

Table 2.2: The c_i and \tilde{c}_i values used for the EMN interaction. The c_i are the LECs from the NN interaction and the \tilde{c}_i are the effective LECs entering the 3N interaction on a N²LO term. The values are taken from [46].

The relativistic corrections lead to contributions to the TPE and to the OPE and contact topologies. The relativistic corrections are dependent on the lowest order NN contact interaction LECs C_S and C_T . Furthermore, these interactions are not unambiguous, since they depend also on the constants $\bar{\beta}_8$ and $\bar{\beta}_9$, which are unitary ambiguity parameters that in turn depend on the parametrization choice or method to construct the potentials. These parameters should be chosen consistent with the NN interaction. For more details about these parameters we refer to [84]. In this reference the quantities $\bar{\beta}_8$ and $\bar{\beta}_9$ are given by $\mu = 4\bar{\beta}_9 + 1$ and $\nu = 2\bar{\beta}_8$. These parameters also play a role in chapter 5, where we probe different sets of them for the SMS NN interactions.

The LECs of the NN EMN interaction which are relevant in the 3N interaction are summarized in tables 2.1 and 2.2. The C_S and C_T values of table 2.1 are fitted to NN data while the π N LECs of table 2.2 are obtained by matching the Roy-Steiner equations to the chiral expansion [77].

The N⁴LO contributions to the 3N are not completely worked out yet. Currently available contributions can be found in [86, 79, 87, 88]. It is not only challenging to derive the terms of the 3N interactions at N⁴LO, but also to determine the appearing LECs at this order. There are ten additional LECs that need to be fitted to few-body data. Due to the fact that we do not have access to all terms at N⁴LO, we neglect these contributions in this thesis and introduce the prime notation N⁴LO', which indicates that we complement the NN N⁴LO interaction with the 3N N³LO interaction using the LECs of the NN N⁴LO interaction.

Similar to the NN interactions, we need to regularize these 3N interactions, ideally consistent with the NN interactions. In the next sections we discuss the different regularizations.

2.4.2 | Local 3N Interaction

One of the first widely used chiral 3N interactions at N²LO was established by Navrátil [41]. This interaction is regularized by multiplying a regulator function on the potential

$$V^{3N}(\vec{q}_1, \vec{q}_2, \vec{q}_3) \rightarrow F(\vec{q}_2, \Lambda_{3N})V^{3N}(\vec{q}_1, \vec{q}_2, \vec{q}_3)F(\vec{q}_3, \Lambda_{3N}) \quad (2.41)$$

with

$$F(q, \Lambda_{3N}) = \exp \left[- \left(\frac{q}{\Lambda_{3N}} \right)^{2n} \right] \quad (2.42)$$

and $n = 2$. Since the regularization is done with the momentum transfer of the second and third nucleon the final interaction is local. The locality of the interaction is beneficial for some few- and many-body approaches. However, we do not exploit these advantages directly. The calculation of the matrix elements of a local 3N interaction is not as demanding as for a non-local one, since these interactions depend only on the momentum transfer, thus we do not introduce an additional angular momentum truncation for this interaction. The regulator function itself is consistent with the regulator function in the EM [73] or EMN [46] NN interactions. Due to the different choice of coordinates of the nucleons employed in the regulator function, the regularization is inconsistent compared to the EM or EMN NN interactions. Navrátil [41] states that by using a power of $n = 2$ the inconsistencies should be of higher order. However, in chapter 4 we will see that the choice of the regularization has a significant effect. We generate matrix elements for this interaction by using the MANYEFF code by Navrátil [89].

2.4.3 | Non-Local 3N Interaction

Alternatively to the local regularized 3N interaction, it is also possible to use a non-local regularization procedure, which would be more consistent in combination with the EM or EMN NN interaction.

This regularization procedure is similar to equation (2.41) but uses instead of the momentum transfer the initial (final) Jacobi momenta $\vec{\pi}_1$ and $\vec{\pi}_2$ ($\vec{\pi}'_1$ and $\vec{\pi}'_2$) of the nucleons as defined in appendix A.2

$$V^{3N}(\vec{\pi}'_1, \vec{\pi}'_2, \vec{\pi}_1, \vec{\pi}_2) \rightarrow F(\pi'_1, \pi'_2, \Lambda_{3N}) V^{3N}(\vec{\pi}'_1, \vec{\pi}'_2, \vec{\pi}_1, \vec{\pi}_2) F(\pi_1, \pi_2, \Lambda_{3N}), \quad (2.43)$$

with the regulator function [48]

$$F(\pi_1, \pi_2, \Lambda_{3N}) = \exp \left[- \left(\frac{\pi_1^2 + \pi_2^2}{2\Lambda_{3N}} \right)^{2n} \right]. \quad (2.44)$$

The power is chosen as $n = 3$ if not stated otherwise. The resulting interactions are non-local, since the use of the Jacobi momenta destroys the spatial locality of the operator structures.

The partial wave decomposition of the unregularized expressions in momentum space is calculated by Hebeler [49] in an efficient way, which takes advantage of the either local or polynomial non-local structure of the 3N topologies at N²LO and N³LO. Please note the different Jacobi coordinate definition in [48, 49], which leads to a slightly different expression for equation (2.44). Since the regularization does not depend on the angular component of the momenta, the regularization of these terms can be carried out in a secondary step during the transformation into the antisymmetric Jacobi HO basis. We will introduce this basis in chapter 3. This two-step procedure allows a reduction of the computational cost, since the expensive calculation of the interaction has to be carried out only once. A variation of the cutoff or the power of the regulator function can be performed subsequently in inexpensive calculations. Nevertheless, to reduce the computational cost only the lowest partial waves are computed. In ref. [49] it has been shown that it is sufficient to truncate the number of partial waves up to the three-body total angular momentum $J_{12} = 9/2$.

Recently, Epelbaum *et al.* [63] have noted that this procedure can lead to issues. The 3N interactions discussed in section 2.4.1 are derived with dimensional regularization. The mixing of the cutoff and dimensional regularization scheme can lead to inconsistencies between two- and three-body forces, which in turn can lead to violations of the chiral symmetry. These inconsistencies arise for 3N interactions at N³LO, in particular for the $2\pi - 1\pi$ topology. In this thesis we assume the absolute effect of this inconsistency to be small, but this assumption needs to be verified in future studies. A preferable approach would be to resolve the issue with a consistent regularization.

2.4.4 | Semi-Local 3N Interaction

The consistently regularized SCS and SMS 3N interactions are currently under development within LENPIC. Currently available are the 3N interactions for both regularizations at N²LO [90, 91]. These interactions use the same regularization procedure as the NN interactions: non-local regularization for the short-range part and local regularization for the long-range part. Hence, the semi-locally regularized 3N interactions inherit features of both the local and the non-local regularization schemes. Here, each topology is regularized differently. In particular, the TPE is regularized locally, the 3N contact is regularized non-locally, and in the OPE plus NN contact diagrams the OPE is regularized locally while the NN contact is regularized non-locally. In contrast to the regularization procedure with the pure non-local regulators, the regularization with the semi-local regulator cannot be performed in a secondary step. The local regulator part depends not only on the Jacobi momenta, but on the momentum transfer and thereby also on the angles of the Jacobi momenta. This angle dependence leads to a coupling of different partial waves. An extensive discussion of these regularizations can also be found in [92].

2.5 | Uncertainty Quantification

One major advantage of interactions constructed within chiral EFT compared to phenomenological ones is the possibility to provide a quantification of theory uncertainties. There are multiple sources of uncertainties we need to investigate:

1. Uncertainties induced by the regulation scheme and scale.
2. Uncertainties arising from the fit of the LECs and the uncertainties of the experimental data used for the fit.
3. Truncation error of the chiral EFT expansion.
4. Other approximations and truncations used in the calculation of the observable of interest.

The impact of 1 can be investigated by using different regularization schemes and scales, for example, the non-local or semi-local regularization schemes discussed in the previous section. A cutoff variation is also possible, but the number of cutoffs is often limited to a narrow range. In addition, a cutoff variation does not provide a quantification of the impact of neglected interaction terms. By a variation of the LECs, probing various fitting procedures and studying the impact of these variation we can estimate the uncertainties of 2. The uncertainties of 3 are probably the most dominant uncertainties. In the following, we discuss two methods to estimate these, which will be used and compared with each other later in this work. The uncertainties of 4 need to be assessed separately, but are, in an *ab initio* framework, the uncertainties we have the best control of.

EKM Uncertainty Quantification Epelbaum, Krebs, and Meißner (EKM) [13] developed an algorithm for estimating the truncation error of the chiral expansion. This method for estimating uncertainties has been applied in numerous few- and many-body applications [13–16]. It is simple and easy to implement, but does not provide a statistical interpretation for the estimated uncertainties.

The basic idea is to assume that the chiral expansion is not only valid for the interaction itself, but also for the observable X of interest. By calculating the observable for each chiral order individual, we refer to this as order by order, we obtain information about the progression of the expansion and can estimate the magnitude of neglected higher order terms. The chiral expansion of an observable X can be written as

$$X^{(n)} = X^{(0)} + \Delta X^{(2)} + \dots + \Delta X^{(n)} \quad (2.45)$$

with

$$\Delta X^{(2)} = X^{(2)} - X^{(0)}, \quad (2.46)$$

$$\Delta X^{(i)} = X^{(i)} - X^{(i-1)} \text{ for } i \geq 3. \quad (2.47)$$

If the chiral expansion for the observable is valid we would expect

$$\Delta X^{(i)} = \mathcal{O}(Q^i X^{(0)}), \quad (2.48)$$

with the chiral expansion parameter $Q = p/\Lambda_\chi \approx 1/3$, which is the ratio of the typical momentum scale and the chiral breakdown scale. In addition to the leading order results, we can incorporate the individual changes between orders. Each correction of order i should be approximately the correction at order j suppressed by the expansion parameter Q^{i+1-j}

$$\Delta X^{(i)} = \mathcal{O}(Q^{i+1-j} \Delta X^{(j)}). \quad (2.49)$$

The uncertainty of a given order Q^i is then estimated via

$$\delta X^{(i)} = \max_{2 \leq j \leq i} \left(Q^{i+1-j} \left| \Delta X^{(j)} \right|, Q^{i+1} \left| X^{(0)} \right| \right). \quad (2.50)$$

This estimate is quite conservative, since it always quantifies the uncertainty based on the largest difference between orders. Furthermore, it provides, as already stated, no statistical interpretation.

Bayesian Uncertainty Quantification A more elaborate truncation error estimation based on Bayesian statistics has been proposed by the BUQEYE collaboration [19]. In this approach, the chiral expansion of an observable $Y^{(n)}$ at order n is given similar to equation (2.45) as

$$Y^{(n)} = Y^{(0)} + \Delta Y^{(1)} + \dots + \Delta Y^{(n)}. \quad (2.51)$$

Here, we have changed the notation to distinguish it from the EKM approach. Instead of using the correction at a given chiral order, we can rewrite it as an series expansion as

$$Y^{(k)} = Y_{\text{ref}} \sum_{n=0}^k c_n Q^n. \quad (2.52)$$

Here, Y_{ref} is a reference scale, which is for instance known from a dimension analysis. In this work, we employ the experimental value as the reference scale due to its simplicity. If an

experimental value is not available, we use an educated guess. The expansion coefficients c_n should then be of natural size, which means to be of the order 1. From a set of results for the lower chiral orders we can directly determine the expansion coefficients $\vec{c}_k = (c_0, c_1, \dots, c_k)$. From the series ansatz it is clear that the truncation error is given by the sum of all neglected terms

$$\delta Y^{(k)} = Y_{\text{ref}} \sum_{n=k+1}^{\infty} c_n Q^n. \quad (2.53)$$

Since the c_n with $n > k$ are not known, we need to predict them in order to obtain the truncation error. We can assume that the unknown c_n have the same properties as the known coefficients. In addition, we make the prior assumption that the c_n are of natural size and have a standard deviation of order 1. In a Bayesian process the c_n from lower orders are used to optimize the prediction of the unknown c_n .

In order to make predictions, we formalize our knowledge as Bayesian priors. The exact choice of the priors has only small impact on the truncation error estimates [19]. Hence, prior choices that yield analytic posteriors are preferred. In this model we assume that the c_n are distributed normally

$$c_n | \bar{c}^2 \sim \mathcal{N}(0, \bar{c}^2) \quad (2.54)$$

around 0 and with the marginal variance \bar{c}^2 , which controls the width of the variation. For \bar{c}^2 we assume a scaled inverse χ^2 distribution

$$\bar{c}^2 \sim \chi^{-2}(\nu_0, \tau_0^2), \quad (2.55)$$

where ν_0 is the number of prior degrees of freedom and τ_0^2 the prior scale. The uninformative choice of this prior has $\nu_0 = 1$ and $\tau_0 = 1$. This particular choice of priors allows to calculate the prior for the truncation error

$$\delta Y^{(k)} | \bar{c}^2, Q \sim \mathcal{N}\left(0, Y_{\text{ref}}^2 \frac{Q^{2(k+1)}}{1 - Q^2} \bar{c}^2\right), \quad (2.56)$$

where we used that the sum of two independent normal distributed random variables $X \sim \mathcal{N}(\mu_x, \sigma_x^2)$ and $Y \sim \mathcal{N}(\mu_y, \sigma_y^2)$ is also normal distributed

$$AX + BY \sim \mathcal{N}(A\mu_x + B\mu_y, A^2\sigma_x^2 + B^2\sigma_y^2). \quad (2.57)$$

Furthermore, the truncation error is a geometrical sum over normally distributed coefficients c_n , which lead to equation (2.56).

We use the Bayes' theorem to incorporate the knowledge of the \vec{c}_k for a posterior distribution of \bar{c}^2

$$\text{pr}(\bar{c}^2 | \vec{c}_k) \propto \text{pr}(\vec{c}_k | \bar{c}^2) \text{pr}(\bar{c}^2) = \text{pr}(\bar{c}^2) \prod_n^k \text{pr}(\vec{c}_n | \bar{c}^2). \quad (2.58)$$

The particular choices for the priors (2.54) and (2.55) have the advantage to lead to a posterior, which is again a scaled inverse χ^2 distribution

$$\bar{c}^2 | \vec{c}_k \sim \chi^{-2}(\nu, \tau^2), \quad (2.59)$$

with

$$\nu = \nu_0 + n_c, \quad (2.60)$$

$$\nu\tau^2 = \nu_0\tau_0^2 + \vec{c}_k^2. \quad (2.61)$$

Here n_c is the number of coefficients in \vec{c}_k that are meaningful, in particular nonzero. We are now in the position to calculate the posterior predictive distribution of the truncation error $\delta Y^{(k)}$ by marginalizing over \vec{c}^2

$$\text{pr}(\delta Y^{(k)} | \vec{c}_k, Q) = \int_0^\infty d\vec{c}^2 \text{pr}(\delta Y^{(k)} | \vec{c}^2, Q) \text{pr}(\vec{c}^2 | \vec{c}_k). \quad (2.62)$$

Here again the choice of the priors is beneficial, since the combination of a normal distribution with an inverse χ^2 distribution leads to a Student-t distribution

$$\delta Y^{(k)} | \vec{c}_k, Q \sim t_\nu \left(0, Y_{\text{ref}}^2 \frac{Q^{2(k+1)}}{1 - Q^2} \tau^2 \right). \quad (2.63)$$

Finally, we obtain the full prediction

$$Y | \vec{Y}^{(k)}, Q \sim t_\nu \left(Y^{(k)}, Y_{\text{ref}}^2 \frac{Q^{2(k+1)}}{1 - Q^2} \tau^2 \right). \quad (2.64)$$

This distribution can be used to estimate the uncertainty due to the chiral truncation error by integrating over it until the desired degree of belief is reached. In our case we use a degree of belief of 95%. Melendez *et al.* [19] refer to this uncertainty estimation model as the pointwise model. This model can be extended to incorporate correlations between observables in the nearby energy range. Furthermore, this model assumes that the chiral expansion parameter Q is known. It is possible to determine Q itself through a Bayesian process. In this work, we will apply only the pointwise model with given $Q = 1/3$ due to its simple applicability. Furthermore, the exact value of Q leads only to minor differences.

For practical calculations we should note that due to the chiral expansion $c_1 = 0$, which need to be accounted for either by setting $c_1 = 0$ and $n_c = 1$ or starting the expansion (2.52) with $n = 1$ instead of 0 and treating the LO as the Q^1 contribution. Both ways result in the same solution.

3 | Solving the Nuclear-Many-Body Problem

The main problem in nuclear structure theory is to solve the stationary Schrödinger equation for a many-body system. In recent years the development in many-body methods and the growing power of high-performance computers has allowed it to solve nuclei up to the medium-mass regime. In this work we mainly use methods that are based on configuration interaction approaches like the no-core shell model (NCSM) [20, 21]. The basic idea of the NCSM is to formulate the stationary Schrödinger equation as a matrix eigenvalue problem and solve it in a suitable finite basis representation. By systematically increasing the model-space dimension one improves the solution until it converges. Using the bare Hamiltonian in the many-body problem leads to a slow convergence with respect to the model space. This convergence behavior can be improved by using renormalization techniques like the similarity renormalization group (SRG) approach [23, 24]. The SRG uses a unitary flow equation to decouple low- and high-momentum states and is thereby an effective prediagonalization method. In addition, the concept of the SRG can also be used to solve the stationary Schrödinger equation itself. In the in-medium similarity renormalization group (IM-SRG) [27–32] we rewrite the Hamiltonian in a normal ordered form with respect to a reference state and use the SRG flow equation to decouple the reference state from all excited states, such that the reference state becomes an eigenstate of the Hamiltonian.

In this thesis we restrict ourselves to the use of the methods introduced above. Nevertheless, there are other powerful methods to solve the nuclear many-body problem. The coupled cluster method [34, 35], for instance, is a decoupling method of the Hamiltonian similar to the IM-SRG, but does not use a unitary transformation. It is also possible to combine the IM-SRG and the NCSM, which leads to the in-medium no-core shell model [36, 37]. In this method the IM-SRG is used as an additional intermediate step to enhance the convergence of the NCSM. An additional class of many-body approaches are quantum Monte Carlo methods [38, 39]. Here, one focuses on optimizing the many-body wave function. This list of methods is not complete, but should give an idea of the different routes to solve the nuclear many-body problem.

In this chapter we will introduce the NCSM, the SRG as well as the IM-SRG. In the final section, we give further information on the determination of radii.

3.1 | No-Core Shell Model

The idea of the standard no-core shell model (NCSM) [20, 21] is conceptually simple yet powerful. The NCSM is in principle capable of calculating ground- and excited-state energies of all nuclei as well as their wave functions simultaneously. Through the wave functions, we gain access to all possible observables. The limit of the NCSM lies in the enormous computational cost. Since the so-called model space increases factorially with the particle number of the considered nucleus, it is, in its standard formulation, currently only applicable

to the p-shell nuclei.

The starting point is the stationary Schrödinger equation

$$\hat{H} |\psi_n\rangle = E_n |\psi_n\rangle, \quad (3.1)$$

with \hat{H} the nuclear many-body Hamiltonian and E_n the n -th energy value to the corresponding eigenstate $|\psi_n\rangle$. By introducing a discrete many-body basis, with $|\Phi_i\rangle$ the basis states and i a collective index for all occurring quantum numbers of the spatial, spin, and isospin parts of the Hilbert space, we can rewrite the stationary Schrödinger equation (3.1) into a matrix eigenvalue problem

$$\sum_j \langle \Phi_i | \hat{H} | \Phi_j \rangle \langle \Phi_j | \psi_n \rangle = E_n \langle \Phi_i | \psi_n \rangle. \quad (3.2)$$

By truncating the basis, we restrict the problem to a model space \mathcal{M} and can numerically solve this matrix-eigenvalue problem within said model space. In practical calculations, we use the Lanczos algorithm [93], which is an efficient procedure to calculate the energetically low-lying eigenvalues and eigenstates. By systematically increasing the model-space dimension, we can increase the accuracy of the calculation until the solution is converged. Often the calculations are not fully converged, but with a suitable extrapolation procedure we can extrapolate to the infinite model space. A standard procedure is to use an exponential ansatz for the extrapolations of energies [94], but there are also extrapolation procedures in development that use Bayesian methods [95] or neural networks [96, 97]. Once we have calculated the eigenstates, any other observable can be obtained by evaluating the expectation values of the corresponding operator with the eigenstates.

3.1.1 | Single-Particle Formulation

The standard basis choice for the NCSM is the harmonic oscillator (HO) basis with the oscillator frequency $\hbar\Omega$ as a free parameter. Here we construct the model space with A -body Slater determinants out of HO single-particle states

$$|n(ls)jm_jtm_t\rangle, \quad (3.3)$$

where n is the radial quantum number. Further, the orbital angular momentum l is coupled with the spin $s = \frac{1}{2}$ to a total angular momentum j with projection m_j and $t = \frac{1}{2}$ is the isospin with projection m_t . Furthermore, we use the symmetries of the Hamiltonian and restrict the model space to a total angular momentum projection $M_J = \sum_i^A m_{j_i}$, total parity $\Pi = \prod_i^A (-1)^{l_i}$, and total isospin projection $M_T = \sum_i^A m_{t_i}$.

In the NCSM, we truncate the HO basis with respect to the total single-particle excitation quanta N_{\max} above the unperturbed Slater determinant. This is illustrated for ^{16}O in figure 3.1. In the unperturbed case all protons and neutrons fill up the 0s and 0p shell. This configuration is for ^{16}O the only possible one for $N_{\max} = 0$. In the illustrated case two protons and one neutron are excited to two shells above their unperturbed states each. Therefore, this configuration is part of all model spaces with $N_{\max} \geq 6$.

With increasing N_{\max} , the energies converge towards the exact value. Since the NCSM is a variational method, each eigenvalue is an upper bound for the exact result. Even more, for the energies the Hylleraas-Undheim theorem [98] holds, which states that all energy eigenvalues drop monotonically with increasing model-space dimension and are bounded from below by the exact solutions. This theorem is only valid for the energies and does not apply to other observables. In addition to the stepwise increase of the model-space dimension with N_{\max} , we vary the HO frequency $\hbar\omega$ to minimize the energies or optimize the convergence pattern.

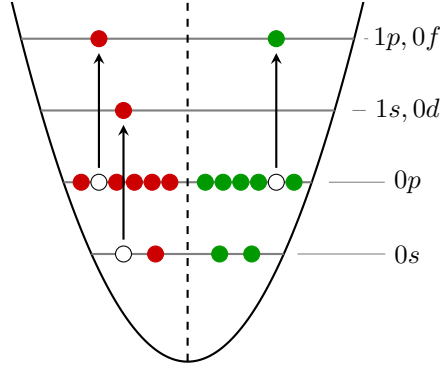


Figure 3.1: Example of a HO basis state configuration for an ^{16}O calculation. In the unperturbed configuration all protons (red) and neutrons (green) are in the $0s$ and $0p$ shell. The configuration with three nucleons excited is part of all model spaces with $N_{\text{max}} \geq 6$.

When we solve the many-body problem, we are only interested in the intrinsic solution. Nevertheless, in the spectrum states can appear that have a center-of-mass contamination. To suppress those states, we can make use of the HO basis, in which the center-of-mass $|\psi_{\text{cm}}\rangle$ and intrinsic part $|\psi_{\text{int}}\rangle$ factorize exactly

$$|\psi\rangle = |\psi_{\text{cm}}\rangle \otimes |\psi_{\text{int}}\rangle. \quad (3.4)$$

We introduce an additional center-of-mass part to the Hamiltonian

$$\hat{H}_{\text{tot}} = \hat{H}_{\text{int}} + \lambda_{\text{cm}} \hat{H}_{\text{cm}}, \quad (3.5)$$

where the center-of-mass Hamiltonian depending on the center-of-mass momentum \hat{P} and coordinate \hat{R} is given by

$$\hat{H}_{\text{cm}} = \frac{\hat{P}^2}{2Am} + \frac{Am\Omega_{\text{cm}}^2}{2} \hat{R}^2 - \frac{3}{2} \hbar \Omega_{\text{cm}}. \quad (3.6)$$

The frequency of the center-of-mass Hamiltonian Ω_{cm} is, but does not need to be chosen the same as the frequency of the basis Ω . By using a non-zero λ_{cm} we can shift the eigenvalues of these contaminated states out of the energetically relevant lower spectrum. This procedure goes back to Gloeckner and Lawson [99].

3.1.2 | Jacobi Formulation

Complementary to the single-particle formulation, we can use a Jacobi basis to construct the model space. In particular, we can use the antisymmetric Jacobi HO basis. This formulation is equivalent to the single-particle formulation, but reduces the model space size significantly. With the Jacobi HO basis, we can separate the center-of-mass part and the intrinsic part explicitly. Since we are only interested in the intrinsic solution, we can omit the center-of-mass degrees of freedom. Furthermore, the basis is coupled to a total angular momentum J and isospin T , thus, we can target the quantum numbers of the specific state, which we are interested in and omit the rest. The Jacobi coordinates are a generalization of the two-body relative and center-of-mass coordinates for more than two particles. Jacobi coordinates are not defined in an unique way. We use the following definition of the spatial Jacobi coordinates

for an A particle system with equal mass:

$$\vec{\xi}_0 = \sqrt{\frac{1}{A}} [\vec{r}_1 + \vec{r}_2 + \cdots + \vec{r}_A], \quad (3.7)$$

$$\vec{\xi}_n = \sqrt{\frac{n}{n+1}} \left[\frac{1}{n} (\vec{r}_1 + \vec{r}_2 + \cdots + \vec{r}_n) - \vec{r}_{n+1} \right]. \quad (3.8)$$

The zeroth coordinate represents the center-of-mass, while the n -th coordinate represents the relative coordinate of the $(n+1)$ -st particle with respect to a cluster of the first n particles. In an analogous way, we can define the Jacobi momentum

$$\vec{\pi}_0 = \sqrt{\frac{1}{A}} [\vec{p}_1 + \vec{p}_2 + \cdots + \vec{p}_A], \quad (3.9)$$

$$\vec{\pi}_n = \sqrt{\frac{n}{n+1}} \left[\frac{1}{n} (\vec{p}_1 + \vec{p}_2 + \cdots + \vec{p}_n) - \vec{p}_{n+1} \right]. \quad (3.10)$$

This particular choice of coordinates has the benefit that the HO Hamiltonian has the same form in single-particle and Jacobi coordinates

$$\hat{H}_{\text{HO}} = \sum_{i=1}^A \left(\frac{\hat{p}_i^2}{2m} + \frac{1}{2} m \Omega^2 \hat{r}_i^2 \right) = \sum_{i=0}^{A-1} \left(\frac{\hat{\pi}_i^2}{2m} + \frac{1}{2} m \Omega^2 \hat{\xi}_i^2 \right). \quad (3.11)$$

The nucleons are fermions, hence, only antisymmetric states need to be considered. While in the single-particle formulation the antisymmetrization is directly obtained by using Slater determinants, in the Jacobi formulation the antisymmetrization is more involved.

Two-Body Basis: A two-body state in the Jacobi HO basis can be written as

$$| N_{\text{cm}(2)} L_{\text{cm}(2)} M_{L_{\text{cm}(2)}} \rangle \otimes | N_1 (L_1 S_1) J_1 M_{J_1} T_1 M_{T_1} \rangle, \quad (3.12)$$

with the radial, orbital angular momentum, and projection quantum numbers $N_{\text{cm}(2)}$, $L_{\text{cm}(2)}$, and $M_{L_{\text{cm}(2)}}$ of the center-of-mass part, respectively. The 2 in the parenthesis indicates that this is the center-of-mass coordinate of two particles. The radial and orbital angular momentum quantum numbers with respect to the first Jacobi coordinate are N_1 and L_1 . The angular momentum L_1 is coupled with the total spin quantum number S_1 of both nucleons to a total angular momentum J_1 with its projection M_{J_1} . Furthermore, we have the total isospin quantum number T_1 and its projection M_{T_1} . The total energy of this state is given by

$$E = E_{\text{cm}} + E_1 = 2N_{\text{cm}(2)} + L_{\text{cm}(2)} + 2N_1 + L_1. \quad (3.13)$$

The center-of-mass part is symmetric by construction, hence, only the relative part needs to be considered in the antisymmetrization process. In the two-body case, the antisymmetrization of the basis can be easily achieved considering only those states that fulfill the antisymmetry condition

$$(-1)^{L_1+S_1+T_1} = -1. \quad (3.14)$$

This condition can be directly obtained by applying the particle-exchange operator on a basis state.

Three-Body Basis: Similar to (3.12), we can write a three-body state as

$$\begin{aligned} & | N_{\text{cm}(3)} L_{\text{cm}(3)} M_{L_{\text{cm}(3)}} \rangle \otimes | E_{12} k_{12} J_{12} M_{J_{12}} T_{12} M_{T_{12}} \rangle = \\ & | N_{\text{cm}(3)} L_{\text{cm}(3)} M_{L_{\text{cm}(3)}} \rangle \otimes | N_1 N_2 [(L_1 S_1) J_1 (L_2 S_2) J_2] J_{12} M_{J_{12}} (T_1 t_3) T_{12} M_{T_{12}} \rangle, \end{aligned} \quad (3.15)$$

where we introduced the total intrinsic energy quantum number of the Jacobi coordinates 1 and 2

$$E_{12} = (2N_1 + L_1) + (2N_2 + L_2) \quad (3.16)$$

and a collective index k_{12} for the quantum numbers $\{N_1, L_1, S_1, J_1, T_1, N_2, L_2, J_2\}$.

The antisymmetrization of the three-body basis is more involved than in the two-body case. The state in equation (3.15) is already antisymmetric regarding particle exchange of the first and second particle if the antisymmetry condition (3.14) is fulfilled, hence, the basis needs only to be antisymmetrized with respect to the third particle. This leads to the antisymmetrizer

$$\hat{\mathcal{A}} = \frac{1}{3}(1 - 2\hat{\mathcal{T}}_{23}), \quad (3.17)$$

with $\hat{\mathcal{T}}_{ij}$ the transposition operator for particle i and j . The matrix elements for this transposition operator in the partially antisymmetrized basis are given by [89]

$$\begin{aligned} & \langle E'_{12} k'_{12} J'_{12} T'_{12} | \hat{\mathcal{T}}_{23} | E_{12} k_{12} J_{12} T_{12} \rangle = \\ & \delta_{J'_{12} J_{12}} \delta_{T'_{12} T_{12}} \delta_{E'_{12}, E_{12}} \sum_{L, S} (-1)^{S_1 + S'_1 + T_1 + T'_1} \hat{L}^2 \hat{S}^2 \hat{J}_1 \hat{J}'_1 \hat{J}_2 \hat{J}'_2 \hat{S}_1 \hat{S}'_1 \hat{T}_1 \hat{T}'_1 \\ & \times \left\{ \begin{array}{ccc} \frac{1}{2} & \frac{1}{2} & S'_1 \\ \frac{1}{2} & S & S_1 \end{array} \right\} \left\{ \begin{array}{ccc} \frac{1}{2} & \frac{1}{2} & T'_1 \\ \frac{1}{2} & T_{12} & T_1 \end{array} \right\} \left\{ \begin{array}{ccc} L_1 & S_1 & J_1 \\ L_2 & \frac{1}{2} & J_2 \\ L & S & J_{12} \end{array} \right\} \left\{ \begin{array}{ccc} L'_1 & S'_1 & J'_1 \\ L'_2 & \frac{1}{2} & J'_2 \\ L & S & J_{12} \end{array} \right\} \\ & \times \langle \langle N'_1 L'_1, N'_2 L'_2 | N_1 L_1, N_2 L_2; L \rangle \rangle_{\frac{1}{3}}. \end{aligned} \quad (3.18)$$

Here, we omitted the projection quantum numbers, since the antisymmetrizer is independent of those. Further, we adopted the short-hand notation $\hat{j} = \sqrt{2j+1}$ and the $\{\dots\}$ with six quantum numbers are 6j-symbols while the $\{\dots\}$ with nine quantum numbers are 9j-symbols. The $\langle \langle \dots | \dots; \dots \rangle \rangle_d$ stands for the harmonic oscillator brackets following [100], see also appendix A.5.

In order to get an antisymmetric basis, we diagonalize the corresponding matrix of the antisymmetrizer numerically. This diagonalization results in eigenstates with eigenvalues one or zero. We are only interested in the eigenstates with eigenvalue one, since those are the antisymmetric states. The entries of the eigenstates are the transformation coefficients into the antisymmetric basis and are called coefficients of fractional parentage (CFPs)

$$c_{k_{12}}^{E_{12}, J_{12}, T_{12}, i_{12}} = \langle E_{12} k_{12} J_{12} T_{12} | E_{12} i_{12} J_{12} T_{12} \rangle. \quad (3.19)$$

The total antisymmetric basis can then be obtained by

$$| E_{12} i_{12} J_{12} T_{12} \rangle = \sum_{k_{12}} c_{k_{12}}^{E_{12}, J_{12}, T_{12}, i_{12}} | E_{12} k_{12} J_{12} T_{12} \rangle, \quad (3.20)$$

where the index i_{12} corresponds to no physical quantum number anymore but to the i_{12} -th eigenvector with eigenvalue one. Note that, this basis has no unique representation and any superposition of the antisymmetric basis states is again an antisymmetric state. Therefore are the CFPs ambiguous and in a practical calculation one should use a defined CFP set.

A-Body Basis: In principle, this procedure can be generalized to construct an antisymmetric A -body basis

$$| E_{12\dots(A-1)} i_{12\dots(A-1)} J_{12\dots(A-1)} T_{12\dots(A-1)} \rangle \quad (3.21)$$

in an iterative way. We start with a partially antisymmetric basis with respect to the n particle subcluster and construct the antisymmetrizer for this subcluster with respect to the $(n+1)$ -st particle. An analytic expression for this antisymmetrizer can be found, for example, in reference [89]. Via diagonalization of the antisymmetrizer we can obtain the CFPs for the $n+1$ particle basis and use the resulting basis for the next iteration until we reach the A -body basis. This procedure is only feasible for light nuclei, since the antisymmetrization becomes computationally demanding. In practical calculations, we use the Jacobi formulation of the NCSM only up to $A = 4$.

3.1.3 | Importance Truncated No-Core Shell Model

One major limiting factor of the NCSM is the rapid combinatorial growth of the model-space dimension. The idea of the importance truncated no-core shell model (IT-NCSM) [22] is to overcome this growth by limiting the number of basis states to the important ones. The solution of an NCSM calculation leads to an eigenstate

$$| \psi_n \rangle = \sum_i c_i^{(n)} | \Phi_i \rangle, \quad (3.22)$$

which is expanded into many-body basis states $| \Phi_i \rangle$ with amplitudes $c_i^{(n)}$. Many of the amplitudes $c_i^{(n)}$ are close to zero. Hence, identifying these basis states a priori and excluding them from the model space reduces the computational cost. The importance of a many-body basis state $| \Phi_i \rangle$ is determined through an importance measure κ , which is motivated physically from first-order multiconfigurational perturbation theory

$$\kappa_i^{(n)} = - \frac{\langle \Phi_i | \hat{H} | \psi_{\text{ref}}^{(n)} \rangle}{\Delta \epsilon_i}. \quad (3.23)$$

The so-called reference states

$$| \psi_{\text{ref}}^{(n)} \rangle = \sum_{i \in \mathcal{M}_{\text{ref}}} c_{i,\text{ref}}^{(n)} | \Phi_i \rangle \quad (3.24)$$

are here a first approximation of the targeted states, which are typically calculated within an NCSM calculation with a smaller N_{max} value that has a feasible model space \mathcal{M}_{ref} size. The $\Delta \epsilon_i$ are the excitation energies of the states $| \Phi_i \rangle$ computed in an independent-particle picture. In the HO basis one uses simply the HO energies $e_a = \hbar \Omega (2n_a + l_a + 3/2)$ for the single-particle energies of the many-body state. This importance measure is not only a good measure for the energy, but also for other observables, since it probes the importance of the state. By including only those basis states with an importance measure $|\kappa_i|$ larger than a threshold value κ_{min} into the importance-truncated model space, one can reduce the model space to a feasible size. The quality of the truncation can be tested by a variation of κ_{min} . In a practical calculation we calculate an observable for a sequence of κ_{min} values and extrapolate to $\kappa_{\text{min}} \rightarrow 0$. The IT-NCSM is still a variational approach and the Hylleraas-Underheim theorem [98] is still valid for the energies of all states. Therefore, the energy eigenvalues decrease monotonically with decreasing κ_{min} . For other observables this theorem is not valid and the extrapolations can be more involved.

In addition to the importance measure an additional truncation parameter, the so-called reference threshold c_{\min} , is used. This truncation is only introduced for technical reasons. In the evaluation of κ_{\min} only basis states with an amplitude $|c_i^{(n)}| \geq c_{\min}$ are considered. This accelerates the evaluation of κ_{\min} and has no significant impact on the result for a valid choice of c_{\min} .

The Hamiltonian does only connect up to two-particle two-hole (2p2h) excitations or three-particle three-hole (3p3h) excitations if three-body operators are used. Hence, the importance measure does not probe basis states that differ by more than 2p2h or 3p3h excitations. A practical IT-NCSM calculation is, therefore, performed in an iterative procedure. In an ordinary NCSM calculation we calculate the first reference states for example in an $N_{\max} = 2$ model space. These reference states are used to filter the $N_{\max} = 4$ model space for a sequence of κ_{\min} values, which leads to a set of important truncated model spaces $\mathcal{M}_{\text{IT}}(\kappa_{\min})$. In each $\mathcal{M}_{\text{IT}}(\kappa_{\min})$ one solves the eigenvalue problem and calculates all intended observables. The solution of the $\mathcal{M}_{\text{IT}}(\kappa_{\min})$ with the smallest κ_{\min} is then used as reference state to truncate the $N_{\max} = 6$ model space.

3.1.4 | Basis Optimizations

The HO basis is a convenient choice for the calculation of matrix elements due to the exact separation of the center-of-mass and intrinsic part, but HO states exhibit a Gaussian fall-off. Hence, a large number of oscillator shells are needed to accommodate the long-range asymptotics of physically realistic states. In particular observables, which are sensitive to the long-range behavior of the wave function like the root-mean-square radius and the electric quadrupole moment, exhibit a slow convergence with respect to model-space size. Hence, using different single-particle bases can lead to a faster convergence than the standard HO choice. In particular, the natural orbitals (NAT) basis [101] has recently been successfully employed. The NAT basis is the eigenbasis of the one-body density matrix, where the density matrix is separately constructed in a different many-body calculation. The method of choice for the calculation of the density matrix is Hartree-Fock plus many-body perturbation theory [102], since it is a computationally cheap but still powerful method. It has been shown that already with the lowest-order correction one obtains an accelerated NCSM model-space convergence. As a beneficial by-product, the convergence of the observable becomes independent of the underlying HO basis frequency $\hbar\Omega$. Hence, a frequency variation becomes obsolete, which in turn reduces the computational cost further. This basis can not only be used in the NCSM but also in other many-body methods like the IM-SRG, which we discuss in section 3.3.

3.1.5 | Normal-Ordered Two-Body Approximation

Including 3N interactions explicitly in the many-body approaches is often highly expensive on the computational and also on the conceptual side. A good compromise has been found to include 3N forces within the Normal-Ordered Two-Body (NO2B) approximation [74] into the calculation. Here the nuclear Hamiltonian is normal ordered with respect to a nucleus-specific reference state, which is a first approximation of the many-body system under consideration. With the normal ordering one transfers contributions of the 3N interaction into lower-particle ranks. It has been shown [74] that by neglecting the residual 3N contributions one deviates typically less than 1% from the results obtained when including the full 3N interaction for most energies of ground and excited states. We will discuss the concept of normal ordering and NO2B in more detail in the context of the IM-SRG, see section 3.3.

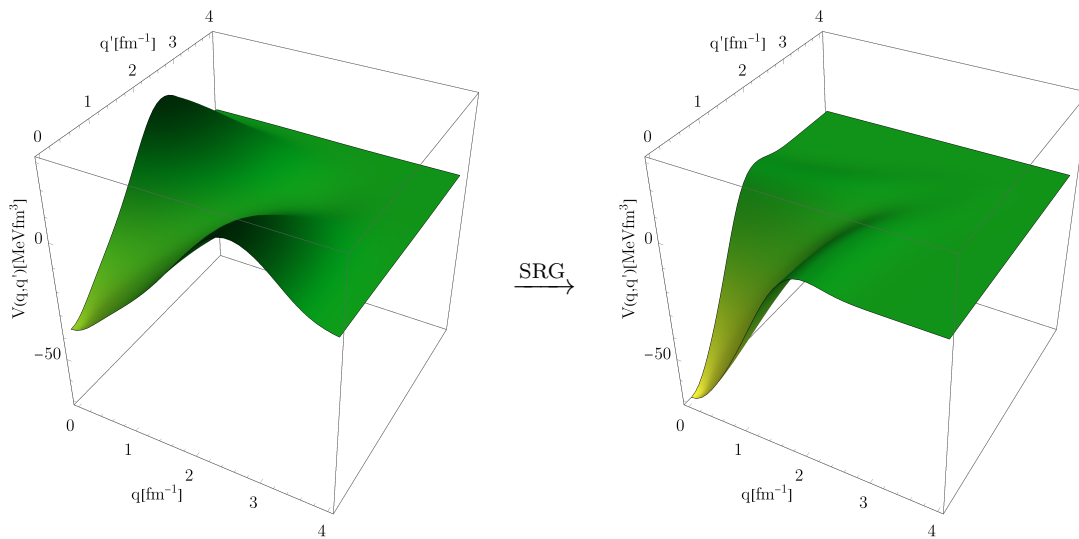


Figure 3.2: Momentum representation of the bare (left) and SRG evolved (right) EM NN at $N^3\text{LO}$ with $\Lambda = 500$ interaction in the $^3\text{S}_1$ channel. The SRG evolution has been performed with $\alpha = 0.08 \text{ fm}^4$.

3.2 | Similarity Renormalization Group

Bare realistic NN interactions, like the chiral interactions described in chapter 2, exhibit a slow convergence with respect to model-space size in many-body methods like the NCSM. A realistic NN interaction consists of a long-range attractive tail, which is dominated by one-pion physics, an intermediate-range attraction, which is also mainly dominated by pion physics, and a strong repulsive core. In momentum space, the strong repulsive core translates into large matrix elements that connect low and high initial and final relative momenta q and q' of the nucleons, see figure 3.2 (left), where we plot the momentum representation of the $^3\text{S}_1$ channel of the EM NN interaction. These couplings reveal themselves in wave functions or probability densities by a significant suppression at short range, which is often referred to as correlation hole or short-range correlation. For example this correlation hole can be seen in the deuteron wave function shown in figure 3.3 calculated with the EM NN interaction. In typical basis representations, which are used in many-body methods, like the HO basis, these short-range correlations are difficult to represent. Hence, a large number of excitation quanta are required to accommodate them and the many-body method converges slowly. We can accelerate the convergence of a many-body method like the NCSM by decoupling low- and high-momentum states. In addition to the short-range correlation, at larger distances the interaction depends strongly on the orientation of the nucleon spins. This tensor correlations originate mainly from the one-pion exchange part in the interaction and can also lead to slow convergence in many-body methods. Hamiltonians derived in chiral EFT are already softer than phenomenological ones, but not soft enough to converge many-body systems larger than $A \approx 4$ within feasible model-space sizes.

The decoupling can be achieved with a unitary transformation of the Hamiltonian. With such a unitary transformation, we do not change the eigenvalues of the Hamiltonian and other operators can be transformed accordingly. In that way other observables than the energy can be obtained consistently. There are various methods that base on unitary transformations to accelerate the convergence of many-body methods with respect to the model space like the unitary correlation operator method (UCOM) [23] or the Okubo–Lee–Suzuki (OLS) [21, 25,

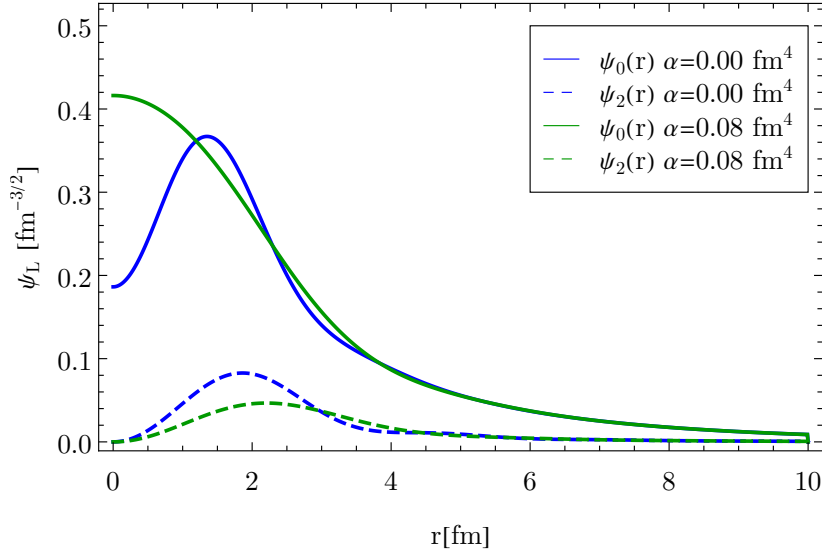


Figure 3.3: Deuteron wave functions obtained with the bare (blue) and SRG evolved (green) EM NN at N³LO with $\Lambda = 500$ interaction. The solid line represents the S-wave and the dashed line the D-wave. The SRG evolution has been performed with $\alpha = 0.08 \text{ fm}^4$.

26] approach.

In UCOM the unitary operator is constructed explicitly in such a way that the nucleons are pushed away from each other outside of the repulsive core. In addition a spin dependent spatial shift perpendicular to the radial direction addresses the tensor correlations. Thus, the short-range and tensor correlations are implanted into the many-body state and thereby the problem is physically motivated approached.

The OLS approach is more technically motivated. The model space is divided into an active and an excluded space. The active space is the model space used in the many-body approach and with a unitary transformation both spaces are fully decoupled. The OLS approach has the disadvantage that it is dependent on the many-body model space and, therefore, the variational principle no longer holds for NCSM like methods, but with increasing model space the calculations still converge towards the exact solution.

With the similarity renormalization group (SRG) [23, 24] we use a more flexible approach with the idea to prediagonalize the Hamiltonian. In the SRG an explicit specification of the unitary operator is not necessary. It tackles multiple sources of correlations at once, and the extension into many-body regime is straight forward. It was developed by Glazek and Wilson [103] and independently by Wegner [104, 105] and uses a continuous unitary transformation of the Hamiltonian

$$\hat{H}_\alpha = \hat{U}_\alpha^\dagger \hat{H}_0 \hat{U}_\alpha \quad (3.25)$$

with \hat{U}_α the unitary operator ($\hat{U}_\alpha^\dagger \hat{U}_\alpha = 1$), α the flow parameter, and $\hat{H}_0 = \hat{H}$ the unevolved or bare Hamiltonian. By taking the derivative of equation 3.25 with respect to α and defining the antihermitian generator

$$\hat{\eta}_\alpha = -\hat{U}_\alpha^\dagger \frac{d\hat{U}_\alpha}{d\alpha}, \quad (3.26)$$

the unitary transformation can be rewritten into a flow equation

$$\frac{d\hat{H}_\alpha}{d\alpha} = [\hat{\eta}_\alpha, \hat{H}_\alpha]. \quad (3.27)$$

The generator of the unitary transformation can be chosen in a commutator form

$$\hat{\eta}_\alpha = [\hat{G}_\alpha, \hat{H}_\alpha] = -\hat{\eta}_\alpha^\dagger, \quad (3.28)$$

such that the antihermiticity is automatically achieved by choosing \hat{G}_α hermitian. This generator governs the flow of the transformation and is chosen to achieve a decoupling low- and high-momentum states. The flexibility in choosing a generator and not having to construct the unitary transformation operators explicitly is one major advantage of the SRG over other methods. There are various generators that have been explored in the past, see [106] and references therein. One of the most intuitive generator is the Wegner generator, where \hat{G}_α is chosen to be the diagonal part of the evolved Hamiltonian in a chosen basis

$$\hat{G}_\alpha = \text{diag}(\hat{H}_\alpha). \quad (3.29)$$

This generator brings the Hamiltonian into a more diagonal form with respect to the chosen basis. This can be easily seen, because if the Hamiltonian is in diagonal form the commutator vanishes and a fix point of the flow equation has been reached. In nuclear structure physics applications the standard choice of generator is

$$\hat{\eta}_\alpha = (2\mu)^2 [\hat{T}_{\text{int}}, \hat{H}_\alpha], \quad (3.30)$$

with $\mu = M_N/2$ the reduced nucleon mass and $\hat{T}_{\text{int}} = \hat{T} - \hat{T}_{\text{cm}}$ the intrinsic kinetic energy. The factor $(2\mu)^2$ is used to fix the units of the flow parameter α to fm^4 . This generator was introduced by Szpigiel and Perry [107] and the basic idea is the same as for the Wegner generator. Since the eigenbasis of the intrinsic kinetic energy is the momentum basis, this generator decouples low- and high-momentum states. In addition to α , a common notation for the flow parameter is $\lambda = \alpha^{-\frac{1}{4}}$, which is a momentum scale. It characterizes the width of the band in momentum space and thereby indicates the magnitude of the momentum transfer that couple in the Hamiltonian.

The effect of the SRG evolution on the interaction matrix elements in momentum space is illustrated in figure 3.2. The large offdiagonal matrix elements in the bare interaction are strongly suppressed after the SRG evolution. At the same time absolute values of the low-momentum matrix elements increase. On the other hand, for the deuteron wave function the short-range correlation hole gets eliminated, see figure 3.3. Thus, we see a clear decoupling of low- and high-momentum states as well as the reduction of the short-range correlations, which was our goal.

The unitary transformation of the Hamiltonian leaves the energy eigenvalues unchanged while the eigenstates change

$$\hat{H}_\alpha | \psi_{n,\alpha} \rangle = \hat{U}_\alpha^\dagger \hat{H} \hat{U}_\alpha \hat{U}_\alpha^\dagger | \psi_n \rangle = \hat{U}_\alpha^\dagger \hat{H} | \psi_n \rangle = \hat{U}_\alpha^\dagger E_n | \psi_n \rangle = E_n \hat{U}_\alpha^\dagger | \psi_n \rangle, \quad (3.31)$$

with $| \psi_{n,\alpha} \rangle = \hat{U}_\alpha^\dagger | \psi_n \rangle$ the evolved basis states. Hence, arbitrary operators \hat{O} for observables other than the energy need to be transformed with the same differential equation

$$\frac{d\hat{O}_\alpha}{d\alpha} = [\hat{\eta}_\alpha, \hat{O}_\alpha]. \quad (3.32)$$

This differential equation usually needs to be solved simultaneous to the differential equation of the Hamiltonian (3.27), since the generator depends on the Hamiltonian. As an alternative to solve the flow-equation for \hat{O} , we can use the differential equation for the unitary operator itself

$$\frac{d\hat{U}_\alpha}{d\alpha} = -\hat{U}_\alpha \hat{\eta}_\alpha \quad (3.33)$$

and determine the evolved operator afterwards

$$\hat{O}_\alpha = \hat{U}_\alpha^\dagger \hat{O} \hat{U}_\alpha. \quad (3.34)$$

In practical applications we need to translate the differential equation (3.27), which is in operator form, into a matrix ordinary differential equation by choosing a basis and solving it numerically.

By choosing a finite basis we need to explore truncation effects. An important issue is that the SRG induces many-body interactions. Even if we start with a two- or three-particle rank interaction, the SRG induces up to A -particle rank contributions. In practical calculations the SRG is truncated at the three-particle rank and induced forces beyond the three-body ones are neglected. Any truncation formally violates the unitarity of the SRG transformation, and thus the truncation at particle rank 3 can lead to a flow-parameter dependence of an observable, which indicates induced higher particle-rank forces. The SRG transformation of higher particle-rank is in principle straight forward but is computationally demanding. The SRG transformation in four-body space has already been performed but only in small model spaces [108] due to its computationally expensiveness. An other issue with four-body forces is that we need to incorporate them into the many-body method of choice, which can also be computational and conceptionally demanding. Instead of incorporating higher particle-rank contributions, we can try to find generators, which induce less many-body forces. To my knowledge, there has not been found a generator yet, which reduces the induced many-body forces and gives a comparable good convergence acceleration of many-body methods. We have studied multiple generators in [106, 109, 110] with little success. Another approach to mitigate the effect of induced many-body forces is the use of a phenomenological four-body force that mimics these induced contributions [111]. Here we still have the issue to incorporate the 4N forces in the many-body methods.

We use for the SRG evolution of the NN interaction the relative-momentum and for the evolution of NN operators the HO basis. The 3N SRG evolution is performed in the antisymmetric Jacobi HO basis described in section 3.1.2. Here, we exploit the symmetries of the Hamiltonian and perform the SRG in each $T_{12}J_{12}\Pi_{12}$ channel separately, where Π_{12} is the parity of the three-body state. Furthermore, it has been found beneficial [108] not to perform the SRG in each HO frequency $\hbar\Omega$ individually, but to perform the SRG in an adequate model space and perform a frequency conversion to the desired $\hbar\Omega$ afterwards. The SRG model space of our choice is $\hbar\Omega_{\text{SRG}} = 36$ MeV. Furthermore, for the different $T_{12}J_{12}\Pi_{12}$ channels we use different $E_{3\text{Max}}$ truncations, which is the maximum three-particle energy quantum number $e_1 + e_2 + e_3 \leq E_{3\text{Max}}$ of the three-body model space. For channels with $J_{12} < 9/2$ we use $E_{3\text{Max}} = 40$ MeV, for channels with $J_{12} = 9/2$ we use $E_{3\text{Max}} = 38$ MeV, and for channels with $J_{12} > 9/2$ we use $E_{3\text{Max}} = 36$ MeV.

In this work we perform the SRG evolution always up to the 3N level, but we distinguish between different sets of input Hamiltonians into the SRG. If we use only the NN interaction in the initial Hamiltonian, we denote the resulting Hamiltonian with NN+3N_{ind}, but if we also include initial 3N interaction terms, we denote these Hamiltonians with NN+3N_{full}. We note further that the initial 3N is only available for the lower J_{12} channels. Therefore, only in those channels are the initial 3N interactions included. For the SCS and SMS interactions we include the 3N interaction in the channels with $J_{12} \leq 9/2$ and the non-local 3N interaction is included in the channels with $J_{12} \leq 13/2$.

As already said, the SRG is a quite flexible method and can also be used for other purposes than the prediagonalization of a Hamiltonian. In the next section we employ the SRG to solve the stationary Schrödinger equation.

3.3 | In-Medium Similarity Renormalization Group

The in-medium similarity renormalization group (IM-SRG) [27–32] is an SRG based approach to solve a many-body problem. Its basic idea is to use the SRG to suppress specific off-diagonal parts of an initial Hamiltonian with respect to a specific many-body basis.

3.3.1 | Second Quantization and Normal Ordering

Before we illustrate the concept of the IM-SRG, we introduce some basic terminology, which we use later on. In second quantization we will use creation \hat{a}^p and annihilation operators \hat{a}_q to create or annihilate particles in the antisymmetric Fock space \mathcal{F}^a with state p or q , respectively. They act on a Slater determinant in the following ways

$$\hat{a}^p | p_1 \dots p_A \rangle = \begin{cases} | pp_1 \dots p_A \rangle & \text{if } p \notin \{p_1, \dots, p_A\} \\ 0 & \text{if } p \in \{p_1, \dots, p_A\} \end{cases}, \quad (3.35)$$

$$\hat{a}_p | p_1 \dots p_A \rangle = \begin{cases} (-1)^{k-1} | p_1 \dots p_{k-1} p_{k+1} \dots p_A \rangle & \text{if } p = p_k \\ 0 & \text{if } p \notin \{p_1, \dots, p_A\} \end{cases}. \quad (3.36)$$

The shorthand notation

$$\hat{a}_{q_1 \dots q_n}^{p_1 \dots p_n} = \hat{a}^{p_1} \dots \hat{a}^{p_n} \hat{a}_{q_n} \dots \hat{a}_{q_1} \quad (3.37)$$

for multiple creation and annihilation operators is convenient to use for arbitrary n -body operators

$$\hat{O}^{[n]} = \frac{1}{(n!)^2} \sum_{p_1 \dots p_n q_1 \dots q_n} O_{q_1 \dots q_n}^{p_1 \dots p_n} \hat{a}_{q_1 \dots q_n}^{p_1 \dots p_n} \quad (3.38)$$

with the matrix element

$$O_{q_1 \dots q_n}^{p_1 \dots p_n} = \langle p_1 \dots p_n | \hat{O} | q_1 \dots q_n \rangle \quad (3.39)$$

of this operator.

The creation and annihilation operators refer always to the vacuum. It is also possible to redefine this reference. If we use an A -body Slater determinant as a reference state $|\psi_{\text{ref}}\rangle = |q_1 \dots q_A\rangle$, we call the occupied single-particle states $|q_1\rangle, \dots, |q_A\rangle$ hole states. States that are not occupied we call particle states. The creation and annihilation operators act on the reference state in the following way

$$\hat{a}^p | \psi_{\text{ref}} \rangle \neq 0, \quad \hat{a}_p | \psi_{\text{ref}} \rangle = 0, \quad \hat{a}^q | \psi_{\text{ref}} \rangle = 0, \quad \hat{a}_q | \psi_{\text{ref}} \rangle \neq 0, \quad (3.40)$$

where p and q indicate particle and hole states, respectively. Hence, we can reinterpret the operators \hat{a}_p and \hat{a}^q as quasiparticle annihilation operators and \hat{a}^p and \hat{a}_q as quasiparticle creation operators, since they act on the reference state in the same way as the creation and annihilation operators on the vacuum state.

We call a set of creation and annihilation operators in normal order, if all quasiparticle annihilation operators are on the right-hand side of all quasiparticle creation operators. The normal ordering operator is indicated through curly brackets enclosing the creation and annihilation operators

$$\{\hat{X}_1 \dots \hat{X}_n\} = \text{sgn}(\pi) \hat{X}_{\pi(1)} \dots \hat{X}_{\pi(n)}, \quad (3.41)$$

where π is a permutation, which rearranges the operators such that normal order is fulfilled. The $\text{sgn}(\pi)$ function indicates the sign of the permutation. The normal ordering depends on the reference state and is not unique. Using p_i for particle and q_i for hole states we can illustrate this in the following example

$$\{\hat{a}_{p_2 q_2}^{p_1 q_1}\} = \{\hat{a}^{p_1} \hat{a}^{q_1} \hat{a}_{q_2} \hat{a}_{p_2}\} = -\hat{a}^{p_1} \hat{a}_{q_2} \hat{a}^{q_1} \hat{a}_{p_2} = \hat{a}_{q_2} \hat{a}^{p_1} \hat{a}^{q_1} \hat{a}_{p_2} = \hat{a}^{p_1} \hat{a}_{q_2} \hat{a}_{p_2} \hat{a}^{q_1} = -\hat{a}_{q_2} \hat{a}^{p_1} \hat{a}_{p_2} \hat{a}^{q_1}. \quad (3.42)$$

One special property of a normal ordered expression is that the expectation value in the reference state vanishes

$$\langle \psi_{\text{ref}} | \{\hat{X}_1 \cdots \hat{X}_n\} | \psi_{\text{ref}} \rangle = 0. \quad (3.43)$$

We discussed here only the normal ordering with respect to a single Slater determinant, but it is possible to extend this procedure to multi-reference states [112].

3.3.2 | IM-SRG Concept

In contrast to the SRG approach discussed before, which we refer to as free-space SRG in the context of the IM-SRG, the IM-SRG is formulated such that all operators are normal ordered with respect to a reference state. This reference state is a first approximation for the targeted state and is typically obtained from a HF or an NCSM calculation. In the normal ordered form, the Hamiltonian for an A -body system with NN and 3N forces can be written as

$$\hat{H} = E + \sum_{pq} f_q^p \{\hat{a}_q^p\} + \frac{1}{2!2} \sum_{pqrs} \Gamma_{rs}^{pq} \{\hat{a}_{rs}^{pq}\} + \frac{1}{3!2} \sum_{pqrst} W_{st}^{pqr} \{\hat{a}_{st}^{pqr}\}, \quad (3.44)$$

by using the Wick theorem [31], where the zero-, one-, two-, and three-body terms are

$$E = \sum_p T_p^p n_p + \frac{1}{2} \sum_{pq} V_{pq}^{pq} n_p n_q + \frac{1}{6} \sum_{pqr} V_{pqr}^{pqr} n_p n_q n_r, \quad (3.45)$$

$$f_q^p = T_q^p + \sum_r V_{qr}^{pr} n_r + \frac{1}{2} \sum_{rs} V_{qrs}^{prs} n_r n_s, \quad (3.46)$$

$$\Gamma_{rs}^{pq} = V_{rs}^{pq} + \frac{1}{4} \sum_t V_{rst}^{pqt} n_t, \quad (3.47)$$

$$W_{st}^{pqr} = V_{st}^{pqr}. \quad (3.48)$$

Here n_p indicates the occupation number. It becomes clear that the normal ordering transfers contributions to lower rank operators and the zero-, one- and two-body parts of the Hamiltonian contain information on the initial 3N interaction. In the so-called NO2B approximation we make use of this and neglect the residual three-body parts in practical calculations. It has been shown that this is a good approximation [113, 74, 114], but it is ongoing work to incorporate the three-body parts in the calculation, which comes with significantly more computational expense.

However, the SRG flow-equation

$$\frac{d\hat{H}(s)}{ds} = [\hat{\eta}(s), \hat{H}(s)] \quad (3.49)$$

is not used to prediagonalize the Hamiltonian for the use in an other many-body approach. Instead the SRG is used to bring the Hamiltonian in a block-diagonal form, such that we

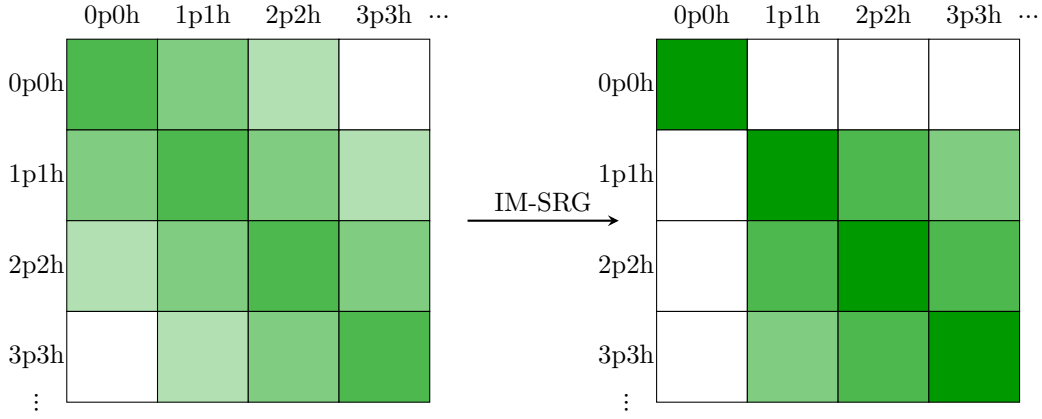


Figure 3.4: Schematic illustration of the model space decoupling pattern in the IM-SRG. On the left side is the initial Hamiltonian and on the right side the final IM-SRG evolved Hamiltonian in the many-body Hilbert space spanned by particle-hole excitations of the reference state.

decouple the reference state entirely from all particle-hole excitations. Here, we use s as flow parameter to distinguish between the IM-SRG and the free-space SRG. This is illustrated in figure 3.4. In the initial NO2B truncated Hamiltonian on the left-hand side, the reference state is coupled with 1p1h and 2p2h excitations. Within the IM-SRG we aim to decouple the reference state from all $A_p A_h$ excitations, as illustrated on the right-hand side. If we achieve this, the reference state is clearly an eigenstate of this Hamiltonian. We cannot guarantee that this is the ground state, this depends on the quality of the reference state. To decouple the reference state we partition the Hamiltonian into a diagonal and an off-diagonal part

$$\hat{H} = \hat{H}_d + \hat{H}_{od}. \quad (3.50)$$

The diagonal and off-diagonal part do not need to be the actual diagonal and off-diagonal part in a matrix representation. In the minimal decoupling scheme one only aims to decouple the one-dimensional block spanned by the reference state from all other particle-hole excitations, thus in the NO2B approximation only the matrix elements that couple the reference state with the 1p1h and 2p2h excitations are identified as the off-diagonal part

$$\langle \psi_{\text{ref}} | \hat{H} \{ \hat{a}_{q_1}^{p_1} \} | \psi_{\text{ref}} \rangle, \quad (3.51)$$

$$\langle \psi_{\text{ref}} | \hat{H} \{ \hat{a}_{q_1 q_2}^{p_1 p_2} \} | \psi_{\text{ref}} \rangle. \quad (3.52)$$

There is a variety of generators available that can be used to decouple the reference state for example the Wegner generator already discussed in the context of free-space SRG, see equation 3.29. Further generators are the White or imaginary-time generators [30]. All these generators are suitable to decouple the reference state and while the decoupling pattern is different during the flow, they lead, if the truncations are chosen well, to the same fix point of the flow. The generators differ mainly in the numerical efficiency and how they induce many-body interactions, since during the SRG flow, we induce many-body interactions similar to the ones in the free-space SRG. The unitarity of the transformation ensures that the spectrum is conserved, but by truncating the flow to, for example, two-body operators, one formally violates the unitarity.

For the calculation of other observables than the energy, we need to perform a simulta-

neous transformation of the corresponding operator

$$\frac{d\hat{O}(s)}{ds} = [\hat{\eta}(s), \hat{O}(s)]. \quad (3.53)$$

3.3.3 | Uncertainties

The results of the IM-SRG calculation have multiple sources for uncertainties. Limited memory space requires to truncate basis sizes, for example by using the HO basis with a maximum principal quantum number e_{\max} and maximum three-particle energy quantum number $e_1 + e_2 + e_3 \leq E_{3\text{Max}}$. These truncations need to be chosen sufficiently large and have to be validated. With SRG evolved interactions, these truncations are usually under control but should be probed especially in heavier nuclei. Furthermore, the NO2B approximation neglects all residual initial three-body operators as well as all appearing higher-body rank operators during the IM-SRG flow. These induced many-body forces are neglected in typical calculations, while there are efforts to include these forces. Another source of uncertainty is the single-particle basis choice itself, which can have an impact on the final result [115]. The typical approach to quantify these uncertainties is by comparison of the results with other many-body methods like coupled cluster [34, 35] and the NCSM, which use different truncations or solving methods. These benchmarks indicate a total uncertainty of $\approx 1 - 2\%$ [113, 112, 29, 74].

3.4 | Calculation of Radii

The radius of a nucleus is one of the basic observables for a comparison of theory and experiment. Although it is one of the basic observables, it is challenging to predict accurate radii. On the one hand, the calculation of radii is more demanding than that of energies, since the variational principle is not valid for other observables than the energy in NCSM like many-body methods. In our framework the radius is usually calculated through expectation value calculations of the corresponding radius operator. Since we are using the SRG to soften the interactions, we need to perform a consistent SRG transformation of this operator. We include SRG corrections up to the two-body level in our calculations. On the other hand, most of the chiral EFT interactions underestimates radii in the medium-mass regime. The first interaction that produced better radii was the NNLO_{sat} interaction [45], which included radii of medium-mass nuclei explicitly in the fit of the LECs. In this thesis, we will construct an interaction, which is suitable to calculate realistic radii.

To compare theory and experiment, we have to overcome an additional obstacle. In experimental setups one measures charge radii, while in theoretical calculation like the NCSM calculations we are calculating the point-proton root-mean-square (rms) radius

$$R_{p,\text{rms}} = \sqrt{\langle \psi_n | \frac{1}{Z} \sum_{i=1}^A (\hat{r}_i - \hat{R})^2 \hat{\Pi}_{p,i} | \psi_n \rangle}, \quad (3.54)$$

where we used the solution of the targeted state $|\psi_n\rangle$, the center-of-mass

$$\hat{R} = \frac{1}{A} \sum_{i=1}^A \hat{r}_i, \quad (3.55)$$

and the proton projection operator

$$\hat{\Pi}_{p,i} = \frac{1}{2} + \hat{t}_{3,i}, \quad (3.56)$$

with $\hat{t}_{3,i}$ the third component of the isospin operator. In this calculation we included two assumptions: First, the nucleons have the same mass and secondly, the proton is a point-like particle. For a comparison with the experiment, we need to take the charge distribution of the proton and neutron into account [116]

$$R_{\text{ch}}^2 = R_{\text{p,rms}}^2 + r_{\text{p,ch}}^2 + \frac{N}{Z} r_{\text{n,ch}}^2, \quad (3.57)$$

with the mean-square charge radii of the proton $r_{\text{p,ch}}^2$ and the neutron $r_{\text{n,ch}}^2$. The neutron does not carry a net charge, but it has a charge distribution, which leads to a $r_{\text{n,ch}}^2 = -0.1161(22) \text{ fm}^2$ [59]. The mean-square charge radius of the proton is given by $r_{\text{p,ch}}^2 = r_{\text{p,E}}^2 + 3/(4m_{\text{p}}^2)$, which is a combination of the electric charge radius of the proton $r_{\text{p,E}}$ and the Darwin-Foldy term [116], with the proton mass m_{p} . In recent years, the electric charge radius of the proton itself has been controversial and has given rise to the so-called proton radius puzzle. The discussion started with the measurement of the proton radius in muonic hydrogen [117], which lead to a significantly smaller $r_{\text{p,E}} = 0.84087(39) \text{ fm}$ compared to the 2014 CODATA value $r_{\text{p,E}} = 0.8751(61) \text{ fm}$ [118]. Since then there have been various remeasurements, which support both claims equally and there is no real solution of this puzzle yet. For instance, the Particle Data Group still lists both values [59]. In the most recent 2018 CODATA update, the muonic measurement has been included in the determination of the proton radius and is now given by $r_{\text{p,E}} = 0.8414(19) \text{ fm}$. To avoid the dependence on the proton radius, we will only present results that do not include these correction terms, for example the point-proton rms or the total rms radius. For the transformation of the experimental values into point-proton rms radii, we will use the older 2014 CODATA value. This leads to $R_{\text{p,rms,exp}} = 1.457(8) \text{ fm}$ instead of $R_{\text{p,rms,exp},\mu} = 1.477(4) \text{ fm}$ for ${}^4\text{He}$. In section 4.4 we will again shortly discuss this discrepancy in ${}^4\text{He}$. The experimental charge radii are taken from reference [119].

In our Jacobi-NCSM calculations, we need to make an additional assumption. Since our basis does not resolve the isospin of a single nucleon, we assume that the total rms radius is equal to the proton rms radius. This is a good approximation for ${}^4\text{He}$, in single-particle NCSM calculations the proton rms radius is only 0.2% larger than the total rms radius, which can be explained by the Coulomb interaction that pushes the protons apart. This difference is smaller than the experimental uncertainty.

4 | Optimization of Non-Local 3N Interactions

Even though interactions from chiral EFT are being used in a vast range of applications, their potential has not been exploited entirely. A widely used chiral EFT interaction is the NN interaction at N³LO by Entem and Machleidt [40] complemented with a local 3N interaction at N²LO [41]. However, with a single interaction at a specific chiral order a systematic uncertainty quantification is not possible. Furthermore, the chiral orders as well as the regularization schemes are inconsistent between the NN and 3N force. This interaction also systematically underestimates nuclear radii, particularly in the medium-mass regime [42–44].

There are other interactions available, for example the NNLO_{sat} interaction [45], which is a pure N²LO interaction with a consistent regularization scheme. This interaction benefits from a simultaneous fitting procedure, which takes into account NN phase-shifts as well as few- and many-body observables. Hence, this interaction also leads to a better description of radii. However, here also only a single chiral order is available such that a systematic order-by-order analysis is not possible.

With the SCS and SMS interactions a more systematic approach is chosen. Here, we can study observables by taking into account a sequence of interactions with increasing chiral orders. Hence, an uncertainty quantification with respect to the chiral truncation error becomes possible. We will explore some properties of these interactions in chapter 5.

In this chapter we will explore the EMN interactions [46], which allow, similarly to the semi-local interactions (SCS and SMS), a systematic improvement by chiral order. First, we will give an update of the EM interaction and explore the difference between a local and a non-local regularization scheme for the 3N force. Then we will employ the EMN interaction with two different fitting procedures for the 3N force and explore the resulting interaction families in the few- and many-body regime. We reported part of the findings discussed in this chapter already in [120].

4.1 | EM Local vs Non-Local 3N

As stated earlier, a widely used interaction is the EM NN interaction in combination with the local 3N interaction by Navrátil [41], where the 3N interaction is fitted to reproduce the half-life and binding energy of the triton [75, 121]. Please note that in the original version of [75] an error in the determination of the half-life lead to the 3N LECs $c_D = -0.2$ and $c_E = -0.205$. Nevertheless, this interaction has been used in a wide range of applications [122, 74–76, 123–125]. It was shown that this interaction overbinds the ground-state energies especially for nuclei with $A \gtrsim 10$ [122, 74, 76].

One can mitigate the overbinding by modifying the regularization of the 3N force and reducing the 3N force cutoff from $\Lambda_{3N} = 500$ MeV to $\Lambda_{3N} = 400$ MeV [74, 29, 108, 36, 113]. This regularization choice is in principle not more inconsistent than choosing the 3N force cutoff equal to the NN force cutoff, since one uses different regularization schemes for the NN and 3N interactions. By reducing the cutoff to $\Lambda_{3N} = 400$ MeV and fitting the c_E to the ground-state energy of ⁴He it is possible to describe ground-state energies up to the oxygen

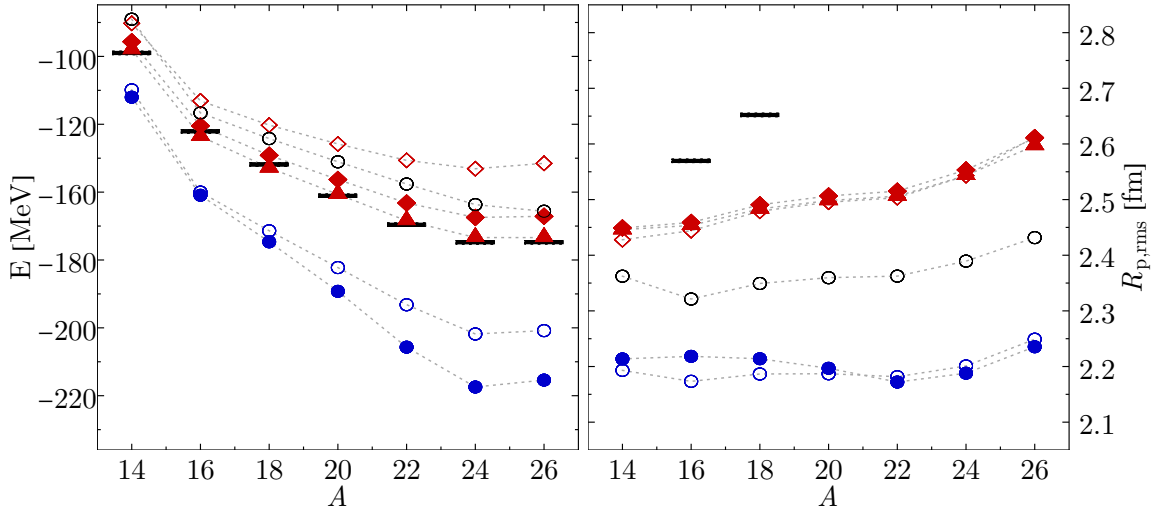


Figure 4.1: Ground-state energies (left) and point-proton rms radii (right) obtained in NCSM-PT calculations for the oxygen isotopes ${}^A\text{O}$ calculated with the EM NN interaction at N^3LO complemented with a local 3N interaction at N^2LO with a cutoff $\Lambda_{3\text{N}} = 400$ MeV (\circ) and 500 MeV (\bullet) as well as a non-local 3N interaction with cutoff $\Lambda_{3\text{N}} = 400$ MeV (\diamond), 500 MeV (\blacklozenge), and 525 MeV (\blacktriangle). Results for the EM NN (\circ) are only shown for comparison. All interactions are SRG evolved with a flow parameter $\alpha = 0.08$ fm 4 .

drip line sufficiently well. However, in medium-mass nuclei the interaction begins to overbind the ground states. Moreover, radii are systematically underestimated even for light nuclei. The cutoff reduction also has an impact on the induced 4N interaction of the SRG evolution. The strength of the induced force is observed to be reduced in comparison with the 500 MeV cutoff for ground-state energies of medium-mass nuclei [76, 74, 122].

In a corrected evaluation of the half-life of the triton [121], $c_{\text{D}} = 0.83$ and $c_{\text{E}} = -0.052$ were determined. This interaction cannot describe ground-state energies of light nuclei as well as the previous version and similarly underestimates radii. In figure 4.1 we show the ground-state energies and point-proton rms radii of the oxygen isotopes for this updated interaction (blue symbols). For the solid symbols, we use a cutoff $\Lambda_{3\text{N}} = 500$ MeV and for the open symbols we use a version with reduced cutoff $\Lambda_{3\text{N}} = 400$ MeV. We use the $c_{\text{D}} = 0.8$ from the half-life fit, while the c_{E} is refitted to the triton binding energy within an NCSM calculation. It is shown in [75, 121] that the determination of the half-life is barely dependent on the 3N force and c_{E} , whereas it depends on c_{D} through the strength of the MEC contact term \hat{d}_{R} . Using this interaction leads to clearly overestimated ground-state binding and underestimated radii in comparison to the experimental values. A cutoff reduction is not able to decrease the ground-state binding to a comparable level of quality as the previous local 3N interaction.

As an alternative to the local 3N force we can use the 3N interaction with a non-local regulator by Epelbaum *et al.* [48], see also section 2.4.3, and thus use the same regularization as in the NN force. Similar to the local 3N case, we are using the N^2LO terms only and retain $c_{\text{D}} = 0.8$ from the half-life determination of the triton and refit c_{E} to the triton binding energy. Please note that in the determination of the half-life Gazit *et al.* [75, 121] use the local regulator for the MEC, hence, the c_{D} choice is again inconsistent. The results shown in this section are not significantly different with a different c_{D} choice, hence, said c_{D} is still suited for this exploratory comparison. The ground-state energies and radii of the oxygen isotopes for this interaction are also shown in figure 4.1 (red symbols). In comparison

with the results for the local 3N interaction the energies are much closer to the experimental values. But the most significant change affects the radii. While the local 3N interaction shrinks the nuclei in comparison to the calculation without 3N force, the non-local 3N force increases the radii. With a consistent cutoff value for NN and 3N interaction of $\Lambda_{3N} = 500$ MeV we slightly underbind the oxygen isotopes, but by modifying the cutoff value we can again reproduce the ground-state energies of the oxygen isotopes. Instead of a reduction in the cutoff value, which leads to a more pronounced underbinding, a small increase to a cutoff $\Lambda_{3N} \approx 525$ MeV is necessary. In the cutoff modified versions, we retain $c_D = 0.8$ and refit c_E to the triton binding energy. The cutoff modification mainly impacts the ground-state energies, while the ground-state radii change only slightly.

4.2 | EMN Complemented with the Non-Local 3N

Instead of using only a single chiral order like in the EM NN interaction case, with the EMN NN interaction family we have the opportunity to perform an order-by-order analysis up to N⁴LO with three different cutoffs. Furthermore, we can complement this interaction with the 3N interaction by Hebeler *et al.* [49] at N²LO and N³LO with a consistent regularization scheme and scale, as discussed in 2.4.

Since there appear no additional LECs in the 3N interaction at N³LO, the only free parameters are c_D and c_E for the 3N interaction at N²LO and N³LO. A natural procedure is to fit these LECs to three-body data, as in the section before, the triton binding energy and the triton β -decay [75, 121]. Other three-body data can be the ³He binding energy, the neutron-deuteron doublet scattering length ² a [48, 126] and other nd and pd scattering data. Using only observables which correlate strongly with each other in the fit can lead to overfitting such that the fitted observables are perfect while a good description of other observables is not achieved. On the other hand, such correlations can be exploited by fitting to one observable and obtaining a good description of the remaining one by construction. The Phillips line [127] is an example for such a correlation between the triton binding energy and ² a_{nd} .

Alternative approaches include four-body data like the binding energy or point-proton radius of ⁴He or even many-body observables like ground-state radii and energies up to the oxygen isotopes [45] or include even nuclear matter quantities into the fitting procedure [128, 129]. There also exists an empirically observed correlation, the so-called Tjon line [130, 131, 126], between the binding energy of the triton and the ground-state energy of ⁴He. We can study the validity of this correlation for the aforementioned interactions.

We will employ different ways to determine the LECs. First, we will fix the c_D - c_E correlation via the triton binding energy and explore the dependence of ground-state energies and radii of light and medium-mass nuclei on the c_D within a natural range. Further on, we will relax the triton constraint and explore additional possibilities to fit c_D and c_E .

4.2.1 | Fitting the LECs to the Triton Binding Energy

The fit of the c_D - c_E correlation is performed by calculating the triton binding energy for a grid of c_D and c_E -values in a natural range and finding the optimal c_D - c_E pair via interpolation. The triton binding energies for the grid points are obtained in Jacobi-NCSM calculations, where we use model spaces up to $N_{\max}=48$ as well as HO frequencies $\hbar\Omega$ in the range of $\hbar\Omega = 20 - 36$ MeV. An exemplary Jacobi-NCSM calculation is shown in figure 4.2. For bare

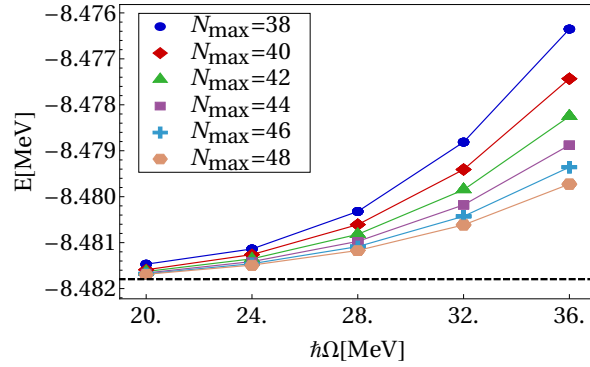


Figure 4.2: Variation of the HO frequency $\hbar\Omega$ in a Jacobi-NCSM calculation of the triton binding energy for the EMN NN interaction complemented with the non-local 3N interaction with cutoff $\Lambda = 500$ MeV at $N^3\text{LO}$ with $c_D = 4.0$ and $c_E = -1.492$. The experimental value is indicated with a dashed line.

interactions, the ground-state energies converge with an uncertainty better than 1 keV and do not need to be extrapolated. Please note that the convergence of the calculation is not as good for every c_D - c_E pair as the one shown in figure 4.2, in which we could assume a smaller uncertainty. The resulting correlations for c_D - c_E are shown in figure 4.3 for the chiral orders $N^2\text{LO}$, $N^3\text{LO}$, and $N^4\text{LO}'$ and the three cutoffs 450, 500, and 550 MeV. The prime notation $N^4\text{LO}'$ indicates that we complement the $N^4\text{LO}$ NN interaction with the $N^3\text{LO}$ 3N interaction only, see also section 2.4.1. We can see that the general behavior is similar for each chiral order. For negative c_D -values the c_E are similar for each cutoff and with increasing c_D the c_E -values fan out in parabola-like functions.

4.2.2 | Exploring c_D in the ${}^4\text{He}$ Energy-Radius Plane

With the c_D - c_E correlation fitted to the triton binding energy, we can explore the c_D trajectories, the observable dependent on c_D , in other systems. We start with the ground-state energy and point-proton rms radius of ${}^4\text{He}$. Figure 4.4 shows the results obtained in Jacobi-NCSM calculations for the bare NN+3N interactions for the three cutoffs and chiral orders $N^2\text{LO}$, $N^3\text{LO}$, and $N^4\text{LO}'$. In addition to the results for the NN+3N interactions, we also show the results for NN only at the corresponding chiral order. The trajectories for the three cutoffs follow similar parabolic curves. With increasing cutoff, the curves shift to lower energies and radii. The energies have an upper bound, which makes it impossible for the cutoffs $\Lambda = 500$ and 550 MeV at $N^3\text{LO}$ and $N^4\text{LO}'$ to reproduce the experimental value for ${}^4\text{He}$ for any c_D -value. While each c_D - c_E pair reproduces the triton binding energy, by construction the ${}^4\text{He}$ ground-state energy can vary in a large range, thus, the Tjon line is not fulfilled for a large set of possible interactions.

Furthermore, we should keep in mind that starting with $N^3\text{LO}$, there exist chiral 4N forces, which we have neglected in our calculations. These forces have been found to be small [132]. Nevertheless, with these forces included it may be possible to reproduce the experimental ground-state energy for ${}^4\text{He}$.

For heavier nuclei than ${}^4\text{He}$, we need to perform the SRG transformation to get converged results. Hence, we explore the impact of the SRG on the ${}^4\text{He}$ observables. In figure 4.5 we show the SRG dependence for the ${}^4\text{He}$ ground-state energy and point-proton rms radius calculated with the NN+3N interaction at $N^2\text{LO}$, $N^3\text{LO}$, and $N^4\text{LO}'$ with cutoff $\Lambda = 500$ MeV. For comparison, we also show the results for the NN+3N_{ind} interaction at the same order and

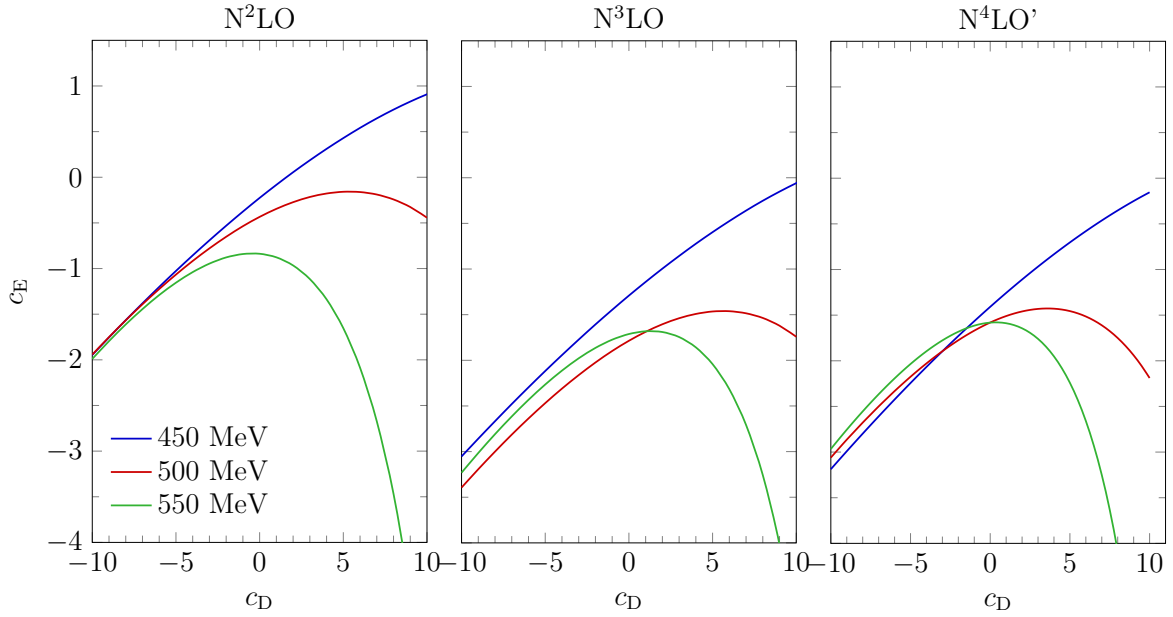


Figure 4.3: Correlation plot between the c_D and c_E -values. The curves indicate the fit to the triton binding energy at the chiral orders N^2LO (left), N^3LO (center), and N^4LO' (right).

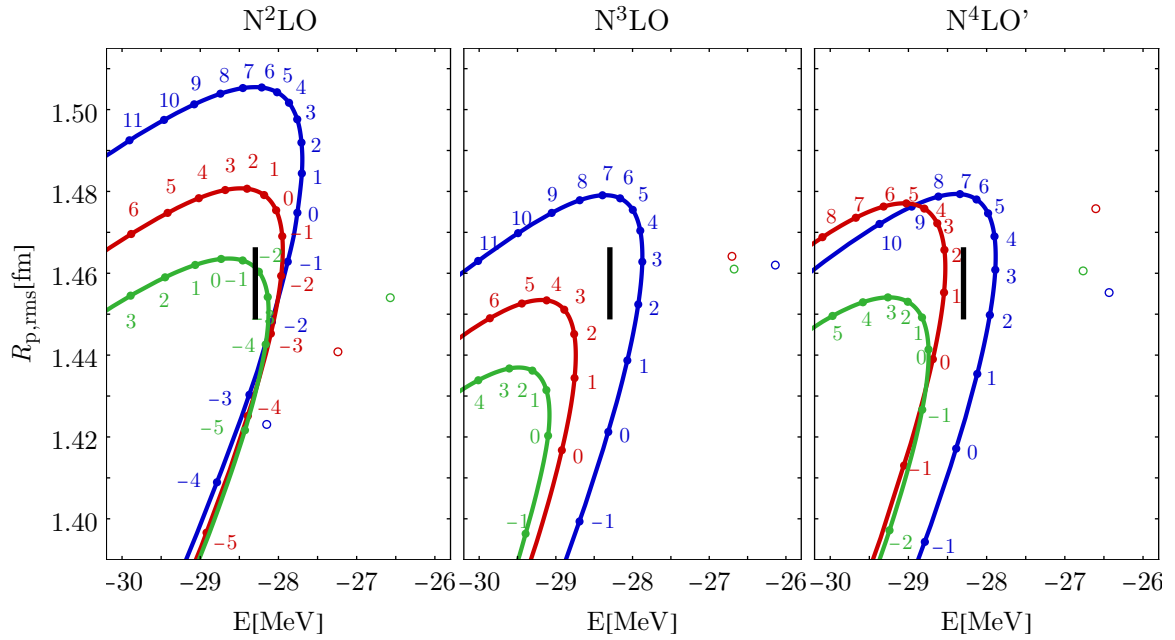


Figure 4.4: Correlation between the point-proton radius and the binding energy of the ground state of ${}^4\text{He}$ calculated in Jacobi-NCSM calculations with the EMN NN interaction complemented with the non-local 3N consistent up to N^3LO . The numeric values indicate the c_D -values while the c_E is fitted to the triton binding energy. The colors indicate the different cutoffs 450 MeV (blue), 500 MeV (red), and 550 MeV (green). The open symbols denote the results for the NN interaction only. The experimental values are indicated through black bars.

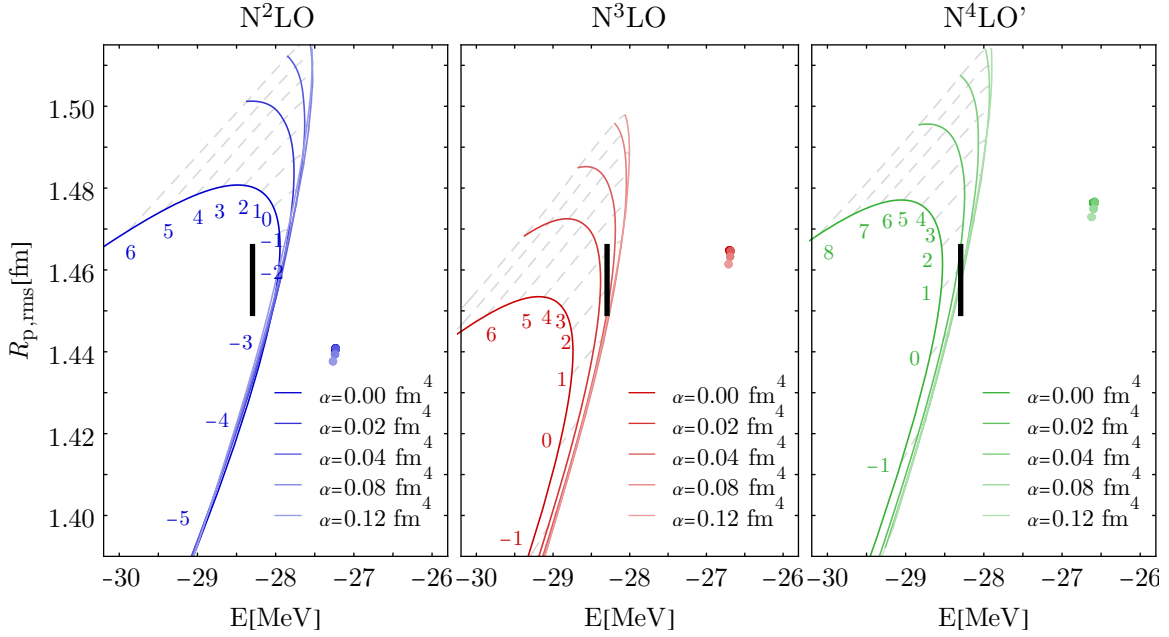


Figure 4.5: SRG dependence of the point-proton radius and the binding energy of the ground state of ${}^4\text{He}$ calculated in Jacobi-NCSM calculations for the chiral orders N^2LO (left), N^3LO (center), and $\text{N}^4\text{LO}'$ (right) with $\Lambda = 500$ MeV. The numeric values indicate the c_D -values while the c_E is fitted to the triton binding energy. The circles are the results for the $\text{NN}+3\text{N}_{\text{ind}}$ interaction. The experimental values are indicated through black bars.

cutoff. We perform the SRG at the NN and 3N level, therefore every change in the energy can be traced back to the neglected induced 4N force. The radius operator is consistently SRG evolved up to the NN level. Hence, the dependence arises from the missing induced 4N force and three- and four-body contributions to the radius operator. In general, the SRG transformation leads to less binding and larger radii. The interactions with larger c_D -values show a stronger α -dependence. Contrary to the bare N^3LO and $\text{N}^4\text{LO}'$ interactions, with the SRG evolved interactions we can reproduce the ${}^4\text{He}$ ground-state energy and radius in a wide range of α -values. Therefore, it is also possible to use the SRG as a tool to optimize the interaction and use α as an additional parameter to fit the interaction. The SRG induced two-body contributions to the radius operator $\Delta R_{p,\text{rms}}^{\text{SRG,NN}}$ shown in figure 4.6 are linearly dependent on the SRG flow parameter α and have a reducing effect on the radius. Nevertheless, this contribution is not enough to compensate the α -dependence. The residual α -dependence follows the rule that less binding leads to a larger radius, which indicates that the missing contribution stems from the induced four-body force. Nevertheless, the variation due to SRG for the radius is only on the percent level.

4.2.3 | Performance in Medium-Mass Nuclei

Similar to the c_D -variation in ${}^4\text{He}$, we can look at the c_D -dependence of medium-mass observables. In this section we restrict ourselves to calculations for the N^3LO interaction with cutoff $\Lambda = 500$ MeV, where the correlation between c_D and c_E is constrained by the triton binding energy. These interactions are SRG evolved up to $\alpha = 0.04$ fm^4 for a better convergence of the many-body method. In the medium-mass regime we use the single-reference IM-SRG for the calculation of ground-state energies and point-proton rms radii, see section 3.3. This method is restricted to closed shell nuclei, hence, we focus on those in this exploration. First, we

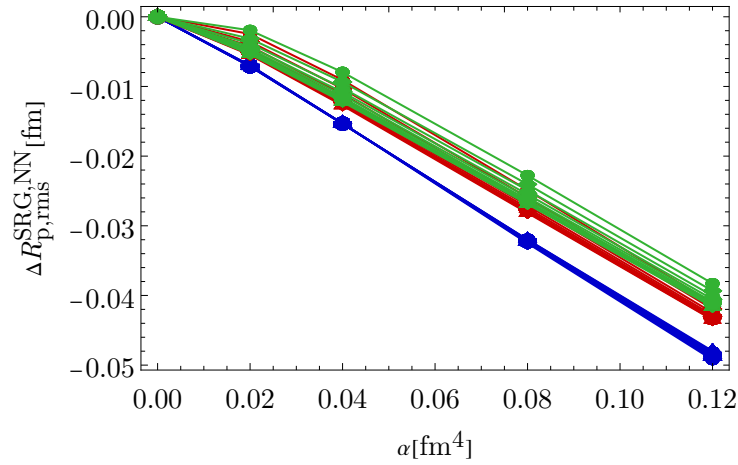


Figure 4.6: Contribution of the SRG induced two-body operator to the radius operator for the ground state of ${}^4\text{He}$. Shown are the results for the chiral orders N^2LO (blue), N^3LO (red), and $\text{N}^4\text{LO}'$ (green) with $\Lambda = 500$ MeV. Different symbols indicate different c_D -values from -2 to 6.

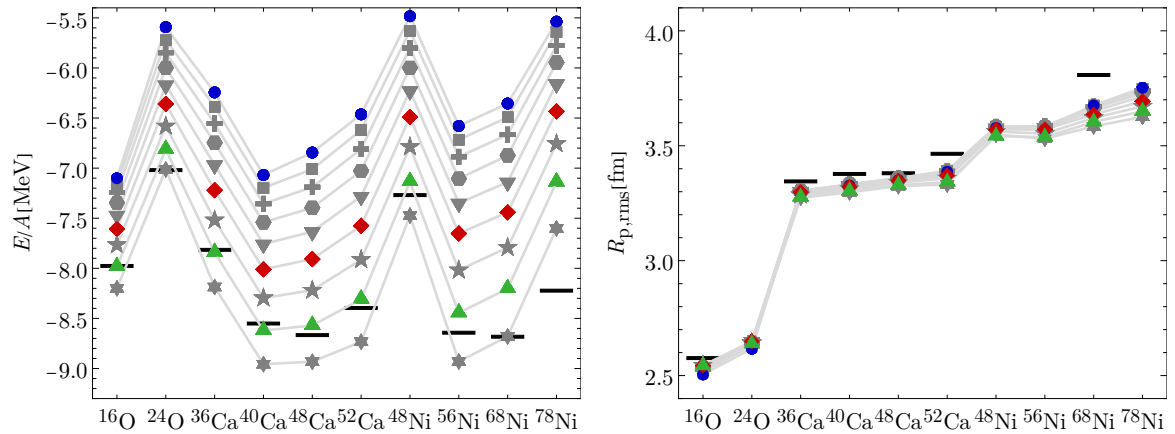


Figure 4.7: Ground-state energies per nucleon and point-proton rms radii of medium-mass nuclei. The results are obtained in IM-SRG calculations with $E_{3\text{Max}} = 14$ and $e_{\text{Max}} = 12$ for the NN+3N interaction at N^3LO with cutoff $\Lambda = 500$ MeV for a range of $c_{\text{DS}} = -3$ (\bullet), -2 (\blacksquare), -1 (\oplus), 0 (\bullet), 1 (\blacktriangledown), 2 (\blacklozenge), 3 (\star), 4 (\blacktriangle), 5 (\star) and c_{E} is fitted to the triton binding energy. The interactions are SRG evolved up to $\alpha = 0.04$ fm^4 . The experimental values are indicated through black bars.

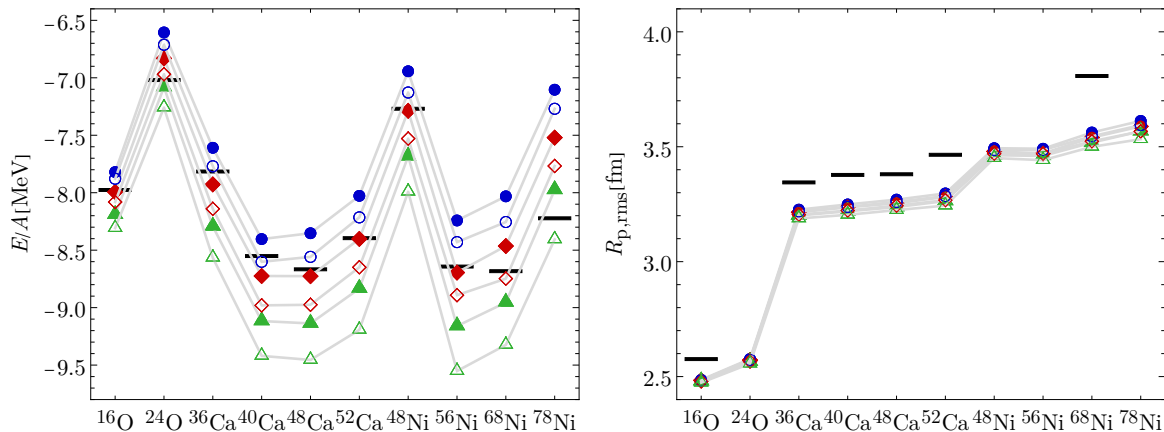


Figure 4.8: Regulator power n -dependence of ground-state energies per nucleon and point-proton rms radii of selected medium-mass nuclei. Solid symbols indicate a regulator power $n = 3$ and open symbols $n = 4$. The results are obtained in IM-SRG calculations with $E_{3\text{Max}} = 14$ and $e_{\text{Max}} = 12$ for the NN+3N interaction at N^3LO with cutoff $\Lambda = 500$ MeV. The different symbols and colors indicate the values of $c_D=3$ (\bullet), 4 (\blacklozenge), and 5 (\blacktriangle) where c_E is fitted to the triton binding energy. All interactions are SRG evolved with $\alpha = 0.08$ fm 4 . The experimental values are indicated through black bars.

will explore the c_D -dependence of these observables. Thereafter, we probe the dependence of the results on the power of the regularization function, the SRG parameter α , and the $E_{3\text{Max}}$ -truncation in the IM-SRG.

The results of the ground-state energies and point-proton rms radii for selected nuclei are shown in figure 4.7 for various c_D -values. In the negative c_D -range all nuclei are underbound. With increasing c_D the ground-state energies systematically decrease until the energies nearly agree with the experimental values for all considered isotopes at $c_D \approx 4$ (\blacktriangle).

If we consider the results of the c_D -variation for ^4He in figure 4.5 (center), we would expect the c_D -value to be around $c_D \approx 2$ (\blacklozenge). Using $c_D = 2$ leads to underbound nuclei in the medium-mass regime. Furthermore, Drischler *et al.* [128] constrain c_D and c_E for the same interaction family in nuclear matter calculations. These interactions are also explored in medium-mass calculations by Hoppe *et al.* [129]. They find the best description of the saturation point around $c_D = -3$ (\bullet), even though the saturation energy E/A is slightly less bound than the empirically one [128] for N^3LO with $\Lambda = 500$ MeV. In this c_D -range all the medium-mass nuclei are significantly underbound. Please note that in said references the N^3LO interaction is used with a slightly different regulator function with a power of $n = 4$ for the 3N interaction instead of $n = 3$ as in our calculation. This difference only has a small effect on the results, see figure 4.8, where we probe the dependence of the energies and radii of medium-mass nuclei on the regulator function in the c_D -range of 3 to 5. The interactions regularized with a regulator function with power $n = 4$ lead to slightly more binding, but the energy difference between $n = 3$ and $n = 4$ is smaller than a $\Delta c_D \approx 1$ shift. We will see later in section 4.3 that the energy difference of $\Delta c_D \approx 1$ is of approximately the same size as the many-body uncertainty.

In contrast to the ground-state energies, the radii are overall close to the experimental values and indicate only a minor c_D -dependence, see figure 4.7. Despite the good description of experimental values, in the considered c_D -range the radii are slightly too small compared with the experiment.

The dependence on the SRG parameter α is explored in figure 4.9 for the interaction

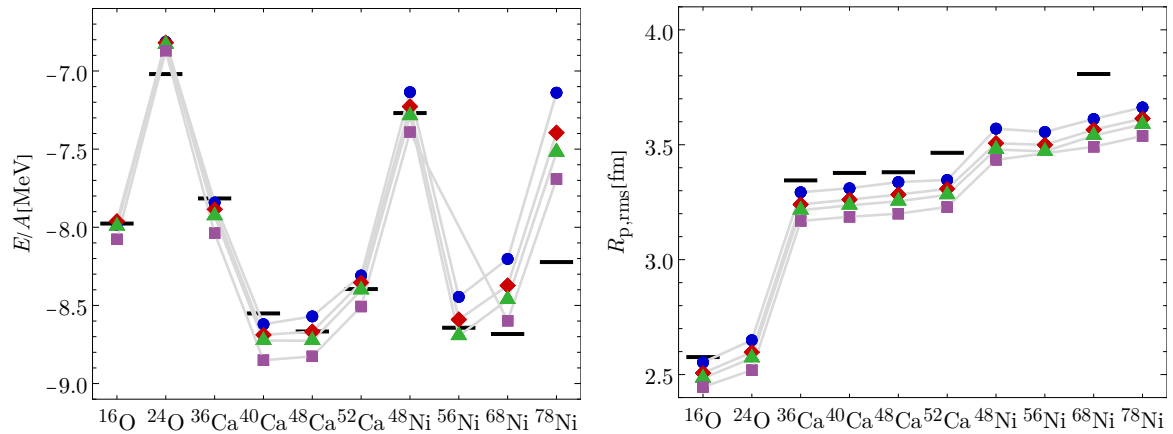


Figure 4.9: SRG parameter dependence of ground-state energies per nucleon and point-proton rms radii of selected medium-mass nuclei. The different symbols indicate the different SRG parameters $\alpha = 0.04 \text{ fm}^4$ (\bullet), 0.0625 fm^4 (\blacklozenge), 0.08 fm^4 (\blacktriangle), and 0.12 fm^4 (\blacksquare). The results are obtained in IM-SRG calculations with $E_{3\text{Max}} = 14$ and $e_{\text{Max}} = 12$ for the NN+3N interaction at N^3LO with cutoff $\Lambda = 500 \text{ MeV}$ with $c_{\text{D}}=4$ and c_{E} is fitted to the triton binding energy. The experimental values are indicated through black bars.

with $c_{\text{D}} = 4$. The ground-state energies and radii of all considered medium-mass nuclei show a similar SRG dependence: with increasing α the nuclei are stronger bound and shrink in size. This behavior is contrary to ${}^4\text{He}$, where larger α lead to less binding and larger radii. The averaged relative difference between $\alpha = 0.04 \text{ fm}^4$ and 0.12 fm^4 is about 2% for the ground-state energies and 4% for the radii.

In figure 4.10 we explore the impact of the $E_{3\text{Max}}$ -truncation, which is the maximum total excitation energy quantum number of three nucleons in the matrix elements entering the IM-SRG calculation. Up to ${}^{40}\text{Ca}$ an $E_{3\text{Max}} = 14$ is sufficiently large to obtain converged ground-state energies and radii. Heavier nuclei should be calculated with an $E_{3\text{Max}} = 16$ and starting with ${}^{68}\text{Ni}$ an $E_{3\text{Max}} = 18$ is necessary.

In summary, we see a clear mismatch in the c_{D} -values which describe ${}^4\text{He}$, medium-mass nuclei, and nuclear matter observables. Furthermore, we have explored the SRG- and $E_{3\text{Max}}$ -dependence of the IM-SRG calculations. In addition to these sources of uncertainty, we need to take into account the uncertainty due to the NO2B approximation used in the IM-SRG. In total we assume the uncertainty of the many-body calculation to be about 2% of the calculated observable.

4.3 | Many-Body Optimized Interactions

In the previous section, we saw that the c_{D} -dependence in medium-mass systems is highly correlated such that by fitting one system, we achieve an overall good description of the ground-state energies and radii. This allows for a fitting procedure where we simply fit c_{D} to the ground-state energy of ${}^{16}\text{O}$, which is the lightest of the selected medium-mass nuclei. We have chosen ${}^{16}\text{O}$, since we can calculate ${}^{16}\text{O}$ also with the NCSM. Therefore, we have the best control over the many-body uncertainties. In figure 4.11, we show a variation of c_{D} for all three cutoffs for the chiral orders N^2LO to $\text{N}^4\text{LO}'$. The calculations are performed with SRG evolved interactions with $\alpha = 0.04 \text{ fm}^4$. For the smallest cutoff $\Lambda = 450 \text{ MeV}$ a large c_{D} -value is necessary to reproduce the ${}^{16}\text{O}$ ground-state energy but with increasing cutoff the optimal

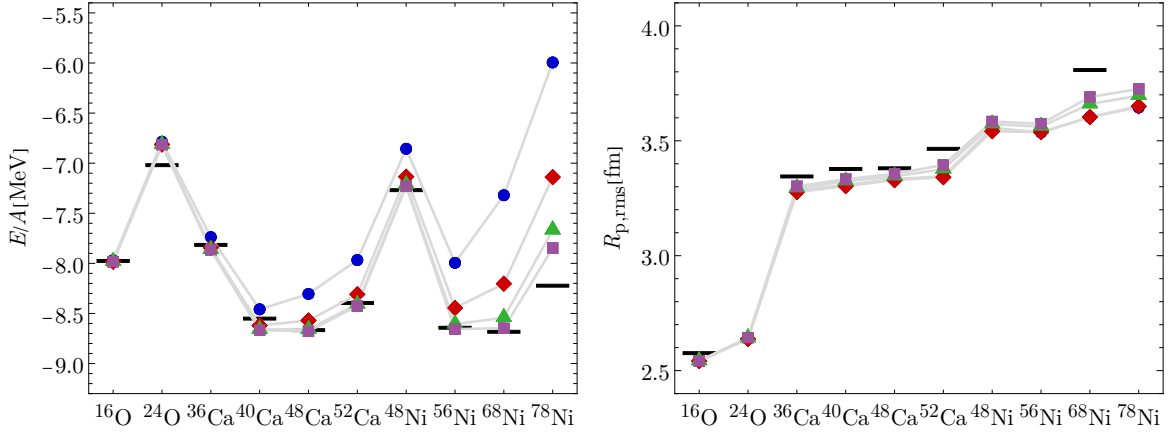


Figure 4.10: Dependence of the ground-state energies per nucleon and point-proton rms radii of medium-mass nuclei on the $E_{3\text{Max}}$ -truncation. The results are obtained in IM-SRG calculations with $E_{3\text{Max}} = 12$ (\bullet), 14 (\blacklozenge), 16 (\blacktriangle), and 18 (\blacksquare). The calculations are done with the NN+3N interaction at N^3LO with cutoff $\Lambda = 500$ MeV with fixed $c_D = 4.0$, $\alpha = 0.04 \text{fm}^4$, and $e_{\text{Max}} = 12$. The experimental values are indicated through black bars.

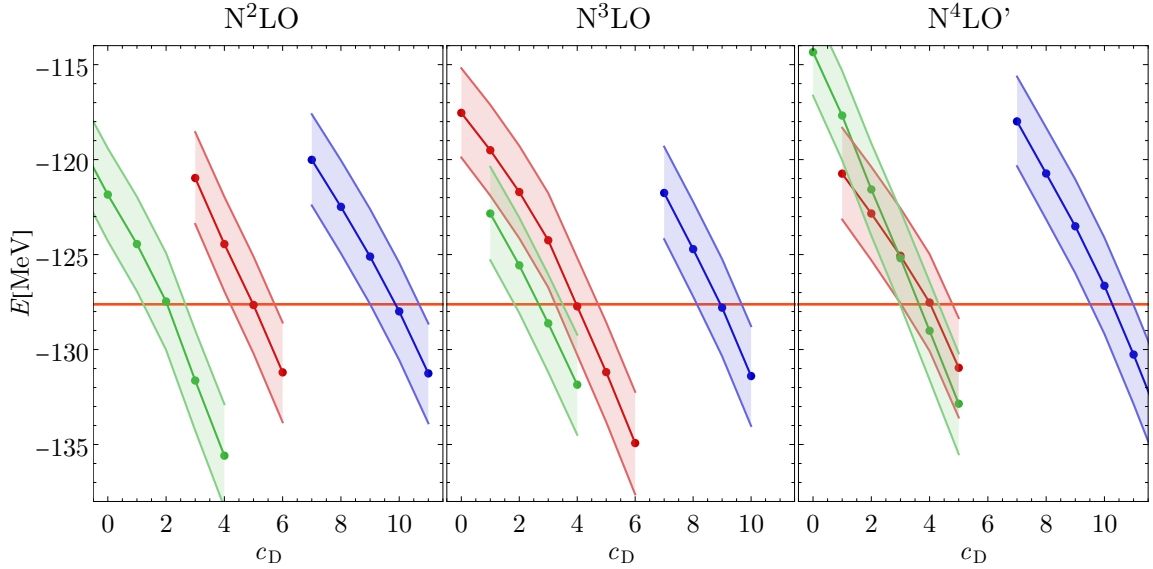


Figure 4.11: Ground-state energy of ^{16}O for a range of c_D -values. Results are obtained in single-reference IM-SRG calculations with NAT basis and NO2B approximation with $E_{3\text{Max}} = 14$ and $e_{\text{Max}} = 12$. Shown are the results for the interactions with cutoffs $\Lambda = 450$ (\bullet), 500 (\bullet), and 550 (\bullet) MeV for the chiral orders N^2LO (left), N^3LO (center), and $\text{N}^4\text{LO}'$ (right). The interactions are SRG evolved with $\alpha = 0.04 \text{fm}^4$ and the experimental ground-state energy is indicated with an orange line.

chiral order	Λ [MeV]	c_D	c_E
N ² LO	450	9.9 ± 0.9	0.901
	500	5.0 ± 0.8	-0.159
	550	2.0 ± 0.8	-0.966
N ³ LO	450	8.9 ± 0.8	-0.162
	500	4.0 ± 0.7	-1.492
	550	2.7 ± 0.9	-1.724
N ⁴ LO'	450	10.3 ± 0.8	-0.127
	500	4.0 ± 1.0	-1.429
	550	3.2 ± 1.0	-1.792

Table 4.1: Optimized c_D and c_E -values in the many-body system.

c_D -values decrease. The c_D and c_E -values that reproduce the ¹⁶O ground-state energy are summarized in table 4.1. The uncertainty bands correspond to the many-body uncertainties estimated before (2%) and are composed of uncertainties due to basis truncations, the NO2B approximation, and induced many-body forces from the SRG, as discussed in section 3.3.3. For c_D the many-body uncertainty translates into roughly an uncertainty of $\Delta c_D \approx 1$. The c_E in table 4.1 corresponds to the value in the center. In the following we will refer to the interactions fitted to the ground-state energies of the triton and ¹⁶O as many-body optimized (MBO) interactions.

Fitting an interaction too precisely to a specific observable can lead to artifacts. While the interaction describes the fitted observable perfectly, other observables may only be described insufficiently. For example, the bare MBO N²LO and N³LO interactions reproduce the triton binding energy perfectly by construction, but the ground-state of ⁴He is about 1 MeV overbound, see table 4.3 for the earlier result. In addition, while we are able to fit the triton within an uncertainty of 1 keV, within the chiral expansion this is not necessary. Using the truncation error estimate of EKM, see section 2.5, to determine the chiral truncation error for the binding energies of triton and ⁴He, we would expect for the cutoff $\Lambda = 500$ MeV at N³LO an uncertainty of

$$\delta E_{N^3LO}(^3\text{H}) = Q^3 |E_{LO}(^3\text{H}) - E_{NLO}(^3\text{H})| = 103 \text{ keV} \quad (4.1)$$

and

$$\delta E_{N^3LO}(^4\text{He}) = Q^3 |E_{LO}(^4\text{He}) - E_{NLO}(^4\text{He})| = 0.46 \text{ MeV}. \quad (4.2)$$

Here we have used $Q = 1/3$ and the results of the LO and NLO energies shown in table 4.3 to calculate the chiral uncertainties. The difference between these energies leads to the largest term in the EKM uncertainty-quantification scheme for this observable. Thus, ground-state energies for the triton and ⁴He, which deviate from the experimental values by the uncertainties $\delta E_{N^3LO}(^3\text{H})$ and $\delta E_{N^3LO}(^4\text{He})$ in (4.1) and (4.2) are perfectly acceptable for the N³LO interaction with $\Lambda = 500$ MeV.

The c_D - c_E values, which fulfill this condition for the triton and ⁴He individually are shown in figure 4.12. The blue trajectory corresponds to the c_D - c_E fit of the triton, where the uncertainty band indicates the c_D - c_E values, which leads to a binding energy within the chiral uncertainty. The band is narrow for negative c_D -values and becomes broader with increasing c_D . This indicates that in the narrow regions slight changes in c_E translates into large changes of the binding energy, while in the region with a broad band larger changes in c_E are possible to have the same effect on the energy. Analogously, we show the optimum

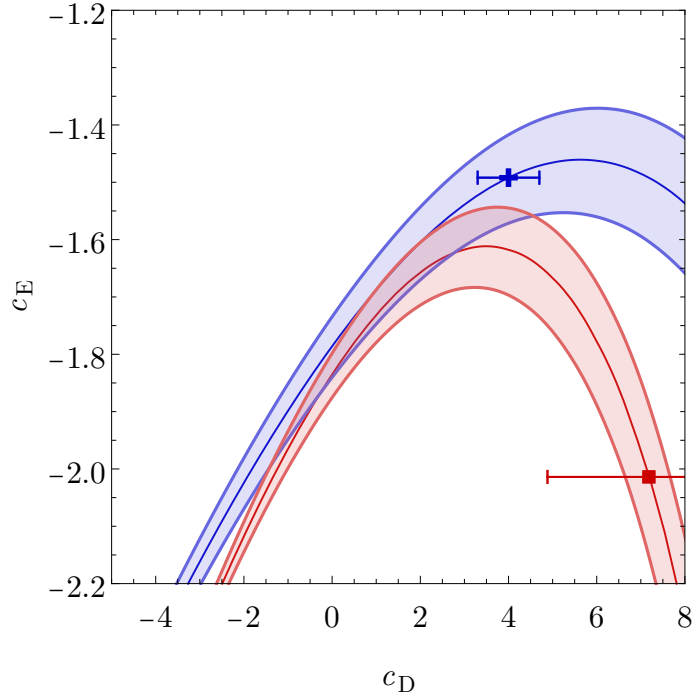


Figure 4.12: The c_D and c_E -values for the N^3LO interaction with cutoff 500 MeV determined through a fit to the $E_{gs}(^3H)$ (blue line), $E_{gs}(^4He)$ (red line), as well as the optimum c_D - c_E pairs for the different optimizations MBO (\oplus), and α -MBO (\blacksquare). The uncertainty bands correspond to the chiral uncertainty at N^3LO .

c_D - c_E trajectory in combination with the uncertainties for 4He in red. The shapes of both trajectories are similar, but the 4He trajectory is slightly shifted towards negative c_E -values and decreases faster for absolute c_D -values. Thus, the optimum trajectories for triton and 4He do not intercept, therefore, there is no c_D - c_E pair that reproduces both the triton and 4He energies perfectly, but the uncertainty bands overlap in the range of $c_D \approx -1.5$ to 4, which indicates that in this area a good description of both energies is possible.

We have multiple options to relax the constraint to the exact triton binding energy. We can follow a protocol similar to the MBO interactions and fit the c_D - c_E correlation to the 4He ground-state energy instead of the triton binding energy. The fit of c_D to the ground-state energy of ^{16}O is shown in figure 4.13 and results in $c_D = 7.2 \pm 2.3$. The slope of the ^{16}O ground-state energy with respect to c_D based on the 4He constraint is not as steep as based on the triton constraint, compare figure 4.11. This leads to a larger uncertainty of c_D in comparison with the MBO c_D . In the following, we refer to this optimization as α -MBO.

In addition to the triton and 4He bands, we indicate the resulting c_D - c_E pairs for the MBO and α -MBO in figure 4.12. While the MBO pair is slightly outside of the 4He band, the α -MBO pair leads to an unsatisfactory description of the triton with a ground-state energy of $E(^3H) = -8.052$ MeV. As said before, the uncertainty of the α -MBO c_D -value is rather large and at the lower end of this uncertainty a better description of triton is possible, even though, it still does not lie within the chiral uncertainty band.

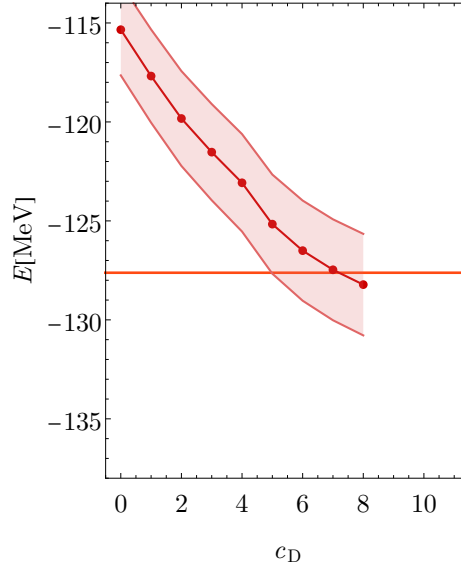


Figure 4.13: Description analogous to figure 4.11, but only for $N^3\text{LO}$ with cutoff 500 MeV and the c_D - c_E -correlation is fitted to the ground-state energy of ${}^4\text{He}$ instead of ${}^3\text{H}$.

4.4 | Few-Body Optimized Interactions

Instead of fitting the LECs in the many-body system, we can optimize the c_D - c_E pair also in the few-body system only. For this purpose, we minimize the mean square relative deviation of the ground-state energies of triton and ${}^4\text{He}$ with respect to the experimental values

$$X_{\text{FBO}}(c_D, c_E)^2 = \frac{1}{2} \left[\left(\frac{E({}^3\text{H}, c_D, c_E) - E_{\text{exp}}({}^3\text{H})}{E_{\text{exp}}({}^3\text{H})} \right)^2 + \left(\frac{E({}^4\text{He}, c_D, c_E) - E_{\text{exp}}({}^4\text{He})}{E_{\text{exp}}({}^4\text{He})} \right)^2 \right]. \quad (4.3)$$

We use this metric so that the deviation of the ${}^4\text{He}$ energy does not have a higher weight than the deviation of the triton energy. Experimental uncertainties are not included in the calculation, since the experimental uncertainties of the energies are extremely small in comparison with the theory uncertainties.

We refer to the optimization via equation 4.3 as few-body optimization (FBO). The optimum c_D - c_E pair of the FBO with $\Lambda = 500$ MeV at $N^3\text{LO}$ is shown in figure 4.14 in combination with the areas that have $X_{\text{FBO}}(c_D, c_E) < 0.010$ and 0.015 (green). The minimum with $X_{\text{FBO}} = 0.0055$ has a lower c_D -value than the MBO and α -MBO interaction. The area with $X_{\text{FBO}}(c_D, c_E) < 0.010$ describes roughly the overlap of the chiral uncertainty bands of the triton and ${}^4\text{He}$ optimizations. Using the estimates of the chiral uncertainties for the ground-state energies in equations (4.1) and (4.2), we obtain a $X_{\text{FBO}}(c_D, c_E) = 0.014$, thus the shown area with $X_{\text{FBO}}(c_D, c_E) < 0.015$ gives an outer boundary condition for c_D - c_E pairs in agreement with the chiral uncertainty estimates.

The corresponding ${}^4\text{He}$ results of the FBO interaction for the ground-state energy and point-proton rms radius are shown in figure 4.15 (left). The areas correspond to the same c_D - c_E areas in figure 4.14 with $X_{\text{FBO}}(c_D, c_E) < 0.010$ and 0.015 . The optimal FBO c_D - c_E pair leads to a slightly underestimated ${}^4\text{He}$ radius, but in the $X_{\text{FBO}}(c_D, c_E) < 0.010$ area c_D - c_E pairs are possible that reproduce radii in accordance with the experiment.

Since the relative deviation is dimensionless, we can easily include other observables like

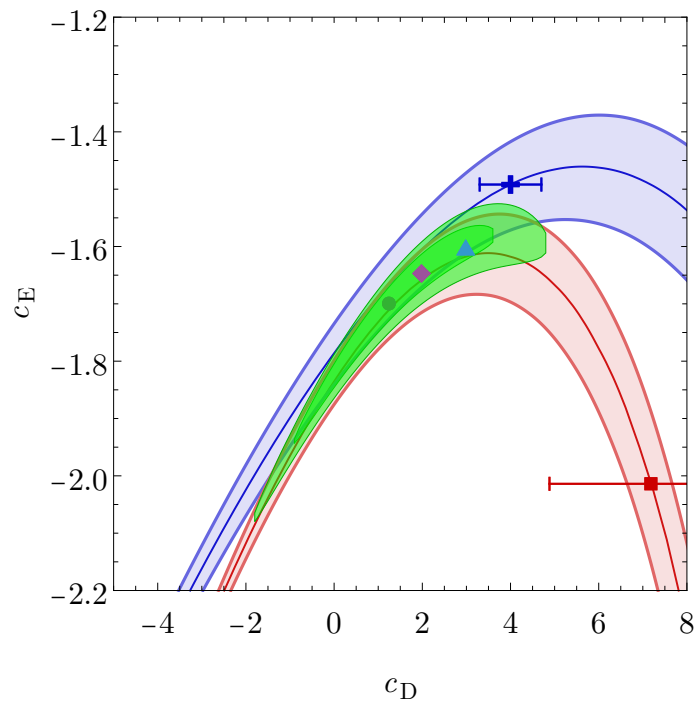


Figure 4.14: The c_D and c_E -values for the N^3LO interaction with cutoff 500 MeV determined through a fit to the $E_{gs}(^3H)$ (blue line), $E_{gs}(^4He)$ (red line), and the uncertainty bands correspond to the chiral uncertainty at N^3LO , as in figure 4.12. In addition, we show the optimum c_D - c_E pairs for the different optimizations MBO (+), α -MBO (■), FBO (●), R-FBO (◆), R_μ -FBO (▲). The green areas correspond to $X_{FBO}(c_D, c_E) < 0.010$ and 0.015 .

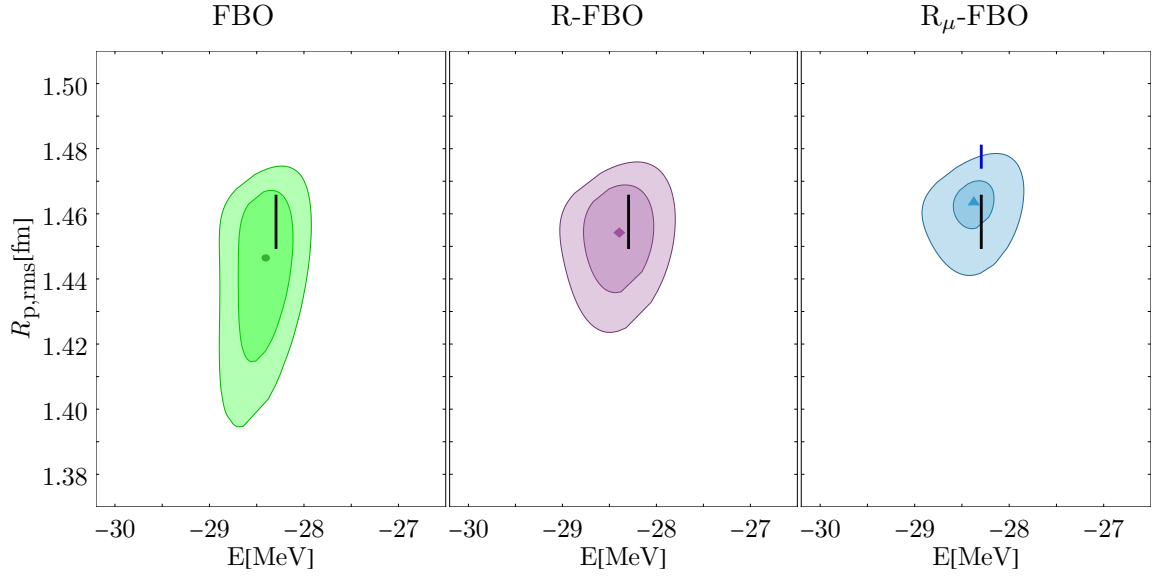


Figure 4.15: Ground-state energy and point-proton rms radius of ${}^4\text{He}$ for FBO (left), R-FBO (center), and R_μ -FBO using the experimental proton radius obtained from muonic hydrogen (right). The areas correspond to $X_{\text{FBO}}(c_D, c_E) < 0.010$ and 0.015 .

radii

$$X_{\text{R-FBO}}(c_D, c_E)^2 = \frac{1}{3} \left[\left(\frac{E({}^3\text{H}, c_D, c_E) - E_{\text{exp}}({}^3\text{H})}{E_{\text{exp}}({}^3\text{H})} \right)^2 + \left(\frac{E({}^4\text{He}, c_D, c_E) - E_{\text{exp}}({}^4\text{He})}{E_{\text{exp}}({}^4\text{He})} \right)^2 + \left(\frac{R_{\text{p,rms}}({}^4\text{He}, c_D, c_E) - R_{\text{p,rms,exp}}({}^4\text{He})}{R_{\text{p,rms,exp}}({}^4\text{He})} \right)^2 \right]. \quad (4.4)$$

We indicate the inclusion of the $R_{\text{p,rms}}$ of ${}^4\text{He}$ in the fit by using the expression R-FBO. This explicit inclusion of the $R_{\text{p,rms}}$ in the fit improves the resulting $R_{\text{p,rms}}$, such that the R-FBO optimum is within experimental uncertainties, see figure 4.15 (center). The shown areas correspond again to $X_{\text{R-FBO}}(c_D, c_E) < 0.010$ and 0.015 and the optimum c_D - c_E pair has a $X_{\text{R-FBO}} = 0.0050$.

The experimental uncertainties of $R_{\text{p,rms}}$ are not as small as the uncertainties of the energies. As discussed in section 3.4, we use the CODATA 2014 experimental proton radius $r_{\text{p,E}} = 0.8751(61)$ fm [118] in the conversion of the experimental R_{ch} into $R_{\text{p,rms}}$. The ongoing proton radius puzzle leads to two distinct solutions for the $R_{\text{p,rms}}$. In figure 4.15 (right), we also show the solution of the R-FBO using the proton radius $r_{\text{p,E}} = 0.84087(39)$ fm [117] obtained from muonic hydrogen indicated with R_μ -FBO. This measurement has also been included in the recent CODATA 2018 value $r_{\text{p,E}} = 0.8414(19)$ fm. The blue bar corresponds to the experimental $R_{\text{p,rms},\mu}$ obtained with this proton radius from muonic hydrogen. Again, we show the areas corresponding to $X_{\text{R}_\mu\text{-FBO}}(c_D, c_E) < 0.010$ and 0.015 as well as the optimum c_D - c_E pair corresponding to a $X_{\text{R}_\mu\text{-FBO}} = 0.0087$. Here, the radius is further increased, but the indicated areas do not enclose $R_{\text{p,rms},\mu}$ and the radius for the optimum R_μ -FBO c_D - c_E pair is outside of the experimental uncertainties.

Between the different optimizations FBO, R-FBO, and R_μ -FBO the ${}^4\text{He}$ energy is nearly unaffected and is slightly overbound. The optimal c_D - c_E pairs for all optimizations are indicated in figure 4.14 and follow closely the trajectory of optimal ${}^4\text{He}$ energy. The inclusion of the radius in the optimization leads to larger c_D inbetween the FBO and MBO optima.

chiral order	Λ [MeV]	c_D	c_E	X_{FBO}
N ² LO	450	6.44	0.586	0.0
		(-2.80 -0.660)	0.0	
	500	1.55	-0.304	0.0
		(-3.84 -0.896)	0.0	
	550	-1.77	-0.866	0.0
		(-4.50 -1.093)	0.0	
N ³ LO	450	6.50	-0.415	0.0
		(0.00 -1.290)	0.0	
	500	1.27	-1.697	0.0055
	550	0.04	-1.774	0.0094
N ⁴ LO'	450	6.86	-0.480	0.0
		(0.37 -1.351)	0.0	
	500	1.41	-1.510	0.0029
	550	-0.32	-1.631	0.0056

Table 4.2: Optimized c_D - and c_E -values in the few-body system as well as the corresponding value of X_{FBO} . In case of two minima, both pairs are given. The pair without parentheses corresponds to the pair that leads to a smaller deviation of the ^{16}O ground-state energy.

Furthermore, in the radius operator applied in the NCSM calculation we omit chiral two-body corrections to the charge density operator, such that we need to assign a larger uncertainty to the calculated value. Due to this incomplete calculation and the larger experimental uncertainty of the radius, we will consider only the FBO interaction for now.

We can perform the optimization of c_D and c_E analogously for the other chiral orders and cutoffs. This leads to the LECs reported in table 4.2. We should note that in case of the N²LO interactions as well as for all chiral orders for the interactions with $\Lambda = 450$ MeV this optimization leads to two distinct optima, where the experimental ground-state energies of ^3H and ^4He are both reproduced. In these cases we use the ^{16}O ground-state energy as additional guidance. The difference to the experimental ^{16}O ground-state energy is in general smaller for the optima with larger c_D -value. Nevertheless, in table 4.2 we report both optima.

4.5 | Globally Optimized Interactions

In the previous sections we optimized c_D and c_E for only two isotopes at the same time. We can easily extend the optimization procedure discussed in the previous section and include more isotopes, for example ^3H , ^4He , ^{16}O , ^{24}O , ^{40}Ca , and ^{48}Ca and minimize the mean-square-relative deviation

$$X_{\text{GBO}}(c_D, c_E)^2 = \frac{1}{n} \sum_{i=1}^n \left(\frac{E(i, c_D, c_E) - E_{\text{exp}}(i)}{E_{\text{exp}}(i)} \right)^2, \quad (4.5)$$

where n indicates the number of the different isotopes i . This optimization we refer to as globally optimized (GBO). The results of the oxygen and calcium isotopes are obtained with IM-SRG calculations and SRG evolved interactions with $\alpha = 0.04 \text{ fm}^4$ while the energies of ^3H and ^4He are obtained in Jacobi-NCSM calculations with bare interactions. This optimization leads to an optimal $c_D = 4.74$ and $c_E = -1.554$ with $X_{\text{GBO}} = 0.016$ and is indicated in figure 4.16 (left). Since the root-mean-square-relative deviation is larger for GBO than for FBO and R-FBO, we indicate the area with $X_{\text{GBO}}(c_D, c_E) < 0.020$ instead of 0.010 and 0.015

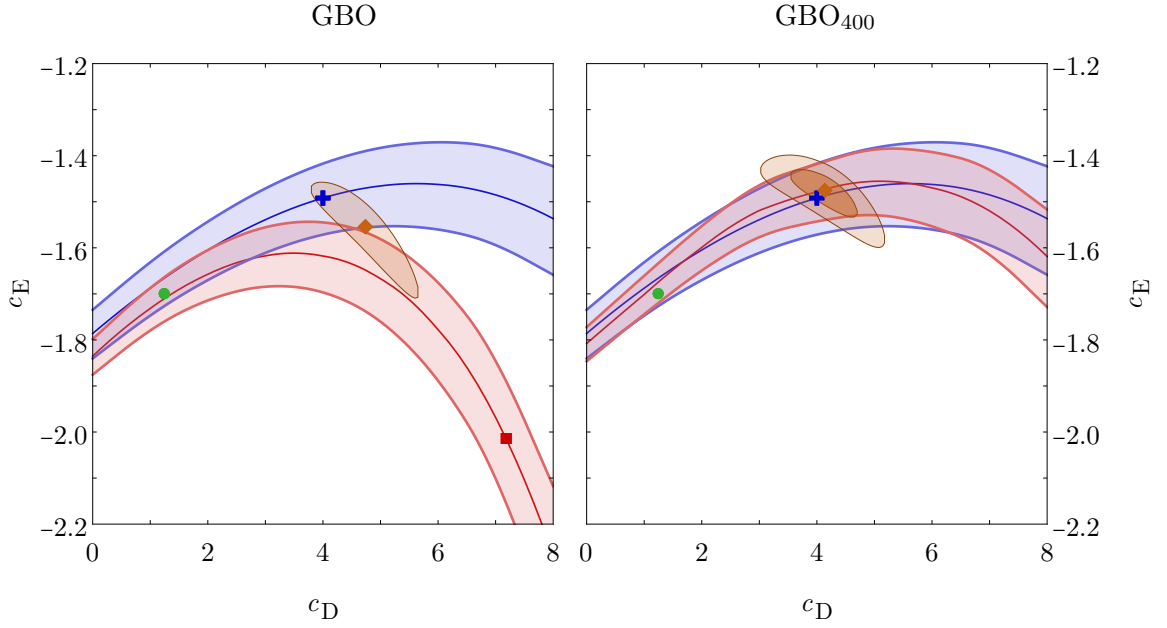


Figure 4.16: Resulting c_D - c_E values of the GBO (left) and GBO₄₀₀ (right) (◆) for the N³LO interaction with $\Lambda = 500$ MeV. In the GBO the ground-state energies of ³H, ⁴He, ¹⁶O, ²⁴O, ⁴⁰Ca, and ⁴⁸Ca are optimized. While in the GBO, we use the bare interaction for the calculation of the ⁴He energy, in the GBO₄₀₀ we use the SRG evolved interaction with $\alpha = 0.04$ fm⁴ to obtain the ⁴He energy. In both cases, the energies of the oxygen and calcium isotopes are obtained with $\alpha = 0.04$ fm⁴ evolved interactions. In addition to the optimum values, we indicate the areas corresponding to $X_{\text{GBO}}(c_D, c_E) < 0.015$ and 0.020 . For reference, we show the results of the different optimizations MBO (⊕), α -MBO (■) as well as the correlation of c_D and c_E by fitting $E_{\text{gs}}(^3\text{H})$ (blue line) or $E_{\text{gs}}(^4\text{He})$ (red line). In the right figure, we show the correlation line for ⁴He based on the SRG evolved interaction. The uncertainty bands correspond to the chiral uncertainty at N³LO.

as before. The GBO result is close to the MBO result, which indicates that the MBO was already a good choice.

In the optimization, we can alternatively use SRG evolved interactions for the light isotopes ³H and ⁴He to be consistent between light and medium mass isotopes. For triton this makes no difference, since we perform the SRG in two- and three-body space. For ⁴He this is different, since the induced 4N interaction is neglected in our calculations. The c_D - c_E correlation band based on the SRG evolved interactions for ⁴He is shown in figure 4.16 (right) and overlaps completely with the triton correlation band. The strong SRG dependence of ⁴He, especially for positive c_D -values, we have already seen in section 4.2.2. The global optimization using the SRG evolved interaction is indicated with GBO₄₀₀ and leads to an optimal $c_D = 4.14$ and $c_E = -1.476$ with $X_{\text{GBO},400} = 0.013$. This pair is in even a better agreement with the MBO result and the root-mean-square-relative deviation is smaller than the GBO result.

Due to the good agreement between MBO and GBO we will not further explore the GBO interaction.

chiral order	Λ [MeV]	FBO			MBO	
		$E_{\text{gs}}(^3\text{H})$ [MeV]	$E_{\text{gs}}(^4\text{He})$ [MeV]	$R_{\text{p,rms}}(^4\text{He})$ [fm]	$E_{\text{gs}}(^4\text{He})$ [MeV]	$R_{\text{p,rms}}(^4\text{He})$ [fm]
LO	500	-11.089	-40.08	1.087	-40.08	1.087
	450	-8.446	-28.41	1.457	-28.41	1.457
NLO	500	-8.306	-27.55	1.476	-27.55	1.476
	550	-7.992	-25.76	1.519	-25.76	1.519
N ² LO	450	-8.480(289)	-28.30(97)	1.506(59)	-29.42(117)	1.498(56)
	500	-8.482(308)	-28.29(107)	1.480(50)	-29.42(154)	1.475(50)
	550	-8.483(425)	-28.30(189)	1.461(63)	-29.45(257)	1.459(64)
N ³ LO	450	-8.485(73)	-28.28(24)	1.479(20)	-29.01(36)	1.475(18)
	500	-8.425(82)	-28.41(27)	1.447(21)	-29.12(41)	1.453(16)
	550	-8.383(118)	-28.48(48)	1.437(20)	-29.50(65)	1.437(19)
N ⁴ LO'	450	-8.480(73)	-28.30(24)	1.479(20)	-29.51(30)	1.470(20)
	500	-8.451(79)	-28.35(27)	1.465(15)	-28.80(49)	1.476(13)
	550	-8.424(111)	-28.41(48)	1.447(17)	-29.32(65)	1.454(16)

Table 4.3: Ground-state energy of ^3H as well as ground-state energy and point-proton rms radius of ^4He for the FBO and MBO interactions. Starting from N²LO, the uncertainties in parenthesis are the chiral truncation uncertainties obtained with the Bayesian uncertainty-quantification scheme, see text for more information. For the many-body uncertainties we assume 1 keV for the triton E_{gs} , 10 keV for the ^4He E_{gs} , and 0.001 fm for the ^4He $R_{\text{p,rms}}$. The ground-state energy of ^3H for the MBO interactions starting from N²LO are fitted to the experimental value and are per construction equal at LO and NLO to the FBO results.

4.6 | Results for Many-Body Systems

In the previous sections we have defined two interaction families, MBO and FBO. Both allow for a theory uncertainty quantification with the EKM and Bayesian uncertainty-quantification schemes. In this section, we will discuss results of these interactions in the many-body systems and explore the different uncertainty-quantification schemes. We start with a compilation of results in the few-body systems ^3H and ^4He . Afterwards, we discuss results in the medium mass systems as well as p-shell results.

4.6.1 | Few-Body Results

In table 4.3 we report the ground-state energies of ^3H and ^4He as well as the corresponding point-proton rms radius of ^4He obtained with the bare MBO and FBO interactions. In addition to the obtained values, we give the chiral truncation uncertainties obtained with the Bayesian uncertainty-quantification scheme. Since we do not have the LO interactions for all cutoffs, we use the NLO results as LO input in the uncertainty-quantification scheme. More details on how we apply the uncertainty-quantification scheme is given in the next section. We see a clear improvement of the ^4He ground-state energy from MBO to FBO while the triton binding energy is only moderately affected.

Furthermore, we see a clear trend for the radii. In both optimizations with increasing cutoff the radii decrease.

4.6.2 | Medium-Mass Properties

Now, we explore results of medium-mass systems. Here, we use the IM-SRG as method of choice. Before we compare the different interactions, we have a closer look on the uncertainty-quantification schemes and how we apply them.

Since we do not have the LO results for all cutoffs and the LO results do not always have physical significance, we do not incorporate them in the uncertainty quantification. Furthermore, at N⁴LO' we have no contribution of the N⁴LO 3N interaction terms. Therefore, we cannot assume that the uncertainty at N⁴LO' scales with Q^5 . Instead, we assume Q^4 . In the determination of the N⁴LO' uncertainties we neglect the results of N³LO and use the N⁴LO' results as alternative N³LO input into the uncertainty-quantification schemes.

First, we will compare the EKM and Bayesian uncertainty-quantification schemes introduced in section 2.5. For this comparison we restrict ourselves to ground-state energies of selected medium-mass nuclei calculated based on the MBO interaction family with $\Lambda = 500$ MeV up to N³LO. The N⁴LO' uncertainties behave similarly to the N³LO uncertainties and are omitted in this comparison for a clearer view. All ground-state energies are obtained in single-reference IM-SRG calculations with $E_{3\text{Max}} = 18$ and $e_{\text{Max}} = 14$ in NO2B approximation in a NAT basis. Furthermore, the interactions are SRG evolved with $\alpha = 0.04$ fm⁴.

In figure 4.17 we employ the EKM uncertainty-quantification scheme as given in equation (2.50). The uncertainties decrease with increasing order and the uncertainties of N³LO are within the uncertainties of N²LO. In addition to the uncertainties $\delta X_{\chi}^{(i)}$ due to the truncation of the chiral expansion we include the many-body uncertainty $\delta X_{\text{mb}}^{(i)} = 0.02X^{(i)}$, which we assume to be 2% of the result $X^{(i)}$ such that the total theory uncertainties are given at chiral order i by

$$\delta X_{\text{th}}^{(i)} = \delta X_{\chi}^{(i)} + \delta X_{\text{mb}}^{(i)}. \quad (4.6)$$

While at N²LO the truncation error dominates the uncertainties, at N³LO the many-body uncertainties are of similar size.

Alternatively a Bayesian uncertainty-quantification scheme is employed as given in equation (2.64). For the reference scale we use the experimental values. The purpose of the reference scale is to scale the expansion coefficients to natural size and the resulting uncertainty bands are robust with respect to variation of this reference scale. The use of an approximate reference scale of, for instance, $X_{\text{ref}} = -9$ A MeV leads to only small deviations of the uncertainties in the range of (1 – 20) A keV. As indicated above, we do not incorporate the LO into the uncertainty quantification. Hence, we use the NLO result as the LO contribution, such that the expansion coefficients c_1 and c_2 of the Bayesian uncertainty-quantification scheme (2.52) vanish and do not contribute to the uncertainty quantification. The coefficient c_1 is already zero, due the vanishing Q^1 contributions in the chiral Hamiltonian.

The prior information of the distribution of the expansion coefficients c_n is parameterized in τ_0 and ν_0 , see section 2.5. An uninformative prior is given by $\tau_0 = 1$ and $\nu_0 = 1$, which is our main parameter set (I). With these parameters, we can tweak the assumption of naturalness of the prior. With increasing orders, which are included in the uncertainty quantification, these parameters are less relevant. The scale τ_0 is the best guess of the marginal variance \bar{c} and ν_0 is the number of degrees of freedom in the scaled inverse χ^2 distribution, which indicates the width of the distribution. For example, in the limit of $\nu_0 \rightarrow \infty$ the prior is a sharp peak at τ_0 . In figure 4.18 we vary these parameters and probe in addition to the uninformative prior the parameter sets ($\tau_0 = 2, \nu_0 = 1$) (II) and ($\tau_0 = 1, \nu_0 = 2$) (III). For the calculation of the uncertainties we employ a 95% confidence interval and, in a first step,

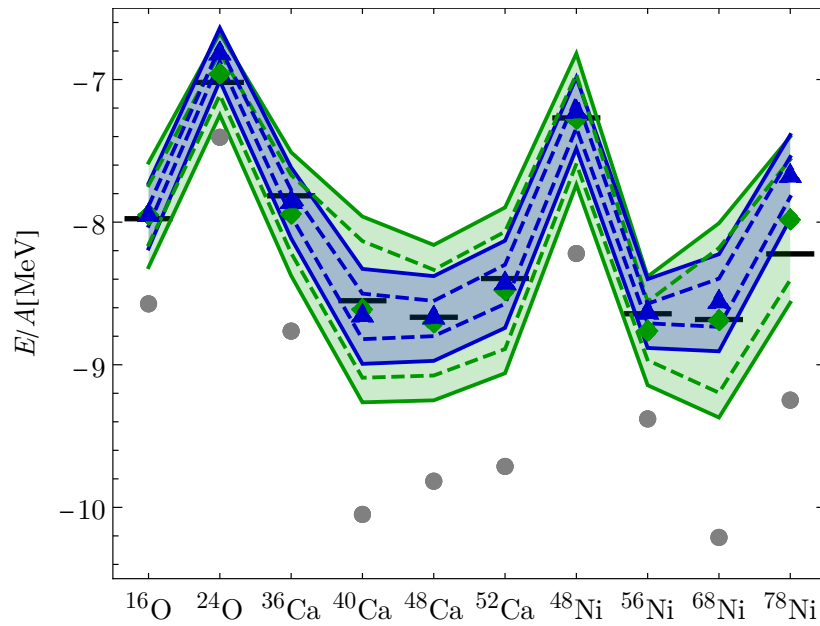


Figure 4.17: Ground-state energies of medium-mass nuclei for the MBO interactions with $\Lambda = 500$ MeV for NLO (\bullet), N^2 LO (\blacklozenge), and N^3 LO (\blacktriangle). The uncertainty bands are estimated with the EKM truncation-error-uncertainty scheme in combination with (solid) and without (dashed) the many-body uncertainties. The results are obtained with single-reference IMSRG calculations with $E_{3\text{Max}} = 18$ and $e_{\text{Max}} = 14$ in NO2B approximation in a NAT basis. All interactions are SRG evolved with $\alpha=0.04$ fm⁴. Experimental values are indicated with black bars.

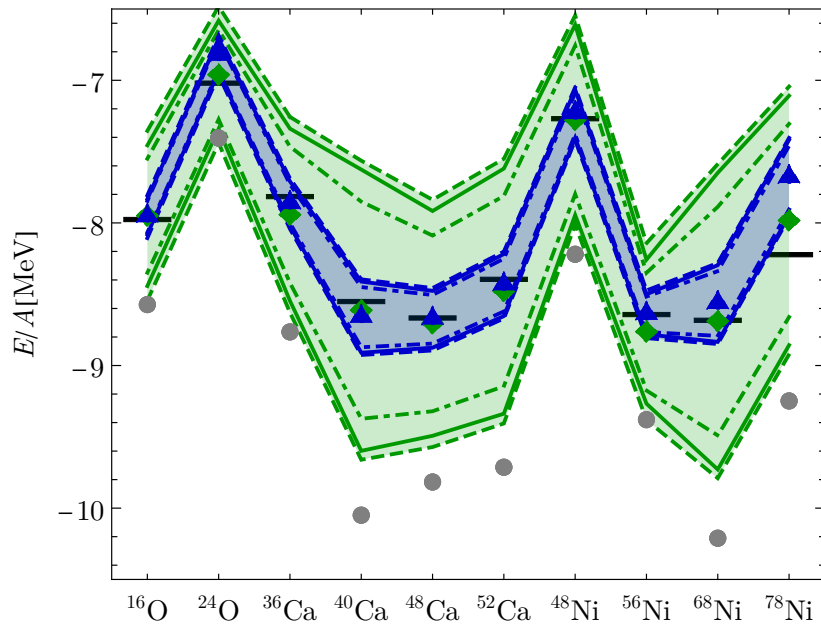


Figure 4.18: Ground-state energies of medium-mass nuclei for the MBO interactions with $\Lambda = 500$ MeV for NLO (\bullet), N^2 LO (\blacklozenge), and N^3 LO (\blacktriangle). The uncertainty bands are determined with the Bayesian uncertainty-quantification approach for the truncation error estimates. We use $\tau_0 = 1$ and $\nu_0 = 1$ (solid lines), $\tau_0 = 2$ and $\nu_0 = 1$ (dashed lines) and $\tau_0 = 1$ and $\nu_0 = 2$ (dot-dashed lines). The results are obtained with single-reference IM-SRG calculations with $E_{3\text{Max}} = 18$ and $e_{\text{Max}} = 14$ in NO2B approximation in a NAT basis. All interactions are SRG evolved with $\alpha = 0.04$ fm 4 . Experimental values are indicated with black bars.

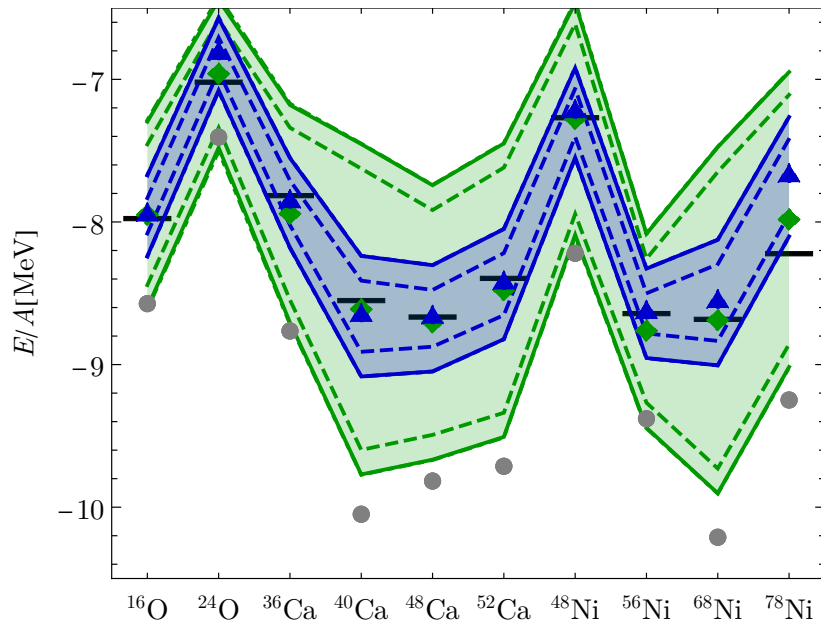


Figure 4.19: As in 4.18 with $\tau_0 = 1$ and $\nu_0 = 1$. We show the results with the truncation error estimates only (dashed lines) and in combination with the many-body uncertainties (solid lines).

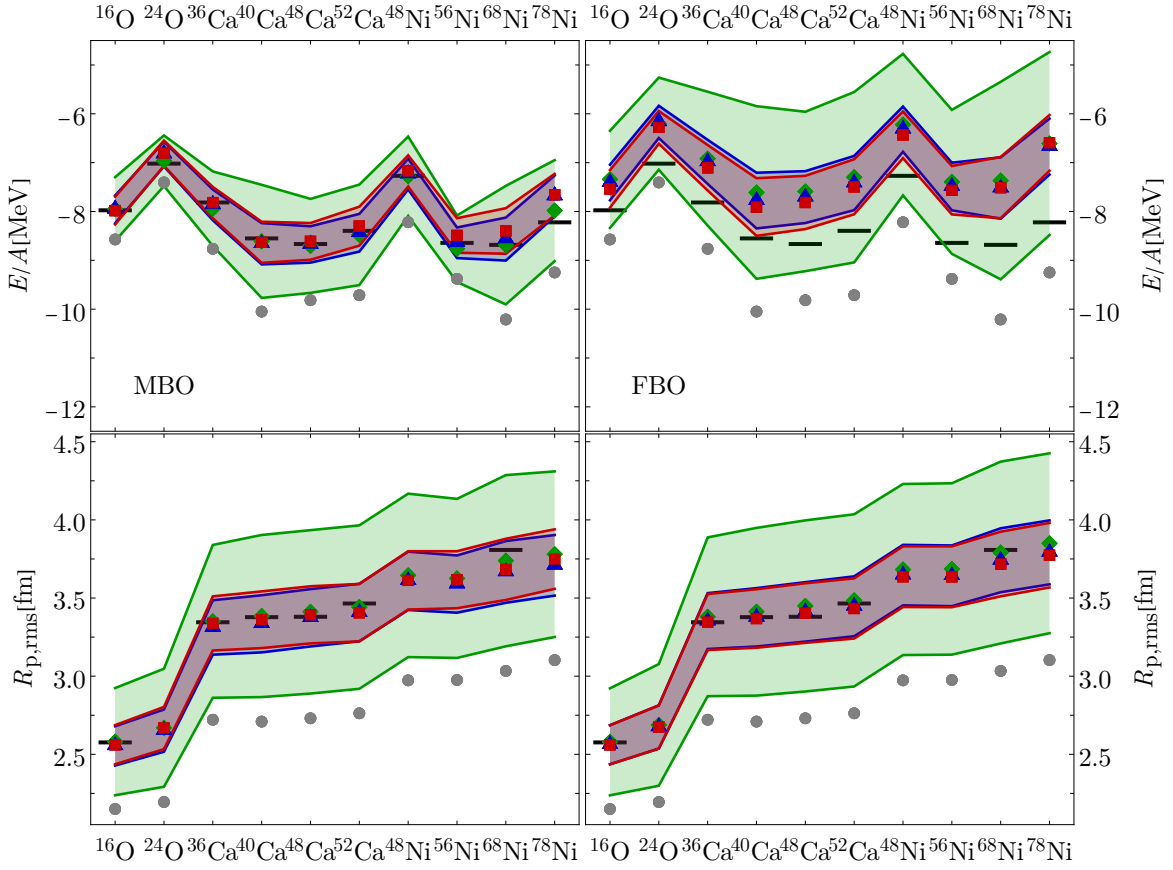
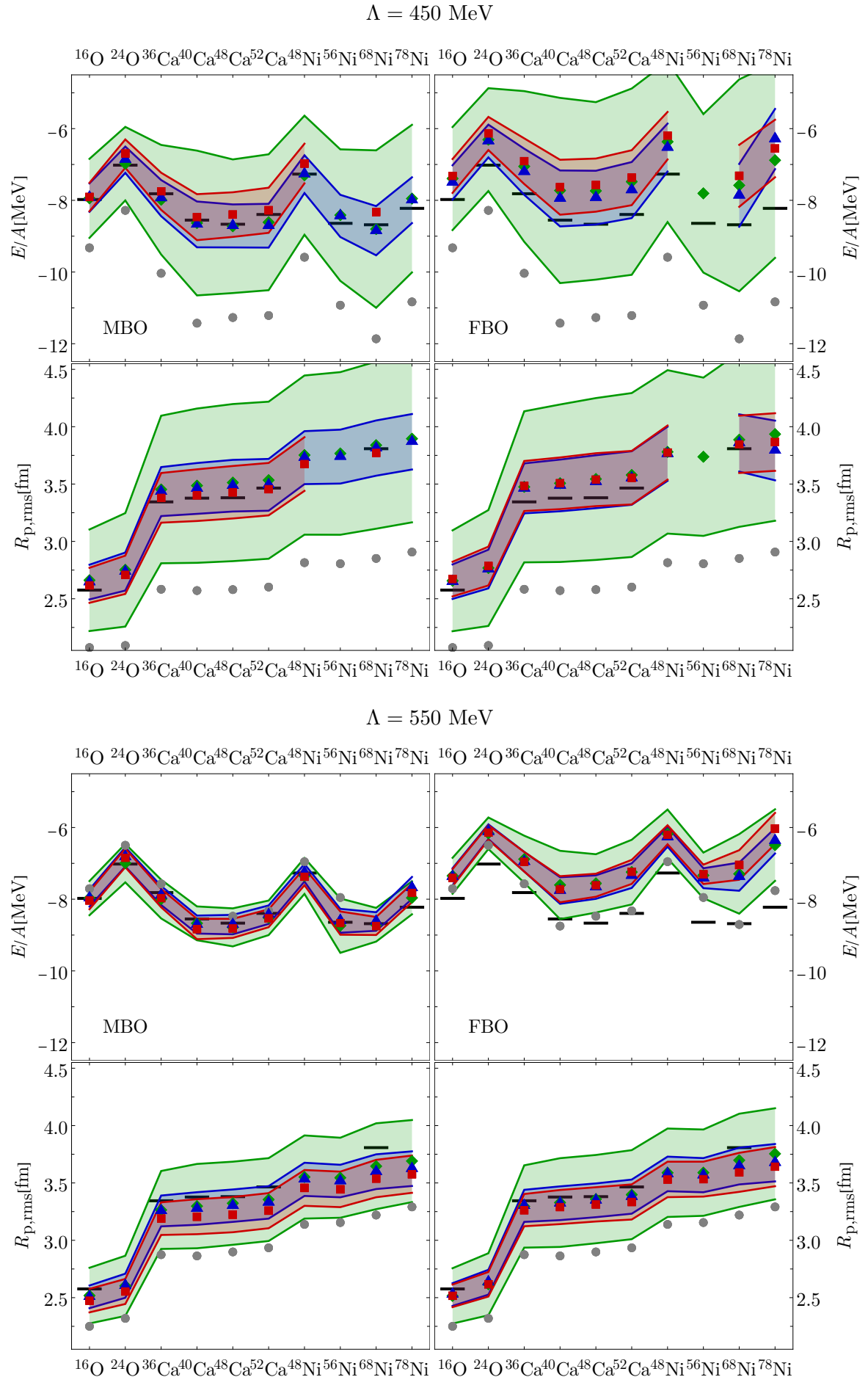


Figure 4.20: Ground-state energies and point-proton rms radii of medium-mass nuclei for the MBO (left) and FBO (right) interactions with $\Lambda = 500$ MeV for NLO (\bullet), N^2 LO (\blacklozenge), N^3 LO (\blacktriangle), and N^4 LO' (\blacksquare). The interactions are SRG evolved to $\alpha = 0.04$ fm 4 . For the IM-SRG calculation, we use $E_{3\text{Max}} = 18$ and $e_{\text{Max}} = 14$ in NO2B approximation in a NAT basis. The uncertainty bands indicate the combined uncertainties from the many-body calculation and the truncation error estimation with the Bayesian approach. Experimental values are indicated with black bars.

we neglect the many-body uncertainties. The choice of the prior has only a small impact on the uncertainties. The largest difference between the uncertainties is between the priors with parameter set (II) and (III). With increasing chiral order the differences decrease. While at N^2 LO the uncertainties vary about 200 A keV, at N^3 LO the uncertainties vary only about 50 A keV. Thus, the resulting uncertainties are stable with respect to the prior choice, especially at N^3 LO, which is most relevant for our purposes. Therefore, in the following we use the uninformative prior to estimate the uncertainties.

In addition to the interaction uncertainties based on the Bayesian uncertainty quantification, we show in figure 4.19 the sum of the interaction and the many-body uncertainties. Similarly to the EKM approach the interaction uncertainties dominate the uncertainty band, but the Bayesian approach leads to larger uncertainties, especially for N^2 LO. The uncertainties of N^3 LO are of similar size, nevertheless, the Bayesian uncertainties are slightly larger. In the following we only use the uncertainties obtained with the Bayesian approach due to its conceptual superiority.

Up to now, we have discussed the different estimations of the uncertainties. Now, we focus on the differences between the MBO and FBO interactions. In figure 4.20 we compare



the resulting ground-state energies and radii using the MBO and FBO interactions with $\Lambda = 500$ MeV. Using the MBO interaction starting from $N^2\text{LO}$, the resulting energies and radii are close to the experimental values. The experimental values are within the uncertainty bands with the exception of the ground-state energy of ^{78}Ni . The picture changes for the FBO interactions. For the FBO interactions the radii are described similarly well but the energies are underbound starting from $N^2\text{LO}$. At $N^3\text{LO}$ and $N^4\text{LO}'$ we obtain ground-state energies where the experimental values all lie outside of the uncertainty bands.

In figure 4.21 we also show the results for the interactions with $\Lambda = 450$ MeV and 550 MeV. For these interactions not every IM-SRG calculation converges, hence the missing data points in the plots. Overall, the picture is similar for all cutoffs. The MBO interactions reproduce the experimental ground-state energies within uncertainties, while the nuclei for the FBO interactions are underbound. In case of the radii, the MBO interaction at $N^4\text{LO}'$ with $\Lambda = 550$ MeV leads to slightly underestimated radii while all other interactions reproduce the experimental values within uncertainties. Here, two mechanisms play a role. First, we can identify the trend that with increasing cutoff the radii decrease and second, the NLO results for $\Lambda = 550$ MeV are already close to the experimental values for both energies and radii. The latter leads to uncertainties due to the chiral truncation that are much smaller than for the other cutoffs. To avoid this effect, the inclusion of the LO results into the uncertainty quantification might be helpful.

We can summarize that due to the inclusion of the ground-state energy of ^{16}O into the fit, the MBO interactions provide an excellent description of ground-state energies of medium mass isotopes. The FBO interactions on the other hand lead to systematically underbound ground states. Both interaction families yield similarly good radii, whereby the radii obtained with the $\Lambda = 450$ MeV interactions are slightly too large. With increasing cutoff the radii shrink such that the radii obtained with the $\Lambda = 550$ MeV interactions are slightly too small.

4.6.3 | Results of p-Shell Isotopes

For the calculation of observables of p-shell nuclei we employ the IT-NCSM. These calculations are performed in model spaces with up to $N_{\text{max}}=10$ for two to five HO frequencies in the range of $\hbar\Omega = 10$ to 20 MeV. The extrapolation procedure is illustrated in figure 4.22 and described in the following. The interactions used in the IT-NCSM calculations are all SRG evolved up to $\alpha = 0.08 \text{ fm}^4$ for a better convergence with respect to model-space size.

The final ground-state energies are determined by an extrapolation of the N_{max} sequence for the frequency with the smallest energy at maximum N_{max} . For the extrapolation to infinite model space size we are using an exponential function

$$E(N_{\text{max}}) = E_{\infty} + A \exp(-BN_{\text{max}}). \quad (4.7)$$

The corresponding extrapolation uncertainty is estimated by the maximum difference to the extrapolations at the neighboring HO frequencies. These extrapolation uncertainties can vary widely depending on the specific model space choices. To gain a more reliable estimation and suppress fluctuations of individual extrapolations, we average the extrapolation uncertainties within an interaction family for a given nucleus, since we assume that the many-body uncertainties for a given nucleus should be of similar size.

The determination of radii is more complicated than the determination of ground-state energies. The radii behave differently regarding N_{max} . They are not bounded from above and the convergence pattern of a N_{max} -sequence can – in most cases – not be described with an exponential course. The behavior is typically dependent on the HO frequency $\hbar\Omega$. For low $\hbar\Omega$ the radii converge from above and for large $\hbar\Omega$ the radii converge from below

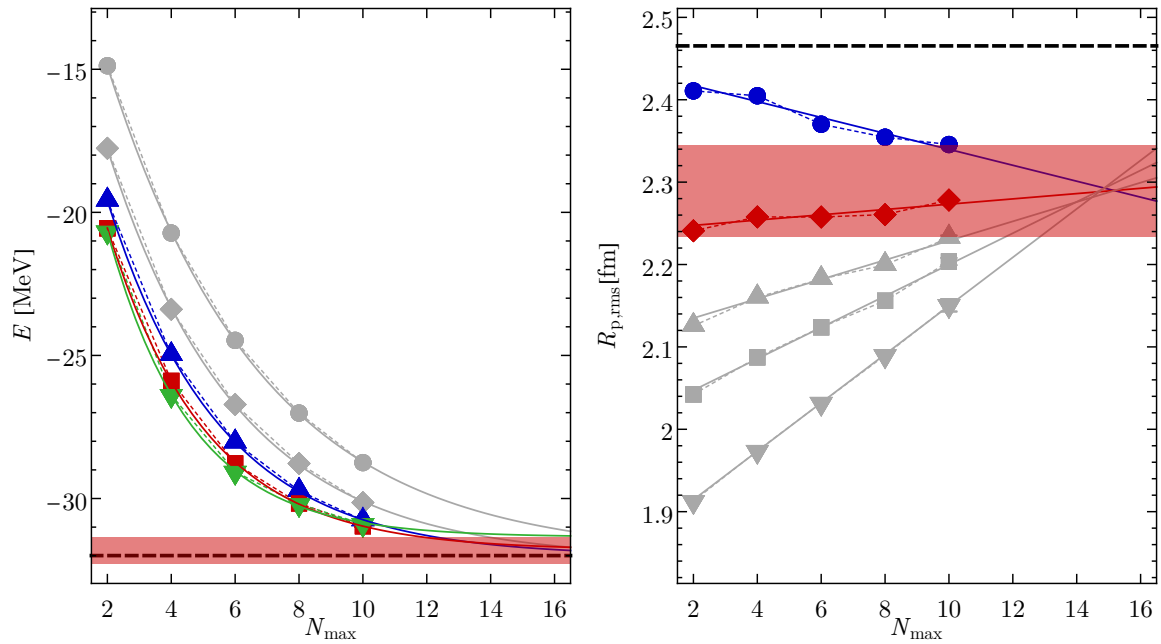


Figure 4.22: Model space extrapolation in the IT-NCSM for the ground-state energy (left) and point-proton rms radius (right) of ${}^6\text{Li}$ obtained with the MBO interaction with cutoff $\Lambda = 500$ MeV at $N^3\text{LO}$ and $\alpha = 0.08$ fm. The different symbol shapes indicate the different HO frequencies $\hbar\Omega = 10$ (\bullet), 12 (\blacklozenge), 14 (\blacktriangle), 16 (\blacksquare), and 20 (\blacktriangledown) MeV. Colored symbols are used in the determination of the extrapolated results and uncertainties while gray data points are neglected as described in the text. The red band is the extracted uncertainty band while the dashed line indicates the experimental result for comparison.

with increasing N_{max} . The pivot point is typically associated with the converged result. We determine the ground-state radii by performing linear fits of the N_{max} -sequences as indicated in figure 4.22. The intersection of the fits with the HO frequencies around or closest to the sign change of the slope is used for the resulting radius value. The uncertainty is estimated by the maximum difference between this obtained value and the results at the last N_{max} value for the considered HO frequencies. Similarly to the ground-state energies the uncertainties of the individual isotopes are averaged within an interaction family to suppress outliers.

The resulting ground-state energies and point-proton radii for selected p-shell isotopes using the MBO and FBO interactions with $\Lambda = 500$ MeV are shown in figure 4.23. The indicated uncertainty bands include the uncertainty of the many-body calculation as discussed above as well as the uncertainties due to the chiral truncation determined with the Bayesian scheme. Both interaction families lead to robust results and converge with increasing chiral order. The ground-state energies determined with the MBO interactions are slightly underbound in comparison to the experimental values but agree within uncertainties. Interestingly, the FBO interactions lead to a stronger underbinding – in this case the experimental values are outside of the uncertainty band.

Both interaction families lead to a similarly good description of the radii. Here, the uncertainties are dominated by many-body uncertainties, since the radii vary only slightly with chiral order.

Even though the FBO interactions are constrained in few-body systems, the MBO interactions yield a better agreement with the experimental ground-state energies of p-shell isotopes. The radii are in good agreement with the experiment for both optimization schemes,

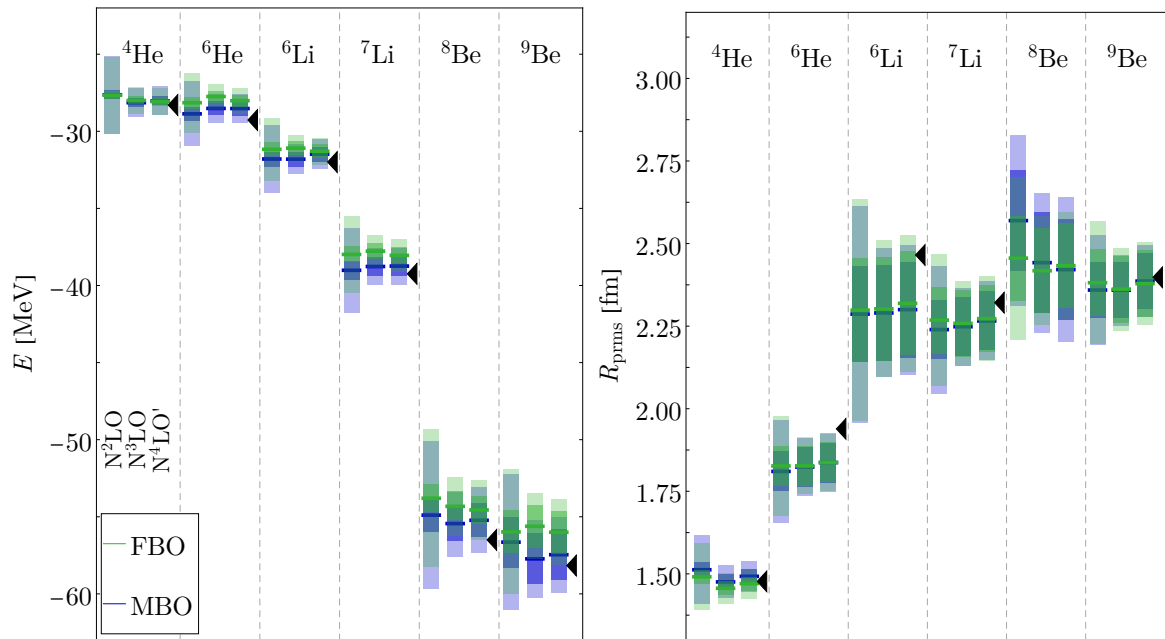


Figure 4.23: Ground-state energies (left) and point-proton rms radii (right) of p-shell nuclei obtained with the FBO (green) and MBO (blue) interactions with cutoff $\Lambda = 500$ MeV. The chiral orders $N^2\text{LO}$, $N^3\text{LO}$ and $N^4\text{LO}'$ are shown. The uncertainty bands are constructed by a combination of many-body uncertainties (dark) and chiral truncation estimates constructed in the Bayesian uncertainty-quantification scheme (light). The experimental values are indicated by black arrows.

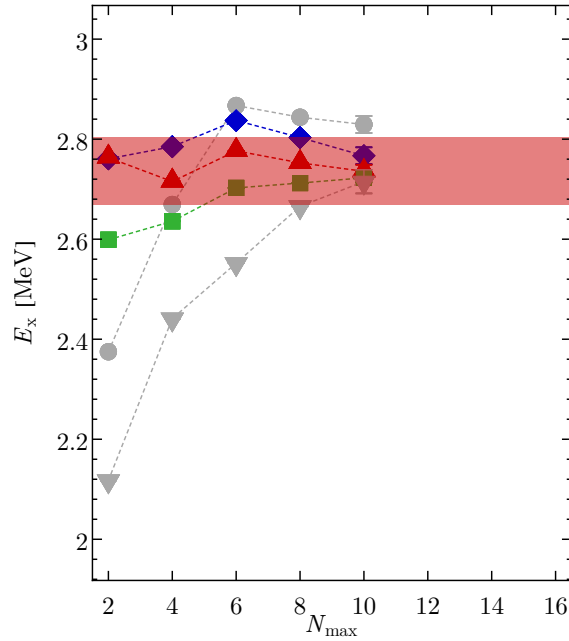


Figure 4.24: Model-space variation in an IT-NCSM calculation for the first excited-state energy of ${}^6\text{Li}$ obtained with the MBO interaction with cutoff $\Lambda = 500$ MeV at $N^3\text{LO}$ and $\alpha = 0.08$ fm. The different symbol shapes indicate the different HO frequencies $\hbar\Omega = 10$ (\bullet), 12 (\blacklozenge), 14 (\blacktriangle), 16 (\blacksquare), and 20 (\blacktriangledown) MeV. Colored symbols are used in the determination of the final result and uncertainty while gray data points are neglected as described in the text. The red band indicates the extracted uncertainty band.

as was the case for the medium-mass regime. Next we explore the influence of the different optimizations on the spectra.

The determination of excitation energies and their uncertainties in an IT-NCSM calculation is exemplarily shown for the first excited-state of ${}^6\text{Li}$ in figure 4.24. The resulting excitation energy is defined as the value at highest N_{max} for the HO frequency that shows the most converged behavior, as determined by visual examination. The corresponding uncertainty is defined as the maximum difference to the values of the neighboring HO frequencies at maximum $N_{\text{max}} - 2$. In the example of ${}^6\text{Li}$ in figure 4.24, we choose $\hbar\Omega = 14$ MeV as the most converged frequency. Therefore, we define the resulting value as the energy given at $N_{\text{max}} = 10$ with $\hbar\Omega = 14$ MeV and the uncertainties are given by the maximum difference of this value with the energy given at $N_{\text{max}} = 8$ for $\hbar\Omega = 12$ MeV and $\hbar\Omega = 16$ MeV. Similar to the ground-state observables, we average over the uncertainties within an interaction family for a given nucleus and state in order to suppress outliers.

In figure 4.25 we show the spectra of ${}^6\text{Li}$, ${}^7\text{Li}$, ${}^8\text{Be}$, and ${}^9\text{Be}$ obtained with the MBO and FBO interaction families with $\Lambda = 500$ MeV. For ${}^6\text{Li}$ we show for each result two uncertainty bars. Both bars include the many-body uncertainties in combination with the chiral truncation error estimates. While for the left-hand bar, we use the EKM approach, we use the Bayesian approach for the right-hand bar. The two approaches behave similarly in excited and ground-state observables. The EKM approach leads to smaller uncertainties than the Bayesian approach, especially at lower orders. At higher orders the differences between both approaches decrease. Henceforth, we use the Bayesian approach only. With few exceptions, higher-order results lie within the uncertainties of the lower orders. In most cases the interaction uncertainties are larger than the many-body uncertainties except for

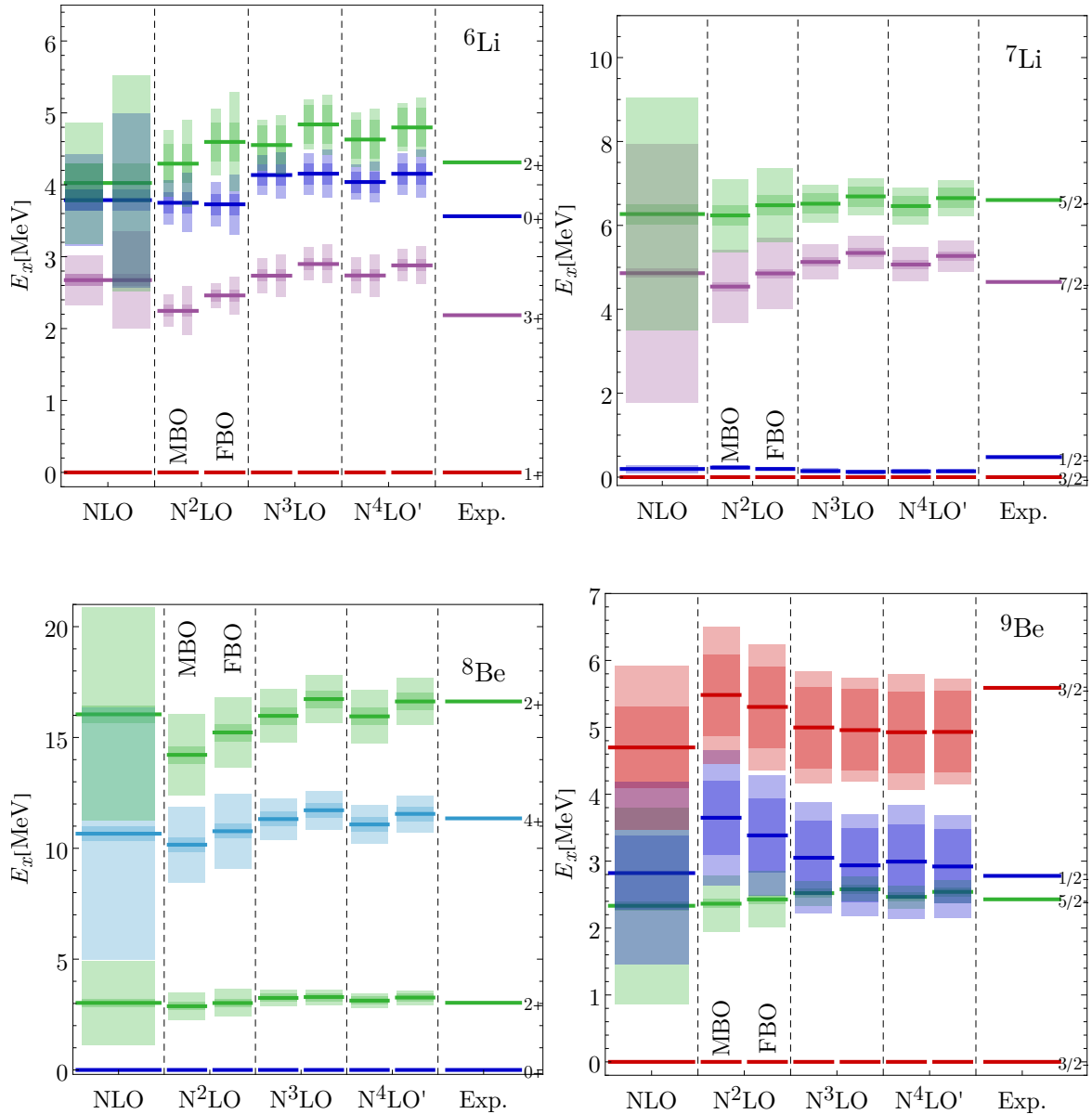


Figure 4.25: Spectra of selected Li and Be isotopes calculated in IT-NCSM calculations with the MBO and FBO interaction families with $\Lambda = 500$ MeV. The uncertainty bars include many-body (dark) and chiral (light) uncertainty estimates. For ${}^6\text{Li}$ we show the chiral uncertainties estimated with the EKM (left) and Bayesian (right) uncertainty quantification. For the other nuclei, we show only the uncertainties derived with the Bayesian uncertainty quantification. Experimental values are taken from [133, 134].

states with very large many-body uncertainties like the $\frac{1}{2}^-$ and $\frac{3}{2}^-$ states of ${}^9\text{Be}$.

Overall, both interaction families lead to similarly good results. Most states agree with experimental values within uncertainties. However, there are a few exceptions. The excitation energies of the ${}^6\text{Li}$ states are systematically too large. When we compare the MBO and FBO interactions, within a chiral order the FBO interactions generally lead to slightly larger excitation energies with the exception of the ${}^9\text{Be}$ $\frac{1}{2}^-$ and $\frac{3}{2}^-$ states. These states also have large error bars driven by the many-body uncertainty, which are larger than 0.5 MeV. An additional exception is the $\frac{1}{2}^-$ state, which has in general an undersized excitation energy but also very small uncertainties.

We have seen that in contrast to the ground-state energies, where the MBO interaction leads to a better agreement with the experiment in both p-shell and medium mass isotopes, the excitation energies are well described by both interaction families. It is worthwhile to mention that both interaction families reproduce the ground-state radii well.

5 | Interactions with Semi-Local Regulators

In the previous chapter we explored interaction families based on the EMN NN interaction in combination with a non-local regularized 3N interaction. The non-local regularization can lead to regulator artifacts [13, 72], since the non-local regulator function cuts into the long-range contributions, which should be given unambiguously through pion physics, see also section 2.3.3. With the idea to reduce this regulator effect Epelbaum *et al.* [13, 14, 78] developed two versions of a regularization scheme that treat short- and long-range contributions differently. In the first version (SCS) short-range contributions are regularized with a non-local and the long-range contributions with a local regularization function. The regularization function acts in configuration space and is parameterized via a cutoff with length scale R . In a second version (SMS) the regularization scheme has been modified such that the regularization function acts in momentum space, which in turn simplifies the numerical calculation of the matrix elements of these interactions, compare also section 2.3.3. The interaction is available from LO up to N⁴LO+ with four different cutoffs Λ .

In this chapter we explore the SMS interaction family in light nuclei. First, we will consider only the NN interaction and later on we will combine it with 3N interactions.

5.1 | Results of the NN Interaction

First we explore the SMS NN interactions without 3N interactions in light nuclei. In figure 5.1 we show the results of Jacobi-NCSM calculations for ground-state observables of ⁴He for the different chiral orders and cutoffs. With increasing chiral order, both energies and radii converge smoothly for all cutoffs. For the energy, the cutoff $\Lambda = 400$ MeV yields the smallest difference to the experimental value and with increasing cutoff, ⁴He is less bound. Hence, the neglected many-body forces need to have an attractive character to reconcile the results with the experiment. The interactions with cutoff $\Lambda = 500$ MeV reproduce the experimental radius value best and with decreasing cutoff the radii decrease. Hence, in this case the smaller cutoffs need to be combined with many-body forces that push the nucleons further apart in order to reduce the difference to the experimental value. Thus, for $\Lambda = 400$ MeV we need a 3N interaction that has barely any influence on the energy but increases the radius. We can conclude that the complemented many-body forces need to have an increasingly binding character with increasing cutoff while at the same time the influence on the radius should decrease. Nevertheless, we should state that even though the $\Lambda = 400$ MeV interactions lead to radii, which deviate the most from the experiment, this discrepancy is only about 0.06 fm.

The picture changes for ¹⁶O. We have calculated ground-state observables of ¹⁶O in NCSM calculations with the NAT basis. The results of these calculations are shown in figure 5.2. The use of the NAT basis makes the results independent of the HO frequency $\hbar\Omega$. Therefore, the many-body uncertainties for the energies are calculated by taking the difference of the extrapolated results and the results at the largest N_{\max} value. For the extrapolation we use an exponential ansatz as before, compare equation (4.7). The extracted radius is defined as the result at the last N_{\max} value and the many-body uncertainty as the difference between

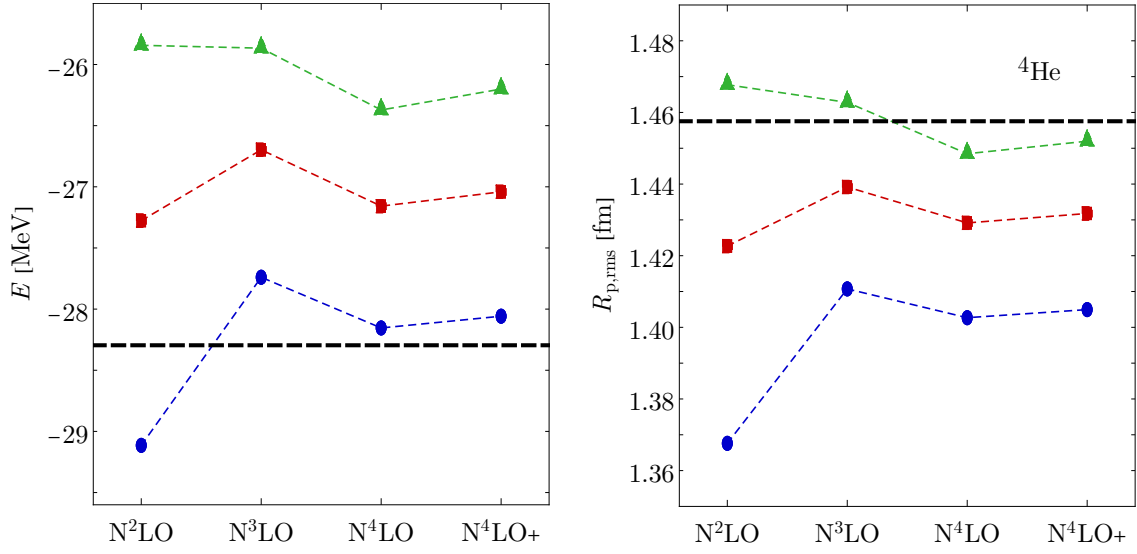


Figure 5.1: Ground-state energies (left) and point-proton radii (right) of ${}^4\text{He}$ calculated with the SMS NN interactions within Jacobi-NCSM calculations up to $N_{\max} = 24$. The shown energies are the minima of the HO frequency variation in the range $\hbar\Omega = 20 - 44$ MeV. Shown are the interactions with the cutoffs $\Lambda = 400$ (blue), 450 (red), and 500 (green) MeV. The dashed black lines indicate the experimental values.

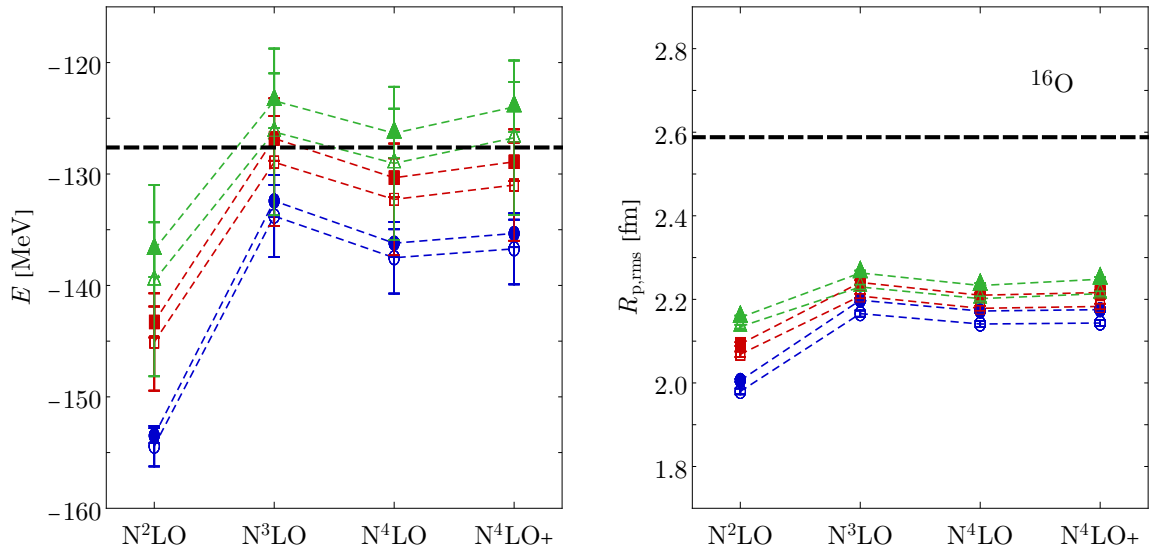


Figure 5.2: Ground-state energies (left) and point-proton radii (right) of ${}^{16}\text{O}$ calculated with the SMS NN+ $3N_{\text{ind}}$ interactions within NCSM calculations with NAT basis up to $N_{\max} = 10$. The shown energies are the extrapolated energies with uncertainties as described in the text. Shown are the interactions with the cutoffs $\Lambda = 400$ (blue), 450 (red), and 500 (green) MeV. The interactions are SRG evolved with flow-parameter $\alpha = 0.02$ fm (open symbols) and $\alpha = 0.04$ fm (filled symbols). The dashed black lines indicate the experimental values.

the results of the last two N_{\max} values. The interactions are SRG evolved to accelerate the convergence of the calculation. The SRG induced 3N forces as well as the induced two-body contributions to the radius operator have been taken into account.

Similarly to ${}^4\text{He}$, the ground-state energy and point-proton radius of ${}^{16}\text{O}$ converge smoothly with respect to chiral order. The energy is well described especially for the cutoffs $\Lambda = 450$ and 500 MeV without the 3N interaction. In contrast to ${}^4\text{He}$, the ground-state radii of ${}^{16}\text{O}$ are about 0.5 fm too small when only the NN interactions are used. This property is independent of the cutoff Λ and also the SRG only leads to small variations between the $\alpha = 0.02$ and 0.04 fm⁴ evolved interactions. Hence, large uncertainties due to missing higher particle-rank SRG contributions are unlikely. An additional 3N force would need to increase the radius significantly and at the same time have only a minor impact on the energy to reconcile the results with the experiment.

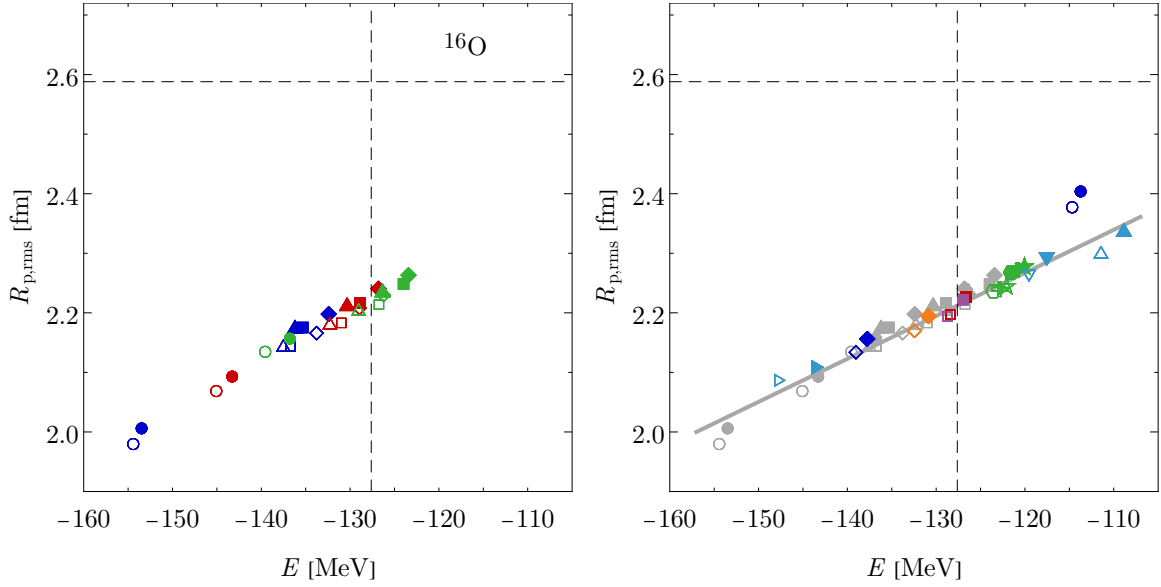
5.2 | Modifications of the NN Interaction

Probing the SMS NN interactions in many-body systems like ${}^{16}\text{O}$ shows that these interactions can describe the ground-state energy very well but the radius is significantly underestimated. These interactions lead to a point-proton radius of about $R_{p,\text{rms}} \approx 2.2$ fm for ${}^{16}\text{O}$, which corresponds to an underestimation of about 15% in comparison with the experiment. If we compare the densities of these nuclei instead of the radii, the small radius leads to a theoretical density that is about 1.6 times denser than the experimental one. Similarly, other observables that depend on powers of the radius, for example electromagnetic observables, cannot be described satisfactorily.

By replotting the results of the energy and radius of ${}^{16}\text{O}$ calculated with the SMS NN interaction in figure 5.3a, we see that there exists a strong linear correlation between the energy and radius for these NN interactions. The resulting radius is negatively linearly dependent on the binding energy of the different NN interactions. This correlation makes it impossible to reproduce both experimental radius and energy. The radius is significantly underestimated unless ${}^{16}\text{O}$ is far too underbound.

Even in the NN interaction, we have parameters, which are not directly constrained by the fit on the phase shifts and other NN data. The choice of these parameters is made in the construction of the interactions. Hence, we explored in collaboration with Reinert and Epelbaum [135] variations of the SMS NN interaction and their impact on the radius and energy description. For instance, we can probe the energy range of the fitting data or use different sets of πN LECs. Furthermore, we have so-called ambiguous parameters in the interaction that need to be chosen in the construction of the interaction. Here, we probe ambiguous parameters of different nature: short-range off-shell terms as well as relativistic ambiguous parameters. In this survey we restricted ourselves to the SMS NN interaction at N⁴LO+ with cutoff $\Lambda = 450$ MeV and SRG parameters $\alpha = 0.04$ and 0.08 fm⁴. At this chiral order the description of the NN scattering data can be achieved in a precision such that the performed adjustments to the interaction have no significant effect on the accuracy of their description. The ground-state energies and radii of ${}^{16}\text{O}$ obtained with these adjusted interactions can be found in figure 5.3b. We have calculated these observables with NCSM calculations with NAT basis as before. The corresponding results for the unaltered version of this interaction is also shown for reference. In addition, the results of the other chiral orders and cutoffs are grayed out as well as the previously found correlation is indicated by a gray line.

We start by modifying the maximum energy E_{lab}^{\max} for the NN data, which is used in the



(a) The shown results are the same as in figure 5.2. The different colors indicate the cutoffs $\Lambda = 400$ (●), 450 (●), and 500 MeV (●) while the different symbol shapes indicate the chiral orders N²LO (●), N³LO (◆), N⁴LO (▲), and N⁴LO+ (■). Open symbols indicate SRG flow-parameter $\alpha = 0.02$ fm⁴ and filled symbols $\alpha = 0.04$ fm⁴.

(b) The shown results correspond to the following modifications of the NN+3N_{ind} interactions: SMS (■), SMS- $E_{lab}^{max}=220$ MeV (■), SMS-KH (◆), SMS- $D_{1S_0}^{off}=3$ (▲), SMS- $D_{3S_1}^{off}=3$ (▼), SMS- $D_{e1}^{off}=3$ (▶), SMS- $\beta_{8/9}=1/2$ (A (⊕), B (⊗), C (⊙)), SCS-N⁴LO $R=1.0$ fm (●), and SCS-HK-N⁴LO+ $R=1.0$ fm (◆). These modifications are applied to the SMS interaction with $\Lambda = 450$ MeV at N⁴LO+ and are explained in the text. The gray symbols correspond to the results of (a) and are given for reference and the gray line indicates the found correlation. Open symbols indicate SRG flow-parameter $\alpha = 0.04$ fm⁴ and filled symbols $\alpha = 0.08$ fm⁴.

Figure 5.3: Correlation plots between the point-proton radius and the energy of the ground-state of ^{16}O for the SMS NN interactions (a) and variations of the SMS NN interaction with cutoff $\Lambda = 450$ MeV at N⁴LO+ (b). The dashed lines correspond to the experimental values.

fit of the interaction. Hereby we can probe the stability of the fit of the NN interaction. We lower $E_{\text{lab}}^{\text{max}}$ from the standard choice of 260 MeV to 220 MeV. This choice has practically no worsening effect of the pp data description [78], while the np data description is slightly improved for data with $E_{\text{lab}} < 200$ MeV and slightly worsened for higher energetical data. The effect on the ground-state energy as well as the radius of ^{16}O is negligibly small. This indicates that the fit of the NN interaction is stable from the point of view of many-body observables.

Starting from N^3LO , the choice of the operator basis, which represents the contact interactions, is ambiguous [78]. With a unitary transformation one can transform this operator basis such that three LECs, namely the short-range off-shell terms D_{150}^{off} , D_{3S1}^{off} , and $D_{\epsilon_1}^{\text{off}}$, are vanishing. This choice is used in the standard version of the SMS NN interaction. The unitary transformation affects also the strength of the 3N interaction and currents. Since we only use the NN interaction, we can indirectly probe the impact of certain 3N interaction and current terms by applying a different choice of these parameters. Reinert and Epelbaum [135] have provided us with versions of the SMS NN interaction in which these parameters are individually set to $3 \cdot 10^4 \text{ (GeV)}^{-6}$. The modifications of the S-channels lead to increased radii and less binding, while the modification of the mixing ϵ_1 -channel decreases the radius and increases the binding energy in comparison with the standard version. These modifications can have a strong impact on the energy and radius but do not lead to results which deviate from the correlation line.

In addition to these off-shell terms, at N^3LO relativistic corrections to the potential start to contribute. These relativistic corrections are scheme-dependent [84] and depend on the unitary ambiguity parameters¹ $\bar{\beta}_8$ and $\bar{\beta}_9$. These parameters are present in the NN and many-body interactions as well as the currents. In a consistent treatment the choice of these parameters should not have an impact, but we can similarly to the short-range off-shell terms indirectly probe their impact by the absence of the many-body interactions as well as the current contributions to the radius. In the standard version of the SMS NN interaction these parameters are chosen as $\bar{\beta}_8 = 1/4$ and $\bar{\beta}_9 = -1/4$. This is also referred to as the “minimal non-locally” choice, since it eliminates complicated terms in the potential that are of non-local form. Here we probe versions with these parameters set to $\bar{\beta}_8 = \bar{\beta}_9 = 1/2$. These come in three different versions where the additional non-local terms in the OPE potential are treated differently: (A) no subtractions and no regularization in k are employed, (B) no subtractions are employed, the additional terms are regularized with a non-local cutoff function, and (C) a single subtraction and no regularization in k is employed. Here, k denotes the momentum corresponding to the energy eigenvalue E in the relativistic Schrödinger equation [13]. The different treatments lead to only minor differences in the ground-state observables of ^{16}O . In general, these versions lead to a larger radius but at the same time smaller binding energy. The results fall on the same correlation line as the other interactions.

Next, we probe the impact of the πN LECs. The standard choice in the SMS NN interactions are the πN LECs obtained by matching the Roy-Steiner equations to the chiral expansion [77]. These LECs have only small uncertainties. Alternatively, we are probing the set of LECs [79] that is obtained by the Karlsruhe-Helsinki (KH) partial-wave analysis [80]. This modification leads to a smaller radius and larger binding energy for ^{16}O in comparison with the standard interaction, but still falls on the correlation line.

The modifications conducted before affect not the regularization procedure. Now, we probe an updated version of the SCS NN interactions at $\text{N}^4\text{LO}+$ with $R = 1.0$ fm, which uses the short range off-shell parameters set to zero and uses the KH πN LECs. In addition,

¹We have adopted the notation of Epelbaum *et al.*[13] where the parameters μ and ν of [84] are given as $\mu = 4\bar{\beta}_9 + 1$ and $\nu = 2\bar{\beta}_8$.

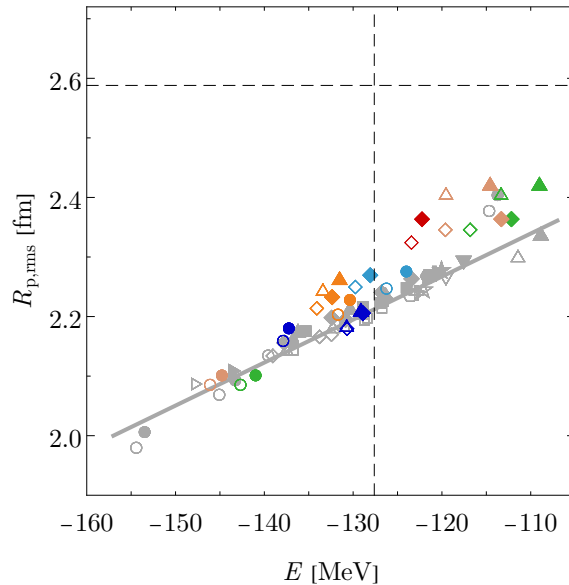


Figure 5.4: Correlation plots between the point-proton radius and the energy of the ground-state of ^{16}O . The grayed out results are the SMS NN+3N_{ind} interactions including variations of figure 5.3b. Furthermore, the different colors indicate the interaction families with corresponding cutoff: SCS ($R = 0.9$ (●), 1.0 (●) fm), EMN ($\Lambda = 450$ (●), 500 (●), and 550 MeV (●)), and EM (●) while the different symbol shapes indicate the chiral orders NLO (▼), N²LO (●), N³LO (◆), and N⁴LO (▲). Open symbols indicate SRG flow-parameter $\alpha = 0.04$ fm⁴ and filled symbols $\alpha = 0.08$ fm⁴. The dashed lines correspond to the experimental values.

we use for reference the standard SCS NN interactions at N⁴LO with $R = 1.0$ fm. The updated version leads to a significantly more bound ^{16}O with smaller radius and lies also on the correlation line. Only the original SCS NN interaction lies slightly above the correlation line.

Up until now, we have seen that all SMS NN interactions including modifications lead to ^{16}O ground-state energies and radii that lie on a correlation line while only the original SCS NN interaction at N⁴LO leads to a result that deviates from that correlation. In figure 5.4 we added further results of chiral NN interactions: for the additional chiral orders and cutoffs of the SCS NN interaction, for the EMN NN interaction family, as well as for the EM NN interaction. In general, the results of the different interactions follow the same trend as the SMS interactions, yet they follow the correlation line not as strictly as the SMS variations. The results of the EMN NN interaction family lie on or slightly above the same correlation line as the SMS NN interactions and follow the same trend. While the N²LO results of the SCS interactions lie also on the correlation line, the higher chiral orders N³LO and N⁴LO of the SCS as well as the EM interaction are above the correlation line. The later ones are all underbound. We can conclude that even though some NN interactions lead to slightly enhanced radii in comparison with the SMS correlation line, the overall description of radii are for all NN interactions similar. Thus, many-body interactions and current contributions to the charge radius operator are needed to reduce the large difference to the experiment.

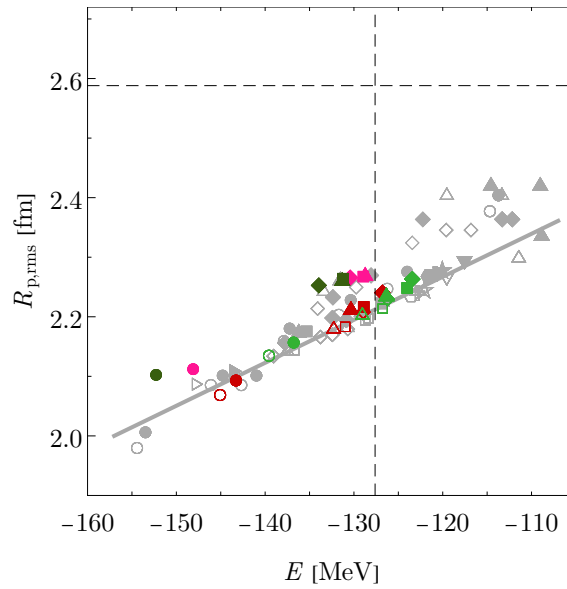


Figure 5.5: Correlation plots between the point-proton radius and the energy of the ground-state of ^{16}O . The grayed out results are the results from before, see figure 5.4. Furthermore, the different colors indicate the different interactions: SMS NN+3N_{ind} ($\Lambda = 450$ (●), 500 (●) MeV), SMS NN+3N_{full} ($\Lambda = 450$ (●), 500 (●) MeV) while the different symbol shapes indicate the chiral orders N²LO (●), N³LO (◆), N⁴LO (▲), and N⁴LO+ (■) of the NN interaction, while the 3N interaction is fixed at N²LO. Open symbols indicate SRG flow-parameter $\alpha = 0.04 \text{ fm}^4$ and filled symbols $\alpha = 0.08 \text{ fm}^4$. The dashed lines correspond to the experimental values.

NN chiral order	Λ [MeV]	c_D	c_E
N ² LO	450	2.4850	-0.5279
	500	-1.6262	-0.0627
N ³ LO	450	1.5281	-0.3540
	500	-0.4344	-0.3106
N ⁴ LO	450	0.6526	-0.3528
	500	-1.5794	-0.3203
N ⁴ LO+	450	0.8918	-0.3860
	500	-1.2788	-0.3821

Table 5.1: The c_D and c_E -values of the SMS interactions with supplemented 3N interaction at N²LO [91, 135].

5.3 | Effects of the 3N Interaction

In the previous section we saw that by using NN interactions only, we get ¹⁶O ground-state energies and radii that fall on a correlation line, which fails to reproduce both experimental energy and radius simultaneously. In this section, we supplement the SMS NN interactions with different 3N interactions. First, we explore the impact of the consistently regularized N²LO 3N interaction on the ¹⁶O ground-state energies and radii correlation. Afterwards, we explore the effect of different regularization procedures on the different 3N topologies.

In the consistently regularized 3N interaction, we use the standard LENPIC choice of the LECs c_D and c_E , which are constrained by the triton binding energy as well as the proton-deuteron differential cross section minimum at the nucleon beam energy $E_N = 70$ MeV [91, 135] and are given in table 5.1 for the cutoffs $\Lambda = 450$ and 500 MeV. As before, we show the resulting ¹⁶O ground-state energies and radii as a correlation plot in figure 5.5, which are obtained in IM-SRG calculations. For comparison we include the NN results shown in figure 5.4 as gray symbols. The inclusion of the 3N interactions leads to results that lie slightly above the correlation line. For the interactions with $\Lambda = 500$ MeV the 3N interaction mainly leads to more binding, such that for all chiral orders ¹⁶O is overbound. The radii are only slightly affected for this cutoff. For $\Lambda = 450$ MeV the picture is somewhat different, the radii are slightly improved and the effect on the energies is not as strong as for $\Lambda = 500$ MeV. In total the results with 3N interaction lie on a slightly shifted correlation line with radii about 0.06 fm larger and lead to results similar to the EMN NN interaction. This is only a small improvement towards the experiment.

Motivated by the results of chapter 4, which indicate that medium-mass isotopes and few-body systems are not necessarily described equally well with the same c_D - c_E pair, we now explore if it is possible to improve the description of the radius by using a different c_D - c_E set. Given that, the non-locally regularized 3N interaction supplemented with the EMN NN interaction has enhanced the description of radii significantly in comparison with a locally regularized 3N interaction, we also probe the impact of the regularization scheme on the individual 3N topologies. Here, we restrict ourselves again to the highest chiral order for the NN interaction, N⁴LO+, in combination with the 3N interaction at N²LO. We show the results of IM-SRG calculations for the ground-state energies and point-proton rms radius of ¹⁶O, ²⁴O, ⁴⁰Ca, and ⁴⁸Ca in figure 5.6 for the cutoff $\Lambda = 500$ MeV. The results are shown for different c_D -values that are of natural size and the corresponding c_E -values are fitted to the triton binding energy.

In the first column the 3N interaction is consistently regularized with the SMS regular-

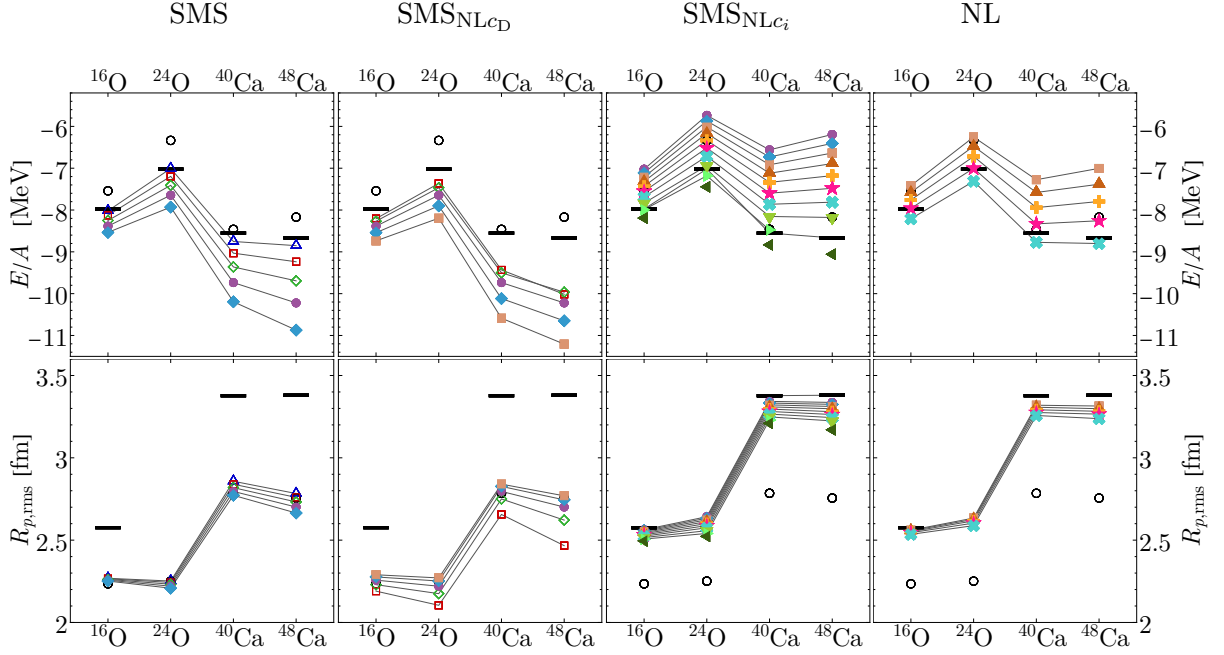


Figure 5.6: Ground-state energies and radii of selected medium-mass nuclei calculated with the SMS NN interaction supplemented with different 3N interactions. In the first column the 3N is regulated with the SMS regularization scheme, in the second column the c_D term is non-locally regularized instead of the SMS regularization scheme, in third column the c_i terms are non-locally regularized, and in the last column all 3N terms are non-locally regularized. The cutoff in the regularization scheme is $\Lambda = 500$ MeV. The results are obtained in IM-SRG calculations and the interactions are SRG evolved with $\alpha = 0.08$ fm⁴. The different symbols indicate the c_D -values of the 3N interaction: $c_D = -3$ (\triangle), -2 (\square), -1 (\diamond), 0 (\bullet), 1 (\blacklozenge), 2 (\blacksquare), 3 (\blacktriangle), 4 (\blackplus), 5 (\blackstar), 6 (\blacktimes), 7 (\blacktriangledown), 8 (\blacktriangleright), 9 (\blacktriangleleft), and 10 (\blacklozenge). The corresponding c_E is fitted to the triton binding energy. The results without initial 3N interaction are indicated with \circ and the experimental values are indicated with black bars.

ization scheme. The comparison of the results with and without the initial 3N force indicates that the 3N force binds the nuclei more and has only a minor influence on the radii. The LENPIC $c_D \approx -1.3$ value leads to overbinding, which increases for heavier isotopes further. With a smaller c_D one would reduce the overbinding and with a $c_D \approx -3$ a good description of the experimental energies is possible. The radii can be slightly improved, but show a much weaker c_D -dependence compared with the energies.

Now, we study if by switching the locally regularized terms to non-locally regularized ones, we can improve the description of the radii. The three-nucleon contact term is already non-locally regularized, hence we do not modify it in this investigation.

First, we use a non-local regulator for the c_D -term. This is shown in the second column of figure 5.6. We again show results for various c_D -values where the corresponding c_E -values are refitted to reproduce the triton binding energy. This switch of regularization scheme leads to underestimated results for both, the energies and radii.

Secondly, we switch the regularization of the two-pion exchange terms parameterized with the c_i to a non-local one and refit the c_E -values. These results are shown in the third column of figure 5.6. This has a strong effect on the energies and radii. The selected nuclei tend to underbind, but for larger c_D -values of around 8 the binding energies can be brought to

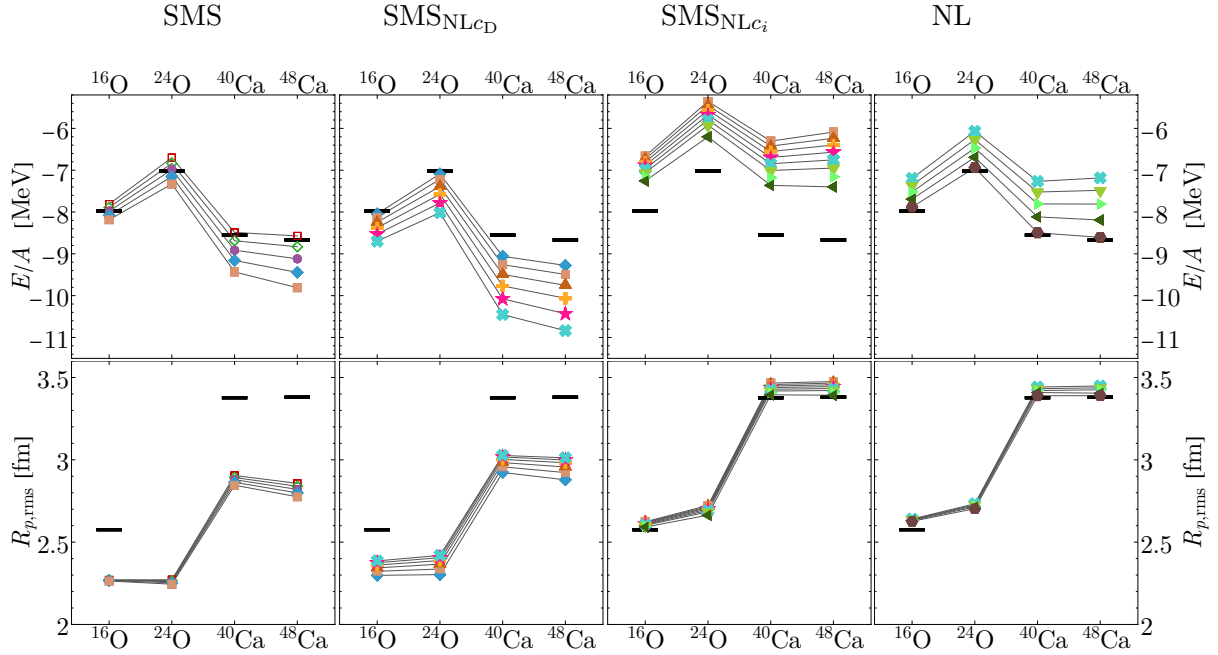


Figure 5.7: Ground-state energies and radii of selected medium-mass nuclei calculated with the SMS NN interaction at N^4LO+ supplemented with different regularized 3N interactions at N^2LO , as in figure 5.6 with cutoff $\Lambda = 450$ MeV. The results are obtained in IM-SRG calculations and the interactions are SRG evolved with $\alpha = 0.08$ fm⁴. The different symbols indicate the c_D -values of the 3N interaction: $c_D = -3(\triangle)$, $-2(\square)$, $-1(\diamond)$, $0(\bullet)$, $1(\blacklozenge)$, $2(\blacksquare)$, $3(\blacktriangle)$, $4(\blackplus)$, $5(\blackstar)$, $6(\blackcross)$, $7(\blacktriangledown)$, $8(\blacktriangleright)$, $9(\blacktriangleleft)$, and $10(\blacklozenge)$. The corresponding c_E is fitted to the triton binding energy. The experimental values are indicated with black bars.

a good agreement with the experimental values. The corresponding radii are substantially enhanced into the range of the experiment.

Lastly, we use a complete non-locally regularized 3N interaction, which is shown in the last column of figure 5.6. The attractive character of the non-locally regularized c_D term can mitigate the binding through the c_i terms and thereby reduce the c_D -value, which is necessary to bring the ground-state energies in agreement with the experiment. The radii are described similarly well.

We show the same analysis as before with the interaction with cutoff $\Lambda = 450$ MeV in figure 5.7. The qualitative behavior is the same, but for this lower cutoff the non-local two-pion term has a stronger repulsive effect. Therefore, larger c_D -values in the range of 10 are necessary to bring the results of the complete non-local 3N into the range of the experiment. This matches the finding of section 4.3, where with increasing cutoff the c_D -value decreases.

In this section we have seen that the SMS 3N interaction at N^2LO acts similarly to the locally regularized 3N interaction in section 4.1 and thereby is not able to enhance the radius of medium-mass nuclei into the range of the experimental values. By using a non-locally regularized 3N interaction, we are able to increase the radii and bring both energies and radii in alignment with experiment. In particular the regularization of the c_i terms has a strong influence on the size of the nuclei. In general, this adjustment of the regularization scheme is undesired, since it destroys the consistency between the NN and 3N force.

How can we reconcile the differences emerging from these regulator schemes? First, in contrast to the non-local regularization scheme the SMS regularization scheme could have a

slower or different convergence such that the radii of medium-mass nuclei are enhanced at higher chiral order. A consistently regularized 3N interaction at $N^3\text{LO}$ is currently under construction. From experience with the non-locally regularized 3N interaction at $N^3\text{LO}$ the effect on the radius is expected to be small. Nevertheless, at $N^2\text{LO}$ the behavior of the locally and non-locally regularized terms was also different. Thus, the $N^3\text{LO}$ 3N interaction can have unanticipated effects. Furthermore, we have not included current contributions to the charge radius operator, which can also have sizeable effects on the radius. The inclusion of these contributions is also ongoing work in LENPIC.

6 | Next-to-Leading Order Contributions to the Magnetic Moment

Electromagnetic observables, like multipole moments and transition strengths, are important quantities for the comparison of theory and experiment. They are complementary observables to energies and probe different aspects of the nucleonic wavefunction.

In many theoretical determinations of these quantities only the leading order contributions, also called impulse approximation contributions, of the nuclear currents have been taken into account [16, 136–138]. Even though the LO contribution is the dominant part, in precision studies higher orders, the so-called meson exchange currents, have to be considered.

The need to introduce exchange currents to satisfy the continuity equation for the electromagnetic current has already been shown by Siegert [139] in 1937. Recently, first explorative results on the impact of electromagnetic currents derived in chiral EFT have been obtained by Marcucci *et al.* [50] as well as by Pastore *et al.* [51]. They show that these currents are not negligible. In the calculations of [50, 51] the authors use a hybrid ansatz with phenomenological interactions to solve the nuclear many-body problem. In Piarulli *et al.* [140] also chiral EFT interactions for nuclei up to $A = 3$ have been used.

In order to fulfill the continuity equation of the electromagnetic currents, the currents should be constructed consistently with the interaction. Furthermore, the consistent treatment of currents allows to connect different processes to fit the LECs of the chiral interaction as for example in the case of the triton beta decay [75, 121], where the weak current contribution is used to fit c_D .

The derivation of currents in chiral EFT has further been studied in [141–143]. The NLO current contribution consists of terms that originate from the one-pion exchange in the interaction. The aim of this chapter is to provide a framework to determine corrections beyond the LO of the magnetic dipole moment operator in NCSM calculations with interactions derived in chiral EFT. Hence, we utilize the one-pion-exchange-current contributions to the magnetic-moment operator as a test case.

We start by introducing the electromagnetic interaction and motivate the origin of the exchange currents. Then, we sketch the expansion of the electromagnetic field into multipoles. These multipoles are the basic components to determine moments and transition strengths, which are in turn sensitive to details of the nuclear wave functions. After this general description of electromagnetic properties, we concentrate on the magnetic dipole moment operator and the derivation of the corresponding matrix elements. Before we can use the matrix elements in an NCSM calculation we explain the consistent treatment of the SRG evolution at the NN level as well as the transformation in a suitable basis representation for NCSM calculations. Finally, we explore the impact of the NLO contribution to the magnetic dipole moment of the ground state and M1 transition strength of the first excited 1^+ state to the ground state in ${}^6\text{Li}$.

6.1 | Electromagnetic Interaction

In this section we introduce the interaction of an electromagnetic field with a nucleus as well as the nuclear currents relevant in this work. The description is guided by [144–146].

A nucleus exposed to an electromagnetic field can be described with the Hamiltonian

$$\hat{H} = \hat{H}_{\text{nuc}} + \hat{H}_{\text{field}} + \hat{H}_{\text{int}}, \quad (6.1)$$

where \hat{H}_{nuc} is the Hamiltonian of the nucleus, \hat{H}_{field} describes the electromagnetic field and \hat{H}_{int} the interaction between both. The interaction can be described up to linear terms in the four-vector potential $A^\mu(\vec{x}, t) = (\phi(\vec{x}, t), \vec{A}(\vec{x}, t))$ with

$$\hat{H}_{\text{int}} = \frac{1}{c} \int d^3x \hat{J}_\mu(\vec{x}, t) A^\mu(\vec{x}, t). \quad (6.2)$$

The four-current density $\hat{J}^\mu = (c\hat{\rho}(\vec{x}, t), \hat{\vec{J}}(\vec{x}, t))$ consists of the nuclear-charge density $\hat{\rho}(\vec{x}, t)$ as well as the nuclear-vector-current density $\hat{\vec{J}}(\vec{x}, t)$ and needs to satisfy the continuity equation

$$\frac{\partial \hat{\rho}(\vec{x}, t)}{\partial t} + \hat{\nabla} \cdot \hat{\vec{J}}(\vec{x}, t) = 0, \quad (6.3)$$

such that the theory fulfills gauge invariance. The density and current operator should be constructed consistently with the nucleonic interaction for instance in the framework of chiral EFT [147, 148, 142, 143, 149]. In this framework the density and current operator is expanded consistently in one-, two- and many-body operators similar to the nuclear forces

$$\hat{\vec{J}}(\vec{x}) = \sum_i^A \hat{\vec{J}}_{[1],i}(\vec{x}) + \sum_{ij}^A \hat{\vec{J}}_{[2],ij}(\vec{x}) + \dots, \quad (6.4)$$

where the number in the square brackets gives the particle rank and the ellipsis indicates higher particle ranks.

In this work we will only consider LO and NLO contributions of these operators. Please note that there exist different conventions in the power counting as well as different methods to construct these currents. In this work we follow the authors of [147–149] in the power counting and description of the currents. At LO and NLO we only consider point-like non-relativistic nucleons with the nuclear charge density given by

$$\hat{\rho}_{[1]}(\vec{x}, \vec{r}_{1\dots A}) = \sum_i^A e \hat{\Pi}_{p,i} \delta(\vec{x} - \vec{r}_i). \quad (6.5)$$

Here, e is the electric charge and

$$\hat{\Pi}_{p,i} = 1 + \hat{\tau}_{3,i} \quad (6.6)$$

the proton projection operator with $\hat{\tau}_{3,i}$ the third part of the reduced isospin operator.

The LO current consists of an orbital part

$$\hat{\vec{J}}_{[1],i}^{\text{LO},o}(\vec{x}, \vec{r}_i) = \frac{e \hat{\Pi}_{p,i}}{2M_N} \left\{ \hat{\vec{p}}_i, \delta(\vec{x} - \vec{r}_i) \right\} \quad (6.7)$$

and a spin part

$$\hat{J}_{[1],i}^{\text{LO},s}(\vec{x}, \vec{r}_i) = c\hat{\nabla} \times \frac{\mu_N}{2} \left(\hat{\Pi}_{p,i}g_p + \hat{\Pi}_{n,i}g_n \right) \hat{\sigma}_i \delta(\vec{x} - \vec{r}_i), \quad (6.8)$$

where M_N is the mass of a nucleon, $\mu_N = e\hbar/(2M_Nc)$ is the nuclear magneton, $\{\dots, \dots\}$ denotes an anticommutator, and the g factors of the proton and the neutron are $g_p = 5.5857$ and $g_n = -3.8261$ [118]. The orbital part can be separated into a center-of-mass and an intrinsic part, such that the complete LO current is given by

$$\hat{J}_{[1]}^{\text{LO}}(\vec{x}, \vec{r}_{1\dots A}) = \hat{J}_{\text{cm}[1]}^{\text{LO}}(\vec{x}, \vec{r}_{1\dots A}) + \hat{J}_{\text{int}[1]}^{\text{LO}}(\vec{x}, \vec{r}_{1\dots A}), \quad (6.9)$$

with

$$\hat{J}_{\text{cm}[1]}^{\text{LO}}(\vec{x}, \vec{r}_{1\dots A}) = \frac{1}{2AM_N} \left\{ \hat{P}_{\text{cm}}, \hat{\rho}_{[1]}(\vec{x}, \vec{r}_{1\dots A}) \right\} \quad (6.10)$$

and

$$\hat{J}_{\text{int}[1]}^{\text{LO}}(\vec{x}, \vec{r}_{1\dots A}) = \sum_i^A \frac{e\hat{\Pi}_{p,i}}{2M_N} \left\{ \hat{p}_i', \delta(\vec{x} - \vec{r}_i) \right\} + \sum_i^A \hat{J}_{[1],i}^{\text{LO},s}(\vec{x}, \vec{r}_i). \quad (6.11)$$

Here

$$\hat{P}_{\text{cm}} = \sum_i^A \hat{p}_i \quad (6.12)$$

is the center-of-mass momentum and

$$\hat{p}_i' = \hat{p}_i - \frac{1}{A} \hat{P}_{\text{cm}} \quad (6.13)$$

denotes the momentum of the i -th nucleon with respect to the center-of-mass of the A -body system. This separation is practical since only the intrinsic current is relevant for the determination of excitation processes.

This one-body current and density satisfies the continuity equation

$$\hat{\nabla} \cdot \hat{J}(\vec{x}, t) = -\frac{\partial \hat{\rho}(\vec{x}, t)}{\partial t} = -\frac{i}{\hbar} \left[\hat{H}_0, \hat{\rho}(\vec{x}, t) \right] \quad (6.14)$$

with

$$\hat{H}_0 = \hat{T} = \sum_i^A \frac{\hat{p}_i^2}{2M_N} \quad (6.15)$$

the non-interacting Hamiltonian given by the kinetic energy. At NLO we further need to consider exchange currents, which occur if the NN interaction exchange charge between two nucleons. This process corresponds to a $\hat{\tau}_i \cdot \hat{\tau}_j$ term in the two-body interaction

$$\hat{V}_{ij} = \hat{V}_{0,ij} + \hat{V}_{\text{ex},ij} \hat{\tau}_i \cdot \hat{\tau}_j, \quad (6.16)$$

such that the Hamiltonian is given by

$$\hat{H}_0 \longrightarrow \hat{T} + \hat{V} = \sum_i^A \frac{\hat{p}_i^2}{2M_N} + \sum_{ij}^A (\hat{V}_{0,ij} + \hat{V}_{\text{ex},ij} \hat{\tau}_i \cdot \hat{\tau}_j). \quad (6.17)$$

Since the density operator (6.5) contains the proton projection operator

$$\hat{\Pi}_{p,i} = 1 + \hat{\tau}_{3,i} \quad (6.18)$$

the commutator in the continuity equation (6.14) includes terms of the form

$$\left[\hat{\vec{\tau}}_i \cdot \hat{\vec{\tau}}_j, \hat{\tau}_{3,i} \right] = - \left[\hat{\vec{\tau}}_i \cdot \hat{\vec{\tau}}_j, \hat{\tau}_{3,j} \right] = \hat{\tau}_{-,i} \hat{\tau}_{+,j} - \hat{\tau}_{+,i} \hat{\tau}_{-,j} = 2i \left[\hat{\vec{\tau}}_i \times \hat{\vec{\tau}}_j \right]_3. \quad (6.19)$$

Therefore, we obtain from the continuity equation (6.14) that the current contribution associated with the exchange process needs to fulfill

$$\hat{\nabla} \cdot \hat{J}_{[2],ij}^{\text{ex}}(\vec{x}, \vec{r}_i, \vec{r}_j) = \frac{e}{\hbar} \left[\hat{\vec{\tau}}_i \times \hat{\vec{\tau}}_j \right]_3 \hat{V}_{\text{ex}}(\vec{r}_i - \vec{r}_j) [\delta(\vec{x} - \vec{r}_i) - \delta(\vec{x} - \vec{r}_j)]. \quad (6.20)$$

Due to translation invariance the exchange current can only depend on $\vec{r}_i - \vec{x}$ and $\vec{r}_j - \vec{x}$, hence, we can use the following Fourier transformations for the exchange current

$$\hat{J}_{[2],ij}^{\text{ex}}(\vec{x}, \vec{r}_i, \vec{r}_j) = \int \frac{d^3 q_i}{(2\pi)^3} \int \frac{d^3 q_j}{(2\pi)^3} e^{i\vec{q}_i(\vec{r}_i - \vec{x})} e^{i\vec{q}_j(\vec{r}_j - \vec{x})} \hat{J}_{[2],ij}^{\text{ex}}(\vec{q}_i, \vec{q}_j) \quad (6.21)$$

and for the exchange potential

$$\hat{V}_{\text{ex}}(\vec{r}) = \int \frac{d^3 q}{(2\pi)^3} e^{i\vec{q}\vec{r}} \hat{V}_{\text{ex}}(\vec{q}) \quad (6.22)$$

to obtain a general relation in momentum space

$$i(\vec{q}_i + \vec{q}_j) \cdot \hat{J}_{[2],ij}^{\text{ex}}(\vec{q}_i, \vec{q}_j) = e \left[\hat{\vec{\tau}}_i \times \hat{\vec{\tau}}_j \right]_3 (\hat{V}_{\text{ex}}(\vec{q}_i) - \hat{V}_{\text{ex}}(\vec{q}_j)). \quad (6.23)$$

The dominant exchange process is the one-pion exchange and the exchange interaction is given by the OPE potential [148]¹

$$\hat{V}_{\text{OPE}}^{\text{NN}}(\vec{q}) = -\frac{g_A^2}{F_\pi^2} \frac{(\hat{\vec{\sigma}}_i \cdot \vec{q})(\hat{\vec{\sigma}}_j \cdot \vec{q})}{q^2 + M_\pi^2} (\hat{\vec{\tau}}_i \cdot \hat{\vec{\tau}}_j), \quad (6.24)$$

or alternatively expressed in configuration space as [145]

$$\hat{V}_{\text{OPE}}^{\text{NN}}(\vec{r}) = \frac{g_A^2}{F_\pi^2} (\hat{\vec{\tau}}_i \cdot \hat{\vec{\tau}}_j) (\hat{\vec{\sigma}}_i \cdot \vec{\nabla})(\hat{\vec{\sigma}}_j \cdot \vec{\nabla}) \frac{e^{-M_\pi r}}{4\pi r}. \quad (6.25)$$

Hence, the NLO contribution to the current needs to fulfill

$$(\vec{q}_i + \vec{q}_j) \cdot \hat{J}_{[2],ij}^{\text{NLO}}(\vec{q}_i, \vec{q}_j) = ie \frac{g_A^2}{F_\pi^2} \left[\hat{\vec{\tau}}_i \times \hat{\vec{\tau}}_j \right]_3 \left[\frac{(\hat{\vec{\sigma}}_i \cdot \vec{q}_i)(\hat{\vec{\sigma}}_j \cdot \vec{q}_i)}{q_i^2 + M_\pi^2} - \frac{(\hat{\vec{\sigma}}_i \cdot \vec{q}_j)(\hat{\vec{\sigma}}_j \cdot \vec{q}_j)}{q_j^2 + M_\pi^2} \right]. \quad (6.26)$$

The processes associated with the NLO current are shown in figure 6.1. Diagram (a) illustrates the LO one-body current contribution, while diagram (b) illustrates the virtual photoproduction of a pion from a nucleon in combination with an absorption by a second nucleon. In literature this diagram is often referred to as seagull diagram and the current is given by [148]

$$\hat{J}_{[2],ij}^{\text{NLO},s}(\vec{q}_i, \vec{q}_j) = -ie \frac{g_A^2}{F_\pi^2} \left[\hat{\vec{\tau}}_i \times \hat{\vec{\tau}}_j \right]_3 \left\{ \frac{\hat{\vec{\sigma}}_i(\hat{\vec{\sigma}}_j \cdot \vec{q}_j)}{q_j^2 + M_\pi^2} - \frac{(\hat{\vec{\sigma}}_i \cdot \vec{q}_i)\hat{\vec{\sigma}}_j}{q_i^2 + M_\pi^2} \right\}. \quad (6.27)$$

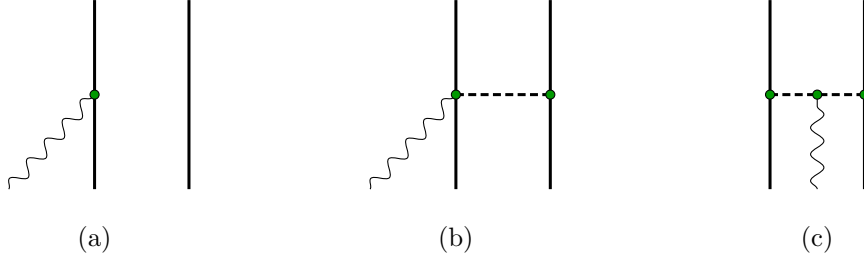


Figure 6.1: Diagrammatic representation of the LO (a) and NLO (b,c) contributions to the nuclear current operator.

Diagram (c) represents the processes where the photon connects with the pion in-flight. The corresponding current is given by [148]

$$\hat{J}_{[2],ij}^{\text{NLO},\pi}(\vec{q}_i, \vec{q}_j) = ie \frac{g_A^2}{F_\pi^2} \left[\hat{\tau}_i \times \hat{\tau}_j \right]_3 (\vec{q}_i - \vec{q}_j) \frac{\hat{\sigma}_i \cdot \vec{q}_i}{q_i^2 + M_\pi^2} \frac{\hat{\sigma}_j \cdot \vec{q}_j}{q_j^2 + M_\pi^2}. \quad (6.28)$$

The individual currents do not fulfill (6.26), while the sum of the currents does.

6.2 | Static Multipole Moments

Intrinsic states of nuclei are characterized by a total angular momentum. Hence, a decomposition of the charge and current operators into terms of operators that correspond to a definite angular momentum transfer is convenient. This allows for the use of reduced matrix elements in combination with the Wigner-Eckart theorem, see appendix A.6. In the derivation of the multipole moments in this and the following section we follow the description of [144].

First, let us consider that the nucleus interacts with a static electromagnetic field. In first-order perturbation theory, this leads to a change of the nuclear energy in the state i by

$$\Delta E_i = \langle \Phi_i | \hat{H}_{\text{int}} | \Phi_i \rangle. \quad (6.29)$$

The interaction Hamiltonian is given by (6.2)

$$\begin{aligned} \hat{H}_{\text{int}} &= \frac{1}{c} \int d^3x \hat{J}_\mu(\vec{x}) A^\mu(\vec{x}) = \int d^3x \hat{\rho}(\vec{x}) \Phi(\vec{x}) - \frac{1}{c} \hat{\vec{J}}(\vec{x}) \cdot \vec{A}(\vec{x}) \\ &= \int d^3x \hat{\rho}(\vec{x}) \Phi(\vec{x}) - \hat{\vec{\mu}}(\vec{x}) \cdot \vec{B}(\vec{x}) \end{aligned} \quad (6.30)$$

where we have introduced the magnetic flux density

$$\vec{B}(\vec{x}) = \vec{\nabla} \times \vec{A}(\vec{x}) \quad (6.31)$$

and the magnetic dipole density $\hat{\vec{\mu}}(\vec{x})$, which is connected with the current density via

$$\hat{\vec{J}}(\vec{x}) = c \vec{\nabla} \times \hat{\vec{\mu}}(\vec{x}). \quad (6.32)$$

¹The OPE potential used by Pastore *et al.* [148] differs by a factor of 4 from (2.23). The origin of this factor is a different parametrization in the Lagrangian, hence, the currents also differ by a factor of 4 in respect to the currents of Kölling *et al.* [142, 143]. In principle, the currents should be chosen consistently with the used interaction.

The sources of the external field are assumed to be far away, thus we can apply the homogeneous Maxwell equations in the region of interest. Therefore, the electric and magnetic field can be written as gradients of scalar fields

$$\vec{E}(\vec{x}) = -\vec{\nabla}\Phi(\vec{x}) \quad \text{and} \quad \vec{B}(\vec{x}) = -\vec{\nabla}\Xi(\vec{x}). \quad (6.33)$$

Furthermore, these fields need to fulfill the Laplace equations

$$\Delta\Phi(\vec{x}) = 0 \quad \text{and} \quad \Delta\Xi(\vec{x}) = 0. \quad (6.34)$$

The general solutions for these Laplace equations can be expressed in spherical coordinates via

$$\Phi(\vec{x}) = \sum_{\lambda\mu} a_{\lambda\mu} x^\lambda Y_{\lambda\mu}(\Omega_x) \quad \text{and} \quad \Xi(\vec{x}) = \sum_{\lambda\mu} b_{\lambda\mu} x^\lambda Y_{\lambda\mu}(\Omega_x), \quad (6.35)$$

with the help of the spherical harmonics $Y_{\lambda\mu}(\Omega_x)$. The coefficients $a_{\lambda\mu}$ and $b_{\lambda\mu}$ relate to various derivatives of the fields. The index λ indicates the multipolarity and μ its projection. Hence, the interaction Hamiltonian can be rewritten as

$$\hat{H}_{\text{int}} = \sum_{\lambda\mu} \left(a_{\lambda\mu} \hat{Q}_{\lambda\mu} + b_{\lambda\mu} \hat{M}_{\lambda\mu} \right), \quad (6.36)$$

where we introduced the electric and magnetic multipole operators

$$\hat{Q}_{\lambda\mu} = \int d^3x \hat{\rho}(\vec{x}) x^\lambda Y_{\lambda\mu}(\Omega_x), \quad (6.37)$$

$$\hat{M}_{\lambda\mu} = \int d^3x \hat{\vec{\mu}}(\vec{x}) \cdot \vec{\nabla} \left(x^\lambda Y_{\lambda\mu}(\Omega_x) \right). \quad (6.38)$$

Furthermore, the magnetic multipole operator can be rewritten such that it depends on the current density:

$$\hat{M}_{\lambda\mu} = \frac{1}{c(\lambda+1)} \int d^3x \left(\vec{x} \times \hat{\vec{J}}(\vec{x}) \right) \cdot \vec{\nabla} \left(x^\lambda Y_{\lambda\mu}(\Omega_x) \right). \quad (6.39)$$

To arrive at equation (6.39), we use the identity

$$\left(\vec{\nabla} \times (\vec{\nabla} \times \vec{x}) \right) x^\lambda Y_{\lambda\mu}(\Omega_x) = (\lambda+1) \vec{\nabla} \left(x^\lambda Y_{\lambda\mu}(\Omega_x) \right) \quad (6.40)$$

and integration by parts. An explicit derivation of identity (6.40) can be found in [150] and [151]. With these operators we can calculate the static electromagnetic moments by evaluating the expectation values

$$Q_{\lambda\mu} = \langle \Psi_n | \hat{Q}_{\lambda\mu} | \Psi_n \rangle \quad \text{and} \quad M_{\lambda\mu} = \langle \Psi_n | \hat{M}_{\lambda\mu} | \Psi_n \rangle, \quad (6.41)$$

where $|\Psi_n\rangle = |\alpha JM\rangle$ is a nuclear state with the total angular momentum J and its projection M . The index α is a collective index over the remaining quantum numbers. Since these operators are spherical tensor operators and $|\Psi_n\rangle$ is an eigenstate of angular momentum, we can apply the Wigner-Eckart theorem and easily calculate the various projections M . Therefore, in the definition of the electromagnetic moments one restricts themselves to the maximum projection quantum number $M = J$.

Before we insert the previously motivated currents of section 6.1 in equation (6.39) in section 6.4, we examine the connection of the multipole operators to the transitions between states.

6.3 | Multipole Transitions

In addition to the energy shift within an electromagnetic field, the interaction Hamiltonian \hat{H}_{int} is also relevant for the description of transitions from an initial nuclear state $|\Psi_i\rangle = |\alpha_i J_i M_i\rangle$ into a final nuclear state $|\Psi_f\rangle = |\alpha_f J_f M_f\rangle$ in combination with the emission or absorption of a photon. The transition probability can be calculated in first-order perturbation theory with Fermi's golden rule [152]

$$T_{fi} = \frac{2\pi}{\hbar} |\langle f | \hat{H}_{\text{int}} | i \rangle|^2 g(E_f). \quad (6.42)$$

Here the initial and final state are a combination of the eigenstates of the nuclear and electromagnetic field Hamiltonian

$$|i\rangle = |\Psi_i\rangle \otimes |\dots n \dots\rangle, \quad (6.43)$$

$$|f\rangle = |\Psi_f\rangle \otimes |\dots n \pm 1 \dots\rangle, \quad (6.44)$$

where the eigenstate of the electromagnetic field Hamiltonian is given in occupation-number representation with respect to multipole modes associated with the photons. Furthermore, the factor $g(E_f)$ denotes the density of states as a function of the energy of the final nucleonic state $E_f = E_i \mp E_k$ given by the energy of the initial state E_i and the photon E_k . The photon can be characterized with its absolute momentum k in combination with its angular momentum component λ and projection μ .

Using the interaction Hamiltonian (6.2) as before, we can decompose the transition probability into an electric ($\sigma = E$) and a magnetic ($\sigma = M$) component

$$T_{fi}(\sigma, k\lambda\mu) = \frac{8\pi(\lambda+1)}{\hbar\lambda((2\lambda+1)!!)^2} \left(\frac{E_k}{\hbar c}\right)^{2\lambda+1} |\langle \Psi_f | \hat{\mathcal{M}}(\sigma, k\lambda\mu) | \Psi_i \rangle|^2, \quad (6.45)$$

with the general electric

$$\begin{aligned} \hat{\mathcal{M}}(E, k\lambda\mu) = \frac{(2\lambda+1)!!}{k^\lambda(\lambda+1)} \int d^3x \left(\hat{\rho}(\vec{x}) Y_{\lambda\mu}(\Omega_x) \frac{\partial}{\partial x} x j_\lambda(kx) \right. \\ \left. + i \frac{k}{c} \hat{\vec{J}}(\vec{x}) \cdot \vec{x} Y_{\lambda\mu}(\Omega_x) j_\lambda(kx) \right) \end{aligned} \quad (6.46)$$

and magnetic

$$\hat{\mathcal{M}}(M, k\lambda\mu) = \frac{-(2\lambda+1)!!}{ck^\lambda(\lambda+1)} \int d^3x \hat{\vec{J}}(\vec{x}) \cdot (\vec{x} \times \nabla) (j_\lambda(kx) Y_{\lambda\mu}(\Omega_x)) \quad (6.47)$$

multipole transition operators. In the long-wavelength limit ($kR \ll 1$, with R the nuclear radius), the Bessel functions can be expanded as

$$j_\lambda(kr) \simeq \frac{(kr)^\lambda}{(2\lambda+1)!!} \left(1 - \frac{1}{2} \frac{(kr)^2}{2\lambda+3} + \dots \right). \quad (6.48)$$

Thus, in leading order the transition multipole operators are equal to the static multipole operators

$$\hat{\mathcal{M}}(E, k\lambda\mu) = \int d^3x \left(\hat{\rho}(\vec{x}) x^\lambda Y_{\lambda\mu}(\Omega_x) + \frac{ik}{\lambda+1} (\vec{r} \times \hat{\vec{\mu}}(\vec{x})) \cdot \vec{\nabla} x^\lambda Y_{\lambda\mu}(\Omega_x) \right) \quad (6.49)$$

$$\approx \int d^3x \hat{\rho}(\vec{x}) x^\lambda Y_{\lambda\mu}(\Omega_x) = \hat{Q}_{\lambda\mu}, \quad (6.50)$$

$$\hat{\mathcal{M}}(M, k\lambda\mu) = \frac{1}{c(\lambda+1)} \int d^3x (\vec{x} \times \hat{\vec{J}}(\vec{x})) \cdot \vec{\nabla} (x^\lambda Y_{\lambda\mu}(\Omega_x)) = \hat{M}_{\lambda\mu}. \quad (6.51)$$

The second term in (6.49) is typically neglected in the long-wave limit, since it is an order kr smaller than the first term [153].

In experiments one usually does not distinguish between the different orientations of the angular momentum. Therefore, we average over the initial projections M_i and sum over the final projections M_f . These sums can be carried out with the help of the Wigner-Eckart theorem, thus, we finally get

$$T_{fi}(\sigma, \lambda) = \frac{1}{2J_i + 1} \sum_{M_i, M_f, \mu} T_{fi}(\sigma, k\lambda\mu) \quad (6.52)$$

$$= \frac{8\pi(\lambda + 1)}{\hbar\lambda((2\lambda + 1)!!)^2} \left(\frac{E_k}{\hbar c}\right)^{2\lambda+1} B(\sigma\lambda, J_i \rightarrow J_f), \quad (6.53)$$

with the reduced transition probability or also called transition strength

$$B(E\lambda, J_i \rightarrow J_f) = \frac{1}{2J_i + 1} |\langle \alpha_f J_f || \hat{Q}_\lambda || \alpha_i J_i \rangle|^2, \quad (6.54)$$

$$B(M\lambda, J_i \rightarrow J_f) = \frac{1}{2J_i + 1} |\langle \alpha_f J_f || \hat{M}_\lambda || \alpha_i J_i \rangle|^2. \quad (6.55)$$

These $B(\sigma\lambda)$ -values are of interest in the comparison between theory and experiment, since the information about the nuclear states are encoded in them. All the other contributions to the transition probability are only kinematic factors.

6.4 | Magnetic Dipole Moment Operator

To probe the NLO contribution of the current, the most relevant electromagnetic multipole operator is the \hat{M}_1 operator, since in the long-wave limit, the electric operator depends only on the density. Furthermore, if allowed, the M1 component has the largest contribution of the magnetic ones. Therefore, we now concentrate on the evaluation of the magnetic dipole moment operator.

The magnetic dipole moment of a nucleus is defined as

$$\mu = \sqrt{\frac{4\pi}{3}} \langle \alpha J J | \hat{M}_{10} | \alpha J J \rangle, \quad (6.56)$$

where the state is aligned along the z -axis. The prefactor $\sqrt{\frac{4\pi}{3}}$ is absorbed in this definition, such that it is identical with the classical dipole moment

$$\hat{\mu} = \sqrt{\frac{4\pi}{3}} \hat{M}_{10} = \hat{\mu}_z \quad (6.57)$$

with

$$\hat{\mu} = \frac{1}{2} \int d^3x \vec{x} \times \hat{\vec{J}}(\vec{x}). \quad (6.58)$$

The magnetic dipole moment operator depends mainly on the underlying current and can similarly be split into its individual particle rank contributions

$$\hat{\mu} = \sum_i^A \hat{\mu}_{[1],i}^{\text{LO}} + \sum_{ij}^A \hat{\mu}_{[2],ij}^{\text{NLO}} + \dots, \quad (6.59)$$

where the ellipsis indicates higher particle-rank and chiral-order contributions.

Leading Order Contribution

The LO magnetic dipole operator is an one-body operator and is given by

$$\hat{\mu}_{[1],i}^{\text{LO}} = \mu_N \left[\hat{\Pi}_{p,i} \hat{l}_i + \left(\hat{\Pi}_{p,i} g_p + \hat{\Pi}_{n,i} g_n \right) \frac{\hat{\sigma}_i}{2} \right] \quad (6.60)$$

with \hat{l}_i the angular momentum operator of the i -th nucleon. Analogously to the current, in an A -body system we can split this operator in an intrinsic and a center-of-mass part. We are again only interested in the intrinsic part, which is

$$\sum_i^A \hat{\mu}_{[1],i}^{\text{LO,int}} = \mu_N \sum_i^A \left[\hat{\Pi}_{p,i} \hat{l}_i + \left(\hat{\Pi}_{p,i} g_p + \hat{\Pi}_{n,i} g_n \right) \frac{\hat{\sigma}_i}{2} \right]. \quad (6.61)$$

Here, the orbital angular momentum operator \hat{l}_i for the i -th nucleon is defined with respect to the center-of-mass

$$\hat{l}_i = \left(\hat{r}_i - \hat{R}_{\text{cm}} \right) \times \left(\hat{p}_i - \frac{1}{A} \hat{P}_{\text{cm}} \right). \quad (6.62)$$

In this form, the LO magnetic dipole operator is no longer an one-body but an A -body operator.

Next-To-Leading Order Contribution

The NLO part can be separated into an orbital part, which depends on the center-of-mass coordinate of the two-body system

$$\hat{R}_{ij} = \frac{1}{2} (\hat{r}_i + \hat{r}_j) \quad (6.63)$$

and an intrinsic part, hence, it is given by [145]

$$\hat{\mu}_{[2],ij}^{\text{NLO}} = \frac{1}{2} \vec{R}_{ij} \times \int d^3x \hat{J}_{[2],ij}^{\text{NLO}}(\vec{x}) + \frac{1}{2} \int d^3x (\vec{x} - \vec{R}_{ij}) \times \hat{J}_{[2],ij}^{\text{NLO}}(\vec{x}). \quad (6.64)$$

The first term is the so-called Sachs moment [154], which can be related to the continuity equation (6.14) via a partial integration [145]

$$\begin{aligned} \hat{\mu}_{[2],ij}^{\text{NLO,Sachs}}(\vec{R}_{ij}, \vec{r}_{ij}) &= \frac{1}{2} \vec{R}_{ij} \times \int d^3x \hat{J}_{[2],ij}^{\text{NLO}}(\vec{x}) \\ &= \frac{1}{2} \vec{R}_{ij} \times \int d^3x x \left(\vec{\nabla} \cdot \hat{J}_{[2],ij}^{\text{NLO}}(\vec{x}) \right) \\ &= \frac{e}{2} \left[\hat{\tau}_i \times \hat{\tau}_j \right]_3 \left(\vec{R}_{ij} \times \vec{r}_{ij} \right) \hat{\mathcal{V}}_{\text{OPE}}^{\text{NN}}(\vec{r}_{ij}), \end{aligned} \quad (6.65)$$

with the relative distance of the two nucleons given by

$$\hat{r}_{ij} = (\hat{r}_i - \hat{r}_j). \quad (6.66)$$

Here $\hat{\mathcal{V}}_{\text{OPE}}^{\text{NN}}(\vec{r})$ is the non-isospin part of the exchange potential (6.25)

$$\hat{\mathcal{V}}_{\text{OPE}}^{\text{NN}}(\vec{r}) = \frac{g_A^2}{F_\pi^2} (\hat{\sigma}_i \cdot \vec{\nabla})(\hat{\sigma}_j \cdot \vec{\nabla}) \frac{e^{-M_\pi r}}{4\pi r}. \quad (6.67)$$

The second term of (6.64) depends only on the relative distance of the nucleons. Using the sum of the currents given by (6.27) and (6.28) leads to [145, 155]

$$\begin{aligned} \hat{\mu}_{[2],ij}^{\text{NLO,int}}(\vec{r}_{ij}) = & \\ - \frac{eM_\pi}{2} \frac{g_A^2}{4\pi F_\pi^2} \left[\hat{\vec{r}}_i \times \hat{\vec{r}}_j \right]_3 & \left[\left(1 + \frac{1}{M_\pi r_{ij}} \right) \left((\hat{\vec{\sigma}}_i \times \hat{\vec{\sigma}}_j) \cdot \vec{e}_{r_{ij}} \right) \vec{e}_{r_{ij}} - (\hat{\vec{\sigma}}_i \times \hat{\vec{\sigma}}_j) \right] e^{-M_\pi r_{ij}}. \end{aligned} \quad (6.68)$$

Now we have explicit expressions for the dipole moment for the LO in equation (6.61) and for the NLO in equations (6.68) and (6.65). The next step is to calculate the matrix elements in an appropriate basis.

6.5 | Matrix Elements of the M1 Operator in a Relative HO Basis

We have calculated the LO and NLO contributions to the magnetic dipole operator in the previous sections. For a pure NCSM calculation we can calculate these operators directly in a single-particle basis. Since we use the SRG to soften the interaction, we need to evolve these operators analogously. We perform the SRG successively in a two- and three-body basis, hence, the leading contribution of the induced operator terms is at particle rank two. To calculate these contributions we need the matrix elements of the M1 operator in a relative two-body basis. Since we need the matrix elements to be in the HO basis for the NCSM calculation, the relative two-body HO basis is an appropriate choice.

To calculate the matrix elements of the LO contribution of the M1 operator, we begin with the A-body M_{10}^{LO} operator

$$\hat{M}_{10}^{\text{LO}} = \sqrt{\frac{3}{4\pi}} \mu_N \sum_{i=1}^A \left[\left\{ g_p \hat{s}_{z,i} + \hat{l}'_{z,i} \right\} \hat{\Pi}_{p,i} + g_n \hat{s}_{z,i} \hat{\Pi}_{n,i} \right], \quad (6.69)$$

where we switched the Pauli matrices into spin operators in comparison with (6.61). In the relative two-body space this leads to

$$\hat{M}_{10}^{\text{LO,2b}} = \sqrt{\frac{3}{4\pi}} \left[\frac{1}{2} (g_p + g_n) \hat{S}_z + \frac{1}{2} \hat{L}'_z + (g_p - g_n) \sum_{i=1}^2 \hat{s}_{z,i} \hat{t}_{3,i} + \frac{1}{2} \hat{L}'_z \hat{T}_3 \right], \quad (6.70)$$

where \hat{S} and \hat{T} are the total spin and total isospin operator of the two-body system. Furthermore, we used that the relative part of the angular momentum operator is given by

$$\hat{L}' = \hat{l}'_1 + \hat{l}'_2 \quad (6.71)$$

and that

$$\hat{l}'_1 = \hat{l}'_2 = \frac{1}{2} \hat{L}' \quad (6.72)$$

holds in a two-body system. Evaluating the $M_{10}^{\text{LO,2b}}$ operator in the relative HO basis leads

to

$$\begin{aligned}
& \langle N(LS)JM, TM_T | M_{10}^{\text{LO},2b} | N'(L'S')J'M', T'M'_T \rangle = \\
& \sqrt{\frac{3}{4\pi}} \mu_N \left[\sum_{M_L, M_S} \{(g_p + g_n)M_S + (1 + M_T)M_L\} \right. \\
& \times \frac{1}{2} \delta_{NN'} \delta_{LL'} \delta_{SS'} \delta_{TT'} \delta_{M_T M'_T} c \left(\begin{array}{cc|c} L & S' & J' \\ M_L & M_S & M \end{array} \right) c \left(\begin{array}{cc|c} L & S & J \\ M_L & M_S & M \end{array} \right) \\
& + (g_p - g_n) \delta_{NN'} \delta_{LL'} \sum_{M'_S} \sum_{M_L, M_S} \sum_{m_{s_1}, m_{s_2}} \sum_{m_{t_1}, m_{t_2}} \\
& \times c \left(\begin{array}{cc|c} L & S' & J' \\ M_L & M_S & M \end{array} \right) c \left(\begin{array}{cc|c} s_1 & s_2 & S' \\ m_{s_1} & m_{s_2} & M_S \end{array} \right) c \left(\begin{array}{cc|c} t_1 & t_2 & T' \\ m_{t_1} & m_{t_2} & M_T \end{array} \right) c \left(\begin{array}{cc|c} L & S & J \\ M_L & M_S & M \end{array} \right) \\
& \times c \left(\begin{array}{cc|c} s_1 & s_2 & S \\ m_{s_1} & m_{s_2} & M_S \end{array} \right) c \left(\begin{array}{cc|c} t_1 & t_2 & T \\ m_{t_1} & m_{t_2} & M_T \end{array} \right) [m_{s_1} m_{t_1} + m_{s_2} m_{t_2}] \Big]. \quad (6.73)
\end{aligned}$$

Here we have decoupled the angular-momentum and spin part to utilize the eigenvalue relations. For the evaluation of the third term in (6.70) we have decoupled the spin and isospin part further into single-particle components. In the end, we are interested in the reduced $M_1^{\text{LO},2b}$ operator, which we obtain by applying the Wigner-Eckart theorem

$$\begin{aligned}
& \langle N(LS)J, TM_T || M_1^{\text{LO},2b} || N'(L'S')J', T'M'_T \rangle = \\
& (-1)^{M-J} \begin{pmatrix} J & 1 & J' \\ -M & 0 & M \end{pmatrix}^{-1} \langle N(LS)JM, TM_T | M_{10}^{\text{LO},2b} | N'(L'S')J'M, T'M'_T \rangle. \quad (6.74)
\end{aligned}$$

A more detailed derivation can be found in [151] and an alternative expression using spherical tensor notation can be found in appendix A.8.

The numerical matrix elements for the Sachs and intrinsic part of the NLO magnetic dipole moment operator used in this thesis were provided by Hernandez [155] in an HO basis. These are obtained by a numerical transformation of the configuration space expressions into the HO basis using the HO eigenfunctions given in equation (A.11). Since the Sachs term (6.65) depends also on the center-of-mass coordinates of the two-body system, we need to extend the basis. Consequently, the operator is given in the coupled form

$$\langle [N_{\text{cm}} L_{\text{cm}}, N(LS)J_{\text{rel}}] J, TM_T || M_1^{\text{NLO},2b} || [N'_{\text{cm}} L'_{\text{cm}}, N'(L'S')J'_{\text{rel}}] J', T'M'_T \rangle \quad (6.75)$$

with the radial and angular momentum quantum numbers of the center-of-mass coordinate N_{cm} and L_{cm} , respectively, as well as for the relative coordinate N and L . The relative angular momentum is coupled with the spin-quantum number S to a relative total angular momentum J_{rel} , which is again coupled with the angular momentum of the center-of-mass coordinate L_{cm} to a total angular momentum of the two-body system J .

On the other hand, the intrinsic contribution does not depend on the center-of-mass coordinate, thus this extension of the basis is not necessary for this contribution. Now, we have the M1 operator in an appropriate basis to perform the consistent SRG transformation, which we describe in the next section.

6.6 | Consistent SRG Transformation

The many-body methods, which we are using, need SRG-evolved interactions as an input in order to obtain converged results. The SRG is described in section 3.2 and for a consistent

result, we need to perform the same SRG transformation on the operators of other observables like the M1 operator

$$\hat{M}_{1,\alpha} = \hat{U}_\alpha^\dagger \hat{M}_{1,\alpha=0} \hat{U}_\alpha. \quad (6.76)$$

In previous work by Mertes [151] it was shown that the consistent SRG treatment of the M1 operator has a small effect of 2% on average, but can reach up to 6% depending on the observable and nucleus. Nevertheless, for precision studies this contribution cannot be neglected.

The unitary operator \hat{U}_α is determined by evaluating equation (3.33) numerically in an HO basis. In a second step, we evaluate equation (6.76). Here we can exploit the symmetries of the unitary operator, which are determined by the choice of the SRG generator $\hat{\eta}_\alpha$. The standard choice of the SRG generator exhibits the same symmetries as the Hamiltonian, hence, the matrix elements of the unitary operator are given as

$$\begin{aligned} & \langle [N_{\text{cm}} L_{\text{cm}}, N(LS) J_{\text{rel}}] J, T M_T | U_\alpha | [N'_{\text{cm}} L'_{\text{cm}}, N'(L'S') J'_{\text{rel}}] J', T' M'_T \rangle \\ & = \delta_{N'_{\text{cm}} N_{\text{cm}}} \delta_{L'_{\text{cm}} L_{\text{cm}}} \delta_{J' J} \delta_{J'_{\text{rel}} J_{\text{rel}}} \delta_{S' S} \delta_{T' T} \delta_{M'_{\text{cm}} M_{\text{cm}}} \langle N(LS) J_{\text{rel}} | U_\alpha | N'(L'S') J_{\text{rel}} \rangle. \end{aligned} \quad (6.77)$$

Therefore, the matrix elements of the SRG-evolved M1 operator can be obtained by

$$\begin{aligned} & \langle [N_{\text{cm}} L_{\text{cm}}, N(LS) J_{\text{rel}}] J, T M_T | M_{1,\alpha} | [N'_{\text{cm}} L'_{\text{cm}}, N'(L'S') J'_{\text{rel}}] J', T' M'_T \rangle \\ & = \sum_{N'', L''} \sum_{N''', L'''} \langle N(LS) J_{\text{rel}} | U_\alpha^\dagger | N''(L''S) J_{\text{rel}} \rangle \\ & \times \langle [N_{\text{cm}} L_{\text{cm}}, N''(L''S) J_{\text{rel}}] J, T M_T | M_{1,\alpha=0} | [N'_{\text{cm}} L'_{\text{cm}}, N''(L'S') J'_{\text{rel}}] J', T' M'_T \rangle \\ & \times \langle N'''(L'''S') J'_{\text{rel}} | U_\alpha | N'(L'S') J'_{\text{rel}} \rangle. \end{aligned} \quad (6.78)$$

The LO and intrinsic part of the NLO M1 operator do not depend on the center-of-mass coordinates, thus, for these operators the number of relevant matrix elements that need to be calculated is reduced and only the relative part is of interest.

Since the initial LO M1 operator is a particle-rank one operator, the evolved operator is a mixture of particle-rank one and two. For the use in an A -body system we need to separate the different contributions. This is achieved by subtracting the initial LO M1 operator from the evolved one. The NLO contribution to the M1 operator is of particle-rank two, thus, this operator does not need to be subtracted.

6.7 | Transformation into Single-Particle Coordinates

The NCSM needs two-body m -scheme matrix elements as an input. Thus, we employ a generalized version of the two-body Talmi-Moshinsky transformation given in [156] for spherical tensor operators. This transformation allows the conversion of matrix elements in a relative basis into the m -scheme. In the first step we sketch the general Talmi-Moshinsky transformation for a single antisymmetrized two-body state, which can also be found in [157, 158], and in a second step we use this result to derive the Talmi-Moshinsky transformation of a generalized spherical tensor operator. The starting point is an antisymmetrized two-body

state

$$\begin{aligned} & | n_1 n_2 [(l_1 s_1) j_1, (l_2 s_2) j_2] JM, (t_1 t_2) TM_T \rangle_a \\ &= \sqrt{2!} \mathcal{A} | n_1 n_2 [(l_1 s_1) j_1, (l_2 s_2) j_2] JM, (t_1 t_2) TM_T \rangle \end{aligned} \quad (6.79)$$

$$= \sqrt{2!} \frac{1}{2} (1 - \mathcal{P}_{12}) | n_1 n_2 [(l_1 s_1) j_1, (l_2 s_2) j_2] JM, (t_1 t_2) TM_T \rangle \quad (6.80)$$

$$\begin{aligned} &= \frac{1}{\sqrt{2}} (| n_1 n_2 [(l_1 s_1) j_1, (l_2 s_2) j_2] JM, (t_1 t_2) TM_T \rangle \\ &\quad - | n_2 n_1 [(l_2 s_2) j_2, (l_1 s_1) j_1] JM, (t_2 t_1) TM_T \rangle) \end{aligned} \quad (6.81)$$

$$\begin{aligned} &= \frac{1}{\sqrt{2}} (| n_1 n_2 [(l_1 s_1) j_1, (l_2 s_2) j_2] JM, (t_1 t_2) TM_T \rangle \\ &\quad - (-1)^{j_1 + j_2 - J + 1 - T} | n_2 n_1 [(l_2 s_2) j_2, (l_1 s_1) j_1] JM, (t_2 t_1) TM_T \rangle) \end{aligned} \quad (6.82)$$

with \mathcal{A} the antisymmetrizer and the permutation operator \mathcal{P}_{12} of particle 1 and 2. Furthermore, we use the symmetries of the Clebsch-Gordan coefficients given in equation (A.13). By recoupling into a (LS) -coupling scheme the first term can be written as

$$\begin{aligned} & | n_1 n_2 [(l_1 s_1) j_1, (l_2 s_2) j_2] JM, TM_T \rangle = \\ & \sum_{\Lambda S} \hat{\Lambda} \hat{S} \hat{j}_1 \hat{j}_2 \begin{Bmatrix} l_1 & l_2 & \Lambda \\ s_1 & s_2 & S \\ j_1 & j_2 & J \end{Bmatrix} | n_1 n_2 [(l_1 l_2) \Lambda, (s_1 s_2) S] JM, TM_T \rangle. \end{aligned} \quad (6.83)$$

Here, we have introduced the shorthand hat notation

$$\hat{x} = \sqrt{2x + 1}. \quad (6.84)$$

In addition, we can use the harmonic oscillator brackets (HOBs), which allow to transform the HO quantum numbers between single and relative coordinates

$$| (n_1 l_1, n_2 l_2) \Lambda M_\Lambda \rangle = \sum_{N_{\text{cm}} L_{\text{cm}}, NL} \langle \langle N_{\text{cm}} L_{\text{cm}}, NL; \Lambda | n_1 l_1, n_2 l_2 \rangle \rangle_1 | (N_{\text{cm}} L_{\text{cm}}, NL) \Lambda M_\Lambda \rangle. \quad (6.85)$$

This leads to

$$\begin{aligned} & | n_1 n_2 [(l_1 s_1) j_1, (l_2 s_2) j_2] JM, TM_T \rangle = \sum_{\Lambda S} \sum_{N_{\text{cm}} L_{\text{cm}}, NL} \hat{\Lambda} \hat{S} \hat{j}_1 \hat{j}_2 \begin{Bmatrix} l_1 & l_2 & \Lambda \\ s_1 & s_2 & S \\ j_1 & j_2 & J \end{Bmatrix} \\ & \langle \langle N_{\text{cm}} L_{\text{cm}}, NL; \Lambda | n_1 l_1, n_2 l_2 \rangle \rangle_1 | N_{\text{cm}} N [(L_{\text{cm}} L) \Lambda, (s_1 s_2) S] JM, TM_T \rangle. \end{aligned} \quad (6.86)$$

In the next step we decouple the center-of-mass part of the angular momentum from the relative one with the help of a 6j-symbol.

$$\begin{aligned} & | n_1 n_2 [(l_1 s_1) j_1, (l_2 s_2) j_2] JM, TM_T \rangle = \\ & \sum_{\Lambda S} \sum_{N_{\text{cm}} L_{\text{cm}}, NL} \sum_{J_{\text{rel}}} (-1)^{L_{\text{cm}} + L + S + J} \hat{\Lambda}^2 \hat{J}_{\text{rel}} \hat{S} \hat{j}_1 \hat{j}_2 \begin{Bmatrix} l_1 & l_2 & \Lambda \\ s_1 & s_2 & S \\ j_1 & j_2 & J \end{Bmatrix} \begin{Bmatrix} L_{\text{cm}} & L & \Lambda \\ S & J & J_{\text{rel}} \end{Bmatrix} \\ & \times \langle \langle N_{\text{cm}} L_{\text{cm}}, NL; \Lambda | n_1 l_1, n_2 l_2 \rangle \rangle_1 | N_{\text{cm}} N [L_{\text{cm}}, \{L (s_1 s_2) S\} J_{\text{rel}}] JM, TM_T \rangle. \end{aligned} \quad (6.87)$$

For the second term in equation (6.82) follows analogously

$$\begin{aligned}
& (-1)^{j_1+j_2-J+1-T} | n_2 n_1 [(l_2 s_2) j_2, (l_1 s_1) j_1] JM, TM_T \rangle \\
&= (-1)^{j_1+j_2-J+1-T} \sum_{\Lambda S} \sum_{N_{\text{cm}} L_{\text{cm}}, NL} \sum_{J_{\text{rel}}} (-1)^{L_{\text{cm}}+L+S+J} \hat{\Lambda}^2 \hat{J}_{\text{rel}} \hat{S} \hat{j}_1 \hat{j}_2 \begin{Bmatrix} l_2 & l_1 & \Lambda \\ s_2 & s_1 & S \\ j_2 & j_1 & J \end{Bmatrix} \\
&\times \left\{ \begin{matrix} L_{\text{cm}} & L & \Lambda \\ S & J & J_{\text{rel}} \end{matrix} \right\} \langle \langle N_{\text{cm}} L_{\text{cm}}, NL; \Lambda | n_2 l_2, n_1 l_1 \rangle \rangle_1 | N_{\text{cm}} N [L_{\text{cm}}, \{L(s_2 s_1) S\} J_{\text{rel}}] JM, TM_T \rangle \\
&\hspace{15em} (6.88)
\end{aligned}$$

$$\begin{aligned}
&= (-1)^{j_1+j_2-J+1-T} \sum_{\Lambda S} \sum_{N_{\text{cm}} L_{\text{cm}}, NL} \sum_{J_{\text{rel}}} (-1)^{L_{\text{cm}}+L+S+J} \hat{\Lambda}^2 \hat{J}_{\text{rel}} \hat{S} \hat{j}_1 \hat{j}_2 \\
&\times (-1)^{l_2+l_1+\Lambda+s_2+s_1+S+j_2+j_1+J} \begin{Bmatrix} l_1 & l_2 & \Lambda \\ s_1 & s_2 & S \\ j_1 & j_2 & J \end{Bmatrix} \left\{ \begin{matrix} L_{\text{cm}} & L & \Lambda \\ S & J & J_{\text{rel}} \end{matrix} \right\} (-1)^{L-\Lambda} \\
&\times \langle \langle N_{\text{cm}} L_{\text{cm}}, NL; \Lambda | n_1 l_1, n_2 l_2 \rangle \rangle_1 | N_{\text{cm}} N [L_{\text{cm}}, \{L(s_2 s_1) S\} J_{\text{rel}}] JM, TM_T \rangle \\
&\hspace{15em} (6.89)
\end{aligned}$$

$$\begin{aligned}
&= \sum_{\Lambda S} \sum_{N_{\text{cm}} L_{\text{cm}}, NL} \sum_{J_{\text{rel}}} (-1)^{T+L+S} (-1)^{L_{\text{cm}}+L+S+J} \hat{\Lambda}^2 \hat{J}_{\text{rel}} \hat{S} \hat{j}_1 \hat{j}_2 \begin{Bmatrix} l_1 & l_2 & \Lambda \\ s_1 & s_2 & S \\ j_1 & j_2 & J \end{Bmatrix} \\
&\times \left\{ \begin{matrix} L_{\text{cm}} & L & \Lambda \\ S & J & J_{\text{rel}} \end{matrix} \right\} \langle \langle N_{\text{cm}} L_{\text{cm}}, NL; \Lambda | n_1 l_1, n_2 l_2 \rangle \rangle_1 | N_{\text{cm}} N [L_{\text{cm}}, \{L(s_2 s_1) S\} J_{\text{rel}}] JM, TM_T \rangle \\
&\hspace{15em} (6.90)
\end{aligned}$$

where we used the symmetry relation (A.21) of the 9j-symbol and relation (A.23) of the HOBs to get the same structure as in equation (6.87). Furthermore, we have used that $s_1 = s_2 = 1/2$ as well as the energy conservation of the HOBs which yields

$$2n_1 + l_1 + 2n_2 + l_2 = 2N_{\text{cm}} + L_{\text{cm}} + 2N + L \quad (6.91)$$

and therefore

$$(-1)^{l_1+l_2} = (-1)^{L_{\text{cm}}+L} \quad (6.92)$$

due to the fact that the radial quantum numbers n_1 , n_2 , N_{cm} , and N are integers. Finally, the two terms (6.87) and (6.90) differ only by the phase factor

$$(-1)^{T+L+S} \quad (6.93)$$

and the ordering of the spins s_1 and s_2 as well as the isospins t_1 and t_2 . Here we can use that the spins and isospins are all equal to $1/2$ such that a switch of $s_1 \leftrightarrow s_2$ and $t_1 \leftrightarrow t_2$ has no effect. This step has to be understood as a renaming and not a recoupling. In the end, we obtain for the antisymmetrized two body state (6.82)

$$\begin{aligned}
& | n_1 n_2 [(l_1 s_1) j_1, (l_2 s_2) j_2] JM, TM_T \rangle_a = \frac{1}{\sqrt{2}} \sum_{\Lambda S} \sum_{N_{\text{cm}} L_{\text{cm}}, NL} \sum_{J_{\text{rel}}} \\
&\times (-1)^{L_{\text{cm}}+L+S+J} (1 - (-1)^{T+L+S}) \hat{\Lambda}^2 \hat{J}_{\text{rel}} \hat{S} \hat{j}_1 \hat{j}_2 \begin{Bmatrix} l_1 & l_2 & \Lambda \\ s_1 & s_2 & S \\ j_1 & j_2 & J \end{Bmatrix} \left\{ \begin{matrix} L_{\text{cm}} & L & \Lambda \\ S & J & J_{\text{rel}} \end{matrix} \right\} \\
&\times \langle \langle N_{\text{cm}} L_{\text{cm}}, NL; \Lambda | n_1 l_1, n_2 l_2 \rangle \rangle_1 | N_{\text{cm}} N [L_{\text{cm}}, (LS) J_{\text{rel}}] JM, TM_T \rangle. \\
&\hspace{15em} (6.94)
\end{aligned}$$

We can conclude that only states with odd $T + L + S$ contribute to the antisymmetric state and other states vanish.

This result for an antisymmetric state can be used to obtain the Talmi-Moshinsky transformation for matrix elements of a spherical tensor operator

$$\begin{aligned}
& {}_a \langle n_1 n_2 [(l_1 s_1) j_1, (l_2 s_2) j_2] JM, TM_T | O_q^k | n'_1 n'_2 [(l'_1 s'_1) j'_1, (l'_2 s'_2) j'_2] J' M', T' M'_T \rangle_a = \\
& = \frac{1}{2} \sum_{\Lambda' S'} \sum_{N'_{\text{cm}} L'_{\text{cm}}, N' L'} \sum_{J'_{\text{rel}}} \sum_{\Lambda S} \sum_{N_{\text{cm}} L_{\text{cm}}, NL} \sum_{J_{\text{rel}}} \hat{j}'_1 \hat{j}'_2 \hat{\Lambda}'^2 \hat{J}'_{\text{rel}} \hat{S}' \hat{j}_1 \hat{j}_2 \hat{\Lambda}^2 \hat{J}_{\text{rel}} \hat{S} \\
& \times \left(1 - (-1)^{T'+L'+S'}\right) \left(1 - (-1)^{T+L+S}\right) \\
& \times (-1)^{L'_{\text{cm}}+L'+S'+J'} \begin{Bmatrix} l'_1 & l'_2 & \Lambda' \\ s'_1 & s'_2 & S' \\ j'_1 & j'_2 & J' \end{Bmatrix} \begin{Bmatrix} L'_{\text{cm}} & L' & \Lambda' \\ S' & J' & J'_{\text{rel}} \end{Bmatrix} \langle \langle N'_{\text{cm}} L'_{\text{cm}}, N' L'; \Lambda' | n'_1 l'_1, n'_2 l'_2 \rangle \rangle_1 \\
& \times (-1)^{L_{\text{cm}}+L+S+J} \begin{Bmatrix} l_1 & l_2 & \Lambda \\ s_1 & s_2 & S \\ j_1 & j_2 & J \end{Bmatrix} \begin{Bmatrix} L_{\text{cm}} & L & \Lambda \\ S & J & J_{\text{rel}} \end{Bmatrix} \langle \langle N_{\text{cm}} L_{\text{cm}}, NL; \Lambda | n_1 l_1, n_2 l_2 \rangle \rangle_1 \\
& \times \langle N_{\text{cm}} N [L_{\text{cm}}, (LS) J_{\text{rel}}] JM, TM_T | O_q^k | N'_{\text{cm}} N' [L'_{\text{cm}}, (L'S') J'_{\text{rel}}] J' M', T' M'_T \rangle. \quad (6.95)
\end{aligned}$$

Now, the Wigner-Eckart theorem allows us to bring this transformation into the reduced form

$$\begin{aligned}
& {}_a \langle n_1 n_2 [(l_1 s_1) j_1, (l_2 s_2) j_2] J, TM_T || O^k || n'_1 n'_2 [(l'_1 s'_1) j'_1, (l'_2 s'_2) j'_2] J', T' M'_T \rangle_a = \\
& = \frac{1}{2} \sum_{\Lambda' S'} \sum_{N'_{\text{cm}} L'_{\text{cm}}, N' L'} \sum_{J'_{\text{rel}}} \sum_{\Lambda S} \sum_{N_{\text{cm}} L_{\text{cm}}, NL} \sum_{J_{\text{rel}}} \hat{j}'_1 \hat{j}'_2 \hat{\Lambda}'^2 \hat{J}'_{\text{rel}} \hat{S}' \hat{j}_1 \hat{j}_2 \hat{\Lambda}^2 \hat{J}_{\text{rel}} \hat{S} \\
& \times \left(1 - (-1)^{T'+L'+S'}\right) \left(1 - (-1)^{T+L+S}\right) \\
& \times (-1)^{L'_{\text{cm}}+L'+S'+J'} \begin{Bmatrix} l'_1 & l'_2 & \Lambda' \\ s'_1 & s'_2 & S' \\ j'_1 & j'_2 & J' \end{Bmatrix} \begin{Bmatrix} L'_{\text{cm}} & L' & \Lambda' \\ S' & J' & J'_{\text{rel}} \end{Bmatrix} \langle \langle N'_{\text{cm}} L'_{\text{cm}}, N' L'; \Lambda' | n'_1 l'_1, n'_2 l'_2 \rangle \rangle_1 \\
& \times (-1)^{L_{\text{cm}}+L+S+J} \begin{Bmatrix} l_1 & l_2 & \Lambda \\ s_1 & s_2 & S \\ j_1 & j_2 & J \end{Bmatrix} \begin{Bmatrix} L_{\text{cm}} & L & \Lambda \\ S & J & J_{\text{rel}} \end{Bmatrix} \langle \langle N_{\text{cm}} L_{\text{cm}}, NL; \Lambda | n_1 l_1, n_2 l_2 \rangle \rangle_1 \\
& \times \langle N_{\text{cm}} N [L_{\text{cm}}, (LS) J_{\text{rel}}] J, TM_T || O^k || N'_{\text{cm}} N' [L'_{\text{cm}}, (L'S') J'_{\text{rel}}] J', T' M'_T \rangle. \quad (6.96)
\end{aligned}$$

Since we have applied the Wigner-Eckart theorem on both sides, the additional factor consisting of a phase and a Clebsch-Gordan coefficient vanishes. Nevertheless, the applicability of the Wigner-Eckart theorem reduces the amount of matrix elements that needs to be calculated to those that fulfill the triangular condition

$$|J' - k| \leq J \leq J' + k. \quad (6.97)$$

Furthermore, the sums can be limited by the energy conservation of the HOBs

$$\delta(2N'_{\text{cm}}+L'_{\text{cm}}+2N'+L')(2n'_1+l'_1+2n'_2+l'_2) \delta(2N_{\text{cm}}+L_{\text{cm}}+2N+L)(2n_1+l_1+2n_2+l_2) \quad (6.98)$$

as well as by constraining for example the spin quantum numbers S and S' via the antisymmetry condition (6.93).

If the spherical tensor operator does not depend on a center-of-mass contribution like the LO M1 operator or the intrinsic part of the NLO, equation (6.96) can be simplified further.

We can apply relation (40) of section 13.1.5 from [159] in combination with the Wigner-Eckart theorem, see also appendix A.7 and obtain

$$\begin{aligned}
& {}_a \langle n_1 n_2 [(l_1 s_1) j_1, (l_2 s_2) j_2] J, T M_T \parallel O^k \parallel n'_1 n'_2 [(l'_1 s'_1) j'_1, (l'_2 s'_2) j'_2] J', T' M'_T \rangle_a = \\
& = \frac{1}{2} \sum_{\Lambda' S'} \sum_{N'_{\text{cm}} L'_{\text{cm}}, N' L'} \sum_{J'_{\text{rel}}} \sum_{\Lambda S} \sum_{N_{\text{cm}} L_{\text{cm}}, N L} \sum_{J_{\text{rel}}} \hat{j}'_1 \hat{j}'_2 \hat{\Lambda}'^2 \hat{J}'_{\text{rel}} \hat{S}' \hat{j}_1 \hat{j}_2 \hat{\Lambda}^2 \hat{J}_{\text{rel}} \hat{S} \\
& \times \left(1 - (-1)^{T'+L'+S'}\right) \left(1 - (-1)^{T+L+S}\right) \\
& \times (-1)^{L'_{\text{cm}}+L'+S'+J'} \begin{Bmatrix} l'_1 & l'_2 & \Lambda' \\ s'_1 & s'_2 & S' \\ j'_1 & j'_2 & J' \end{Bmatrix} \begin{Bmatrix} L'_{\text{cm}} & L' & \Lambda' \\ S' & J' & J'_{\text{rel}} \end{Bmatrix} \langle \langle N'_{\text{cm}} L'_{\text{cm}}, N' L'; \Lambda' | n'_1 l'_1, n'_2 l'_2 \rangle \rangle_1 \\
& \times (-1)^{L_{\text{cm}}+L+S+J} \begin{Bmatrix} l_1 & l_2 & \Lambda \\ s_1 & s_2 & S \\ j_1 & j_2 & J \end{Bmatrix} \begin{Bmatrix} L_{\text{cm}} & L & \Lambda \\ S & J & J_{\text{rel}} \end{Bmatrix} \langle \langle N_{\text{cm}} L_{\text{cm}}, N L; \Lambda | n_1 l_1, n_2 l_2 \rangle \rangle_1 \\
& \times \delta_{L'_{\text{cm}} L_{\text{cm}}} \delta_{N'_{\text{cm}} N_{\text{cm}}} (-1)^{J'+J_{\text{rel}}+L'_{\text{cm}}-k} \begin{Bmatrix} J'_{\text{rel}} & L'_{\text{cm}} & J' \\ J & k & J_{\text{rel}} \end{Bmatrix} \\
& \times \langle N (L S) J_{\text{rel}}, T M_T \parallel O^k \parallel N' (L' S') J'_{\text{rel}}, T' M'_T \rangle. \tag{6.99}
\end{aligned}$$

Now, we have the M1 operator in a basis that can be used as input into the NCSM calculation.

6.8 | ⁶Li Results

We use ⁶Li to study the role of the current contributions of the M1 operator, since it is the lightest non-strange hadronic system with a dominant internal electromagnetic decay from its first excited 0⁺ state to the 1⁺ ground-state. This makes the transition strength accessible in precision studies in theory as well as in experiment. In addition to the transition strength, we also probe the magnetic dipole moment $\mu(1^+)$ of the ground state and compare the different contributions of the various M1 terms.

Before we explore the impact of different contributions of the M1 operator and interactions, we start by testing the dependence of the results on the truncations. Also we explain the determination of the magnetic dipole moment $\mu(1^+)$ of the ground state and the magnetic dipole transition strength $B(M1, 0^+ \rightarrow 1^+)$ from the first 0⁺ to the ground state of ⁶Li in an IT-NCSM calculation.

First, we probe the dependence of the IT-NCSM calculation on the $E_{\text{max}, M1}$ truncation, which is the maximum two-body energy $E_{\text{max}, M1} = 2N_{\text{cm}} + L_{\text{cm}} + 2N + L$ of the Sachs term of the NLO M1 operator. We introduced this truncation, since the Sachs term depends not only on the relative but also on the center-of-mass coordinates, which significantly increases the number of matrix elements. This truncation becomes relevant in equation (6.78), where we calculate the SRG transformation of the M1 operator. Since the SRG transformation connects states of low- and high-energies, we are sensitive to energy quantum numbers of the bare M1 operator larger than the N_{max} truncation of the NCSM calculation. For the M1 operator terms that only depend on the relative coordinate, we use $E_{\text{max}} = 150$, which is sufficiently large. In figure 6.2 we show the results of the $\mu(1^+)$ and the $B(M1, 0^+ \rightarrow 1^+)$ value for the MBO interaction at N²LO with $\Lambda = 500$ MeV of an IT-NCSM calculation with $\hbar\Omega = 20$ MeV. We see the strongest impact of the $E_{\text{max}, M1}$ truncation on the $B(M1, 0^+ \rightarrow 1^+)$ value already at $N_{\text{max}} = 2$, which increases up to an $E_{\text{max}, M1} = 16$. From $E_{\text{max}, M1} = 24$ upwards the results lie practically on top of each other. With increasing N_{max} the results are only shifted

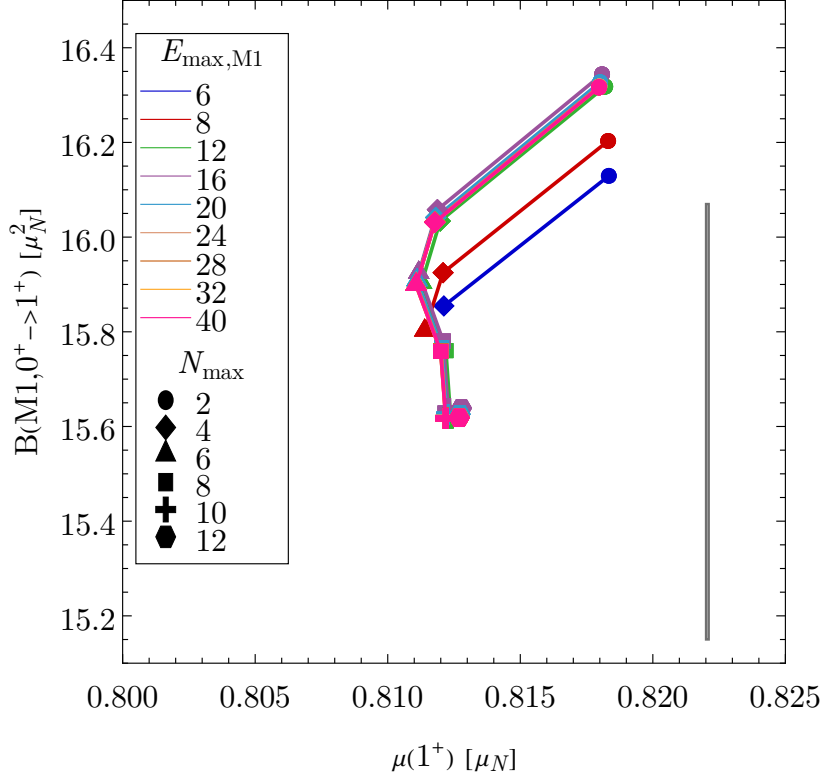


Figure 6.2: Convergence of the IT-NCSM calculation of ${}^6\text{Li}$ with respect to $E_{\text{max},\text{M1}}$. In the calculation we use $\hbar\Omega = 20$ MeV and the last two N_{max} results are IT-extrapolated. Shown are the results for the MBO N^2LO interaction with cutoff $\Lambda = 500$ MeV. Furthermore, the full NLO M1 operator is employed. The gray box indicates the experimental $\mu(1^+)$ [133] and $B(M1, 0^+ \rightarrow 1^+)$ [160] values. The experimental uncertainties of $\mu(1^+)$ are scaled with a factor of 100 to make them visible on this scale.

parallelly. The effect of the $E_{\text{max},\text{M1}}$ truncation on the $\mu(1^+)$ is very small, this is also related to the observation that the $\mu(1^+)$ changes only slightly with the inclusion of the Sachs term, which we discuss later. In the following we use $E_{\text{max},\text{M1}} = 40$, which is sufficient for these observables.

Next, we discuss the truncations of the IT-NCSM, in particular the dependencies on the κ_{min} and N_{max} truncation, and how we define the resulting values and corresponding uncertainties. We exemplarily show the $N_{\text{max}} = 12$ IT-extrapolation of the dipole moment and the transition strength for the MBO interaction at N^3LO with $\Lambda = 500$ MeV in figure 6.3. While the dipole moment of the ground state only shows a small dependence on κ_{min} , the transition strength decreases for $\kappa_{\text{min}} \rightarrow 0$. In case of energies we benefit from the monotonous decrease with the κ_{min} -sequence. This is not the case for these M1 observables, which can fluctuate along the κ_{min} -sequence. These fluctuations are on a small scale, but they make polynomial extrapolations very sensitive on the chosen κ_{min} -sequence, especially the results for the smallest κ_{min} -values can decide if the extrapolations bend upwards or downwards. This can be seen in figure 6.3, where we show polynomial extrapolations with different degrees for different endpoints of the κ_{min} -sequence. Thus, the most reliable result is given by using a linear extrapolation towards $\kappa_{\text{min}} \rightarrow 0$. As stated above, the general trend of the κ_{min} -sequences is different for the dipole moment and the transition strength. Therefore, we use different uncertainty estimates for both observables. Since the slope of the κ_{min} -sequence results for the dipole moment is not steep and the extrapolated results are within

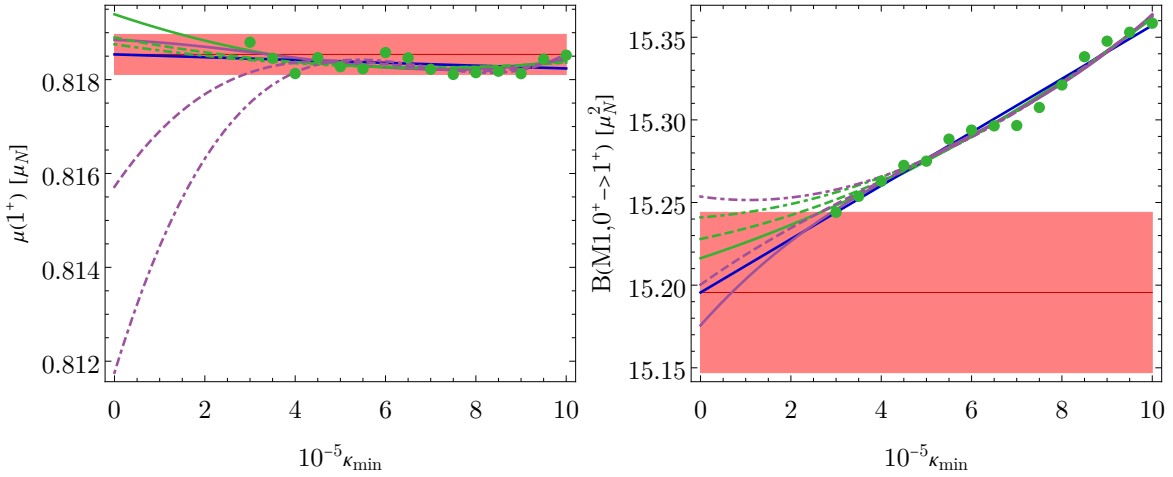


Figure 6.3: Importance truncation extrapolation within the IT-NCSM calculation at $N_{\max} = 12$ for the $\mu(1^+)$ (left) and $B(M1, 0^+ \rightarrow 1^+)$ (right) of ${}^6\text{Li}$ calculated with the MBO $N^3\text{LO}$ interaction with $\Lambda = 500$ MeV. Shown are different polynomial extrapolations: linear (blue line), quadratic (green lines), cubic (violet lines). While we use all data points in the fit of the solid lines, in the fit of the dashed lines we neglect the data points at smallest κ_{\min} , and for the dot-dashed lines the data points for the two smallest κ_{\min} -values. The red lines indicate the extracted values and the band denotes the corresponding IT-uncertainties as explained in the text.

the range of the κ_{\min} -sequence, we define the maximum difference between the extrapolated value and the results of the κ_{\min} -sequence as the uncertainty of the IT-extrapolation. The slope for the transition strength is steeper and decreasing, thus, we are using the difference between the extrapolated value and the result for the smallest κ_{\min} -value as an estimate for the uncertainty.

With these definitions of the IT-extrapolated values and corresponding uncertainties, we explore the N_{\max} -sequence for three HO frequencies $\hbar\Omega = 16, 20,$ and 24 MeV for the $N^3\text{LO}$ MBO interaction with $\Lambda = 500$ MeV. These are shown in figure 6.4 in a combined plot of the dipole moment and the transition strength. Since the gaps between the results of $N_{\max} = 8$ and the first IT-extrapolated results at $N_{\max} = 10$ are particularly large and between $N_{\max} = 10$ and 12 particularly small, we show in addition to the N_{\max} -sequences also the κ_{\min} -sequences for the last two N_{\max} -values 10 and 12 to stress the validity of the extrapolations within the given uncertainties. The dipole moment can be constrained from above and below, since it converges for $\hbar\Omega = 24$ MeV from below and for $\hbar\Omega = 16$ MeV from above. At the same time, the transition strength converges only from above for the considered HO frequencies.

In the following, we define the results of the IT-NCSM calculation as the obtained value from the central HO frequency $\hbar\Omega = 20$ MeV for the largest $N_{\max} = 12$. The many-body uncertainties are defined as the maximum difference of this result to the values of the neighboring frequencies $\hbar\Omega = 16$ and 24 MeV at $N_{\max} = 12$ including IT-uncertainties. This result with uncertainty is indicated as the red box in figure 6.4.

In figure 6.5 we explore the impact of the consistent SRG evolution of the M1 operator and the NLO M1 operator contribution as well as the dependence on different interactions.

The choice of the M1 operator has the largest impact on the result. Using the bare LO M1 operator leads to the largest dipole moments and in comparison with the experiment to slightly too small transition strengths. With a consistent treatment of the LO M1 operator

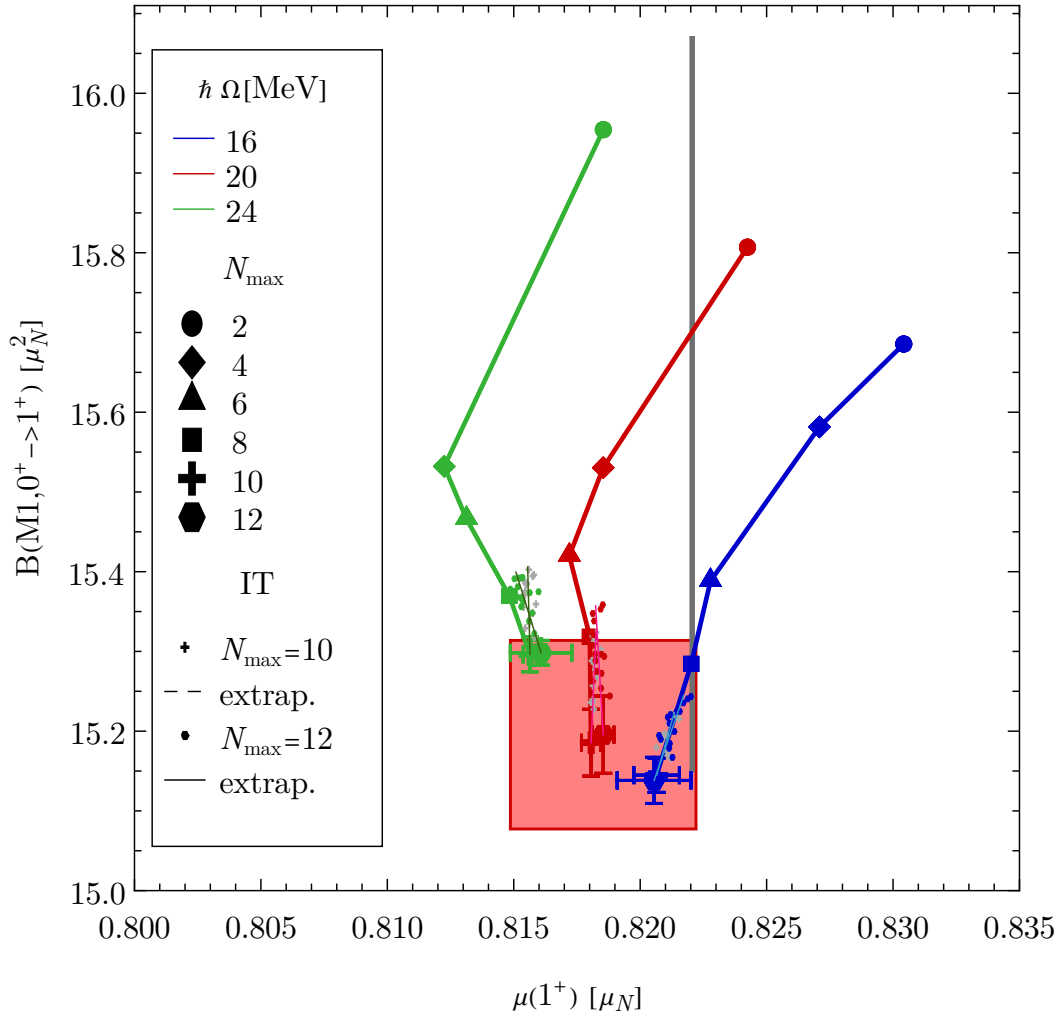


Figure 6.4: Model-space variation in an IT-NCSM calculation for the $\mu(1^+)$ and $B(M1, 0^+ \rightarrow 1^+)$ of ${}^6\text{Li}$ calculated with the MBO N^3LO interaction with $\Lambda = 500$ MeV. The red box indicates the extracted values with many-body uncertainties. The gray box indicates the experimental $\mu(1^+)$ [133] and $B(M1, 0^+ \rightarrow 1^+)$ [160] values. The experimental uncertainties of $\mu(1^+)$ are scaled with a factor of 100 to make them visible on this scale.

due to SRG the dipole moment becomes approximately 2% smaller and improves the result with respect to the experiment. At the same time the transition strength is approximately 4% reduced and is dependent on the interaction approximately 7-10% too small in comparison with the experiment.

The inclusion of the NLO two-body current contribution to the M1 operator increases the transition strength, such that the transition strength improves and is in accordance with the experiment within uncertainties. The dipole moment on the other hand is only slightly enhanced. The small influence on the dipole moment can be understood, since the ground state of ${}^6\text{Li}$ is approximately a ${}^4\text{He}$ core with a deuteron halo. The ${}^4\text{He}$ core has a $J = 0$ state and, therefore, a vanishing magnetic dipole moment. Hence, the magnetic dipole moment is mainly given by the deuteron cluster. This can be seen since the free deuteron has a similar magnetic dipole moment of $\mu = 0.8574 \mu_N$ [161]. The deuteron has a $T = 0$ state and thus the NLO two-body contribution to the M1 operator does not contribute, since the NLO contribution is an isovector operator and the deuteron is in an isoscalar state.

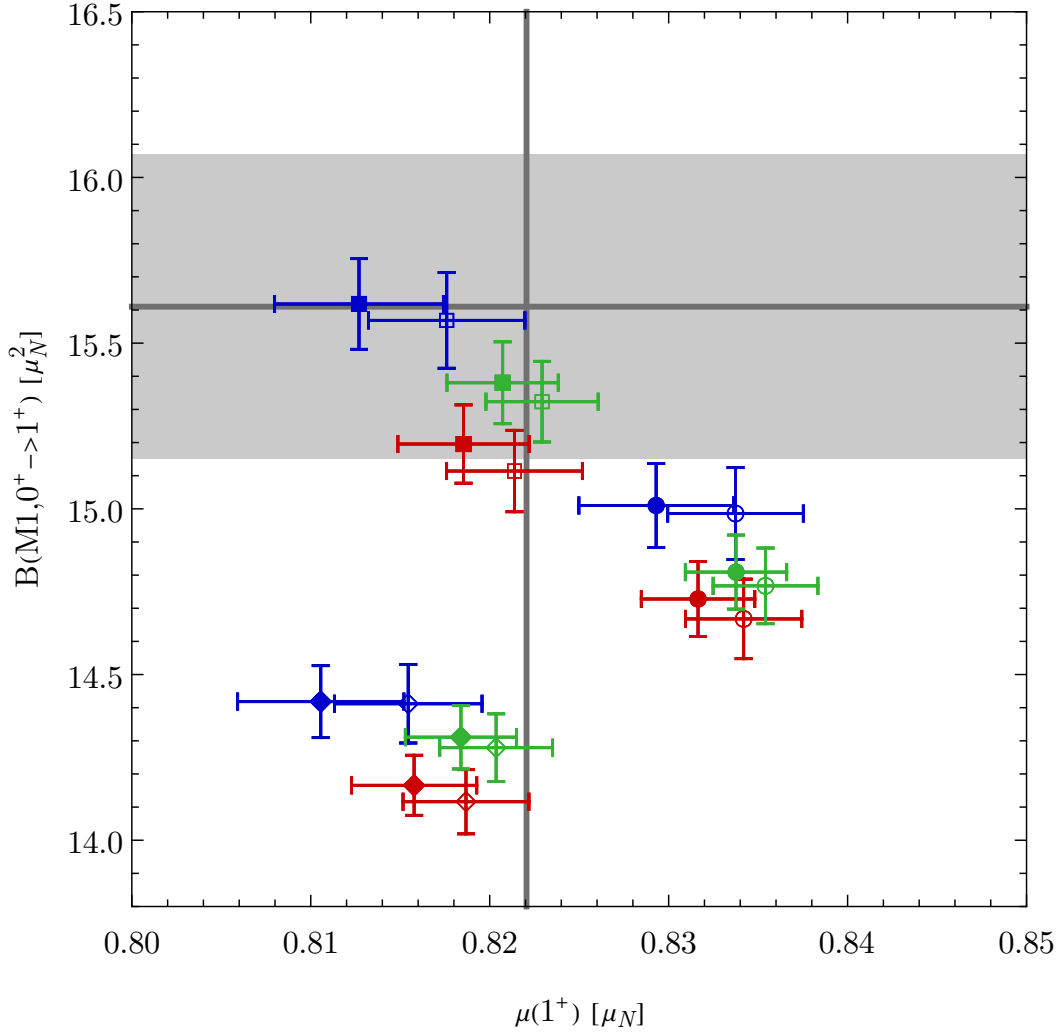


Figure 6.5: Results of the $\mu(1^+)$ and $B(M1, 0^+ \rightarrow 1^+)$ of ${}^6\text{Li}$ for different chiral orders N^2LO (blue), N^3LO (red), and $\text{N}^4\text{LO}'$ (green) of the MBO (solid symbols) and FBO (open symbols) interactions, both with $\Lambda = 500$ MeV. The different symbol shapes indicate the applied M1 operator: bare LO M1 (\bullet), SRG evolved LO M1 (\blacklozenge), and SRG evolved NLO M1 (\blacksquare). The experimental values are indicated with gray bands and the central value with a gray line. The experimental uncertainties of the dipole moment are not visible at this scale.

The different results with respect to the interactions are close to each other and differ up to 1% for the dipole moment and up to 3% for the transition strength. Thus, both the consistent SRG-evolution of the M1 operator and the NLO contribution to the M1 operator have a larger impact on the result than the choice of the interaction. Nevertheless, we can find small trends using different interactions. While the FBO interactions lead to a slightly larger dipole moment, the MBO interactions lead to a slightly larger transition strength, but the differences in the results arising from the different 3N interaction constraints are within many-body uncertainties. Furthermore, the results converge smoothly with increasing chiral order of the interactions. The dipole moment increases slightly and the transition strength has an alternating convergence pattern with increasing chiral order. In addition, the best calculations, interactions at $\text{N}^4\text{LO}'$ and NLO M1 operator, lead also to the result closest to the experiment. We note that even though both, the interactions and the currents, are

based on chiral EFT our calculation is not fully consistent, since we do not use interactions and currents at the same order. Therefore, a consistent uncertainty quantification via an order-by-order analysis is not appropriate.

We can compare our results with quantum Monte Carlo calculations [51] using the Argonne v_{18} NN [1] and Illinois-2 3N [4] potentials. Instead of only M1 current contributions up to NLO they even include contributions up to N^3LO . In these calculations the transition strength is increased from $B(M1_{\text{LO}}, 0^+ \rightarrow 1^+) = 13.18(7) \mu_N^2$ to $16.08(8) \mu_N^2$ [51]. Thus, their calculated current contribution to the transition strength is three times as large as our calculated contribution. The magnetic moment increased by $0.02 \mu_N$, where only N^2LO and N^3LO contribute. This effect is of the same size as the SRG correction in our calculation. Thus, we can expect that higher chiral-order contributions also are of the same size as the considered ones.

We also reported in [160] about these findings using a previous version of the FBO interactions. In these interactions the $c_{\text{D-CF}}$ correlation of the 3N interactions is constrained by the triton binding energy and the c_{D} is chosen to fit the ${}^4\text{He}$ ground-state energy and radius best. These results are shown in figure 6.6 and are within uncertainties of the FBO interactions and reveal the same systematic. In addition, we have used the EM NN interaction complemented with a local 3N interaction with $c_{\text{D}} = 0.8$, compare section 4.1. The results of this interaction follow the same pattern.

We can summarize that in this first fully chiral study, both a consistent treatment of the M1 operator with respect to SRG and the inclusion of the NLO two-body current contribution are found to have relevant effects. Therefore, they are necessary in precision calculations to bring theory and experiment in agreement.

We note that in this study not all inconsistencies could be addressed. In a more extensive study one should include higher-order contributions such that the interactions and currents are consistent at a given chiral order. Furthermore, the regularization of the currents should also be consistently chosen with the interactions.

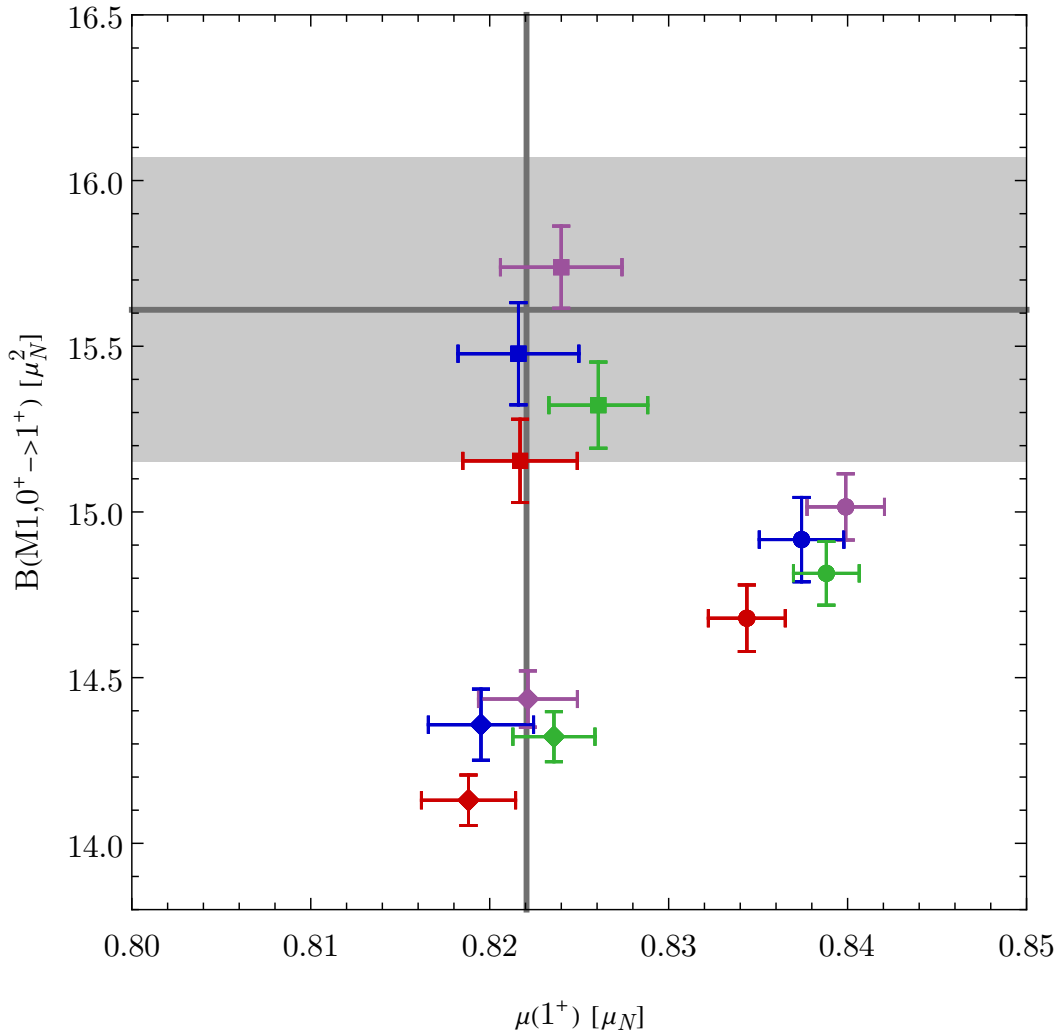


Figure 6.6: Results of the $\mu(1^+)$ and $B(M1, 0^+ \rightarrow 1^+)$ of ${}^6\text{Li}$ as reported in reference [160]. Shown are the results of the different chiral orders N²LO (blue), N³LO (red), and N⁴LO (green) of the interactions with $\Lambda = 500$ MeV of an earlier version of the FBO interactions as described in the text with $\Lambda = 500$ MeV. In addition, the results of the EM NN interaction complemented with a local 3N at N²LO with $\Lambda = 500$ MeV and $c_D = 0.8$ are shown in violet. The different symbol shapes indicate the applied M1 operator: bare LO M1 (●), SRG evolved LO M1 (◆), and SRG evolved NLO M1 (■). The experimental values are indicated with gray bands and the central value with a gray line. The experimental uncertainties of the dipole moment are not visible at this scale.

7 | Conclusion

In this thesis, we benefitted from the current advances in both chiral EFT and many-body approaches. State-of-the-art many-body methods, like the NCSM and the IM-SRG, in combination with SRG evolved interactions enable us to solve the stationary Schrödinger equation for a vast range of light- and medium-mass nuclei. In the past, chiral interactions came only at a specific order, which does not allow for an uncertainty quantification via a systematic order-by-order analysis. With the new EMN, SCS and SMS NN interaction families, we are now capable to estimate the uncertainties arising from the NN interaction via a systematic order-by-order analysis. For an accurate description of many-body observables also 3N interactions are essential.

In an initial assessment of the regulator form for the 3N interaction in combination with the EM NN interaction, we found that the regulator choice of the 3N interaction has a strong effect on many-body observables, especially the radii. A local regulator leads to strong underbinding and too small radii, especially in medium-mass nuclei. With a non-local regulator the description of radii is tremendously improved.

In this thesis we constructed families of chiral NN plus 3N interactions based on the EMN NN interactions. At N²LO and N³LO the 3N interactions were constructed with consistent chiral order, non-local regulator, and cutoff values. We studied the dependence of light- and medium-mass nuclei on the 3N interaction LECs, c_D and c_E . We found a discrepancy between the LECs needed for an optimal description of light- and medium-mass nuclei as well as for nuclear matter. Based on these findings we introduced two optimization schemes of these parameters and defined correspondingly two interaction families, FBO and MBO. The FBO interactions optimize the ground-state energies of ³H and ⁴He, while the MBO interactions optimize the ground-state energies of ³H and ¹⁶O. A global optimization of medium-mass nuclei confirmed that fitting the ground-state energy of ¹⁶O also leads to a good description of other closed shell medium-mass nuclei. In the medium-mass nuclei, an accurate description of ground-state energies and radii up to the Ni isotopes is possible. In the few-body sector, bare MBO interactions lead to an overbound ⁴He ground-state. For medium-mass nuclei we use SRG evolved interactions and for ⁴He the induced 4N interactions of the SRG evolution are not negligible. The SRG can reconcile the ground-state energy of ⁴He with the experiment, thus, the SRG can also be used as a tool to optimize the interaction.

We studied the performance of both interaction families for ground-state energies and radii of light- and medium-mass nuclei as well as for the spectra of p-shell nuclei. In these calculations, we estimated the uncertainties for both the many-body approach and the interaction. The uncertainties due to the chiral truncation were estimated with a state-of-the-art approach rooted in Bayesian statistics. Both interaction families converge smoothly with increasing chiral order and the uncertainty bands of higher orders lie within the bands of lower orders. This exploration indicated that the FBO interactions lead to a systematic underestimation of binding energies of light- and medium-mass nuclei ground-states. In contrast, the MBO interactions describe the experimental ground-state energies within uncertainty bands. The corresponding radii are not as sensitive to the optimization procedure and lead to similarly good results, which agree with the experiment. With few exceptions the spectra of both interaction families are in good agreement with experiment. In the medium-mass regime we performed also a cutoff variation, which revealed only a small cutoff dependence

with overlapping uncertainty bands.

With, in particular, the MBO interactions, we have now a chiral NN plus 3N interaction family, which can be used in *ab initio* nuclear structure calculations with fully quantified uncertainties. This interaction family describes many different nuclear observables with an accuracy that is superior to previous interactions. We still have challenges left, for example to reconcile the simultaneously good description of many-body observables with the description of nuclear matter. Further studies need to be conducted to find the limitations of this interaction family.

But for reliable predictions it is favorable not to be restricted to a single interaction family with a specific regularization procedure. In this thesis, we also studied the SMS NN interactions in ^{16}O , which revealed that these interactions lead to too small radii. Furthermore, the ground-state energy and radius correlate linearly for all versions of this interaction. Modifications of the SMS NN interactions as well as consistent 3N interactions at N^2LO could not improve the description. The modification of the regularization of individual 3N terms revealed that in particular the TPE term is very sensitive to the regularization choice. It has become evident that the regularization procedure, in particular, local and non-local regularization of the 3N interaction, has a strong influence on many-body observables. At this point in time, we cannot explain the mechanism behind these differences. A possibility is a different chiral convergence, such that in the SMS regularization scheme the radii of medium-mass nuclei are enhanced at a higher chiral order. Furthermore, neglected current contributions to the charge-radius operator can have a sizeable effect. Both consistent 3N interactions at N^3LO and current contributions are currently under development within LENPIC.

For accurate and precision studies of electromagnetic observables like multipole moments and transition strengths, we need in addition to an accurate interaction also consistent exchange currents. In this work, we developed the necessary framework to include exchange-current contributions to the $M1$ operator in IT-NCSM calculations. This comprised the correct treatment in the SRG as well as the transformation into a suitable single-particle basis representation. This led to the first fully chiral determination of the magnetic dipole moment of the ground state of ^6Li as well as the magnetic dipole transition strength from the first 0^+ to the 1^+ ground state of ^6Li including the NLO current contribution to the $M1$ operator. This study showed that both the consistent treatment in the SRG and the exchange-current contribution to the $M1$ operator are important to match theory and experiment. The next steps are to incorporate higher orders of the exchange currents and match the regularization between the currents and the interactions. The higher orders are needed for a systematic uncertainty quantification.

In conclusion, in this work we improved the precision of *ab initio* nuclear structure calculations by providing a chiral NN plus 3N interaction family with an accurate description of a broad range of nuclei and developed a framework to incorporate exchange current contributions to the $M1$ operator in IT-NCSM calculations.

A | Appendix

A.1 | Isospin and Projection Operators

We define the proton projection operator as

$$\hat{\Pi}_{p,i} = \frac{1}{2} + \hat{t}_{3,i} = \frac{1 + \hat{\tau}_{3,i}}{2} \quad (\text{A.1})$$

and the neutron projection operator as

$$\hat{\Pi}_{n,i} = \frac{1}{2} - \hat{t}_{3,i} = \frac{1 - \hat{\tau}_{3,i}}{2}, \quad (\text{A.2})$$

with $t_3 = \frac{1}{2}$ for the proton and $t_3 = -\frac{1}{2}$ for the neutron. The reduced isospin operator is defined as

$$\hat{\tau} = 2\hat{t}. \quad (\text{A.3})$$

A.2 | Jacobi Coordinates

Dealing with many particles makes the use of suitable coordinate systems necessary. Instead of using single-particle coordinates, the Jacobi coordinates are an established coordinate system. These coordinates are a generalization of the two-body relative and center-of-mass coordinates for multiple particles. There is no unique way to define Jacobi coordinates. We are using the following definition of the spatial Jacobi coordinates for an A particle system with equal mass:

$$\vec{\xi}_0 = \sqrt{\frac{1}{A}} [\vec{r}_1 + \vec{r}_2 + \cdots + \vec{r}_A], \quad (\text{A.4})$$

$$\vec{\xi}_n = \sqrt{\frac{n}{n+1}} \left[\frac{1}{n} (\vec{r}_1 + \vec{r}_2 + \cdots + \vec{r}_n) - \vec{r}_{n+1} \right]. \quad (\text{A.5})$$

Here \vec{r}_i is the single-particle coordinate of the i -th particle and the $\vec{\xi}_0$ coordinate is proportional to the center-of-mass coordinate. The following coordinates $\vec{\xi}_i$ are constructed successively as relative position between the center-of-mass of the first i particle cluster and the $(i+1)$ th particle.

In an analogous way, we can define the momentum Jacobi coordinates

$$\vec{\pi}_0 = \sqrt{\frac{1}{A}} [\vec{p}_1 + \vec{p}_2 + \cdots + \vec{p}_A], \quad (\text{A.6})$$

$$\vec{\pi}_n = \sqrt{\frac{n}{n+1}} \left[\frac{1}{n} (\vec{p}_1 + \vec{p}_2 + \cdots + \vec{p}_n) - \vec{p}_{n+1} \right]. \quad (\text{A.7})$$

A.3 | Harmonic Oscillator Basis

The harmonic oscillator (HO) is an important system in quantum mechanics. It has notable properties, which make it widely used as a basis. For example, it can be solved analytically and in a many-body system, we can separate the intrinsic and center-of-mass part exactly. The Hamiltonian of the HO is given by

$$\hat{H} = \frac{\hat{p}^2}{2m} + \frac{m\omega^2 \hat{x}^2}{2} = \frac{\hbar\omega}{2} \left(a^2 \hat{k}^2 + \frac{\hat{x}^2}{a^2} \right). \quad (\text{A.8})$$

Here, $\hat{p} = \hbar \hat{k}$ is the momentum operator and \hat{k} the corresponding wave vector. The position operator is \hat{x} , while the mass of the particle is given by m . The HO is characterized by the HO frequency ω or the HO length $a = \sqrt{\frac{\hbar}{m\omega}}$. In momentum space, the eigenfunction is given by

$$\psi_{nlm_l}(\vec{k}) = \langle \vec{k} | nlm_l \rangle = R_{nl}(k) Y_{lm_l}(\theta, \phi), \quad (\text{A.9})$$

with the spherical harmonics $Y_{lm_l}(\theta, \phi)$ and

$$R_{nl}(k) = \sqrt{\frac{2(n!)a^3}{\Gamma(n+l+\frac{3}{2})}} (ka)^l e^{-\frac{1}{2}(ka)^2} L_n^{l+\frac{1}{2}}(ka)^2, \quad (\text{A.10})$$

where $L_n^\alpha(x)$ are the generalized Laguerre polynomials, n is the radial quantum number and l the angular momentum quantum number. The eigenfunctions in configuration space are similar

$$\psi_{nlm_l}(\vec{r}) = \langle \vec{r} | nlm_l \rangle = R_{nl}(r) Y_{lm_l}(\theta, \phi), \quad (\text{A.11})$$

with

$$R_{nl}(r) = \sqrt{\frac{2(n!)a^3}{\Gamma(n+l+\frac{3}{2})}} \left(\frac{r}{a}\right)^l e^{-\frac{1}{2}\left(\frac{r}{a}\right)^2} L_n^{l+\frac{1}{2}}\left(\frac{r}{a}\right)^2. \quad (\text{A.12})$$

A.4 | Clebsch Gordan, 3J, 6J and 9J

An important symmetry of Clebsch-Gordan coefficients, which we utilize in this work, is (see e.g. equation (10) of Varshalovich [159] page 245)

$$c \left(\begin{array}{cc|c} j_1 & j_2 & J \\ m_1 & m_2 & M \end{array} \right) = (-1)^{j_1+j_2-J} c \left(\begin{array}{cc|c} j_2 & j_1 & J \\ m_2 & m_1 & M \end{array} \right). \quad (\text{A.13})$$

With a 6j-symbol one can recouple three angular momenta

$$\langle [j_1, (j_2, j_3)j_{23}] j' m' | [(j_1, j_2)j_{12}, j_3] j m \rangle = \quad (\text{A.14})$$

$$= \delta_{jj'} \delta_{mm'} (-1)^{j_1+j_2+j_3+j} \sqrt{(2j_{12}+1)(2j_{23}+1)} \left(\begin{array}{ccc} j_1 & j_2 & j_{12} \\ j_3 & j & j_{23} \end{array} \right) \quad (\text{A.15})$$

$$= \delta_{jj'} \delta_{mm'} (-1)^{j_1+j_2+j_3+j} \hat{j}_{12} \hat{j}_{23} \left(\begin{array}{ccc} j_1 & j_2 & j_{12} \\ j_3 & j & j_{23} \end{array} \right), \quad (\text{A.16})$$

where we used the hat notation

$$\hat{x} = \sqrt{2x + 1}. \quad (\text{A.17})$$

Recoupling of coupling schemes with the 9j-symbol (see e.g. equation (5) of Varshalovich [159] page 334)

$$\langle [(j_1 j_2) j_{12}, (j_3 j_4) j_{34}] j m \mid [(j_1 j_3) j_{13}, (j_2 j_4) j_{24}] j' m' \rangle \quad (\text{A.18})$$

$$= \delta_{jj'} \delta_{mm'} \sqrt{(2j_{12} + 1)(2j_{13} + 1)(2j_{24} + 1)(2j_{34} + 1)} \begin{Bmatrix} j_1 & j_2 & j_{12} \\ j_3 & j_4 & j_{34} \\ j_{13} & j_{24} & j \end{Bmatrix} \quad (\text{A.19})$$

$$= \delta_{jj'} \delta_{mm'} \hat{j}_{12} \hat{j}_{13} \hat{j}_{24} \hat{j}_{34} \begin{Bmatrix} j_1 & j_2 & j_{12} \\ j_3 & j_4 & j_{34} \\ j_{13} & j_{24} & j \end{Bmatrix}. \quad (\text{A.20})$$

Useful symmetry relations of the 9j-symbol are found in Varshalovich [159] page 342, whereby the exchange of columns is of particular importance for us

$$\begin{Bmatrix} j_{11} & j_{12} & j_{13} \\ j_{21} & j_{22} & j_{23} \\ j_{31} & j_{32} & j_{33} \end{Bmatrix} = (-1)^{j_{11}+j_{12}+j_{13}+j_{21}+j_{22}+j_{23}+j_{31}+j_{32}+j_{33}} \begin{Bmatrix} j_{12} & j_{11} & j_{13} \\ j_{22} & j_{21} & j_{23} \\ j_{32} & j_{31} & j_{33} \end{Bmatrix}. \quad (\text{A.21})$$

A.5 | Harmonic Oscillator Brackets

We use the harmonic oscillator brackets (HOBs) [162] following [100], which allow to transform the HO quantum numbers between single and relative coordinates

$$|(n_1 l_1, n_2 l_2) \Lambda M_\Lambda\rangle = \sum_{N_{\text{cm}} L_{\text{cm}}, NL} \langle \langle N_{\text{cm}} L_{\text{cm}}, NL; \Lambda | n_1 l_1, n_2 l_2 \rangle \rangle_1 | (N_{\text{cm}} L_{\text{cm}}, NL) \Lambda M_\Lambda \rangle. \quad (\text{A.22})$$

In this work we use the following symmetry relation of the HOBs

$$\langle \langle n_1 l_1, n_2 l_2; \Lambda | NL, nl \rangle \rangle_d = (-1)^{L-\Lambda} \langle \langle n_2 l_2, n_1 l_1; \Lambda | NL, nl \rangle \rangle_{\frac{1}{d}}, \quad (\text{A.23})$$

see e.g. equation (3.62) of reference [157].

A.6 | Wigner-Eckart Theorem

The Wigner-Eckart theorem allows to reduce a spherical tensor operator T_q^k of rank k and projection q such that the dependence on the projection quantum numbers is fully described by a geometrical factor, which is given by a Clebsch-Gordan coefficient or a 3j-symbol

$$\langle \zeta' \mathcal{J}' \mathcal{M}_{\mathcal{J}'} \mid T_q^k \mid \zeta \mathcal{J} \mathcal{M}_{\mathcal{J}} \rangle = \hat{\mathcal{J}}'^{-1} c \left(\begin{array}{c} \mathcal{J} \\ \mathcal{M}_{\mathcal{J}} \end{array} \begin{array}{c} k \\ q \end{array} \middle| \begin{array}{c} \mathcal{J}' \\ \mathcal{M}_{\mathcal{J}'} \end{array} \right) \langle \zeta' \mathcal{J}' \parallel T^k \parallel \zeta \mathcal{J} \rangle \quad (\text{A.24})$$

$$= (-1)^{\mathcal{J}' - \mathcal{M}_{\mathcal{J}'}} \left(\begin{array}{c} \mathcal{J}' \\ -\mathcal{M}_{\mathcal{J}'} \end{array} \begin{array}{c} k \\ q \end{array} \begin{array}{c} \mathcal{J} \\ \mathcal{M}_{\mathcal{J}} \end{array} \right) \langle \zeta' \mathcal{J}' \parallel T^k \parallel \zeta \mathcal{J} \rangle. \quad (\text{A.25})$$

A.7 | Embedding an Operator That Depends Only on One Angular Momentum

According to Varshalovich [159] equation (40) of section 13.1.5 on page 481 the following relation holds true:

$$\langle n'_1 n'_2 (j'_1, j'_2) J' M' | O_q^k(1) | n_1 n_2 (j_1, j_2) J M \rangle = \quad (\text{A.26})$$

$$\delta_{j'_2 j_2} \delta_{n'_2 n_2} (-1)^{J+j'_1+j_2-k} \hat{J}_c \begin{pmatrix} J & k & J' \\ M & q & M' \end{pmatrix} \begin{Bmatrix} j_1 & j_2 & J \\ J' & k & j'_1 \end{Bmatrix} \langle n'_1 j'_1 || O^k(1) || n_1 j_1 \rangle. \quad (\text{A.27})$$

With the Wigner-Eckart theorem (appendix A.6) it follows that

$$\langle n'_1 n'_2 (j'_1, j'_2) J' M' | O_q^k(1) | n_1 n_2 (j_1, j_2) J M \rangle = \quad (\text{A.28})$$

$$\hat{j}'^{-1} c \begin{pmatrix} J & k & J' \\ M & q & M' \end{pmatrix} \langle n'_1 n'_2 (j'_1, j'_2) J' || O^k(1) || n_1 n_2 (j_1, j_2) J \rangle. \quad (\text{A.29})$$

In combination we get

$$\langle n'_1 n'_2 (j'_1, j'_2) J' || O^k(1) || n_1 n_2 (j_1, j_2) J \rangle = \quad (\text{A.30})$$

$$\delta_{j'_2 j_2} \delta_{n'_2 n_2} (-1)^{J+j'_1+j_2-k} \hat{j}' \hat{j} \begin{Bmatrix} j_1 & j_2 & J \\ J' & k & j'_1 \end{Bmatrix} \langle n'_1 j'_1 || O^k(1) || n_1 j_1 \rangle \quad (\text{A.31})$$

A.8 | M1 Operator with Spherical Tensor Matrix Elements Expressions

An alternative expression for the matrix elements of the leading $M_1^{\text{LO},2\text{b}}$ operator can be derived in spherical tensor notation. The starting point is the two-body $M_1^{\text{LO},2\text{b}}$ operator as given by

$$M_1^{\text{LO},2\text{b}} = \sqrt{\frac{3}{4\pi}} \left[\frac{1}{2} (g_p + g_n) S + \frac{1}{2} L + (g_p - g_n) \sum_{i=1}^2 s_i t_{3,i} + \frac{1}{2} L T_3 \right]. \quad (\text{A.32})$$

This leads us to

$$\begin{aligned} & \langle N(LS) J, T M_T || M_1^{\text{LO},2\text{b}} || N'(L'S') J', T' M'_T \rangle = \\ & \sqrt{\frac{3}{4\pi}} \left[\frac{1}{2} (g_p + g_n) (-1)^{L'+S'+J+1} \delta_{L,L'} \delta_{S,S'} \delta_{M_T, M'_T} \delta_{T, T'} \hat{J} \hat{J}' \hat{S} \begin{Bmatrix} S & J & L \\ J' & S & 1 \end{Bmatrix} \sqrt{S(S+1)} \right. \\ & + \frac{1}{2} (1 + M_T) (-1)^{L+S+J'+1} \delta_{L,L'} \delta_{S,S'} \delta_{M_T, M'_T} \delta_{T, T'} \hat{J} \hat{J}' \hat{L} \begin{Bmatrix} L & J & S \\ J' & L & 1 \end{Bmatrix} \sqrt{L(L+1)} \\ & + \sqrt{\frac{3}{8}} (g_p - g_n) (-1)^{L'+S'+J+1} \delta_{L,L'} \hat{J} \hat{J}' \hat{S} \hat{S}' \begin{Bmatrix} S & J & L' \\ J' & S' & 1 \end{Bmatrix} \begin{Bmatrix} 1/2 & S & 1/2 \\ S' & 1/2 & 1 \end{Bmatrix} \\ & \left. \times \left((-1)^{S'} - (-1)^S \right) \delta_{M_T, M'_T} (\delta_{T,1} \delta_{T',0} + \delta_{T,0} \delta_{T',1}) + \left((-1)^{S'} + (-1)^S \right) M_T \delta_{M_T, M'_T} \delta_{T', T} \right] \quad (\text{A.33}) \end{aligned}$$

with

$$\hat{x} = \sqrt{2x+1}. \quad (\text{A.34})$$

Bibliography

- [1] **R. B. Wiringa, V. G. J. Stoks, and R. Schiavilla.** *Accurate nucleon-nucleon potential with charge-independence breaking.* Phys. Rev. C, 51:38–51, Jan 1995. doi: 10.1103/PhysRevC.51.38. URL <https://link.aps.org/doi/10.1103/PhysRevC.51.38>.
- [2] **R. Machleidt.** *High-precision, charge-dependent Bonn nucleon-nucleon potential.* Phys. Rev. C, 63:024001, Jan 2001. doi: 10.1103/PhysRevC.63.024001. URL <https://link.aps.org/doi/10.1103/PhysRevC.63.024001>.
- [3] **N. Kalantar-Nayestanaki and E. Epelbaum.** *The three-nucleon system as a laboratory for nuclear physics: The need for 3N forces.* International Journal of Phytoremediation, 17(3):22–30, 2007. ISSN 15497879. doi: 10.1080/10506890701404222.
- [4] **S. C. Pieper, V. R. Pandharipande, R. B. Wiringa, and J. Carlson.** *Realistic models of pion-exchange three-nucleon interactions.* Phys. Rev. C, 64:014001, Jun 2001. doi: 10.1103/PhysRevC.64.014001. URL <https://link.aps.org/doi/10.1103/PhysRevC.64.014001>.
- [5] **R. Machleidt and D. Entem.** *Chiral effective field theory and nuclear forces.* Physics Reports, 503(1):1 – 75, 2011. ISSN 0370-1573. doi: <https://doi.org/10.1016/j.physrep.2011.02.001>. URL <http://www.sciencedirect.com/science/article/pii/S0370157311000457>.
- [6] **E. Epelbaum, H.-W. Hammer, and U.-G. Meißner.** *Modern theory of nuclear forces.* Rev. Mod. Phys., 81:1773–1825, Dec 2009. doi: 10.1103/RevModPhys.81.1773. URL <https://link.aps.org/doi/10.1103/RevModPhys.81.1773>.
- [7] **E. Epelbaum.** *Nuclear forces from chiral effective field theory: a primer.* jan 2010. URL <http://arxiv.org/abs/1001.3229>.
- [8] **S. Scherer and M. R. Schindler.** *A Primer for Chiral Perturbation Theory*, volume 830 of *Lecture Notes in Physics*. Springer Berlin Heidelberg, Berlin, Heidelberg, 2012. ISBN 978-3-642-19253-1. doi: 10.1007/978-3-642-19254-8. URL <http://link.springer.com/10.1007/978-3-642-19254-8>.
- [9] **R. Baron, P. Boucaud, P. Dimopoulos, R. Frezzotti, D. Palao, G. Rossi, F. Farchioni, G. Munster, T. Sudmann, V. Gimenez, G. Herdoiza, K. Jansen, V. Lubicz, S. Simula, C. Michael, L. Scorzato, A. Shindler, C. Urbach, and U. Weneer.** *Light meson physics from maximally twisted mass lattice QCD.* Journal of High Energy Physics, 2010(8), 2010. ISSN 10298479. doi: 10.1007/JHEP08(2010)097.
- [10] **T. Inoue, S. Aoki, T. Doi, T. Hatsuda, Y. Ikeda, N. Ishii, K. Murano, H. Nemura, and K. Sasaki.** *Equation of State for Nucleonic Matter and its Quark Mass Dependence from the Nuclear Force in Lattice QCD.* Phys. Rev. Lett., 111:112503, Sep 2013. doi: 10.1103/PhysRevLett.111.112503. URL <https://link.aps.org/doi/10.1103/PhysRevLett.111.112503>.

- [11] **S. R. Beane, E. Chang, S. Cohen, W. Detmold, H. W. Lin, K. Orginos, A. Parreño, M. J. Savage, and B. C. Tiburzi.** *Magnetic Moments of Light Nuclei from Lattice Quantum Chromodynamics.* Phys. Rev. Lett., 113:252001, Dec 2014. doi: 10.1103/PhysRevLett.113.252001. URL <https://link.aps.org/doi/10.1103/PhysRevLett.113.252001>.
- [12] **K. Orginos, A. Parreño, M. J. Savage, S. R. Beane, E. Chang, and W. Detmold.** *Two nucleon systems at $m_\pi \sim 450$ MeV from lattice QCD.* Phys. Rev. D, 92:114512, Dec 2015. doi: 10.1103/PhysRevD.92.114512. URL <https://link.aps.org/doi/10.1103/PhysRevD.92.114512>.
- [13] **E. Epelbaum, H. Krebs, and U.-G. Meißner.** *Improved chiral nucleon-nucleon potential up to next-to-next-to-next-to-leading order.* Eur. Phys. J. A 51, 53, 2015. doi: 10.1140/epja/i2015-15053-8. URL <https://doi.org/10.1140/epja/i2015-15053-8>.
- [14] **E. Epelbaum, H. Krebs, and U.-G. Meißner.** *Precision Nucleon-Nucleon Potential at Fifth Order in the Chiral Expansion.* Phys. Rev. Lett., 115:122301, Sep 2015. doi: 10.1103/PhysRevLett.115.122301. URL <https://link.aps.org/doi/10.1103/PhysRevLett.115.122301>.
- [15] **S. Binder, A. Calci, E. Epelbaum, R. J. Furnstahl, J. Golak, K. Hebel, H. Kamada, H. Krebs, J. Langhammer, S. Liebig, P. Maris, U.-G. Meißner, D. Minossi, A. Nogga, H. Potter, R. Roth, R. Skibiński, K. Topolnicki, J. P. Vary, and H. Witala.** *Few-nucleon systems with state-of-the-art chiral nucleon-nucleon forces.* Phys. Rev. C, 93:044002, Apr 2016. doi: 10.1103/PhysRevC.93.044002. URL <https://link.aps.org/doi/10.1103/PhysRevC.93.044002>.
- [16] **S. Binder, A. Calci, E. Epelbaum, R. J. Furnstahl, J. Golak, K. Hebel, T. Hüther, H. Kamada, H. Krebs, P. Maris, U.-G. Meißner, A. Nogga, R. Roth, R. Skibiński, K. Topolnicki, J. P. Vary, K. Vobig, and H. Witala.** *Few-nucleon and many-nucleon systems with semilocal coordinate-space regularized chiral nucleon-nucleon forces.* Phys. Rev. C, 98:014002, Jul 2018. doi: 10.1103/PhysRevC.98.014002. URL <https://link.aps.org/doi/10.1103/PhysRevC.98.014002>.
- [17] **R. J. Furnstahl, N. Klco, D. R. Phillips, and S. Wesolowski.** *Quantifying truncation errors in effective field theory.* Phys. Rev. C, 92:024005, Aug 2015. doi: 10.1103/PhysRevC.92.024005. URL <https://link.aps.org/doi/10.1103/PhysRevC.92.024005>.
- [18] **J. A. Melendez, S. Wesolowski, and R. J. Furnstahl.** *Bayesian truncation errors in chiral effective field theory: Nucleon-nucleon observables.* Phys. Rev. C, 96:024003, Aug 2017. doi: 10.1103/PhysRevC.96.024003. URL <https://link.aps.org/doi/10.1103/PhysRevC.96.024003>.
- [19] **J. A. Melendez, R. J. Furnstahl, D. R. Phillips, M. T. Pratola, and S. Wesolowski.** *Quantifying correlated truncation errors in effective field theory.* Physical Review C, 100(4):1–25, 2019. ISSN 24699993. doi: 10.1103/PhysRevC.100.044001.
- [20] **P. Navrátil, S. Quaglioni, I. Stetcu, and B. R. Barrett.** *Recent developments in no-core shell-model calculations.* Journal of Physics G: Nuclear and Particle Physics, 36(8):083101, may 2009. doi: 10.1088/0954-3899/36/8/083101. URL <https://doi.org/10.1088/0954-3899/36/8/083101>.

- [21] **B. R. Barrett, P. Navrátil, and J. P. Vary.** *Ab initio no core shell model.* Progress in Particle and Nuclear Physics, 69(1):131–181, 2013. ISSN 01466410. doi: 10.1016/j.ppnp.2012.10.003. URL <http://dx.doi.org/10.1016/j.ppnp.2012.10.003>.
- [22] **R. Roth.** *Importance truncation for large-scale configuration interaction approaches.* Phys. Rev. C, 79:064324, Jun 2009. doi: 10.1103/PhysRevC.79.064324. URL <https://link.aps.org/doi/10.1103/PhysRevC.79.064324>.
- [23] **R. Roth, T. Neff, and H. Feldmeier.** *Nuclear structure in the framework of the Unitary Correlation Operator Method.* Progress in Particle and Nuclear Physics, 65(1): 50 – 93, 2010. ISSN 0146-6410. doi: <https://doi.org/10.1016/j.ppnp.2010.02.003>. URL <http://www.sciencedirect.com/science/article/pii/S0146641010000335>.
- [24] **R. J. Furnstahl and K. Hebeler.** *New applications of renormalization group methods in nuclear physics.* Rep. Prog. Phys., 76:6301, Nov 2013. doi: 10.1088/0034-4885/76/12/126301. URL <https://iopscience.iop.org/article/10.1088/0034-4885/76/12/126301>.
- [25] **K. Suzuki and S. Y. Lee.** *Convergent Theory for Effective Interaction in Nuclei**. Progress of Theoretical Physics, 64(6):2091–2106, 12 1980. ISSN 0033-068X. doi: 10.1143/PTP.64.2091. URL <https://doi.org/10.1143/PTP.64.2091>.
- [26] **K. Suzuki and R. Okamoto.** *Degenerate Perturbation Theory in Quantum Mechanics.* Progress of Theoretical Physics, 70(2):439–451, 08 1983. ISSN 0033-068X. doi: 10.1143/PTP.70.439. URL <https://doi.org/10.1143/PTP.70.439>.
- [27] **H. Hergert, S. K. Bogner, S. Binder, A. Calci, J. Langhammer, R. Roth, and A. Schwenk.** *In-medium similarity renormalization group with chiral two- plus three-nucleon interactions.* Phys. Rev. C, 87:034307, Mar 2013. doi: 10.1103/PhysRevC.87.034307. URL <https://link.aps.org/doi/10.1103/PhysRevC.87.034307>.
- [28] **K. Tsukiyama, S. K. Bogner, and A. Schwenk.** *In-Medium Similarity Renormalization Group For Nuclei.* Phys. Rev. Lett., 106:222502, Jun 2011. doi: 10.1103/PhysRevLett.106.222502. URL <https://link.aps.org/doi/10.1103/PhysRevLett.106.222502>.
- [29] **H. Hergert, S. Binder, A. Calci, J. Langhammer, and R. Roth.** *Ab Initio Calculations of Even Oxygen Isotopes with Chiral Two-Plus-Three-Nucleon Interactions.* Phys. Rev. Lett., 110:242501, Jun 2013. doi: 10.1103/PhysRevLett.110.242501. URL <https://link.aps.org/doi/10.1103/PhysRevLett.110.242501>.
- [30] **H. Hergert, S. Bogner, T. Morris, A. Schwenk, and K. Tsukiyama.** *The In-Medium Similarity Renormalization Group: A novel ab initio method for nuclei.* Physics Reports, 621:165 – 222, 2016. ISSN 0370-1573. doi: <https://doi.org/10.1016/j.physrep.2015.12.007>. URL <http://www.sciencedirect.com/science/article/pii/S0370157315005414>. Memorial Volume in Honor of Gerald E. Brown.
- [31] **H. Hergert, S. K. Bogner, J. G. Lietz, T. D. Morris, S. Novario, N. M. Parzuchowski, and F. Yuan.** *In-Medium Similarity Renormalization Group Approach to the Nuclear Many-Body Problem.* Lect. Notes Phys., 936:477–570, 2017. doi: 10.1007/978-3-319-53336-0_10.

- [32] **K. Vobig**. *Electromagnetic Observables and Open-Shell Nuclei from the In-Medium No-Core Shell Model*. PhD thesis, Technische Universität Darmstadt, 2020. URL <http://tuprints.ulb.tu-darmstadt.de/11375/>.
- [33] **H. Hergert**. *A Guided Tour of ab initio Nuclear Many-Body Theory*. *Frontiers in Physics*, 8, 2020. ISSN 2296424X. doi: 10.3389/fphy.2020.00379.
- [34] **G. Hagen, T. Papenbrock, D. J. Dean, and M. Hjorth-Jensen**. *Ab initio coupled-cluster approach to nuclear structure with modern nucleon-nucleon interactions*. *Physical Review C - Nuclear Physics*, 82(3):1–22, 2010. ISSN 1089490X. doi: 10.1103/PhysRevC.82.034330.
- [35] **G. Hagen, T. Papenbrock, M. Hjorth-Jensen, and D. J. Dean**. *Coupled-cluster computations of atomic nuclei*. *Reports on Progress in Physics*, 77(9):096302, sep 2014. doi: 10.1088/0034-4885/77/9/096302. URL <https://doi.org/10.1088/2F0034-4885%2F77%2F9%2F096302>.
- [36] **E. Gebrerufael, K. Vobig, H. Hergert, and R. Roth**. *Ab Initio Description of Open-Shell Nuclei: Merging No-Core Shell Model and In-Medium Similarity Renormalization Group*. *Phys. Rev. Lett.*, 118:152503, Apr 2017. doi: 10.1103/PhysRevLett.118.152503. URL <https://link.aps.org/doi/10.1103/PhysRevLett.118.152503>.
- [37] **E. Gebrerufael**. *In-Medium No-Core Shell Model for Ab Initio Nuclear Structure Calculations*. PhD thesis, Technische Universität Darmstadt, 2017. URL <http://tuprints.ulb.tu-darmstadt.de/6910/>.
- [38] **J. Carlson, S. Gandolfi, F. Pederiva, S. C. Pieper, R. Schiavilla, K. E. Schmidt, and R. B. Wiringa**. *Quantum Monte Carlo methods for nuclear physics*. *Rev. Mod. Phys.*, 87:1067–1118, Sep 2015. doi: 10.1103/RevModPhys.87.1067. URL <https://link.aps.org/doi/10.1103/RevModPhys.87.1067>.
- [39] **J. Lynn, I. Tews, S. Gandolfi, and A. Lovato**. *Quantum Monte Carlo Methods in Nuclear Physics: Recent Advances*. *Annual Review of Nuclear and Particle Science*, 69(1):279–305, 2019. doi: 10.1146/annurev-nucl-101918-023600. URL <https://doi.org/10.1146/annurev-nucl-101918-023600>.
- [40] **D. R. Entem and R. Machleidt**. *Chiral 2π exchange at fourth order and peripheral NN scattering*. *Phys. Rev. C*, 66:014002, Jul 2002. doi: 10.1103/PhysRevC.66.014002. URL <https://link.aps.org/doi/10.1103/PhysRevC.66.014002>.
- [41] **P. Navrátil**. *Local three-nucleon interaction from chiral effective field theory*. *Few-Body Systems*, 41(3-4):117–140, 2007. ISSN 0177-7963. doi: 10.1007/s00601-007-0193-3. URL <http://dx.doi.org/10.1007/s00601-007-0193-3>.
- [42] **V. Lapoux, V. Somà, C. Barbieri, H. Hergert, J. D. Holt, and S. R. Stroberg**. *Radii and Binding Energies in Oxygen Isotopes: A Challenge for Nuclear Forces*. *Phys. Rev. Lett.*, 117:052501, Jul 2016. doi: 10.1103/PhysRevLett.117.052501. URL <https://link.aps.org/doi/10.1103/PhysRevLett.117.052501>.
- [43] **A. Cipollone, C. Barbieri, and P. Navrátil**. *Chiral three-nucleon forces and the evolution of correlations along the oxygen isotopic chain*. *Physical Review C - Nuclear Physics*, 92(1):1–12, 2015. ISSN 1089490X. doi: 10.1103/PhysRevC.92.014306.

- [44] **V. Somà, A. Cipollone, C. Barbieri, P. Navrátil, and T. Duguet.** *Chiral two- and three-nucleon forces along medium-mass isotope chains.* Phys. Rev. C, 89(6):1–5, 2014. ISSN 1089490X. doi: 10.1103/PhysRevC.89.061301.
- [45] **A. Ekström, G. R. Jansen, K. A. Wendt, G. Hagen, T. Papenbrock, B. D. Carlsson, C. Forssén, M. Hjorth-Jensen, P. Navrátil, and W. Nazarewicz.** *Accurate nuclear radii and binding energies from a chiral interaction.* Phys. Rev. C, 91:051301, May 2015. doi: 10.1103/PhysRevC.91.051301. URL <https://link.aps.org/doi/10.1103/PhysRevC.91.051301>.
- [46] **D. R. Entem, R. Machleidt, and Y. Nosyk.** *High-quality two-nucleon potentials up to fifth order of the chiral expansion.* Phys. Rev. C, 96:024004, Aug 2017. doi: 10.1103/PhysRevC.96.024004. URL <https://link.aps.org/doi/10.1103/PhysRevC.96.024004>.
- [47] *Low Energy Nuclear Physics International Collaboration.* www.lenpic.org. Accessed: 2021-04-11.
- [48] **E. Epelbaum, A. Nogga, W. Glöckle, H. Kamada, U.-G. Meißner, and H. Witała.** *Three-nucleon forces from chiral effective field theory.* Phys. Rev. C, 66:064001, Dec 2002. doi: 10.1103/PhysRevC.66.064001. URL <https://link.aps.org/doi/10.1103/PhysRevC.66.064001>.
- [49] **K. Hebeler, H. Krebs, E. Epelbaum, J. Golak, and R. Skibiński.** *Efficient calculation of chiral three-nucleon forces up to N^3LO for *ab initio* studies.* Phys. Rev. C, 91:044001, Apr 2015. doi: 10.1103/PhysRevC.91.044001. URL <https://link.aps.org/doi/10.1103/PhysRevC.91.044001>.
- [50] **L. E. Marcucci, M. Pervin, S. C. Pieper, R. Schiavilla, and R. B. Wiringa.** *Quantum Monte Carlo calculations of magnetic moments and $M1$ transitions in $A \leq 7$ nuclei including meson-exchange currents.* Phys. Rev. C, 78:065501, Dec 2008. doi: 10.1103/PhysRevC.78.065501. URL <https://link.aps.org/doi/10.1103/PhysRevC.78.065501>.
- [51] **S. Pastore, S. C. Pieper, R. Schiavilla, and R. B. Wiringa.** *Quantum Monte Carlo calculations of electromagnetic moments and transitions in $A \leq 9$ nuclei with meson-exchange currents derived from chiral effective field theory.* Phys. Rev. C, 87:035503, Mar 2013. doi: 10.1103/PhysRevC.87.035503. URL <https://link.aps.org/doi/10.1103/PhysRevC.87.035503>.
- [52] **R. Aaij and others.** *Observation of $J/\psi\phi$ Structures Consistent with Exotic States from Amplitude Analysis of $B^+ \rightarrow J/\psi\phi K^+$ Decays.* Phys. Rev. Lett., 118:022003, Jan 2017. doi: 10.1103/PhysRevLett.118.022003. URL <https://link.aps.org/doi/10.1103/PhysRevLett.118.022003>.
- [53] **LHCb collaboration.** *Observation of structure in the J/Ψ -pair mass spectrum.* Science Bulletin, 65(23):1983–1993, 2020. ISSN 2095-9273. doi: <https://doi.org/10.1016/j.scib.2020.08.032>. URL <https://www.sciencedirect.com/science/article/pii/S2095927320305685>.
- [54] **R. Aaij and others.** *Observation of a Narrow Pentaquark State, $P_c(4312)^+$, and of the Two-Peak Structure of the $P_c(4450)^+$.* Phys. Rev. Lett., 122:222001, Jun 2019. doi: 10.1103/PhysRevLett.122.222001. URL <https://link.aps.org/doi/10.1103/PhysRevLett.122.222001>.

- [55] **S. Bethke.** *Experimental tests of asymptotic freedom.* Progress in Particle and Nuclear Physics, 58(2):351–386, 2007. ISSN 01466410. doi: 10.1016/j.pnnp.2006.06.001.
- [56] **S. Weinberg.** *Phenomenological Lagrangians.* Physica A: Statistical Mechanics and its Applications, 96(1):327 – 340, 1979. ISSN 0378-4371. doi: [https://doi.org/10.1016/0378-4371\(79\)90223-1](https://doi.org/10.1016/0378-4371(79)90223-1). URL <http://www.sciencedirect.com/science/article/pii/0378437179902231>.
- [57] **J. Gasser and H. Leutwyler.** *Chiral perturbation theory to one loop.* Annals of Physics, 158(1):142 – 210, 1984. ISSN 0003-4916. doi: [https://doi.org/10.1016/0003-4916\(84\)90242-2](https://doi.org/10.1016/0003-4916(84)90242-2). URL <http://www.sciencedirect.com/science/article/pii/0003491684902422>.
- [58] **J. Gasser and H. Leutwyler.** *Chiral perturbation theory: Expansions in the mass of the strange quark.* Nuclear Physics B, 250(1):465 – 516, 1985. ISSN 0550-3213. doi: [https://doi.org/10.1016/0550-3213\(85\)90492-4](https://doi.org/10.1016/0550-3213(85)90492-4). URL <http://www.sciencedirect.com/science/article/pii/0550321385904924>.
- [59] **M. Tanabashi and others.** *Review of Particle Physics.* Phys. Rev. D, 98:030001, (2018) and 2019 update. doi: 10.1103/PhysRevD.98.030001. URL <https://link.aps.org/doi/10.1103/PhysRevD.98.030001>.
- [60] **A. Manohar and H. Georgi.** *Chiral quarks and the non-relativistic quark model.* Nuclear Physics B, 234(1):189 – 212, 1984. ISSN 0550-3213. doi: [https://doi.org/10.1016/0550-3213\(84\)90231-1](https://doi.org/10.1016/0550-3213(84)90231-1). URL <http://www.sciencedirect.com/science/article/pii/0550321384902311>.
- [61] **V. Bernard, N. Kaiser, J. Kambor, and U.-G. Meißner.** *Chiral structure of the nucleon.* Nuclear Physics B, 388(2):315–345, 1992. ISSN 0550-3213. doi: [https://doi.org/10.1016/0550-3213\(92\)90615-I](https://doi.org/10.1016/0550-3213(92)90615-I). URL <https://www.sciencedirect.com/science/article/pii/055032139290615I>.
- [62] **E. Jenkins and A. V. Manohar.** *Baryon chiral perturbation theory using a heavy fermion lagrangian.* Physics Letters B, 255(4):558–562, 1991. ISSN 0370-2693. doi: [https://doi.org/10.1016/0370-2693\(91\)90266-S](https://doi.org/10.1016/0370-2693(91)90266-S). URL <https://www.sciencedirect.com/science/article/pii/037026939190266S>.
- [63] **E. Epelbaum, H. Krebs, and P. Reinert.** *High-precision nuclear forces from chiral EFT: State-of-the-art, challenges and outlook.* pages 1–44, 2019. URL <http://arxiv.org/abs/1911.11875>.
- [64] **E. Epelbaum, W. Glöckle, and U.-G. Meißner.** *Nuclear forces from chiral Lagrangians using the method of unitary transformation (I): Formalism.* Nuclear Physics A, 637(1):107 – 134, 1998. ISSN 0375-9474. doi: [https://doi.org/10.1016/S0375-9474\(98\)00220-6](https://doi.org/10.1016/S0375-9474(98)00220-6). URL <http://www.sciencedirect.com/science/article/pii/S0375947498002206>.
- [65] **E. Epelbaum, W. Glöckle, and U.-G. Meißner.** *Nuclear forces from chiral Lagrangians using the method of unitary transformation II: The two-nucleon system.* Nuclear Physics A, 671(1):295 – 331, 2000. ISSN 0375-9474. doi: [https://doi.org/10.1016/S0375-9474\(99\)00821-0](https://doi.org/10.1016/S0375-9474(99)00821-0). URL <http://www.sciencedirect.com/science/article/pii/S0375947499008210>.

- [66] **S. Ôkubo**. *Diagonalization of Hamiltonian and Tamm-Dancoff Equation*. Progress of Theoretical Physics, 12(5):603–622, 11 1954. ISSN 0033-068X. doi: 10.1143/PTP.12.603. URL <https://doi.org/10.1143/PTP.12.603>.
- [67] **S. Weinberg**. *Nuclear forces from chiral lagrangians*. Physics Letters B, 251(2):288 – 292, 1990. ISSN 0370-2693. doi: [https://doi.org/10.1016/0370-2693\(90\)90938-3](https://doi.org/10.1016/0370-2693(90)90938-3). URL <http://www.sciencedirect.com/science/article/pii/0370269390909383>.
- [68] **S. Weinberg**. *Effective chiral lagrangians for nucleon-pion interactions and nuclear forces*. Nuclear Physics B, 363(1):3–18, 1991. ISSN 0550-3213. doi: [https://doi.org/10.1016/0550-3213\(91\)90231-L](https://doi.org/10.1016/0550-3213(91)90231-L). URL <https://www.sciencedirect.com/science/article/pii/055032139190231L>.
- [69] **S. Weinberg**. *Three-body interactions among nucleons and pions*. Physics Letters B, 295(1):114 – 121, 1992. ISSN 0370-2693. doi: [https://doi.org/10.1016/0370-2693\(92\)90099-P](https://doi.org/10.1016/0370-2693(92)90099-P). URL <http://www.sciencedirect.com/science/article/pii/037026939290099P>.
- [70] **H.-W. Hammer, S. König, and U. van Kolck**. *Nuclear effective field theory: Status and perspectives*. Rev. Mod. Phys., 92:025004, Jun 2020. doi: 10.1103/RevModPhys.92.025004. URL <https://link.aps.org/doi/10.1103/RevModPhys.92.025004>.
- [71] **J. Behrendt, E. Epelbaum, J. Gegelia, U. G. Meißner, and A. Nogga**. *Two-nucleon scattering in a modified Weinberg approach with a symmetry-preserving regularization*. European Physical Journal A, 52(9), 2016. ISSN 1434601X. doi: 10.1140/epja/i2016-16296-5.
- [72] **A. Dyhdalo, R. J. Furnstahl, K. Hebeler, and I. Tews**. *Regulator artifacts in uniform matter for chiral interactions*. Phys. Rev. C, 94:034001, Sep 2016. doi: 10.1103/PhysRevC.94.034001. URL <https://link.aps.org/doi/10.1103/PhysRevC.94.034001>.
- [73] **D. R. Entem and R. Machleidt**. *Accurate charge-dependent nucleon-nucleon potential at fourth order of chiral perturbation theory*. Phys. Rev. C, 68:041001, Oct 2003. doi: 10.1103/PhysRevC.68.041001. URL <https://link.aps.org/doi/10.1103/PhysRevC.68.041001>.
- [74] **R. Roth, S. Binder, K. Vobig, A. Calci, J. Langhammer, and P. Navrátil**. *Medium-Mass Nuclei with Normal-Ordered Chiral $NN+3N$ Interactions*. Phys. Rev. Lett., 109:052501, Jul 2012. doi: 10.1103/PhysRevLett.109.052501. URL <https://link.aps.org/doi/10.1103/PhysRevLett.109.052501>.
- [75] **D. Gazit, S. Quaglioni, and P. Navrátil**. *Three-Nucleon Low-Energy Constants from the Consistency of Interactions and Currents in Chiral Effective Field Theory*. Phys. Rev. Lett., 103:102502, Sep 2009. doi: 10.1103/PhysRevLett.103.102502. URL <https://link.aps.org/doi/10.1103/PhysRevLett.103.102502>.
- [76] **R. Roth, J. Langhammer, A. Calci, S. Binder, and P. Navrátil**. *Similarity-Transformed Chiral $NN + 3N$ Interactions for the *Ab Initio* Description of ^{12}C and ^{16}O* . Phys. Rev. Lett., 107:072501, Aug 2011. doi: 10.1103/PhysRevLett.107.072501. URL <https://link.aps.org/doi/10.1103/PhysRevLett.107.072501>.

- [77] **M. Hoferichter, J. Ruiz de Elvira, B. Kubis, and U.-G. Meißner.** *Matching Pion-Nucleon Roy-Steiner Equations to Chiral Perturbation Theory.* Phys. Rev. Lett., 115:192301, Nov 2015. doi: 10.1103/PhysRevLett.115.192301. URL <https://link.aps.org/doi/10.1103/PhysRevLett.115.192301>.
- [78] **P. Reinert, H. Krebs, and E. Epelbaum.** *Semilocal momentum-space regularized chiral two-nucleon potentials up to fifth order.* Eur. Phys. J. A 54, 86, 2018. doi: 10.1140/epja/i2018-12516-4. URL <https://doi.org/10.1140/epja/i2018-12516-4>.
- [79] **H. Krebs, A. Gasparyan, and E. Epelbaum.** *Chiral three-nucleon force at N^4LO : Longest-range contributions.* Phys. Rev. C, 85:054006, May 2012. doi: 10.1103/PhysRevC.85.054006. URL <https://link.aps.org/doi/10.1103/PhysRevC.85.054006>.
- [80] **R. Koch.** *A calculation of low-energy πN partial waves based on fixed- t analyticity.* Nuclear Physics A, 448(4):707 – 731, 1986. ISSN 0375-9474. doi: [https://doi.org/10.1016/0375-9474\(86\)90438-0](https://doi.org/10.1016/0375-9474(86)90438-0). URL <http://www.sciencedirect.com/science/article/pii/0375947486904380>.
- [81] **U. van Kolck.** *Few-nucleon forces from chiral Lagrangians.* Phys. Rev. C, 49:2932–2941, Jun 1994. doi: 10.1103/PhysRevC.49.2932. URL <https://link.aps.org/doi/10.1103/PhysRevC.49.2932>.
- [82] **V. Bernard, E. Epelbaum, H. Krebs, and U.-G. Meißner.** *Subleading contributions to the chiral three-nucleon force: Long-range terms.* Phys. Rev. C, 77:064004, Jun 2008. doi: 10.1103/PhysRevC.77.064004. URL <https://link.aps.org/doi/10.1103/PhysRevC.77.064004>.
- [83] **V. Bernard, E. Epelbaum, H. Krebs, and U.-G. Meißner.** *Subleading contributions to the chiral three-nucleon force. II. Short-range terms and relativistic corrections.* Phys. Rev. C, 84:054001, Nov 2011. doi: 10.1103/PhysRevC.84.054001. URL <https://link.aps.org/doi/10.1103/PhysRevC.84.054001>.
- [84] **J. L. Friar.** *Equivalence of nonstatic two-pion-exchange nucleon-nucleon potentials.* Phys. Rev. C, 60:034002, Jul 1999. doi: 10.1103/PhysRevC.60.034002. URL <https://link.aps.org/doi/10.1103/PhysRevC.60.034002>.
- [85] **R. Machleidt.** *Private communication.*
- [86] **L. Girlanda, A. Kievsky, and M. Viviani.** *Subleading contributions to the three-nucleon contact interaction.* Phys. Rev. C, 84:014001, Jul 2011. doi: 10.1103/PhysRevC.84.014001. URL <https://link.aps.org/doi/10.1103/PhysRevC.84.014001>.
- [87] **H. Krebs, A. Gasparyan, and E. Epelbaum.** *Chiral three-nucleon force at N^4LO . II. Intermediate-range contributions.* Phys. Rev. C, 87:054007, May 2013. doi: 10.1103/PhysRevC.87.054007. URL <https://link.aps.org/doi/10.1103/PhysRevC.87.054007>.
- [88] **E. Epelbaum, J. Golak, K. Hebeler, H. Kamada, H. Krebs, U. G. Meißner, A. Nogga, P. Reinert, R. Skibiński, K. Topolnicki, Y. Volkotrub, and H. Witała.** *Towards high-order calculations of three-nucleon scattering in chiral effective field theory.* 2019. URL <http://arxiv.org/abs/1907.03608>.

- [89] **P. Navrátil, G. P. Kamuntavičius, and B. R. Barrett.** *Few-nucleon systems in a translationally invariant harmonic oscillator basis.* Phys. Rev. C, 61:044001, Mar 2000. doi: 10.1103/PhysRevC.61.044001. URL <https://link.aps.org/doi/10.1103/PhysRevC.61.044001>.
- [90] **E. Epelbaum, J. Golak, K. Hebeler, T. Hüther, H. Kamada, H. Krebs, P. Maris, U.-G. Meißner, A. Nogga, R. Roth, R. Skibiński, K. Topolnicki, J. P. Vary, K. Vobig, and H. Witała.** *Few- and many-nucleon systems with semilocal coordinate-space regularized chiral two- and three-body forces.* Phys. Rev. C, 99:024313, Feb 2019. doi: 10.1103/PhysRevC.99.024313. URL <https://link.aps.org/doi/10.1103/PhysRevC.99.024313>.
- [91] **P. Maris, E. Epelbaum, R. J. Furnstahl, J. Golak, K. Hebeler, T. Hüther, H. Kamada, H. Krebs, U.-G. Meißner, J. A. Melendez, A. Nogga, P. Reinert, R. Roth, R. Skibiński, V. Soloviov, K. Topolnicki, J. P. Vary, Y. Volkotrub, H. Witała, and T. Wolfgruber.** *Light nuclei with semilocal momentum-space regularized chiral interactions up to third order.* pages 1–21, 2020. URL <http://arxiv.org/abs/2012.12396>.
- [92] **K. Hebeler.** *Three-nucleon forces: Implementation and applications to atomic nuclei and dense matter.* Physics Reports, 2020. ISSN 03701573. doi: 10.1016/j.physrep.2020.08.009.
- [93] **C. Lanczos.** *An iteration method for the solution of the eigenvalue problem of linear differential and integral operators.* J. Res. Natl. Bur. Stand. B, 45:255–282, 1950. doi: 10.6028/jres.045.026.
- [94] **P. Maris, J. P. Vary, and A. M. Shirokov.** *Ab initio no-core full configuration calculations of light nuclei.* Phys. Rev. C, 79:014308, Jan 2009. doi: 10.1103/PhysRevC.79.014308. URL <https://link.aps.org/doi/10.1103/PhysRevC.79.014308>.
- [95] **P. Christians.** *Development of a Bayesian Analysis for the No-Core Shell Model.* Bachelor’s thesis, Technische Universität Darmstadt, 5 2020.
- [96] **G. A. Negoita, J. P. Vary, G. R. Luecke, P. Maris, A. M. Shirokov, I. J. Shin, Y. Kim, E. G. Ng, C. Yang, M. Lockner, and G. M. Prabhu.** *Deep learning: Extrapolation tool for ab initio nuclear theory.* Phys. Rev. C, 99:054308, May 2019. doi: 10.1103/PhysRevC.99.054308. URL <https://link.aps.org/doi/10.1103/PhysRevC.99.054308>.
- [97] **C. Wenz.** *Applications of Machine Learning in NCSM Calculations.* Bachelor’s thesis, Technische Universität Darmstadt, 10 2020.
- [98] **E. A. Hylleraas and B. Undheim.** *Numerische Berechnung der 2 S-Terme von Ortho- und Par-Helium.* Zeitschrift für Physik, 65(11-12):759–772, 1930. ISSN 14346001. doi: 10.1007/BF01397263. URL <https://doi.org/10.1007/BF01397263>.
- [99] **D. Gloeckner and R. Lawson.** *Spurious center-of-mass motion.* Physics Letters B, 53(4):313 – 318, 1974. ISSN 0370-2693. doi: [https://doi.org/10.1016/0370-2693\(74\)90390-6](https://doi.org/10.1016/0370-2693(74)90390-6). URL <http://www.sciencedirect.com/science/article/pii/0370269374903906>.

- [100] **G. Kamuntavičius, R. Kalinauskas, B. Barrett, S. Mickevičius, and D. Germanas.** *The general harmonic-oscillator brackets: compact expression, symmetries, sums and Fortran code.* Nuclear Physics A, 695(1–4):191 – 201, 2001. ISSN 0375-9474. doi: [http://dx.doi.org/10.1016/S0375-9474\(01\)01101-0](http://dx.doi.org/10.1016/S0375-9474(01)01101-0). URL <http://www.sciencedirect.com/science/article/pii/S0375947401011010>.
- [101] **A. Tichai, J. Müller, K. Vobig, and R. Roth.** *Natural orbitals for ab initio no-core shell model calculations.* Phys. Rev. C, 99:034321, Mar 2019. doi: 10.1103/PhysRevC.99.034321. URL <https://link.aps.org/doi/10.1103/PhysRevC.99.034321>.
- [102] **A. Tichai, J. Langhammer, S. Binder, and R. Roth.** *Hartree–Fock many-body perturbation theory for nuclear ground-states.* Physics Letters B, 756:283 – 288, 2016. ISSN 0370-2693. doi: <https://doi.org/10.1016/j.physletb.2016.03.029>. URL <http://www.sciencedirect.com/science/article/pii/S0370269316002008>.
- [103] **S. D. Glazek and K. G. Wilson.** *Perturbative renormalization group for Hamiltonians.* Phys. Rev. D, 49:4214–4218, Apr 1994. doi: 10.1103/PhysRevD.49.4214. URL <http://link.aps.org/doi/10.1103/PhysRevD.49.4214>.
- [104] **F. Wegner.** *Flow-equations for Hamiltonians.* Annalen der Physik, 506(2):77–91, 1994. ISSN 1521-3889. doi: 10.1002/andp.19945060203. URL <http://dx.doi.org/10.1002/andp.19945060203>.
- [105] **F. J. Wegner.** *Flow equations for Hamiltonians.* Nuclear Physics B - Proceedings Supplements, 90(0):141 – 146, 2000. ISSN 0920-5632. doi: 10.1016/S0920-5632(00)00911-7. URL <http://www.sciencedirect.com/science/article/pii/S0920563200009117>.
- [106] **T. Hüther.** *Alternative Generators for the Similarity Renormalization Group.* Master’s thesis, Technische Universität Darmstadt, 3 2016.
- [107] **S. Szpigel and R. J. Perry.** *The Similarity Renormalization Group.* Quantum Field Theory, A 20th Century Profile, 2000. URL <https://arxiv.org/abs/hep-ph/0009071>.
- [108] **A. Calci.** *Evolved Chiral Hamiltonians at the Three-Body Level and Beyond.* PhD thesis, Technische Universität Darmstadt, Juni 2014. URL <http://tuprints.ulb.tu-darmstadt.de/4069/>.
- [109] **M. Dupper.** *Similarity Renormalization Group transformation chiraler Wechselwirkungen.* Bachelor’s thesis, Technische Universität Darmstadt, 2 2018.
- [110] **E. Schultheis.** *Evolution of the Hamiltonian via the Similarity Renormalization Group.* Bachelor’s thesis, Technische Universität Darmstadt, 9 2019.
- [111] **T. Wolfgruber.** *Phenomenological Four-Nucleon Interactions in the NCSM.* Master’s thesis, Technische Universität Darmstadt, 10 2019.
- [112] **H. Hergert, S. K. Bogner, T. D. Morris, S. Binder, A. Calci, J. Langhammer, and R. Roth.** *Ab initio multireference in-medium similarity renormalization group calculations of even calcium and nickel isotopes.* Phys. Rev. C, 90:041302, Oct 2014. doi: 10.1103/PhysRevC.90.041302. URL <https://link.aps.org/doi/10.1103/PhysRevC.90.041302>.

- [113] **S. Binder, J. Langhammer, A. Calci, and R. Roth.** *Ab initio path to heavy nuclei.* Physics Letters B, 736:119 – 123, 2014. ISSN 0370-2693. doi: <https://doi.org/10.1016/j.physletb.2014.07.010>. URL <http://www.sciencedirect.com/science/article/pii/S0370269314004961>.
- [114] **S. Binder, P. Piecuch, A. Calci, J. Langhammer, P. Navrátil, and R. Roth.** *Extension of coupled-cluster theory with a noniterative treatment of connected triply excited clusters to three-body Hamiltonians.* Physical Review C, 88(5):054319, nov 2013. ISSN 0556-2813. doi: 10.1103/PhysRevC.88.054319. URL <https://link.aps.org/doi/10.1103/PhysRevC.88.054319>.
- [115] **R. Roth.** *Towards Accurate Calculations of Medium-Mass Nuclei.* Presentation at Progress in Ab Initio Techniques in Nuclear Physics, TRIUMF, Vancouver, CA, March 5, 2020. URL https://abinitio.triumf.ca/2020/rroth_triumf2020_web.pdf.
- [116] **J. L. Friar, J. Martorell, and D. W. L. Sprung.** *Nuclear sizes and the isotope shift.* Phys. Rev. A, 56:4579–4586, Dec 1997. doi: 10.1103/PhysRevA.56.4579. URL <https://link.aps.org/doi/10.1103/PhysRevA.56.4579>.
- [117] **R. Pohl, A. Antognini, F. D. Amaro, D. S. Covita, A. Dax, S. Dhawan, L. M. P. Fernandes, A. Giesen, T. Graf, P. Indelicato, L. Julien, C.-y. Kao, P. Knowles, E.-o. L. Bigot, T. W. Ha, A. M. Lopes, L. Ludhova, C. M. B. Monteiro, T. Nebel, Y.-w. Liu, F. C. A. Veloso, and F. Kottmann.** *The size of the proton.* 466(July):1–5, 2010. doi: 10.1038/nature09250.
- [118] **P. J. Mohr, D. B. Newell, and B. N. Taylor.** *CODATA recommended values of the fundamental physical constants: 2014.* Rev. Mod. Phys., 88:035009, Sep 2016. doi: 10.1103/RevModPhys.88.035009. URL <https://link.aps.org/doi/10.1103/RevModPhys.88.035009>.
- [119] **I. Angeli and K. Marinova.** *Table of experimental nuclear ground state charge radii: An update.* Atomic Data and Nuclear Data Tables, 99(1):69 – 95, 2013. ISSN 0092-640X. doi: <https://doi.org/10.1016/j.adt.2011.12.006>. URL <http://www.sciencedirect.com/science/article/pii/S0092640X12000265>.
- [120] **T. Hüther, K. Vobig, K. Hebeler, R. Machleidt, and R. Roth.** *Family of chiral two- plus three-nucleon interactions for accurate nuclear structure studies.* Physics Letters B, 808:135651, 2020. ISSN 0370-2693. doi: <https://doi.org/10.1016/j.physletb.2020.135651>. URL <https://www.sciencedirect.com/science/article/pii/S0370269320304548>.
- [121] **D. Gazit, S. Quaglioni, and P. Navrátil.** *Erratum: Three-Nucleon Low-Energy Constants from the Consistency of Interactions and Currents in Chiral Effective Field Theory [Phys. Rev. Lett. 103, 102502 (2009)].* Phys. Rev. Lett., 122:029901, Jan 2019. doi: 10.1103/PhysRevLett.122.029901. URL <https://link.aps.org/doi/10.1103/PhysRevLett.122.029901>.
- [122] **R. Roth, A. Calci, J. Langhammer, and S. Binder.** *Evolved chiral NN + 3N Hamiltonians for ab initio nuclear structure calculations.* Phys. Rev. C, 90:024325, Aug 2014. doi: 10.1103/PhysRevC.90.024325. URL <https://link.aps.org/doi/10.1103/PhysRevC.90.024325>.

- [123] **E. D. Jurgenson, P. Navrátil, and R. J. Furnstahl.** *Evolution of Nuclear Many-Body Forces with the Similarity Renormalization Group.* Phys. Rev. Lett., 103:082501, Aug 2009. doi: 10.1103/PhysRevLett.103.082501. URL <https://link.aps.org/doi/10.1103/PhysRevLett.103.082501>.
- [124] **E. D. Jurgenson, P. Navrátil, and R. J. Furnstahl.** *Evolving nuclear many-body forces with the similarity renormalization group.* Phys. Rev. C, 83:034301, Mar 2011. doi: 10.1103/PhysRevC.83.034301. URL <https://link.aps.org/doi/10.1103/PhysRevC.83.034301>.
- [125] **E. D. Jurgenson, P. Maris, R. J. Furnstahl, P. Navrátil, W. E. Ormand, and J. P. Vary.** *Structure of p -shell nuclei using three-nucleon interactions evolved with the similarity renormalization group.* Phys. Rev. C, 87:054312, May 2013. doi: 10.1103/PhysRevC.87.054312. URL <https://link.aps.org/doi/10.1103/PhysRevC.87.054312>.
- [126] **M. Piarulli, A. Baroni, L. Girlanda, A. Kievsky, A. Lovato, E. Lusk, L. E. Marcucci, S. C. Pieper, R. Schiavilla, M. Viviani, and R. B. Wiringa.** *Light-Nuclei Spectra from Chiral Dynamics.* Phys. Rev. Lett., 120:052503, Feb 2018. doi: 10.1103/PhysRevLett.120.052503. URL <https://link.aps.org/doi/10.1103/PhysRevLett.120.052503>.
- [127] **V. Efimov and E. G. Tkachenko.** *On the correlation between the triton binding energy and the neutron-deuteron doublet scattering length.* Few-Body Systems, 4(2): 71–88, Jun 1988. ISSN 1432-5411. doi: 10.1007/BF01076330. URL <https://doi.org/10.1007/BF01076330>.
- [128] **C. Drischler, K. Hebeler, and A. Schwenk.** *Chiral Interactions up to Next-to-Next-to-Next-to-Leading Order and Nuclear Saturation.* Physical Review Letters, 122(4):42501, 2019. ISSN 10797114. doi: 10.1103/PhysRevLett.122.042501. URL <https://doi.org/10.1103/PhysRevLett.122.042501>.
- [129] **J. Hoppe, C. Drischler, K. Hebeler, A. Schwenk, and J. Simonis.** *Probing chiral interactions up to next-to-next-to-next-to-leading order in medium-mass nuclei.* Phys. Rev. C, 100:024318, Aug 2019. doi: 10.1103/PhysRevC.100.024318. URL <https://link.aps.org/doi/10.1103/PhysRevC.100.024318>.
- [130] **A. Nogga, H. Kamada, and W. Glöckle.** *Modern Nuclear Force Predictions for the α Particle.* Phys. Rev. Lett., 85:944–947, Jul 2000. doi: 10.1103/PhysRevLett.85.944. URL <https://link.aps.org/doi/10.1103/PhysRevLett.85.944>.
- [131] **L. Platter, H.-W. Hammer, and U.-G. Meißner.** *On the correlation between the binding energies of the triton and the α -particle.* Physics Letters B, 607(3):254 – 258, 2005. ISSN 0370-2693. doi: <https://doi.org/10.1016/j.physletb.2004.12.068>. URL <http://www.sciencedirect.com/science/article/pii/S0370269304017484>.
- [132] **S. Schulz.** *Four-Nucleon Forces in Ab Initio Nuclear Structure.* PhD thesis, Technische Universität Darmstadt, Februar 2018. URL <http://tuprints.ulb.tu-darmstadt.de/7384/>.
- [133] **D. Tilley, C. Cheves, J. Godwin, G. Hale, H. Hofmann, J. Kelley, C. Sheu, and H. Weller.** *Energy levels of light nuclei $A=5, 6, 7$.* Nuclear Physics A, 708(1): 3 – 163, 2002. ISSN 0375-9474. doi: [https://doi.org/10.1016/S0375-9474\(02\)00597-3](https://doi.org/10.1016/S0375-9474(02)00597-3). URL <http://www.sciencedirect.com/science/article/pii/S0375947402005973>.

- [134] **D. Tilley, J. Kelley, J. Godwin, D. Millener, J. Purcell, C. Sheu, and H. Weller.** *Energy levels of light nuclei $A=8,9,10$.* Nuclear Physics A, 745(3):155 – 362, 2004. ISSN 0375-9474. doi: <https://doi.org/10.1016/j.nuclphysa.2004.09.059>. URL <http://www.sciencedirect.com/science/article/pii/S0375947404010267>.
- [135] **P. Reinert and E. Epelbaum.** *Private communication.*
- [136] **A. Calci and R. Roth.** *Sensitivities and correlations of nuclear structure observables emerging from chiral interactions.* Phys. Rev. C, 94:014322, Jul 2016. doi: 10.1103/PhysRevC.94.014322. URL <https://link.aps.org/doi/10.1103/PhysRevC.94.014322>.
- [137] **N. M. Parzuchowski, S. R. Stroberg, P. Navrátil, H. Hergert, and S. K. Bogner.** *Ab initio electromagnetic observables with the in-medium similarity renormalization group.* Phys. Rev. C, 96:034324, Sep 2017. doi: 10.1103/PhysRevC.96.034324. URL <https://link.aps.org/doi/10.1103/PhysRevC.96.034324>.
- [138] **I. J. Shin, Y. Kim, P. Maris, J. P. Vary, C. Forssén, J. Rotureau, and N. Michel.** *Ab initio core solutions for 6Li .* Journal of Physics G: Nuclear and Particle Physics, 44(7):075103, may 2017. doi: 10.1088/1361-6471/aa6cb7. URL <https://doi.org/10.1088/1361-6471/aa6cb7>.
- [139] **A. J. Siegert.** *Note on the interaction between nuclei and electromagnetic radiation.* Physical Review, 52(8):787–789, 1937. ISSN 0031899X. doi: 10.1103/PhysRev.52.787.
- [140] **M. Piarulli, L. Girlanda, L. E. Marcucci, S. Pastore, R. Schiavilla, and M. Viviani.** *Electromagnetic structure of $A = 2$ and 3 nuclei in chiral effective field theory.* Phys. Rev. C, 87:014006, Jan 2013. doi: 10.1103/PhysRevC.87.014006. URL <https://link.aps.org/doi/10.1103/PhysRevC.87.014006>.
- [141] **T.-S. Park, D.-P. Min, and M. Rho.** *Chiral Lagrangian Approach to Exchange Vector Currents in Nuclei.* Nuclear Physics A, 596(3-4):515–552, may 1995. ISSN 03759474. doi: 10.1016/0375-9474(95)00406-8. URL [http://dx.doi.org/10.1016/0375-9474\(95\)00406-8](http://dx.doi.org/10.1016/0375-9474(95)00406-8).
- [142] **S. Kölling, E. Epelbaum, H. Krebs, and U. G. Meißner.** *Two-pion exchange electromagnetic current in chiral effective field theory using the method of unitary transformation.* Physical Review C - Nuclear Physics, 80(4):1–14, 2009. ISSN 1089490X. doi: 10.1103/PhysRevC.80.045502.
- [143] **S. Kölling, E. Epelbaum, H. Krebs, and U.-G. Meißner.** *Two-nucleon electromagnetic current in chiral effective field theory: One-pion exchange and short-range contributions.* Phys. Rev. C, 84:054008, Nov 2011. doi: 10.1103/PhysRevC.84.054008. URL <https://link.aps.org/doi/10.1103/PhysRevC.84.054008>.
- [144] **P. Ring and P. Schuck.** *The Nuclear Many-Body Problem.* Springer, 1980.
- [145] **T. E. O. Ericson and W. Weise.** *Pions and Nuclei*, volume 74. Clarendon Press, Oxford, UK, 1988. ISBN 978-0-19-852008-5.
- [146] **H. Arenhövel.** *Mr. Maxwell’s journey into hadron country (electromagnetic currents in nuclei).* Czechoslovak Journal of Physics, 43(3-4):207–258, mar 1993. ISSN 0011-4626. doi: 10.1007/BF01589846. URL <http://link.springer.com/10.1007/BF01589846>.

- [147] **S. Pastore, R. Schiavilla, and J. L. Goity.** *Electromagnetic two-body currents of one- and two-pion range.* Phys. Rev. C, 78:064002, Dec 2008. doi: 10.1103/PhysRevC.78.064002. URL <https://link.aps.org/doi/10.1103/PhysRevC.78.064002>.
- [148] **S. Pastore, L. Girlanda, R. Schiavilla, M. Viviani, and R. B. Wiringa.** *Electromagnetic currents and magnetic moments in chiral effective field theory (χ EFT).* Phys. Rev. C, 80:034004, Sep 2009. doi: 10.1103/PhysRevC.80.034004. URL <https://link.aps.org/doi/10.1103/PhysRevC.80.034004>.
- [149] **S. Bacca and S. Pastore.** *Electromagnetic reactions on light nuclei.* Journal of Physics G: Nuclear and Particle Physics, 41(12):123002, nov 2014. doi: 10.1088/0954-3899/41/12/123002. URL <https://doi.org/10.1088/0954-3899/41/12/123002>.
- [150] **C. Stumpf.** *Nuclear Spectra and Strength Distributions from Importance-Truncated Configuration-Interaction Methods.* PhD thesis, Technische Universität Darmstadt, April 2018. URL <http://tuprints.ulb.tu-darmstadt.de/7571/>.
- [151] **L. Mertes.** *Precision Calculation of Electromagnetic Observables for Light Nuclei.* Master's thesis, Technische Universität Darmstadt, 2017.
- [152] **E. Fermi.** *Nuclear Physics.* University of Chicago Press, 1950.
- [153] **J. D. Jackson.** *Classical Electrodynamics.* John Wiley, 3 edition, 1998. ISBN 978-0-471-30932-1.
- [154] **R. H. Dalitz.** *The sachs exchange moment.* Physical Review, 95(3):799–800, 1954. ISSN 0031899X. doi: 10.1103/PhysRev.95.799.
- [155] **O. J. Hernandez.** *Nuclear structure corrections in muonic atoms with statistical uncertainty quantification.* PhD thesis, The University of British Columbia, 2019.
- [156] **R. Roth, P. Papakonstantinou, N. Paar, H. Hergert, T. Neff, and H. Feldmeier.** *Hartree-Fock and many body perturbation theory with correlated realistic NN interactions.* Phys. Rev. C, 73:044312, Apr 2006. doi: 10.1103/PhysRevC.73.044312. URL <https://link.aps.org/doi/10.1103/PhysRevC.73.044312>.
- [157] **J. Langhammer.** *Consistent chiral three-nucleon interactions in nuclear structure.* Master's thesis, Technische Universität Darmstadt, 9 2010.
- [158] **A. Calci.** *Ab Initio Nuclear Structure with SRG-Transformed Chiral NN plus NNN Interactions.* Master's thesis, Technische Universität Darmstadt, 9 2010.
- [159] **D. Varshalovich, A. Moskalev, and V. Khersonskii.** *Quantum Theory Of Angular Momentum.* World Scientific, 1988.
- [160] **U. Friman-Gayer, C. Romig, T. Hüther, K. Albe, S. Bacca, T. Beck, M. Berger, J. Birkhan, K. Hebeler, O. J. Hernandez, J. Isaak, S. König, N. Pietralla, P. C. Ries, J. Rohrer, R. Roth, D. Savran, M. Scheck, A. Schwenk, R. Seutin, and V. Werner.** *Role of Chiral Two-Body Currents in ${}^6\text{Li}$ Magnetic Properties in Light of a New Precision Measurement with the Relative Self-Absorption Technique.* Phys. Rev. Lett., 126:102501, Mar 2021. doi: 10.1103/PhysRevLett.126.102501. URL <https://link.aps.org/doi/10.1103/PhysRevLett.126.102501>.

-
- [161] **N. J. Stone.** *INDC International Nuclear Data Committee TABLE OF NUCLEAR MAGNETIC DIPOLE AND ELECTRIC QUADRUPOLE MOMENTS.* INDC International Nuclear Data Committee, 0658(February):171, 2014. URL <http://www-nds.iaea.org/publications>.
- [162] **M. Moshinsky.** *Transformation brackets for harmonic oscillator functions.* Nuclear Physics, 13(1):104–116, oct 1959. ISSN 00295582. doi: 10.1016/0029-5582(59)90143-9. URL <https://linkinghub.elsevier.com/retrieve/pii/0029558259901439>.

Danksagung

Hiermit möchte ich mich bei allen bedanken, die mich beim Verfassen dieser Arbeit begleitet haben.

Mein besonderer Dank gilt Robert Roth, der mich in seiner Arbeitsgruppe aufgenommen hat. Ich danke dir für die langjährige gute Betreuung und die hilfreichen Diskussionen, Ratschläge und Korrekturen. Diese haben maßgeblich zum Gelingen der Arbeit beigetragen.

Vielen Dank auch an Kai Hebler für die Übernahme des Zweitgutachtens sowie der Bereitstellung von Matrixelementen, ohne die diese Arbeit nicht möglich gewesen wäre.

Der ganzen Arbeitsgruppe danke ich auch ganz herzlich. Ihr habt eine Atmosphäre geschaffen, in der ich mich immer wohlfühlt habe. Für gemeinsame Diskussionen und Fehlersuche, die Zeit am Rande von Konferenzenbesuchen, Spieleabende und Spaziergänge geht ein Dank an Laura Mertes, Stefan Alexa, Klaus Vobig, Christina Stumpf, Roland Wirth, Stefan Schulz, Tobias Wolfgruber, Marco Knöll, Julius Müller, Alexander Tichai, Eskendr Gebrerufael und Tobias Mongelli. Den vorangegangenen Generationen, sowie den Master- und Bachelorstudenten, die wichtige Vorarbeiten für meine Arbeit geleistet haben, gehört auch mein Dank.

Ich danke ebenfalls Oscar Javier Hernandez für die Bereitstellung von Matrixelementen für die Strombeiträge. Thank you very much.

Allen Beteiligten in LENPIC danke ich für die gemeinsame Zusammenarbeit, insbesondere Patrik Reinert und Evgeny Eppelbaum.

Meiner Familie und meinen Freunden, danke dafür, dass ihr da seid, wenn man euch braucht.

Und zu guter Letzt geht ein herzlicher Dank an Ann-Kathrin Grefe dafür, dass du mich in allem unterstützt.

Lebenslauf

Persönliche Daten

Name: Thomas Hüther
Geburtsdatum: 05.11.1988
Geburtsort: Offenbach am Main
Nationalität: deutsch

Akademische Ausbildung

2016 - 2021 Promotion Physik, TU Darmstadt
2012 - 2016 Masterstudium Physik, TU Darmstadt, Abschluss: M.Sc.
2009 - 2012 Bachelorstudium Physik, TU Darmstadt, Abschluss: B.Sc.
2005 - 2008 Gewerblich-technische Schulen Offenbach, Abschluss: Abitur

Veröffentlichungen

- 1) P. Maris, E. Epelbaum, R. J. Furnstahl, J. Golak, K. Hebeler, T. Hüther, H. Kamada, H. Krebs, Ulf-G. Meißner, J. A. Melendez, A. Nogga, P. Reinert, R. Roth, R. Skibinski, V. Soloviov, K. Topolnicki, J. P. Vary, Yu. Volkotrub, H. Witala, T. Wolfgruber, [Light nuclei with semilocal momentum-space regularized chiral interactions up to third order](#), *Phys. Rev. C* 103, 054001 (2021)
- 2) U. Friman-Gayer, C. Romig, T. Hüther, K. Albe, S. Bacca, T. Beck, M. Berger, J. Birkhan, K. Hebeler, O. J. Hernandez, S. König, N. Pietralla, P. C. Ries, J. Rohrer, R. Roth, D. Savran, M. Scheck, A. Schwenk, R. Seutin, V. Werner, [Role of chiral two-body currents in 6-Li magnetic properties in light of a new precision measurement with the relative self-absorption technique](#), *Phys. Rev. Lett.* 126, 102501 (2021)
- 3) S. Heil, M. Petri, K. Vobig, D. Bazin, J. Belarge, P. Bender, B. A. Brown, R. Elder, B. Elman, A. Gade, T. Haylett, J. D. Holt, T. Hüther, A. Hufnagel, H. Iwasaki, N. Kobayashi, C. Loelius, B. Longfellow, E. Lunderberg, M. Mathy, J. Menendez, S. Paschalis, R. Roth, A. Schwenk, J. Simonis, I. Syndikus, D. Weisshaar, K. Whitmore, [Electromagnetic properties of 21-O for benchmarking nuclear Hamiltonians](#), *Phys. Lett. B* 809, 135678 (2020)
- 4) T. Hüther, K. Vobig, K. Hebeler, R. Machleidt, R. Roth, [Family of Chiral Two- plus Three-Nucleon Interactions for Accurate Nuclear Structure Studies](#), *Phys. Lett. B.* 808, 135651 (2020)
- 5) A. D'Alessio, T. Mongelli, M. Arnold, S. Bassauer, J. Birkhan, M. Hilcker, T. Hüther, J. Isaak, L. Jürgensen, T. Klaus, P. von Neumann-Cosel, N. Pietralla, V. Yu. Ponomarev, P. C. Ries, R. Roth, M. Singer, G. Steinhilber, K. Vobig, V. Werner, [Precision](#)

- measurement of the E2 transition strength to the 2+1 state of 12-C, *Phys. Rev. C* 102, 011302(R) (2020)
- 6) B. Maaß, T. Hüther, J. Krause, J. Krämer, K. König, A. Lovato, P. Müller, M. Puchalski, K. Pachucki, R. Roth, R. Sanchez, F. Sommer, R.B. Wiringa, W. Nörtershäuser, **Nuclear Charge Radii of 10,11-B**, *Phys. Rev. Lett.* 122, 182501 (2019)
- 7) E. Epelbaum, J. Golak, K. Hebeler, T. Hüther, H. Kamada, H. Krebs, P. Maris, U.-G. Meißner, A. Nogga, R. Roth, R. Skibinski, K. Topolnicki, J. P. Vary, K. Vobig, H. Witala, **Few- and many-nucleon systems with semilocal coordinate-space regularized chiral two- and three-body forces**, *Phys. Rev. C* 99, 024313 (2019)
- 8) S. Binder, A. Calci, E. Epelbaum, R.J. Furnstahl, J. Golak, K. Hebeler, T. Hüther, H. Kamada, H. Krebs, P. Maris, U.-G. Meißner, A. Nogga, R. Roth, R. Skibinski, K. Topolnicki, J.P. Vary, K. Vobig, H. Witala **Few- and Many-Nucleon Systems with Semilocal Coordinate-Space Regularized Chiral Nucleon-Nucleon Forces**, *Phys. Rev. C* 98, 014002 (2018)

Erklärung gemäß §9 Promotionsordnung

Hiermit versichere ich, dass ich die vorliegende Dissertation selbstständig angefertigt und keine anderen als die angegebenen Quellen und Hilfsmittel verwendet habe. Alle wörtlichen und paraphrasierten Zitate wurden angemessen kenntlich gemacht. Die Arbeit hat bisher noch nicht zu Prüfungszwecken gedient.

Datum, Ort

Unterschrift